

UNIVERSIDADE DE LISBOA
INSTITUTO SUPERIOR TÉCNICO

**Development of the instrumentation and
readout schemes of MARTA, an upgrade
of the Pierre Auger Observatory**

Ricardo Jorge Barreira Luz

Supervisor: Doctor Pedro Jorge dos Santos de Assis
Co-Supervisor: Doctor Pedro Miguel Félix Brogueira

Thesis approved in public session to obtain the PhD Degree in
Technological Physics Engineering

Jury final classification: Pass with Distinction

2020

UNIVERSIDADE DE LISBOA
INSTITUTO SUPERIOR TÉCNICO

**Development of the instrumentation and
readout schemes of MARTA, an upgrade
of the Pierre Auger Observatory**

Ricardo Jorge Barreira Luz

Supervisor: Doctor Pedro Jorge dos Santos de Assis

Co-Supervisor: Doctor Pedro Miguel Félix Brogueira

Thesis approved in public session to obtain the PhD Degree in
Technological Physics Engineering

Jury final classification: Pass with Distinction

Jury

Chairperson: Doctor Mário João Martins Pimenta, Instituto Superior Técnico, Universidade de Lisboa

Members of the Committee:

Doctor Paulo Jorge Ribeiro da Fonte, Instituto Superior de Engenharia de Coimbra, Instituto Politécnico de Coimbra

Doctor Patrícia Carla Serrano Gonçalves, Instituto Superior Técnico, Universidade de Lisboa

Doctor Luís Humberto Viseu Melo, Instituto Superior Técnico, Universidade de Lisboa

Doctor Pedro Jorge dos Santos de Assis, Instituto Superior Técnico, Universidade de Lisboa

Doctor Pierre Andréas Michel Barrillon, Centre de Physique des Particules de Marseille, Laboratory of the CNRS/ University of Air-Marseille, France

Doctor Federico Andrés Sanchez, ITeDA - Instituto de Tecnologías en Detección y Astropartículas, Argentina

Funding institutions: Grant PD/BD/113488/2015 from FCT - Fundação para a Ciência e Tecnologia and IDPASC Portugal.

Resumo

O Observatório Pierre Auger é um detetor híbrido que estuda as cascatas de partículas criadas na interação dos raios cósmicos de alta energia com a atmosfera da Terra, combinando duas das técnicas de maior sucesso utilizadas para medir estas partículas: detetores de superfície (SD), que medem as partículas no chão com tanques de Cherenkov, e detetores de fluorescência (FD), que captam a luz de fluorescência emitida pelo azoto atmosférico quando este é excitado pelas partículas da cascata. Apesar de o Observatório ter sido fundamental ao publicar alguns dos mais importantes resultados experimentais em raios cósmicos de alta energia, ainda existem várias questões em aberto. Uma delas é sobre o modo como a cascata de partículas se desenvolve, questão que é crucial na operação do Observatório. Nomeadamente, existe uma discrepância entre o número de muões medidos pelo detetor de superfície e o número previsto pelos modelos que descrevem as cascatas. Os muões são essenciais no desenvolvimento da cascata, visto que, sendo sempre resultado do decaimento dos hádrons, permitem estudar as suas interações.

MARTA (acrónimo para Muon Array with RPCs for Tagging Air showers) propõe fazer uma medida direta, independente e precisa da componente muónica das cascatas. Com MARTA é esperado conseguir, não só perceber a causa desta discrepância, mas também estudar as interações hadrónicas, melhorar a sensibilidade dos detetores às diferentes composições dos raios cósmicos e reduzir as incertezas sistemáticas das diferentes medidas. A proposta é adicionar detetores do tipo RPC (acrónimo para Resistive Plate Chamber) por baixo dos detetores de superfície do Observatório. Desta forma, todas as outras componentes da cascata são absorvidas na água, enquanto os muões a atravessam e são detetados outra vez pelas RPCs. RPCs são detetores gasosos de partículas carregadas utilizados em diversas aplicações, conhecidos por serem robustos, baratos, terem altas eficiências de deteção, e uma excelente resolução espacial e temporal. Devido às suas características, estes detetores são maioritariamente utilizados em condições laboratoriais. Porém, durante o processo de desenvolvimento de MARTA, foi mostrado que as RPCs podem ser operadas nas condições ambientais adversas que são características de experiências como o Observatório Pierre Auger.

O objetivo desta tese é o desenvolvimento da front-end utilizada para adquirir os dados de MARTA. O sistema tem que conseguir discriminar e medir a carga dos sinais rápidos que são gerados na RPC, ter baixo consumo de energia e ser compacto de forma a respeitar os requisitos da operação de detetores no campo, e ser estável e fiável para poder ser operado com o mínimo de manutenção possível. A solução encontrada que preenche todos os requisitos foi utilizar um ASIC, que faz a digitalização dos sinais da RPC, e uma FPGA para gerir as aquisições, bem como o armazenamento e transferência de dados. No total, três versões do sistema foram produzidas e testadas, dois protótipos e uma versão final. Firmware e software foram desenvolvidos para correr a aquisição e controlar todos os componentes da front-end. O sistema foi validado, mostrando ser capaz que medir não só o número de partículas que atravessam o detetor, mas também a carga que estas induzem na RPC. Por fim, as aplicações da front-end foram descritas, incluindo uma pequena matriz de sete estações onde a versão final da board vai ser instalada. O objetivo principal destas estações será estudar o conceito de MARTA e o quão útil será a medição simultânea das RPCs com os tanques. Também vai servir para continuar a estudar o desempenho das RPCs e calibrar outros detetores instalados na mesma região. Além disso, este sistema foi também utilizado num hodoscópio que vai testar os novos cintiladores do Observatório e num detetor que vai estudar uma mina inativa utilizando tomografia de muões.

Palavras-chave: Aquisição de dados; Eletrónica de front-end; Detetores de partículas; Detetores RPC; Projecto MARTA; Medição da componente muónica das cascatas atmosféricas; Detetor de superfície; Observatório Pierre Auger; Raios Cósmicos de Altas Energias.

Abstract

The Pierre Auger Observatory is a hybrid detector that studies the extensive air showers (EAS) produced in the interaction of the highest energy cosmic rays with the Earth's atmosphere. It combines two of the most successful techniques used to detect this phenomenon: a Surface Detector (SD), that samples the particles at the ground using water-Cherenkov tanks (WCD), and a Fluorescence Detector (FD), that collects the fluorescence light emitted by the atmospheric nitrogen excited by the shower's particles. Although the Observatory has been successful and has published some of the most important results in experimental ultra high energy cosmic rays (UHECR), there are still many open questions. One of them is about the development of the air shower, which is fundamental for the Observatory's operation. Namely, there is a known discrepancy between the number of muons measured by the Observatory and the ones predicted in the models developed to describe the EAS. Muons are essential in the shower development since they are one of the best links to the hadronic interactions.

The Muon Array with RPCs for Tagging Air showers (MARTA), proposes to perform a direct, independent, and accurate measurement of the muonic content of the EAS. With it, it is expected to understand not only what might cause this discrepancy, but also be able to study hadronic interactions at the highest energies, improve the detector's composition sensitivity, and reduce the systematic uncertainties of many different measurements. MARTA proposes to add Resistive Plate Chambers (RPCs) underneath the Observatory's WCD to perform this measurement. This way, all other detectable components of the air shower will be absorbed by the water mass, while the muons transverse it to be detected again by the RPCs. RPCs are widely used gaseous detectors of charged particles, that are known for being robust, low-cost, have high detection efficiency, and excellent spatial and time resolutions. Due to their characteristics, these detectors have mostly been used in laboratory conditions. However, during the development process of MARTA, it has been proven that they can be operated in the harsh environmental conditions, that are typical of field operation in experiments like the Pierre Auger Observatory.

The objective of this thesis was the development of the MARTA front-end acquisition system. It had to be able to discriminate and measure the charge of the fast avalanche pulses generated in the RPC, be low power and compact to comply with the demands of field operation, as well as stable and reliable for low maintenance operation. The solution found that filled all the requirements had its two main components, an ASIC to perform the digitization of the RPC signals, and an FPGA to manage the acquisition as well as data storage and transfer. During the development process, two prototypes and a final version were produced, tested, and debugged. Custom firmware and software were written to run the acquisition and control all the components. The system was validated, showing that it was able to successfully measure not only the particle hits in the detector but also the charge induced. Lastly, the applications of the MARTA front-end were described that include an engineering array (EA) of seven stations, where the production version of the board will be installed. The main goal of this array is to study the MARTA concept performance and how useful the combined measurement can be. It will also be used to keep studying the RPCs in the field and to cross-calibrate other detectors installed in the same region of the array. The system was also installed in a hodoscope that will be used to test the Observatory's new scintillators, as well as in a detector that will be used to study a decommissioned mine using muon tomography.

Keywords: Data acquisition; Front-end electronics; Particle detectors; RPC detectors; MARTA enhancement; Measurement of the muonic component of air showers; Surface Detector; Pierre Auger Observatory; Ultra High Energy Cosmic Rays.

Acknowledgements

I would like to thank my supervisors Pedro Assis and Pedro Brogueira, firstly for the opportunity to this work, but also all the support, guidance and patience, without which this thesis could not be done.

A big thank you to Miguel, Zé Carlos, and Luís Mendes for their work, encouragement and valuable help. Without such a great team, this thesis would not exist. We all know that this work is as much as mine as it is yours.

Thank you to Liliana and Ruben for being the best office mates one could ask for. Not only for always be available to answer my sometimes naive questions but also for enduring me, my loud music and the floor kicking noises that came with it.

Special thanks to everyone at LIP's Auger group, Bernardo, Felix, Lorenzo, Mario, Pedro Abreu, Raul, and Sofia. Your availability and support were essential for this work.

A special thanks to Marco, with whom I shared the experience of being a PhD student. Although we end up never working together, all your support and your aptitude to listen and help me with all my problems were essential in this process.

Thank you to everyone at the Coimbra RPC group and workshop who always receive me well during my visits. Special thanks to Alberto and Luís Lopes for their help and availability to always answer my questions about RPCs.

Thank you to the Omega group for their support during this development.

Thank you to all the colleagues at the Pierre Auger Collaboration. Special thanks to the Observatory's staff and the ITeDA colleagues who were always gracious during my times in Argentina.

Thank you to all the colleagues at CBPF for their support during my stays in Rio.

Thank you to everyone at LIP. A special thanks to Natalia, João Pedro and Ofélia at LIP's secretary who were always available to help with anything I needed.

Thank you to LIP's computing group for their patience. Here I have to mention Aparício, Hugo, Nuno, João Paulo and Samuel, who help me solve countless problems through the years.

Thank you to all the LIP and IDPASC students, with whom I shared many workshops, schools and even lunches and coffee breaks. You are too many to mention, but without your support and experience sharing, none of this would be possible.

Um obrigado especial ao Pinela, Foka, Andreia, Borges e Tiago Gil, por serem melhores amigos do que eu sou. Sem o vosso apoio e amizade tinha sido muito mais difícil. Muito obrigado por todos os almoços e jantares, concertos, voltas de bicicleta, e viagens que me ajudaram a esquecer que tinha uma tese para acabar.

Muito obrigado aos meus colegas e amigos do técnico Valadeiro, Rafael e Brás. Podemos estar todos em sítios diferentes na vida, 5 anos depois de acabarmos o mestrado, mas sem o vosso encorajamento e ajuda não estaria a acabar esta tese.

Obrigado a toda a minha família, pais, irmãos, primos e tios que sempre me apoiaram e nunca questionaram as minhas decisões. Um grande obrigado aos meus pais, Maria Antónia e Jorge, e ao meu irmão Luís por toda a ajuda não só nesta fase da minha vida, mas desde sempre. Se cheguei tão longe devo-o inteiramente a vocês.

Thank you again to Luís Luz for helping edit most of the pictures in this work.

Lastly, I acknowledge the financial support given by the Portuguese Fundação para a Ciência e Tecnologia (FCT) and IDPASC Portugal, under grant PD/BD/113488/2015.

Contents

| | |
|---|--------------|
| List of Figures | xiii |
| List of Tables | xxiii |
| List of Abbreviations | xxv |
| 1 Introduction | 1 |
| 2 Cosmic rays | 5 |
| 2.1 Historical review of cosmic-ray studies | 5 |
| 2.2 Cosmic Rays characteristics | 6 |
| 2.3 Extensive air showers | 7 |
| 2.4 Detection techniques | 11 |
| 2.4.1 Direct detection | 11 |
| 2.4.2 Ground based indirect detection | 11 |
| 2.4.2.1 Particle detectors | 13 |
| 2.4.2.2 Light detectors | 14 |
| 2.4.2.3 Radio detectors | 15 |
| 3 Pierre Auger Observatory | 17 |
| 3.1 Detectors | 17 |
| 3.1.1 Surface Detector | 19 |
| 3.1.2 Fluorescence Detector | 20 |
| 3.1.3 Scintillator Surface Detector | 21 |
| 3.1.4 Other detectors | 22 |
| 3.1.4.1 AERA | 22 |
| 3.1.4.2 AMIGA | 22 |
| 3.2 Data acquisition and triggers | 23 |
| 3.2.1 SD signal digitization and triggers | 24 |
| 3.2.2 FD signal digitization and triggers | 25 |
| 3.3 Event reconstruction | 26 |
| 3.3.1 SD reconstruction | 26 |
| 3.3.2 FD reconstruction | 28 |
| 3.4 Selected results | 29 |
| 3.4.1 Energy spectrum | 30 |

| | | |
|----------|--|-----------|
| 3.4.2 | Mass composition | 31 |
| 3.4.3 | Arrival Directions | 32 |
| 3.4.4 | Number of muons | 32 |
| 4 | The MARTA enhancement | 35 |
| 4.1 | Concept and design | 36 |
| 4.2 | Station description | 37 |
| 4.3 | Expected performance | 40 |
| 4.3.1 | Station performance | 40 |
| 4.3.2 | Array performance | 41 |
| 4.3.3 | Combined measurement | 42 |
| 4.4 | Engineering array | 43 |
| 5 | Resistive Plate Chambers | 47 |
| 5.1 | Signal generation | 48 |
| 5.2 | Applications | 52 |
| 5.3 | Signal readout | 53 |
| 5.3.1 | Avalanche mode | 54 |
| 5.3.2 | Streamer mode | 56 |
| 5.4 | MARTA RPC | 57 |
| 6 | Prototype readout electronics for MARTA | 65 |
| 6.1 | Description | 65 |
| 6.1.1 | Front-end | 66 |
| 6.1.2 | Motherboard | 67 |
| 6.2 | Characterization | 68 |
| 6.2.1 | Test bench description | 69 |
| 6.2.2 | Gain | 70 |
| 6.2.3 | Noise | 73 |
| 6.2.4 | Crosstalk | 73 |
| 6.2.5 | Trigger efficiency | 74 |
| 6.2.6 | Propagation time | 75 |
| 6.2.7 | Power consumption | 76 |
| 6.2.8 | Summary | 77 |
| 6.3 | PREC applications | 77 |
| 7 | MARTA front-end | 81 |
| 7.1 | Requirements | 82 |
| 7.2 | MAROC | 84 |
| 7.3 | Design and prototypes | 87 |
| 7.4 | Firmware and software implementation | 91 |
| 7.4.1 | Module 1: Communication | 92 |

| | | |
|-----------|---|------------|
| 7.4.1.1 | USB | 92 |
| 7.4.1.2 | LVDS | 93 |
| 7.4.2 | Module 2: ASIC configuration | 95 |
| 7.4.3 | Module 3: Hit measurement | 96 |
| 7.4.4 | Module 4: Charge measurement | 98 |
| 7.4.5 | Other modules | 101 |
| 8 | Performance and test results of the front-end | 103 |
| 8.1 | Hit measurement | 104 |
| 8.1.1 | RPC efficiency | 104 |
| 8.1.2 | Trigger efficiency | 107 |
| 8.2 | Charge measurement | 109 |
| 8.2.1 | Using generated signals | 111 |
| 8.2.2 | Using RPC signals | 114 |
| 8.2.2.1 | Hold delay and threshold optimization | 115 |
| 8.2.2.2 | Charge distribution for different reduced electric fields | 118 |
| 8.3 | Differential lines | 120 |
| 8.4 | Summary | 122 |
| 9 | Applications | 123 |
| 9.1 | Engineering array | 123 |
| 9.2 | Hodoscope | 126 |
| 9.2.1 | Prototype setup | 126 |
| 9.2.2 | Final setup | 131 |
| 9.2.2.1 | Simulation | 133 |
| 9.3 | Muon tomography | 139 |
| 9.4 | Summary | 144 |
| 10 | Conclusions | 145 |
| | Appendices | 149 |
| | A - MAROC configurable parameters | 151 |
| | B - Hodoscope trajectory calculations | 153 |

List of Figures

| | | |
|-----|--|----|
| 2.1 | Cosmic ray energy spectrum for $E > 10^{12}$ eV. It shows a compilation of data points obtained by different experiments. The flux was multiplied by $E^{2.5}$ to accentuate the spectrum feature, like the <i>knee</i> at $\sim 5 \times 10^{15}$ eV, and the <i>ankle</i> at $\sim 5 \times 10^{18}$ eV. For energies greater than $\sim 5 \times 10^{19}$ eV a strong suppression is noticeable. Taken from [20]. | 7 |
| 2.2 | Extensive air shower representation. After the first interaction the particles created can be divided into three components: electromagnetic, hadronic and muonic. An undetectable neutrino component is also present. Taken from [25]. | 8 |
| 2.3 | Average lateral (left) and longitudinal (right) shower profiles for a vertical proton-induced shower of 10^{19} eV. The lateral distribution is calculated using the depth of the Pierre Auger Observatory (see chapter 3). Taken from [20]. | 10 |
| 2.4 | Schematic view of some detectors used to perform direct measurements of cosmic rays. FERMI-LAT: the ACD, the TKR and the CAL. AMS-02: the TRD, the TOF, the tracker layers, the ECAL and the RICH. CREAM-II: the TCD, the CD, the SCD and the CAL. PAMELA: the TOF scintillators (S1–S3), the TKR, the CAL and the neutron detector. In the case of PAMELA and AMS-02, the magnets are not represented. Taken from [42]. | 12 |
| 2.5 | Schematic overview of the ground detection techniques. Taken from [43] and [44]. | 13 |
| 3.1 | Layout of the Pierre Auger Observatory. Each black dot corresponds to one of the 1660 SD stations. In blue are the four FD telescopes and respective field of view. The laser facilities CLF and XLF are marked, as well as the additional HEAT telescope, the AMIGA and AERA arrays, and the BLS. Taken from [1]. | 18 |
| 3.2 | Representation of a hybrid event in the Pierre Auger Observatory. One of the FD sites detects the EAS using the fluorescence light emitted in the atmosphere while the SD stations measure the particle when they hit the ground. The red line represents the shower axis. Taken from [63]. | 19 |
| 3.3 | WCD part of the SD. Left: A line of SD stations in the typical landscape of the Observatory’s site. Right: Picture of an SD station in the field and its main components. Taken from [1]. | 20 |

| | | |
|------|--|----|
| 3.4 | FD. Left: FD building and communication antenna at the Coihueco site. Right: Schematic view of the telescope with a description of its main components. Taken from [1]. | 21 |
| 3.5 | A SD station with an SSD scintillator on top. Left: Drawing of the tank and all its components with the new detector on top. Right: An SD station in the field with the scintillator installed. Taken from [64]. | 22 |
| 3.6 | The SD local and array level triggers. Left: The 3 trigger levels of the surface array. T1 and T2 are station triggers and T3 is an array trigger generated by the CDAS. The two main types of T1s, ToT and TH are shown. The recently implemented T1 trigger, ToTd and MoPS, are not represented but follow the same sequence as the ToT. Right: The two T3 pattern, ToT2C ₁ &3C ₂ (circles) and 2C ₁ &3C ₂ &4C ₄ (squares). These figures are based on the ones presented in [1]. | 25 |
| 3.7 | SD reconstruction. Left: Schematic representation of the evolution of the shower front. Right: Example of an LDF fit. The estimated value of the shower size S(1000) is indicated. Taken from [1]. | 27 |
| 3.8 | Left: Correlation between S ₃₈ and the FD energy. The data points are hybrid events. Right: Energy resolution of the SD estimated from hybrid events when the FD resolution is fixed to 7.6%. Taken from [77]. | 28 |
| 3.9 | FD reconstruction. Left: Diagram of the geometrical shower reconstruction of the FD. Right: Reconstructed longitudinal profile: energy deposited as a function of the atmospheric depth. Taken from [67] and [1]. | 29 |
| 3.10 | Energy spectrum measured by the Pierre Auger Observatory. Left: Spectra measured with different analysis techniques. Right: Combination of the several spectra in the left plot. Taken from [77]. | 30 |
| 3.11 | Measurements of $\langle X_{\max} \rangle$ (left) and $\sigma(X_{\max})$ (right) compared to the predictions for proton and iron nuclei of the hadronic interaction models EPOS-LHC, Sibyll 2.3c and QGSJetII-04. Taken from [86]. | 31 |
| 3.12 | Sky map in galactic coordinates showing the cosmic-ray flux for energies above 8×10^{18} eV smoothed with a 45° top-hat function. The galactic centre is at the origin. The cross indicates the measured dipole direction; the contours denote the 68% and 95% confidence level regions. Taken from [3]. | 32 |
| 3.13 | The Pierre Auger Observatory results for the average logarithmic muon content $\langle \ln R_{\mu} \rangle$ as a function of the average maximum shower depth $\langle X_{\max} \rangle$ at 10^{19} eV. The lines denote the distinct models' predictions for different primary compositions. Taken from [93] (updated). | 33 |

- 4.1 Representation of the MARTA station, illustrating its concept. Four RPCs (each with an area of $1.5 \times 1.2 \text{ m}^2$) are placed under a WCD. The top of the concrete structure is a square with side length of 3.6 m and a height of 15cm. The total height of the structure is 40 cm. The water inside the tank forms a cylinder with 1.2 m of height and 3.6 m of diameter. Taken from [4]. 36
- 4.2 Schematic representation of the MARTA station. Four modules (blue), containing the RPC sensitive volume, readout grid, detector monitoring, data acquisition, power, and HV, are placed below the WCD. A Central Unit (green) manages the modules and works as an interface with the WCD. . . . 38
- 4.3 Left: Mass crossed by inclined particles, with a zenith angle of 40° , before hitting the RPCs. The circle indicates the area covered by the WCD. Right: Simulated traces of the WCD and the RPC signals. Taken from [4]. 41
- 4.4 LDF of the muon density. Left: Simulated result of the RPC hits density as a function of the shower core distance. A proton shower with $E = 10^{19.8} \text{ eV}$ and $\theta = 38^\circ$ was used. The RPC hit density is given in m^2 . Right: Results of the mean ρ_{1000} and β for different energy and composition showers. Multiple showers (~ 300) were simulated for each point. Taken from [4]. 42
- 4.5 MARTA EA. Left: Representation of the EA. The seven stations are laid out in a hexagonal configuration with one in the middle. These are stations of the Infill array, meaning they are 750 m apart. The total area occupied is 1.46 km^2 . Right: Map with the stations where the EA will be installed. The MARTA stations are represented with orange circles. The other stations of the Infill are the blue circles. For reference, the yellow marker shows the Coihueco FD site. 43
- 4.6 Number of events expected for different primary energy in the MARTA EA. The red line shows the events with triggered MARTA stations while the black line shows the number of events where the core of the EAS is expected to be inside the MARTA hexagon. Taken from [114]. 44
- 4.7 Peter Mazur SD station in the Infill with MARTA RPCs installed inside the support concrete structure. Extra solar panels and batteries were mounted to not interfere with the standard operation of this WCD. 45
- 5.1 Cross-section of the original single gap RPC (left) and the first RPC configuration with two gaps (right). In both cases bakelite was used as resistive plates. Based on the drawings presented in [95] and [118]. 47
- 5.2 RPC avalanche models applied to detector data. Left: Charge versus applied voltage fitted to the logistic model function presented in equation 5.1. Taken from [129]. Right: Charge spectrum of the RPC signals (data from [130]) fitted to the gamma distribution presented in 5.2. Taken from [131]. 50

| | | |
|------|---|----|
| 5.3 | RPC signals for a single gap detector with different HVs applied. Top left: 9.4 kV applied. Avalanche signal. Top right: 9.6 kV applied. Avalanche and streamer signal separated. Bottom left: 10.2 kV applied. Avalanche and streamer signal closer together. Bottom right: 10.2 kV applied. Avalanche and streamer signal merged. Taken from [137]. | 51 |
| 5.4 | Transverse view of the ATLAS muon spectrometer. RPCs are indicated. Taken from [155] | 53 |
| 5.5 | Block diagram of the HARDROC 3B analog part. Taken from [186]. | 55 |
| 5.6 | Block diagram of a FEERIC channel. Taken from [188]. | 55 |
| 5.7 | Block diagram of a HADES FEE channel. Taken from [195]. | 56 |
| 5.8 | Schematic drawing with the dimensions of the first MARTA prototype. The gas gap and glass dimensions are different from the ones chosen for the production version (1 mm gas gap and 1.2×1.5 m ² glasses). Taken from [96]. | 58 |
| 5.9 | MARTA RPC. Left: Readout plane configuration and detector dimensions. Right: Schematic of the detector aluminium box, readout plane, sensors layer, and detector volume. Taken from [4] and [98]. | 58 |
| 5.10 | 3D CAD of the aluminium box where the sensitive volume and the readout pad plane are placed. The small extra compartment houses the electronics subsystems: HV (red), gas monitoring bubbler block (yellow), front-end board (centre green board), PSU, and other monitoring (left green boards). Taken from [5]. | 58 |
| 5.11 | Avalanche (right) and streamer (left) signals measured with a Rhode & Schwarz RTO 1014 oscilloscope [200]. | 59 |
| 5.12 | The charge spectrum of MARTA RPCs measured in the laboratory for four months. There is a clear separation between the avalanche spectrum (left) and the streamer spectrum (right). Taken from [97]. | 60 |
| 5.13 | Laboratory test of MARTA RPCs. The top four plots show the efficiency, charge and streamer fraction as a function of the E/N as well as the efficiency vs the charge. The middle and bottom plot show the results of the dynamic HV adjustment. Taken from [97] and [98]. | 61 |
| 5.14 | Performance of an RPC in the field, operating at 4 cc/min, for more than a year and a half. The temperature and pressure inside the aluminium box are shown, as well as the HV, adjusted to keep the E/N constant (left). On the right is shown the distribution of E/N since March 2016. Taken from [5]. | 63 |
| 5.15 | Detector efficiency measured in the Observatory's site. Data taking suffered several interruptions during the one and a half year period due to readout system malfunctions. The efficiency was kept stable over time, with an average of 86.2%. Taken from [5]. | 63 |

| | | |
|-----|--|----|
| 6.1 | Block diagram of the PREC system. In the top rectangle, each one of the 13 peripheral FPGAs is connected to a PREC-FE via LVDS and to the central FPGA using the data, clock, and trigger lines. In the bottom rectangle, the PREC-FE is detailed, with the digitization stage followed by a buffer that drives the differential signal through long cables. | 66 |
| 6.2 | PREC-FE picture. | 67 |
| 6.3 | PREC-MB picture. | 68 |
| 6.4 | Representation of the test setup. The signal generator outputs a negative square wave into a small injector board with a 1 pF capacitor. The signal is then input into the PREC system. P1 to P5 shows the points where measurements were performed using the oscilloscope. | 69 |
| 6.5 | Measurement results of the gain and charge gain. Top left: V_{in} as a function of charge. The experimental points were fitted to a linear function. Top right: Histogram and Gaussian fit for the case $Q = 300$ fC, $T = 24.7$ °C and $V_{analog} = 12$ V. Middle: V_{amp} as a function of the charge. For each temperature (left) and V_{analog} (right) ten charges were measured and fitted to a linear function. The fit results are presented in table 6.1. Bottom: Variation of the charge gain and gain with the temperature (left) and V_{analog} (right). The data was again fitted to a linear function. In all the plots, except for the bottom left one, the data errors fall within the marker used for each data point. | 72 |
| 6.6 | PREC noise measurement. Left: Example of a baseline sample in a $10 \mu s$ window. A histogram was acquired using an oscilloscope measurement option, at room temperature and with the power supply at 10 V. The histogram was then fitted to a Gaussian distribution yielding $\sigma = 0.449$ mV, and mean = 0.197 mV. Right: σ results of the Gaussian distributions for different V_{analog} values. Four runs (full marker points) were performed for each power supply, and an extra ten runs for the values 12 V and 12.5 V (open marker points). The data errors fall within the marker used for each data point. | 73 |
| 6.7 | Crosstalk measurement results. Left: Screenshot of the oscilloscope measurement for the signals in P1 (V_{in}) and P2 (V_{scho}) of the channel with an input, and P3 (V_{amp}) of the adjacent one. In this case, the amplitude used was 2 V. Right: Histograms of the amplifiers output's baseline for the adjacent channel and respective Gaussian fits before and after the arrival of a signal. | 74 |
| 6.8 | Threshold efficiency measurement results. Left: Example of the measurement of the number of peaks in both the generator and peripheral FPGA output, over a time window of 200 ms. Right: Trigger efficiency s-curves for the three charges measured, at room temperature and with $V_{analog} = 12$ V. The data errors fall within the marker used for each data point. | 75 |

| | | |
|------|--|-----|
| 6.9 | Propagation time measurement results. The time measured between the PREC-FE input and the correspondent peripheral FPGA input in the PREC-MB is shown, using a cable of 1 m (left) and 42 cm (right) to connect the boards. | 76 |
| 6.10 | PREC instaled in the Observatory's site during the RPC tests under a WCD. Picture courtesy of Luís Mendes. | 78 |
| 7.1 | MAROC 3/3A block diagram. Taken from [218]. | 84 |
| 7.2 | Oscilloscope screenshot of the first measurement of RPC signals being read by the MAROC. Yellow: RPC signal after the internal ASIC amplification. Blue: bipolar fast shaper output. Lilac: discriminator output. Taken from [217]. | 86 |
| 7.3 | Fast shaper (left) and slow shaper (right) response to a typical RPC signal. | 87 |
| 7.4 | MARTA DAQ first prototype (top), secont prototype (second from the top), production version (third from the top), and both mezzanine input boards (bottom). Bottom left: mezzanine with MMCX connectors, used for development. Bottom right: mezzanine without connectors, the signal cables are soldered. | 88 |
| 7.5 | MARTA front-end block diagram. | 90 |
| 7.6 | Example of an LVDS transmission seen using SignalTap. A request is received in the lines LVDS_in and a response sent in LVDS_out. In both directions, line '0' is the trigger, not used for communication, '1' the enable, '2' the data, and '3' the clock. | 94 |
| 7.7 | Block diagram of the software and firmware module to program the ASIC's configuration. | 95 |
| 7.8 | Block diagram of the software and firmware module that controls the hit measurement. A timing diagram is also shown (not to scale). | 97 |
| 7.9 | Hold1 setup with all relevant signals. The discriminator output starts a counter that will send Hold1 to low when the hold delay value is reached. The sample and hold will keep the peak held so that the ADC can read its value. | 99 |
| 7.10 | Block diagram of the software and firmware module that controls the charge measurement. A timing diagram is also shown (not to scale). | 100 |
| 8.1 | Representation of setup used to measure the efficiency: a test RPC was placed in a hodoscope that allowed to track the crossing particles' trajectory. | 105 |

- 8.2 Left: Measurement data: position the particles crossed the test RPC versus which of the acquisitions systems registered the event. The readout pads position and the hodoscope dimensions are drawn over the data (red for the HADES FEE and blue for the MARTA front-end). For reference, pads 1 and 64 are identified. Right: The 16 pads used for the efficiency measurement. The distribution of pads per DAQ is given. A zoom of one of them is presented, showing the division in nine equal parts. The efficiency was determined using events that crossed the central division of the pad. 106
- 8.3 Measured efficiency versus pad number. The pad distributuin can be found in figure 8.2. 107
- 8.4 Trigger efficiency of the hit measurement versus the input charge for seven different temperatures. The charge was swept in the region where the efficiency transitions from 0 to 1. In the right plot is presented a zoom-in of the data points near the maximum efficiency. 108
- 8.5 MARTA RPC charge distribution acquired with a Rhode & Schwarz RTO 1014 oscilloscope. 109
- 8.6 Charge measurement pedestal. In all plots, the x-axis corresponds to the ADC output (ADC units) and the y-axis to the number of events. Since signals were only being input into one channel of the ASIC, number 27, in all the others, the baseline of the slow shaper was measured. 110
- 8.7 Left: ADC output versus hold delay for different slow shaper configurations: c_{fc} was kept constant at 2100 fF, and six c_{RCbuf} values were used. The slow shaper waveforms were obtained. For each, the peak was extracted by fitting a Gaussian to the point near the maximum. The data errors fall within the marker used for each data point. Right: Histogram for the point $c_{fc} = 2100$ fF, $c_{RCbuf} = 2250$ fF, and hold delay = 23, on the left plot. The mean of the Gaussian fit was taken as the measurement result. 111
- 8.8 ADC output as a fuction of the hold delay for six input charges using $c_{fc} = 2100$ fF, $c_{RCbuf} = 2250$ fF. The data errors fall within the marker used for each data point. 112
- 8.9 Measurement of known input charges with the optimized configuration and hold delay. The data errors fall within the marker used for each data point. Left: Results in the charge range of 0 to 20 pC. An interpolation was obtained for the data points. Right: Zoom-in and linear fit for the region from 0 to 1 pC. The standard deviation of the Gaussian fit for each of the data point is presented in the bottom. 113
- 8.10 Charge measurement for different channels using the same input charge. . . 114

- 8.11 ADC output as a function of the hold delay for real RPC signals. The coloured scale shows the normalized number of events. The plot shape follows closely a slow shaper signal typical waveform. The insert shows the measurement for hold delay = 29 clk and the fit to the gamma distribution (expression 8.2). 115
- 8.12 Top: ADC output as a function of the hold delay in the range of 0 to 80 clk for the four discriminator threshold values tested. The coloured scale shows the normalized number of events. The maximum of each distribution was obtained using function 8.2, and after these were fitted to expression 8.3 to get the slow shaper peak. Bottom: Maximums of the distributions as a function of the hold delay for the discriminator threshold values used. The fits for each curve are also shown. 117
- 8.13 Distribution for the slow shaper peak (hold delay = 29 clk) using the four discriminator threshold values tested. The three higher threshold spectra were scaled so that their peak would match the correspondent point in the 210 distribution. 118
- 8.14 Top: Self-trigger (blue) and coincidence trigger (black) charge spectra using two discriminator thresholds: 210 (left) and 240 (right). Bottom: Same distributions as the top left plot, but this time the coincidence histogram was scaled so that the fall of the spectra would overlap. The self-trigger distribution was fitted to a function (red line) that is the sum of a Gaussian (blue line) and equation 8.2 (green line). 119
- 8.15 Charge spectra for six different E/N. Each of them was fitted to the gamma distribution of equation 8.2. 120
- 8.16 Charge distribution average versus the E/N. The data points were fitted to the logistic function of equation 5.1 yielding a χ^2/ndf of 1.96. 121
- 8.17 Representation of the setup used to test the front-end's LVDS links. 121
- 9.1 Front-end connected inside the MARTA module's aluminium box. The 64 RPC cables are soldered to the mezzanine boards, the differential communication lines are connected using the two blue ethernet cables, power is coming through the connector on the top left, and a I²C cable allow to read the temperature and humidity sensors. 124
- 9.2 Quality control measurement of the charge distribution for two RPCs after they are assembled. Top: The results are the expected ones, with the pedestal overlapping the spectra peak. Bottom: Most of the events are to the left of the pedestal, showing something went wrong in the construction process. 125

- 9.3 Top: Hodoscope prototype stand in the Observatory’s assembly building. The RPCs are placed on the higher and lower shelf, separated by 1.07 m. On the middle shelf, inside a wooden box is the small scintillator. Bottom: Representation of the side (left) and top (right) views of the prototype hodoscope setup. The scintillator used to assess the system’s performance is also shown. 127
- 9.4 Events distribution per RPC on the prototype hodoscope. Top: Pad and time distribution of the coincidence events in the top (left) and bottom (right) RPC. Middle left: Time distribution of coincidence events that crossed pad 36 of the bottom RPC. Middle right: Pad distribution of the coincidence event in the bottom RPC. Bottom: Angular distributions of the particles’ trajectories. The azimuth (left) and zenith (right) angles are shown. 129
- 9.5 Left: Coincidence event distribution in the scintillator plane. The coloured scale represents the normalized number of events. The red line roughly denotes the test scintillator’s position. Right: Typical event acquired by the PicoScope. In black is the test scintillator waveform, while in red is shown the trigger sent by front-end’s FPGA. 130
- 9.6 Results of the measurement of the small scintillator with the prototype hodoscope. Left: Efficiency as a function of the position. The scintillator was considered active when the signal was in the time region of $-2.1 \mu\text{s}$ to $-1.3 \mu\text{s}$ and crossed a threshold of -5 mV . Right: Average test scintillator signal peak. The absolute value of each signal was obtained and its average per position plotted. 131
- 9.7 RPC hodoscope final setup. Top: Picture of the setup installed in the Observatory’s assembly building. Electronics are placed on the top shelf, RPCs on the second from the top and bottom shelves, and the SSD module on the second shelf from the bottom. Bottom: Representation of the setup. All relevant dimensions are shown. 132
- 9.8 Representation of the SSD. Left: The two modules are shown, each with twelve scintillator bars. The gap that divides them will host the fibers connected to the PMT. Taken from [64]. Right: Diagram of a fiber inside the scintillator. A particle crossing is represented in grey. The two paths the particles can go through are shown in red and blue. Based on the drawings presented in [239]. 133
- 9.9 Simulation’s visualization of a particle going through the setup. 134
- 9.10 Simulation results: average charge (number of photoelectrons) as a function of the position the particle crossed the SSD. 134
- 9.11 Top: Charge (number of photoelectrons) as a function of the zenith angle. The data points were scaled so that at 35° the charge would be 1. The results were fitted to the function $a/\cos(\theta)$. Bottom: Charge corrected with the particle’s zenith angle as a function of the position. 135

| | | |
|------|--|-----|
| 9.12 | Charge (number of photoelectrons) corrected with the particle's zenith angle as a function of the position, with the RPCs of each plane 0.685 cm apart. . | 136 |
| 9.13 | Charge (number of photoelectrons) corrected with the particle's zenith angle as a function of the x coordinate in the SSD. The results of the two studied configurations are presented. While for the blue points the RPCs were 0.285 m apart, for the red ones these were 0.685 m from each other. A fit was performed to the red data using the expression of equation 9.1. The position of the RPCs for each configuration and of the scintillator is also shown. | 137 |
| 9.14 | Charge (number of photoelectrons) corrected with the particle's zenith angle as a function of the particle's position for the two scenarios where fibers were <i>broken</i> . Top: One fiber was <i>broken</i> at (0.24, -0.125) m. Bottom: Four fibers were <i>broken</i> at (-0.24, -0.375) m, (-0.24, -0.125) m, (-0.24, 0.125) m, and (-0.24, 0.375) m. | 138 |
| 9.15 | Average of the charge (number of photoelectrons) corrected with the particle's zenith angle as a function of the y coordinate. The cases of no <i>broken</i> fibers (black), one <i>broken</i> fiber (red), and four <i>broken</i> fibers (blue) are plotted. | 138 |
| 9.16 | Picture of the four detectors being tested in the laboratory, before they are moved to the mine. | 140 |
| 9.17 | Layout of the PCB readouts. While three of the RPCs use the left layout with a mix of pads and strips, the fourth one has 64 strips with the length of the PCB, shown in the right diagram. | 141 |
| 9.18 | Pedestal of a channel's charge distribution. The data was fitted to a Gaussian, and the results used to determine if a particle crossed the detector. In this case, the results yield mean = 148.912 ± 0.001 ADC units, $\sigma = 1.181 \pm 0.001$ ADC units, and constant = $(4.703 \pm 0.005) \times 10^5$ events. | 141 |
| 9.19 | Position particle crossed the three bottom RPC of the tomography detector. The trajectory of the particle is visible, with the position painted in red corresponding to the bottom RPC, in yellow the middle one, and in blue the top one. | 142 |
| 9.20 | Efficiency of the pads in the central core, using vertical events. An insert was added, showing the position of each pad. | 143 |
| B.1 | Angles representation. ϕ is the azimuthal angle and θ the zenithal angle. . . | 153 |

List of Tables

| | | |
|-----|---|-----|
| 3.1 | Fit results of expression 3.8 to the data presented in the right plot of figure 3.10 [77]. | 31 |
| 5.1 | Summary of the present front-end systems used for readout of avalanche RPC signals. | 56 |
| 6.1 | Fit results for charge gain and gain for different temperatures (top) and different V_{analog} (bottom). | 71 |
| 6.2 | Power consumption for 8 values of V_{analog} , at room temperature. | 77 |
| 7.1 | USB communication protocol. Based on [229]. | 93 |
| 7.2 | LVDS communication protocol. | 94 |
| 8.1 | Fit results of the slow shaper peak for the six curves shown in the left plot of figure 8.7. | 112 |
| 8.2 | Maximum of the curves shown in figure 8.8. For each charge, the ADC output at hold delay = 23 clk is also presented. | 113 |
| 8.3 | LVDS links test results for the four acquisitions performed. | 122 |
| A.1 | MAROC configuration bits. The table includes the bit's name, number, line, and possible input in the .txt file, the default MARTA configuration, and comments on each parameter. For more information, refer to the ASIC datasheet [103, 104]. '1' is 'enable' unless stated. | 151 |

List of Abbreviations

- Offline** The Pierre Auger Observatory’s analysis software framework. 23, 37, 133, 144
- 3D** three-dimensional. xvi, 52, 53, 58
- AC** alternating current. 24, 66
- ACD** Anti-Coincidence Detector. xiii, 12
- ADC** analog-to-digital converter. xviii–xx, xxii, xxiii, 24, 25, 81, 82, 86, 89–91, 98, 99, 101, 102, 104, 110–113, 115–117, 141, 146, 151
- AERA** Auger Engineering Radio Array. xiii, 2, 15, 18, 19, 22, 43
- AGASA** Akeno Giant Air Shower Array (an experiment in Japan). 14
- AIRES** AIR-shower Extended Simulations, an EAS simulation software. 10
- ALICE** A Large Ion Collider Experiment (an experiment at CERN). 52, 54–56
- AMIGA** Auger Muons and Infill for the Ground Array. xiii, 2, 18, 19, 22, 34, 39, 43, 44
- AMS** Antimatter Spectrometer (an experiment in a satellite). xiii, 11, 12
- ARGO-YBJ** Astrophysical Radiation with Ground-based Observatory at YangBaJing (an experiment in Tibet). 14, 52
- ASIC** Application Specific Integrated Circuits. xviii, xix, xxiii, 3, 38, 54–56, 65, 81–86, 89, 91, 95, 96, 98, 99, 101, 103, 104, 108–111, 113, 114, 122, 143, 145–147, 151
- a.s.l.** above sea level. 17, 40, 41
- ATLAS** A Toroidal LHC Apparatus (an experiment at CERN). xvi, 52–54, 56
- BaBar** (an experiment at SLAC). 52, 57
- BELLE** (an experiment at KEK). 52
- BESIII** Beijing Spectrometer III (an experiment at IHEP). 52
- BGA** ball grid array. 89, 91

- BGO-EGG** (an experiment at LEPS2). 52
- BLS** Balloon Launching Site. xiii, 18, 21
- CAL** Calorimeter. xiii, 12
- CALICE** Calorimeter for Linear Collider Experiment (a projected experiment for the International Linear Collider). 54, 56
- CASA-BLANCA** Chicago Air Shower Array - Broad Lateral Non-imaging Cherenkov Array (an experiment in Utah, USA). 15
- CBM** Compressed Baryonic Matter, (an experiment at FAIR). 52, 54, 56
- CD** Cherenkov Detector. xiii, 11, 12
- CDAS** Central Data Acquisition System. xiv, 23–26, 39, 44, 126
- CERN** European Organization for Nuclear Research (a laboratory in Switzerland). 52
- CIC** constant intensity cut. 27, 28
- CLF** Central Laser Facility. xiii, 18, 21
- CMB** cosmic microwave background. 7
- CMS** Compact Muon Solenoid (an experiment at CERN). 52, 54, 56
- CORSIKA** COsmic Ray SIMulations for KAscade (an EAS simulation software). 10
- COVER_PLASTEX** (an experiment in the UK). 52
- CREAM** Cosmic-Ray Energetics And Mass (a balloon experiment). xiii, 11, 12
- CTA** Cherenkov Telescope Array (an experiment in Chile). 14
- DAC** digital-to-analog converter. 66, 67, 85
- DAQ** data acquisition. xviii, xix, 2, 3, 38, 40, 65, 68, 77, 78, 87–91, 105–107, 122, 146, 147
- DC** direct current. 151
- E/N** reduced electric field. xvi, xx, 39, 59–63, 104, 114, 118, 120, 121, 146
- EA** engineering array. xv, 2, 35, 39, 40, 43, 44, 62, 64, 90, 123, 144, 146
- EAS** Extensive Air Shower. xiii, xv, 1, 2, 5–7, 9, 10, 15, 17–19, 21, 22, 30–32, 35, 37, 42–44, 48, 52, 53
- ECAL** Electromagnetic Calorimeter. xiii, 11, 12

- e-CRLab** Cosmic Rays electronics laboratory, at LIP. 87
- EPOS** Energy conserving quantum mechanical multiple scattering approach, based on Partons, Off-shell remnants and Splitting of partons ladders (a model for high energy hadronic interactions). xiv, 10, 31, 42
- EPROM** erasable programmable read-only memory. 89
- FAIR** Facility for Antiproton and Ion Research (a laboratory in Germany). 52
- FD** Fluorescence Detector. xiii–xv, 2, 17–21, 23, 26–29, 31, 43, 44
- FEC** Front-End Card. 57
- FEERIC** Front-End Electronics Rapid Integrated Circuit (an ASIC). xvi, 55, 56
- FERMI-LAT** Fermi Large Area Telescope (an experiment in a satellite). xiii, 11, 12
- FIFO** First In First Out. 57, 92, 96, 98, 101, 128
- FLT** FD first level trigger. 25
- FOPI** (an experiment at GSI). 52, 56
- FPGA** Field-Programmable Gate Array. xvii, xviii, xxi, 22, 25, 26, 38, 39, 57, 65–70, 74–77, 81, 83, 86, 87, 89, 91–93, 95, 96, 98, 99, 101, 102, 104, 111, 120, 121, 128, 130, 132, 145, 147
- FWHM** Full Width at Half Maximum. 47, 53
- GEANT4** GEometry ANd Tracking (a simulation framework). 40, 126, 133, 146
- GSI** GSI Helmholtz Centre for Heavy Ion Research (a laboratory in Germany). 52
- GZK** Greisen-Zatsepin-Kuz'min. 7
- HADES** High Acceptance Di-Electron Spectrometer (an experiment at GSI). 52, 56
- HADES FEE** HADES front-end electronics. xvi, xix, 56, 103, 105–107, 146
- HARDROC** Hadronic RPC ReadOut Chip (an ASIC). xvi, 54–56, 81
- HARP** Hadron Production Experiment (an experiment at CERN). 52, 56
- HAWC** High-Altitude Water Cherenkov Observatory (an experiment in Mexico). 14
- HEAT** High Elevation Auger Telescopes. xiii, 18, 20, 30, 44
- H.E.S.S.** High Energy Stereoscopic System (an experiment in Namibia). 14

HiRes High Resolution Fly's Eye Cosmic Ray Detector (an experiment in Utah, USA).
14

HPS Hard Processor System. 39, 93

HV high voltage. xv, xvi, 36–39, 47–49, 51, 57–63, 83, 118, 124, 143, 146

I/O Input/Output. 68, 89

I²C Inter-Integrated Circuit. xx, 39, 58, 59, 67, 89, 108, 123, 124

IACT Imaging Atmospheric Cherenkov Telescopes. 14

IC integrated circuits. 54–56, 65, 76

ICAL Iron Calorimeter (at INO). 52, 55

IceTop (an experiment in Antarctica). 14

ICRC International Cosmic Ray Conference. 30, 31

ICT Instituto de Ciências da Terra, Universidade de Évora (a research institution in Portugal). 139

IHEP Institute of High Energy Physics (in China). 52

INO India-based Neutrino Observatory. 52, 55

JINR Joint Institute for Nuclear Research (a laboratory in Russia). 52

JTAG an industry standard used to test PCBs. 89

KASCADE-Grande Karlsruhe Shower Core and Array DEtector - Grande (an experiment in Germany). 7, 14, 30

KEK High Energy Accelerator Research Organization (a laboratory in Japan). 52

L3 (an experiment at CERN). 52

LDF lateral distribution function. xiv, xv, 26, 27, 41–43, 147

LEMO a connector. 69, 70, 83, 87, 89, 96, 101

LEPS2 Laser Electron Photon Experiment at SPring-8 (in Japan). 52

LHC Large Hadron Collider (a collider at CERN). xiv, 10, 31, 33, 42

LHCb Large Hadron Collider beauty (an experiment at CERN). 52

LIDAR Light Detection And Ranging. 21

- LIP** Laboratório de Instrumentação e Física Experimental de Partículas (a research institution in Portugal). 1, 87, 123, 139
- LNGS** Laboratori Nazionali del Gran Sasso (a laboratory in Italy). 52
- LSB** least significant bit. 92, 93
- LVDS** low-voltage differential signal. xvii, xviii, xx, xxiii, 38, 39, 55–57, 65–67, 76, 83, 89–96, 101, 102, 104, 120–122
- MAGIC** Major Atmospheric Gamma Imaging Cherenkov Telescopes (an experiment in the Canary Islands, Spain). 14
- MAROC** Multi Anode Read-Out Chip. xviii, xxiii, 3, 38, 55, 81, 82, 84–87, 89, 91, 92, 95, 103, 105, 108, 110, 122, 145, 146, 151
- MARTA** Muon Array with RPCs for Tagging Air showers. xv, xvi, xviii–xx, xxiii, 1–3, 33–40, 42–45, 48, 53, 55–62, 65, 69, 78, 81–84, 86–91, 96, 98, 102, 103, 105–110, 114, 116, 118, 123, 124, 126, 132, 133, 139, 143–147, 151
- MICTOR** Matched Impedance ConnectOR. 87, 91
- MIP** minimum ionizing particles. 52
- MMCX** micro-miniature coaxial connector. xviii, 66, 87, 88
- MONOLITH** (an experiment at LNGS). 52
- MoPS** multiplicity of positive steps. xiv, 24, 25
- MPD** Muon Production Depth. 42
- MSB** most significant bit. 92, 93
- MUX** Multiplexer. 85
- NICA** Nuclotron-based Ion Collider fAcility (an experiment at JINR). 52
- NINO** (an ASIC). 54, 56
- NKG** Nishimura-Kamata-Greisen. 9, 26
- OMEGA** Organisation de MicroÉlectronique Générale Avancée (an institution in France). 55, 81, 84
- OPERA** Oscillation Project with Emulsion-tRacking Apparatus (an experiment at LNGS). 52, 57
- PADI** Preamplifier-discriminator (an ASIC). 54, 56

- PAMELA** Payload for Antimatter Matter Exploration and Light-nuclei Astrophysics (an experiment in a satellite). xiii, 11, 12
- PCB** Printed Circuit Board. xxii, 37, 57, 66, 87, 90, 91, 123, 140, 141, 145
- PET** Positron Emission Tomography. 52, 53
- PETIROC** Positron Emission Tomography Integrated ReadOut Chip (an ASIC). 55
- PHENIX** Pioneering High Energy Nuclear Interaction eXperiment (an experiment at RHIC). 52
- PID** particle identification. 52
- PLD** Programmable Logic Device. 24
- PLL** phase-locked loop. 89, 101, 121
- PMT** photomultiplier. xxi, 15, 19–21, 24, 25, 29, 65, 78, 79, 81, 127, 130, 131, 133, 144, 145, 147
- PREC** Prototype Readout Electronics for Counting particles. xvii, xviii, 40, 56, 64–66, 68, 69, 73, 76–79, 81, 144, 146, 147
- PREC-FE** PREC Front-End. xvii, xviii, 65–70, 74–79
- PREC-MB** PREC Motherboard. xvii, xviii, 65, 67–70, 75, 76, 78, 83
- PSU** power supply unit. xvi, 37, 39, 58, 59, 83, 84, 123
- QDC** charge-to-digital converter. 54
- QGSJet** Quark Gluon String Model with mini-Jet (a model for high energy hadronic interactions). xiv, 10, 31, 42
- R&D** Reasearch and development. 15, 37, 65
- RC** resistor–capacitor circuit. xix, 59, 82, 85, 86, 111, 112, 114, 151
- RHIC** Relativistic Heavy Ion Collider (a colider at the Brookhaven National Laboratory, USA). 52
- RICH** Ring Imageing Cherenkov Detector. xiii, 12
- ROC** ReadOut Chip (an ASIC family by OMEGA). 55
- ROOT** (a data analysis framework). 91, 98, 128, 133
- RPC** Resistive Plate Chamber. xv, xvi, xviii–xxiii, 1–3, 14, 35–45, 47–65, 69, 77–79, 81–83, 85–87, 89, 91, 96, 98, 99, 103–110, 114–116, 118, 120, 122–147, 153

- SCD** Silicon Charge Detector. xiii, 12
- SD** Surface Detector. xiii–xv, 2, 17–31, 35–37, 39, 40, 42–45, 83, 126
- SDHCAL** Semi-Digital Hadronic CALorimeter (at CALICE). 54
- SDP** shower detector plane. 28, 29
- Sibyll** (a model for high energy hadronic interactions). xiv, 10, 31
- SKIROC** Silikon Kalorimeter ReadOut Chip (an ASIC). 55
- SLAC** Stanford Linear Accelerator Center (in California, USA). 52
- SLT** FD second level trigger. 26
- SMA** SubMiniature version A connector. 83, 87, 89, 96, 101, 116
- SoC** System on Chip. 39
- SSD** Scintillator Surface Detector. xiv, xxi, xxii, 2, 18, 21, 22, 34, 43, 44, 126, 131–138, 144, 146
- STAR** Solenoidal Tracker at RHIC (an experiment at RHIC). 52
- T1** SD first level trigger. xiv, 24, 25, 39, 83, 98, 126
- T2** SD second level trigger. xiv, 24, 25, 39, 83
- T3** SD third level trigger. xiv, 24–26, 39, 126
- T4** SD fourth level trigger. 25
- TA** Telescope Array (an experiment in Utah, USA). 14
- TAIGA** Tunka Advanced Instrument for cosmic ray physics and Gamma Astronomy (an experiment in Siberia). 15
- TCD** Timing Charge Detector. xiii, 12
- TDC** time-to-digital converter. 54, 78
- TH** threshold. xiv, 24, 25
- TKR** Tracker. xiii, 12
- TLT** FD third level trigger. 26
- TOF** Time of Flight. xiii, 11, 12, 52, 54, 56, 78
- TOMUVOL** TOmographie avec des MUons atmosphériques des VOLcans (an experiment in France). 53

- ToT** time over threshold. xiv, 24, 25, 54
- ToTd** time over threshold deconvoluted. xiv, 24, 25
- TPCB** Tank Power Control Board. 20
- TRAGALDABAS** TRAsGo for the AnaLysis of the nuclear matter Decay, the Atmosphere, the earth B-field And the Solar activity (an experiment in Spain). 53
- TRD** Transition Radiation Detector. xiii, 11, 12
- tRPC** timing RPC. 48, 56
- Tunka-133** (an experiment in Siberia). 15
- Tunka-Rex** Tunka Radio Extension (an experiment in Siberia). 15
- Tuska-Grande** (an experiment in Siberia). 14
- UB** unified board. 24, 132
- UHECR** ultra high energy cosmic rays. 1, 7, 14, 19, 29, 31–33, 37
- UMD** Underground Muon Detector. 22, 23, 44
- USB** Universal Serial Bus. xxiii, 66–68, 83, 84, 87, 89, 91–95, 101, 123, 139
- UTP** Unshield Twisted Pair cable. 67, 69, 93
- UUB** upgraded unified board. 132, 133
- UV** ultraviolet. 10, 17, 21, 51
- VEM** Vertical Equivalent Muon. 19, 24, 27, 28, 78
- VERITAS** Very Energetic Radiation Imaging Telescope Array System (an experiment in Arizona, USA). 14
- WCD** water-Cherenkov detector. xiii, xv, xviii, 1, 2, 17–24, 26, 33–42, 44, 45, 57, 62, 78, 83, 96, 98, 101, 144, 147
- WLAN** Wireless Local Area Network. 20
- WLS** wavelength-shifting. 21, 23
- X_{\max} depth maximum shower size. xiv, 9, 10, 18, 28, 29, 31–33
- XLF** eXtreme Laser Facility. xiii, 18, 21

1 Introduction

More than 100 years after their initial discovery, the study of Cosmic Rays is still the focus of many experiments. Questions like what is their origin and chemical composition, or how are these accelerated in space, are still open to debate. It is now known, that their energy spectrum ranges over 11 orders of magnitude, from the GeV to the most energetic particles, with energies as high as 10^{20} eV, known as ultra high energy cosmic rays (UHECR). While for the lower energies these particles can be detected directly in satellites, UHECR have rates as low as 1 particle/km²/century. Thus, direct detection in orbit is not an option, leaving us to measure the product of their collisions with the atmosphere. After the initial collision between the primary cosmic ray and the atmospheric nuclei, secondary particles are created that will collide again, producing more new particles. This cascade process, known as Extensive Air Shower (EAS), repeats until the particles reach the Earth's surface where they can be detected. Large detector's arrays have been used to study these rare events.

The Pierre Auger Observatory [1], located in western Argentina, is an experiment dedicated to the study of the most energetic cosmic rays that covers an area of 3000 km². In its 20 years of operation, the Observatory has published some of the most important experimental results in UHECR. This include, the confirmation of a suppression at the end of the energy flux [2], or more recently a dipolar anisotropy that was found in the arrival directions of cosmic rays above 8×10^{18} eV [3]. The understanding of the EAS is fundamental for the Observatory's operation. Many efforts have been put into their description and modelling. However, there is a discrepancy between the number of muons measured by the Observatory's detectors and the ones predicted in models. It might be because the number of muons is extracted indirectly from data that is a combination of the different components of the shower (muonic, electromagnetic and hadronic). Thus, the discrepancy calls for new, direct, and independent measurement of the muonic content of the air shower. Such measurement will allow, among other things, to better understand the shower development, in particular, the high energy hadronic interactions.

MARTA [4] was proposed by the LIP's group working at the Pierre Auger Observatory to perform the muon measurement. Resistive Plate Chamber (RPC) detectors will be placed below the Observatory's water-Cherenkov detector (WCD). The latter will absorb all the other showers' detectable components, with most muons transversing it to be again detected in the RPCs. That is the main advantage of this setup: the same muons are

measured by the two detectors, allowing combined analysis and even cross-calibrations. However, until the introduction of MARTA, RPCs have mostly been used in laboratory conditions. Due to the large area covered, the 1660 WCDs, part of the Observatory's array, are installed 1.5 km apart in isolated locations that in most cases are hard to reach. It also means that the detectors are exposed to the atmospheric conditions, that in the Observatory's site can be quite harsh. Several studies have been performed showing that, although the conditions are not favourable, it is possible to have a operate these detectors with stable efficiencies [5].

The work in this thesis is about the instrumentation of the MARTA RPCs. Namely, two data acquisition (DAQ) systems that were put together to measure the RPC signals. The first system was designed as a proof of concept, without any concerns with the requirements of outdoors operation. It was mostly used to show that the RPCs could be operated in the field. As part of this work, a full characterization of this system was performed. The second and final system, the main focus of this thesis, consists of a new RPC readout that was designed, tested and validated, following the strict requirements of an experiment like The Pierre Auger Observatory: low power and maintenance, compact, and reliable. This system will be installed in a small seven stations engineering array (EA) of MARTA at the Observatory's site. The array main goals are to study the performance of the combined measurement and how the RPCs will behave in the field. It can also be used to cross-calibrate other new detectors that are installed in the same region of the array, e.g., AMIGA, SSD, and AERA. The developed DAQ has also been installed in other setups that use MARTA or MARTA-like RPCs.

This thesis is organized as follows:

- In **chapter 2** a brief overview of cosmic rays is given. It includes a historical review of their discovery and the description of the different feature of their energy spectrum. Then EAS are discussed, including the different components of the cascade and the lateral and longitudinal parameterizations of the shower. Lastly, the detection technics of cosmic rays are presented, including direct technics, particle detectors installed in satellites, and the indirect ones, that measure the particles of the EAS as well as the light and radio waves emitted by these.
- In **chapter 3** the Pierre Auger Observatory is described. An overview of different type of detectors is given, focusing mostly on the SD, where the MARTA engineering array will be installed, and the FD, that measures the fluorescence light emitted by the shower. The acquisition electronics and triggers, as well as, the data reconstruction of these two main detectors are also presented. Lastly, some of the most important results of the Observatory are mentioned. The muon problem, discussed above, is expanded upon.
- In **chapter 4** the MARTA project is introduced. More details about the concept and design mentioned above are presented. An overview of the station and its components is given. It includes the detector, the electronics, of which several are new

developments, and the support structure. Then the results of MARTA's simulation are shown. Both the simulation of a station and a potential full MARTA array are discussed. Lastly, the engineering array is described.

- In **chapter 5** RPC detectors are described. Firstly, the detector's evolution since their introduction is given, and then the signal generation inside the detector is discussed. In the latter, some models used to describe the RPC signals are presented. After, a list of applications of RPCs in particle and astroparticle physics is mentioned. An overview of past readout systems for this type of detector is given. Lastly, the MARTA RPC is presented, including its design and the laboratory and field tests performed to the detector.
- In **chapter 6** the first prototype data acquisition system designed for MARTA is presented and characterized. Namely, the gain, noise, crosstalk, threshold efficiency, and power consumption of this system were studied, and the results are reported. The applications of this system are listed, including the RPC field tests mentioned before.
- In **chapter 7** the final data acquisition system is presented. A list of requirements is first showed, and after the main component of the system, the MAROC ASIC [6], is described. The design of the board is discussed, including the evolution of the different versions. Lastly, the firmware and software modules are detailed, e.g., the communication with the data concentrator and the two acquisition modes available: hit and charge measurement.
- In **chapter 8** the performance of the new data acquisition system is assessed using laboratory test benches. Mainly the two acquisition modes were tested. For the hit measurement, the efficiency of an RPC was determined, and the results compared with the ones obtained using an established RPC DAQ. The charge acquisition was studied using generator signals and real RPC signals. The measurement was optimized for the two signal types.
- In **chapter 9** some applications of the MARTA detectors and data acquisition system are shown. Firstly, an overview of the engineering array status is given, including detectors production. A hodoscope of MARTA RPCs to test scintillators is presented. A first version of this setup was built and tested, validating the concept. The second version was built and simulated. Lastly, a detector to perform muon tomography, with RPCs, that also uses the electronics developed in this work, is mentioned. Some test data of these RPCs is presented.
- In **chapter 10** the thesis is summarized, conclusions are drawn, and some future work is discussed.

2 Cosmic rays

Cosmic rays are extremely energetic particles that travel through space. These are either elementary particles or nuclei that are created in the most violent events in the universe. Some, after traveling through space for millions of light-years, will collide with the Earth's atmosphere. The by-products of such collisions, particle cascades in the atmosphere, have been studied since the beginning of the 20th century.

In this chapter, a brief description of cosmic rays is given. Namely, a historical review is presented and its characteristics are discussed. Extensive Air Showers (EAS), the cascade of particles created when the cosmic ray collides with the atmosphere, are described. The detection techniques, both direct and indirect (EAS measurement), are also mentioned.

2.1 Historical review of cosmic-ray studies

In the early 20th century, the theories of radiation were well established. Several experiments were studying this subject, one of which was using an electroscope to measure the ionization of the air. Unexpectedly, the instrument would measure such phenomena without the presence of any radioactivity source. Theories were quickly proposed saying that these ionizations were the result of radiation emitted by the Earth's surface. To validate them, in 1910 Thomas Wulf took an electroscope to top of the Eiffel tower (at ~ 300 m), expecting a decrease in the rate of ionizations. The results were inconclusive, showing that the rate would decrease with elevation but not by as much as it was expected [7]. After Wulf's conclusion, several follow up experiments were performed to understand the origin of these particles. While Domenico Pacini measured the rate of ionizations underwater, showing a decrease when compared to the number at the water's surface [8], Albert Gockel performed the first hot air balloon measurements. He took an electroscope up to 3000 m, revealing that the rate did not decrease with altitude [9]. The issue was finally settled a few years later by Victor Hess, in 1912. Hess performed a series of measurements at extreme altitudes (up to 5400 m) also using a balloon. He concluded that the rate of ionizations would first decrease with altitude, and then, at about 1000 m, it started to increase considerably [10]. At 5000 m the number of ionizations was five times higher than at the ground. This result proved that this radiation was of cosmic origin for which Hess won the 1936 Nobel Prize. The term *cosmic ray* was later coined by Robert Millikan to describe this phenomenon.

In the late twenties, with the invention of the Geiger counter, new experiments were conducted, like [11–13]. Namely, in 1934, Rossi reported that two widely separated counters would discharge simultaneously [14]. This observation would later be confirmed in detail by Pierre Auger in 1937 [15]. An array of Geiger counters was used to measure cosmic rays, showing temporal correlation over several square meters. These results introduced the term Extensive Air Shower (EAS). Auger theorized that the energetic primary cosmic ray would interact with the molecules in the atmosphere, producing a large shower of secondary particles.

In the 1950s, with the introduction of accelerators, cosmic rays were no longer the primary tool for particle physics research. They were, however, extremely important in the early discovery of elementary particles like the positron [16], the muon [17], and the pion [18]. Although the development of accelerators has created powerful machines able to collide millions of particles every second, the energies observed in cosmic rays are still far beyond the ones produced in those machines. Cosmic rays continued being studied in the second half of the 20th century in experiments like the Volcano Ranch array where air showers were first measured with primary energy above 10^{20} eV [19].

More than a century after their discovery, there are still many unknowns about cosmic rays. Nowadays, experiments are trying to understand both the origins of cosmic rays and how these particles propagate in the universe. Their focus is mostly on the following three aspects: the energy spectrum, the primary composition, and the arrival direction.

One should finally reflect on the importance of the instruments for these discoveries. In most of the milestones described in this brief review, the development of new detectors, like the electroscope and the Geiger counter, or the improved experimental apparatus, like the array of counters used by Auger, showed being fundamental. These are small examples of how building new and improve techniques is the first and maybe most important step of all experiments.

2.2 Cosmic Rays characteristics

The flux of cosmic rays as a function of the primary energy is known as the *energy spectrum*. A compilation of measurements of the cosmic ray energy spectrum is shown in figure 2.1. The flux decreases significantly with energy following the power-law $E^{-\gamma}$ with γ , the spectral index. While for particles in the order of 10^{15} eV, the flux corresponds to about one particle per square meter per year, for the highest observed energies, there is less than one particle per square kilometer per century.

In the spectrum presented, the flux was multiplied by $E^{2.5}$ to emphasize some of its features. Namely, the *knee* at $\sim 5 \times 10^{15}$ eV, and the *ankle* at $\sim 5 \times 10^{18}$ eV. These are notable shifts in the slope that corresponds to variations in the spectral index. It changes from $\gamma = 2.7$ before the *knee*, to $\gamma = 3.3$ before the *ankle*, and back to $\gamma = 2.7$ after. The last feature of the spectrum is the strong suppression of the flux at energies higher than $\sim 5 \times 10^{19}$ eV.

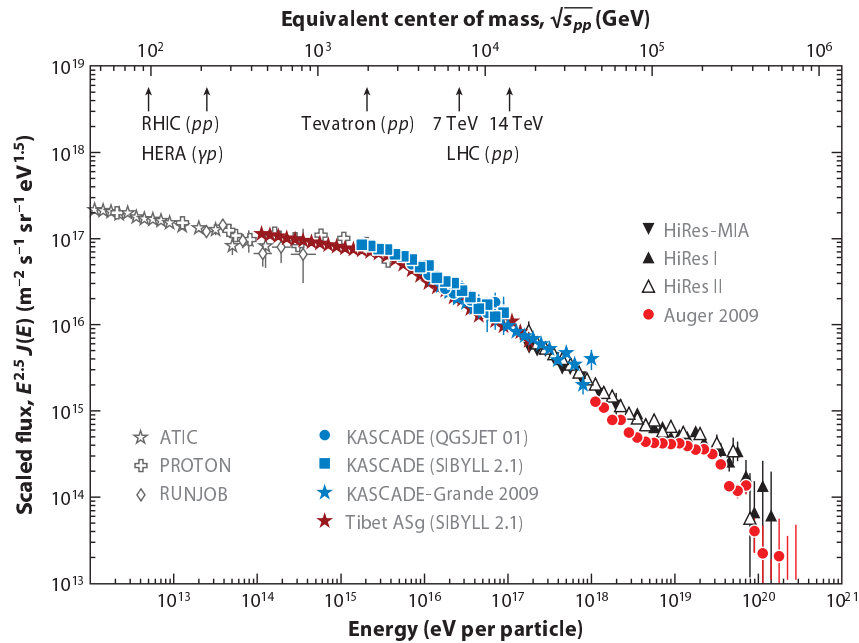


Figure 2.1: Cosmic ray energy spectrum for $E > 10^{12}$ eV. It shows a compilation of data points obtained by different experiments. The flux was multiplied by $E^{2.5}$ to accentuate the spectrum feature, like the *knee* at $\sim 5 \times 10^{15}$ eV, and the *ankle* at $\sim 5 \times 10^{18}$ eV. For energies greater than $\sim 5 \times 10^{19}$ eV a strong suppression is noticeable. Taken from [20].

The *knee* can be explained, according to results published by the KASCADE-Grande experiment [21], by the composition of the cosmic ray at these energies. It corresponds to a sharp decrease in the observed flux of light nuclei. The particles at the *ankle* and at the suppression are the highest energy cosmic rays. At energies above 8×10^{18} eV these were shown to be of extragalactic origin [3], and so travel vast distances between the source and the Earth. Although still open to debate, the suppression can be explained as propagational effects due to the particles' interaction with the cosmic microwave background (CMB). Such phenomena is known as the Greisen-Zatsepin-Kuz'min (GZK) effect [22, 23]

While for the primary cosmic rays with energies below the *knee* the composition is well-documented [24], because direct measurements using balloons or satellites are possible, for higher energies the flux becomes too small. So one has to study the secondary particles created in the collisions with the atmosphere to conclude the primary's characteristics.

2.3 Extensive air showers

EASs are the result of the interaction of the primary high-energy cosmic rays with the atmosphere. Their detection at ground level is, as already mentioned, fundamental to accurately infer properties of the colliding particles, like their energy, mass, charge, etc. For that reason, the understanding of the particle's behavior in the shower is of the utmost importance when studying the highest energy cosmic rays (UHECR). An EAS representation is shown in figure 2.2.

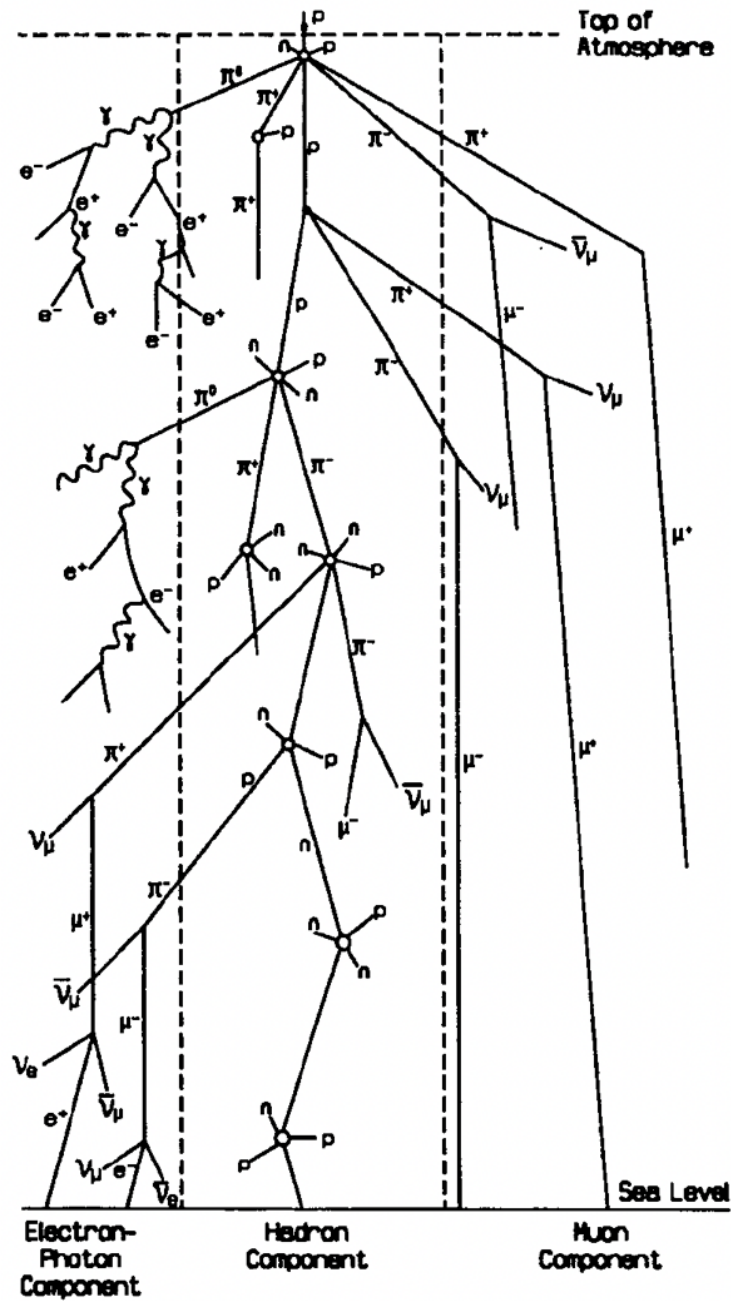


Figure 2.2: Extensive air shower representation. After the first interaction the particles created can be divided into three components: electromagnetic, hadronic and muonic. An undetectable neutrino component is also present. Taken from [25].

After the first interaction, the secondary particles created also interact, producing new tertiary particles. The process goes on, generating a cascade of particles. The air shower, initiated by the interaction of a hadronic particle (like a proton), can be categorized in three components (as shown in figure 2.2): electromagnetic (electrons, positrons and photons), muonic (muons) and hadronic (mainly pions, kaons and protons). If the primary particle is, however, an electron, positron, or photon, the induced shower is nearly pure electromagnetic.

If the primary cosmic ray is a proton or a nuclei, almost all particles produced in the first interaction are hadrons, among which the most abundant are by far the pion ($> 60\%$). The charged pions, π^+ and π^- , will be responsible for the creation of new hadrons, as well as muons from their decay, that will mostly travel to the ground. During the muons production and decay, a neutrino component is originated that is undetectable. The neutral pion decay, π^0 , is responsible for feeding the electromagnetic component of the cascade. This component represents the majority of the shower, carrying more than 90% of its energy.

The number of particles in the EAS increases with the depth of the atmosphere, reaching a maximum point. After, due to energy loss, absorption, and decays, the number of particles starts decreasing. This maximum is known as the depth maximum shower size (X_{\max}). It is one of the main observables in air shower physics, and it depends on the energy and composition of the primary particles, as well as the atmosphere's density.

The air shower front forms a disk of particles with a thickness of a few meters, that can extend over several hundred meters. The shower can be parameterized in two directions: longitudinal and lateral. The Gaisser-Hillas function [26] describes the longitudinal development of the shower:

$$N(X) = N_{max} \left(\frac{X - X_0}{X_{max} - X_0} \right)^{\frac{X_{max} - X_0}{\lambda}} \exp \left(- \frac{X_{max} - X_0}{\lambda} \right) \quad (2.1)$$

where $N(X)$ is the number of particles at depth X , N_{max} the number of particles at depth X_{max} , X_0 the depth of the first interaction, and λ the effective interaction length.

In the Nishimura-Kamata-Greisen (NKG) equation [27], the lateral profile of pure electromagnetic showers was solved analytically. It describes the density of particles, ρ , as a function of the distance to the shower axis, r , and the shower age, s . For showers induced by nuclei, this equation was modified to account for the hadronic component. A parameterization was presented in [28] with an additional correction factor:

$$\rho(r, s) = \frac{C_1(s)N_e}{2\pi r_1^2} \left(\frac{r}{r_1} \right)^{s-2} \left(1 + \frac{r}{r_1} \right)^{s-4.5} \left(1 + C_2 \left(\frac{r}{r_1} \right)^\delta \right) \quad (2.2)$$

where $\frac{C_1(s)N_e}{2\pi r_1^2}$ is a shower normalization parameter, with N_e the electron shower size, and $C_1(s)$ a function of s . The parameters r_1 and C_2 are constants and δ is a free parameter of the parameterization. The shower age, s , is a function of the depth X and maximum

depth X_{\max} .

Monte Carlo simulations are used to study the development of the shower and its properties. These are complex systems that require three-dimensional tracking of the particles and need to take into account variables like the variation of the atmosphere's density with the altitude and the Earth's magnetic field. The most widely used simulations programs of EAS are AIRES [29] and CORSIKA [30]. The interactions are simulated using different hadronic interaction models like QGSJetII-04 [31], EPOS-LHC [32] and Sibyll 2.3d [33]. A detailed description of the models and their systematic uncertainties can be found in [34].

Figure 2.3 shows the lateral and longitudinal profiles of the different components of the shower. These were simulated using CORSIKA for proton-induced showers of 10^{19} eV. Although most of the particles that will reach the ground are part of the electromagnetic component, valued information can be gained from the measurement of the muons. They are an important tool to probe the hadronic interactions at high energy since these particles are a direct consequence of the hadrons' decay in the shower. Unlike the hadrons, they lose energy only by ionization, and so most of them reach the ground, as already mentioned.

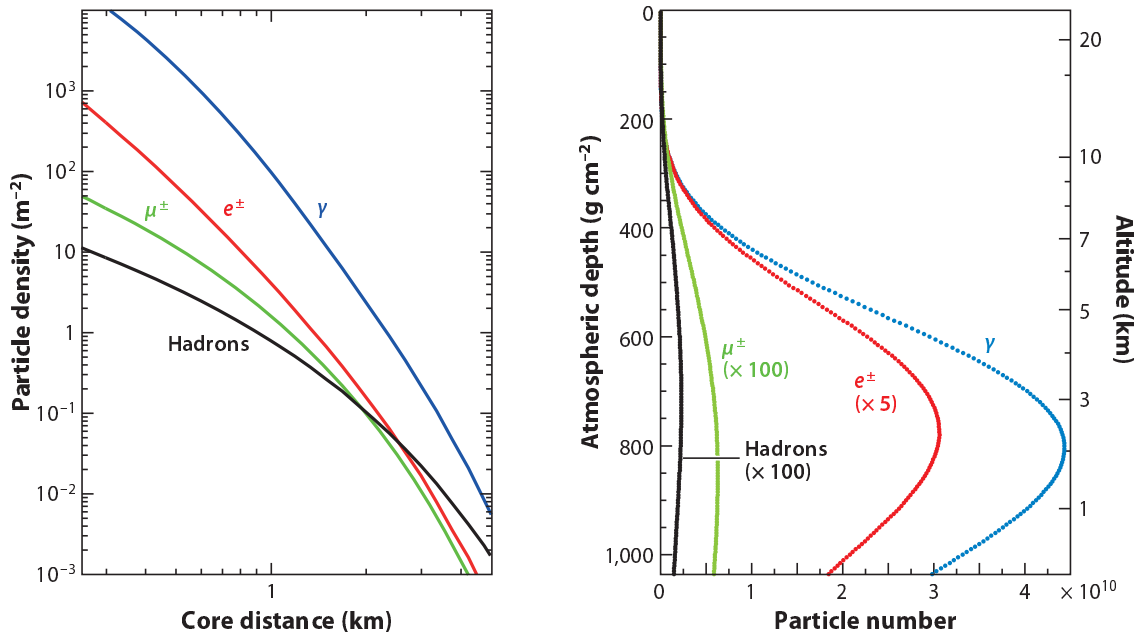


Figure 2.3: Average lateral (left) and longitudinal (right) shower profiles for a vertical proton-induced shower of 10^{19} eV. The lateral distribution is calculated using the depth of the Pierre Auger Observatory (see chapter 3). Taken from [20].

During the shower development radio waves, Cherenkov radiation and fluorescence light are emitted. Cherenkov radiation [35] is produced when a particle travels at a speed greater than the speed of light in a medium. In the case of EASs, it is emitted by the secondary charged particles (mostly electrons and positrons) traveling faster than the speed of light in the air. Fluorescence light is created when the shower particles ionize the nitrogens molecules in the air. These then emit ultraviolet (UV) light during the de-excitation

process. Lastly, radio waves are also produced by the air shower, by charged particles, due to the geomagnetic and Askaryan effects [36]. The radio signals have a wavelength of a few meters and are generated instantaneously [37].

2.4 Detection techniques

As mentioned previously, the main purpose of the study of cosmic rays is to determine their energy, composition, and arrival direction. Their detection can be done directly using balloons or satellite-borne detectors, or indirectly by measuring the air shower. Both methods have their advantage and are complementary to each other. The most accurate way to measure the primary is using detectors at the top of the atmosphere in balloons or satellites. However, these carriers have strict space and weight limitations, which make it impossible to have enough statistics of particles with energies higher than 10^{14} eV. For that reason, the result of the higher energy particles interaction with the atmosphere is usually measured indirectly at the ground, using either particles, light, or radio detectors.

2.4.1 Direct detection

The historical review of section 2.1 showed the importance of high altitude detection. Most of the first measurements were performed in balloons. However, with the introduction of satellites in 1957 (Soviet's Sputnik I), detectors started being sent to space for cosmic-ray measurements. Geiger counters were sent up in the second installment of the Sputnik mission and in some of the first Explorer satellites. More recent satellite-based experiments like FERMI-LAT [38], PAMELA [39], and AMS-02 [40], and balloon-based like CREAM-II [41], have much more complex detection techniques. These are, most of the time, based in the same concepts as the ones used in accelerators particle physics. Figure 2.4 shows a schematic representation of the detectors in the experiments mentioned above.

Magnetic spectrometers and calorimeters are the main detection techniques uses. The first allows distinguishing the charge of the particles while the second allows measuring the particles' energy. Tracking detectors that record the particle's path are also used. Position-sensitive detectors are placed in the detection path to reconstruct the particle track. Particle identification is also required and can be performed in multiple ways. Here, the measurement of dE/dx , TOF systems, CD, and TRD are used. The AMS-02 detector, an 8500 kg machine installed in the International Space Station, uses TRD, TOF, and CD for particle identification, an ECAL, and several tracking layers in the middle of a superconducting magnet, forming a magnetic spectrometer. An extensive review of space-based cosmic ray detectors is given in [42].

2.4.2 Ground based indirect detection

The indirect measurement of cosmic rays is done by studying the extensive air shower. Particles are sampled at the ground using arrays with one or more detector types. The

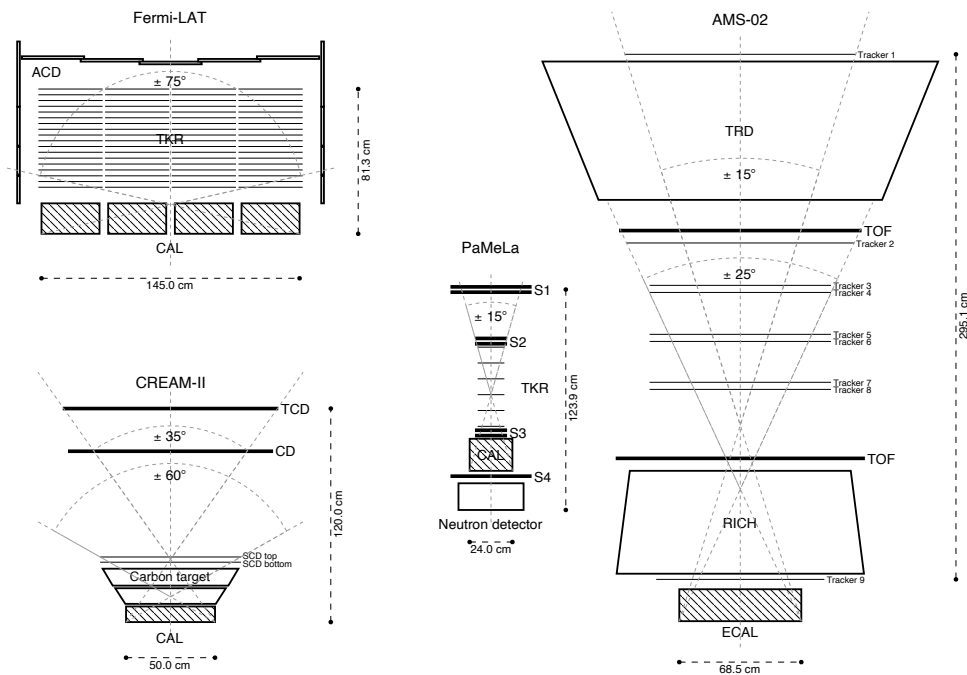


Figure 2.4: Schematic view of some detectors used to perform direct measurements of cosmic rays. FERMI-LAT: the Anti-Coincidence Detector (ACD), the Tracker (TKR) and the Calorimeter (CAL). AMS-02: the Transition Radiation Detector (TRD), the Time of Flight (TOF), the tracker layers, the Electromagnetic Calorimeter (ECAL) and the Ring Imaging Cherenkov Detector (RICH). CREAM-II: the Timing Charge Detector (TCD), the Cherenkov Detector (CD), the Silicon Charge Detector (SCD) and the CAL. PAMELA: the TOF scintillators (S1–S3), the TKR, the CAL and the neutron detector. In the case of PAMELA and AMS-02, the magnets are not represented. Taken from [42].

advantages, when compared with direct detection, are the larger effective areas, wider field of view, the longer duty cycles, and the easier maintenance. Furthermore, these features allow measuring higher statistics of cosmic rays with higher energies.

In figure 2.5, are represented the different techniques used to detect air showers. It includes particle detection, Cherenkov and fluorescence light, and radio detection. To collect the most information about the air showers, hybrid detection, with two or more sampling techniques, is employed by some experiments. However, a few uncertainties have to be taken into account when measuring air showers. Some examples are the atmospheric conditions that are ever-changing, leading to fluctuations in the showers, and the lack of an absolute energy calibration that may lead to slight disagreements between the results of different experiments.

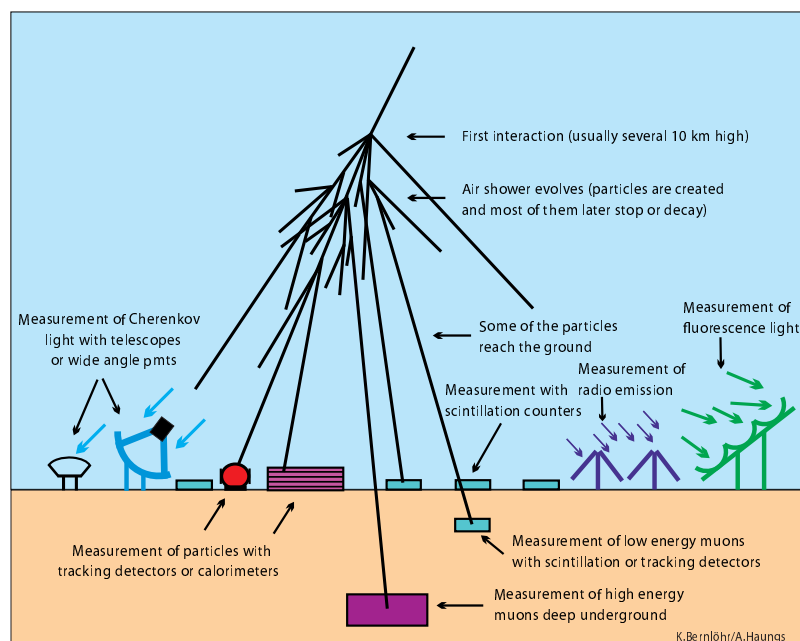


Figure 2.5: Schematic overview of the ground detection techniques. Taken from [43] and [44].

2.4.2.1 Particle detectors

Measuring the lateral distribution of air showers at the ground requires an array of particle detectors. These are usually scattered in a large area with fixed spacing between each other. As seen in figure 2.3, for a 10^{19} eV vertical shower, particles can be detected in a radius of more than a kilometer away from the shower core. For different energy thresholds, one should expect not only different array areas, because of the flux of particles, but also different spacing between the detectors. Example, for air showers with primary above 10^{18} eV, the distance between detectors can be about a kilometer.

The main advantages of this detection technique are that it can cover larger areas at a lower cost, has a large field of view (full sky coverage), and long duty-cycles (usually above 90%). However, the detectors are usually not build to distinguish the different components of the shower, and as already mentioned, having an independent measurement of the

muonic component can be of paramount importance to studying the shower's hadronic interactions. For that reason, in some experiments, particle detectors are also placed below absorbers, which will only let muons through. In some cases, these are buried underground, as shown in figure 2.5, placed below a sheet of led or water.

The most commonly used detectors are water-Cherenkov tanks (Pierre Auger Observatory [1], see section 3.1.1, HAWC [45] and IceTop [46]), and scintillators (KASCADE-Grande [47], Tuska-Grande [48], AGASA [49] and TA [50]). Some less commonly used detectors are the RPCs (see chapter 5), used at ARGO-YBJ [51] to detect air showers produced by cosmic gamma-radiation, and the liquid ionization chambers of KASCADE-Grande that measures the hadronic component of the shower.

The particle detectors at the ground allow obtaining the lateral distribution and the arrival time of the shower. With these, the incident direction of the shower and the energy of the primary cosmic ray can be reconstructed.

2.4.2.2 Light detectors

The shower emits two types of lights when travel through the atmosphere: fluorescence and Cherenkov. Optical detectors at the ground detect the photons patterns that reflect the evolution of the shower in the atmosphere. These detectors can, for the most part, be divided into three categories: fluorescence mirror telescopes, Cherenkov mirror telescopes, also known as Imaging Atmospheric Cherenkov Telescopes (IACT), and wide-angle Cherenkov counter arrays.

Fluorescence and Cherenkov mirror telescopes have similar concepts: light is reflected and focused by a large mirror into a photon-sensitive camera. They can have a high angular resolution, but can not look at the full sky, making observations limited to their field of view. The main disadvantage of mirror telescopes is their low duty cycle at around 10%. Since these are sensitive to the atmosphere conditions, light pollution, and the sky background light, they can only be operated during dry, clear, and moonless nights. The fact that the emission of fluorescence is weaker than Cherenkov light makes it so, the accuracy of those detectors is more dependent on its surrounding conditions.

Since the cone of Cherenkov light produced by the air shower is narrow [35], especially at high energies, it requires for the detectors to be pointed roughly at the shower axis. For that reason, Cherenkov light detectors are typically not used in the UHECR range, where the flux of particles is low. Experiments such as H.E.S.S. [52], MAGIC [53], VERITAS [54], and CTA [55] use IACT to measure gamma-ray induced showers. On the other hand, the fluorescence light produced by the air shower is emitted isotropically, making it a great tool to measure the shower development even if the shower axis is kilometers away from the detector. Moreover, the energy threshold of fluorescence telescopes is in the 10^{17} eV, as the light from less energetic showers is too weak to be measured. This technique is used in UHECR experiments like HiRes [56], The Pierre Auger Observatory [1], and TA [50], allowing to determine the longitudinal profile of the shower.

Cherenkov counter arrays also measure the Cherenkov light cone produced by the

EAS. These are composed of a large-size photomultiplier (PMT) with a Winston-cone light collector on its entrance window. The PMTs are designed to cover a substantial fraction of the sky. Multiple detectors are usually deployed in arrays using a spacing of about 100 m. CASA-BLANCA [57], Tunka-133 [58] and its successor TAIGA [59] use these arrays to detect air showers produced by cosmic rays and gamma rays.

2.4.2.3 Radio detectors

The first detection of radio emissions from air showers was performed in the 1960s [60], soon after the discovery of the radion emissions principles (mentioned in section 2.3). However, at the time, it was extremely difficult to distinguish these signals from the radio background signals produced by electronic systems and even other natural sources. In the 2000s, this technique was pick up again with success, and some reconstruction results have been presented. Radio antennas are usually used in large arrays since these are low-cost detectors with stable performance and 100% duty cycle. Examples of experiments are the AERA [61] array at the Pierre Auger Observatory, and the Tunka-Rex [62]. It is, however, important to notice that this technique should still be considered in the R&D stage.

3 Pierre Auger Observatory

The Pierre Auger Observatory [1], located in the Pampa Amarilla in western Argentina, is the world's largest cosmic-ray observatory. It is installed on a high plain near the Andean Mountains at an altitude of about 1400 m above sea level (a.s.l.) and covers an area of 3000 km². The Observatory's main objectives are probing the origin and characteristics of cosmic rays above 10¹⁷ eV as well as studying the development of the air shower. The Observatory's central campus is located in the city of Malargüe, in the southwest tip of the area covered. More than 500 physicists are part of the Pierre Auger Collaboration hailing from nearly 100 institutions.

In this chapter, the Pierre Auger Observatory is introduced. The detectors, data acquisition systems, trigger, and event reconstruction are explained. Finally, some experimental results are presented, which include the EAS muon number problem.

3.1 Detectors

The Pierre Auger Observatory is a hybrid detector that combines multiple detection techniques to measure EAS. The main detectors of the Observatory are the Surface Detector (SD) and the Fluorescence Detector (FD). While the SD is an array of 1660 water-Cherenkov detector (WCD), the FD is composed of 27 fluorescence telescopes, installed in 4 sites that overlook the SD. In figure 3.1 these detectors are represented on a map of the area. The 4 FD sites, Los Leones, Los Morados, Loma Amarilla and Coihueco, are represented in blue, while each black dot is an SD station.

The hybrid design provides two independent observation techniques of the EAS that are complementary and allow for cross-checks as well as measurement redundancy. This way, whenever a shower is generated in the atmosphere, the SD measures a slice of the EAS at ground level by being responsive to the electromagnetic and muonic components of the shower. The data acquired by this array allows to determine the arrival directions and to estimate the energy of the primary cosmic-ray. On the other hand, the FD provides information about the development of the cascade by measuring the fluorescence light produced by the shower in the atmosphere. This light is emitted isotropically in the UV part of the spectrum and it is mostly produced by the electromagnetic component of the shower, as already mentioned. It is proportional to the energy deposit in the atmosphere by the EAS, allowing to determine, once again, the primary energy. The FD measurement

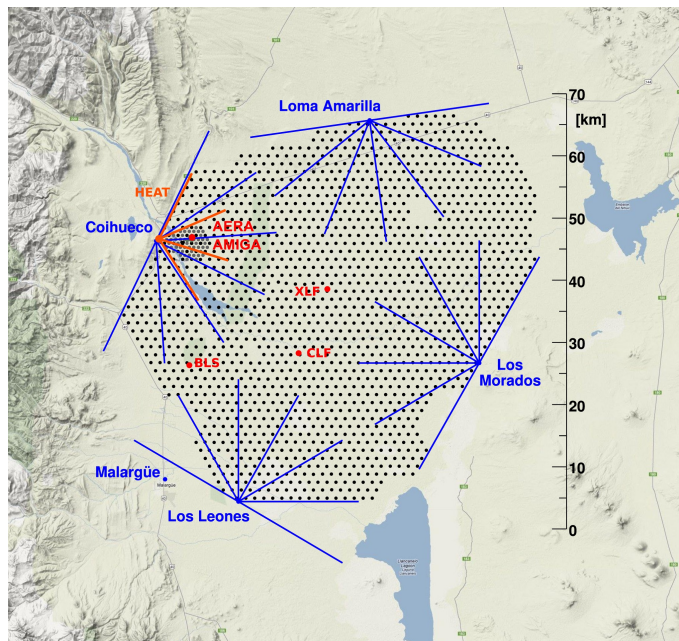


Figure 3.1: Layout of the Pierre Auger Observatory. Each black dot corresponds to one of the 1660 SD stations. In blue are the four FD telescopes and respective field of view. The laser facilities Central Laser Facility (CLF) and eXtreme Laser Facility (XLF) are marked, as well as the additional HEAT telescope, the AMIGA and AERA arrays, and the Balloon Launching Site (BLS). Taken from [1].

also gives information about the depth maximum shower size (X_{\max}) a crucial indicator of the primary mass composition. The combination of the data of the two detectors gives a comprehensive reconstruction of the shower. Moreover, if more than two FD telescopes measure the same shower (frequent for high energy events), multiple reconstructions of the shower are possible providing important cross-checks. A typical hybrid event is represented in figure 3.2, where the Los Leones FD telescope (blue) traces the longitudinal shower profile and the WCDs (white dots) measure the same shower. Observations using the FD are, however, limited to a duty cycle of $\sim 15\%$ since these telescopes can only be operated during dark nights with good weather. The SD operates continuously 24 hours a day.

New detectors are being added to the Observatory in what is called Auger Prime [64]. The main upgrade will be the addition of a detector to the SD stations. A plastic scintillator, Scintillator Surface Detector (SSD), will be placed on top of the WCD allowing for a new and complementary measurement of the air shower at ground level. This will enhance the Observatory capabilities to measure the air shower and address many of the open questions about the primary cosmic rays and EAS. Namely, the main objective is to give a better understanding of the mass composition and the origin of the flux suppression. Smaller arrays of other detectors like AERA [61] and AMIGA [65] are now also part of the Observatory, being installed in the Infill region of the array. This is a region of the array near the Coihueco FD site where the density of SD stations is higher. There, instead of the standard distance of 1500 m between WCDs, these are either 750 m apart or 433 m, in a even smaller portion of the array. The addition of different detectors to the Observatory

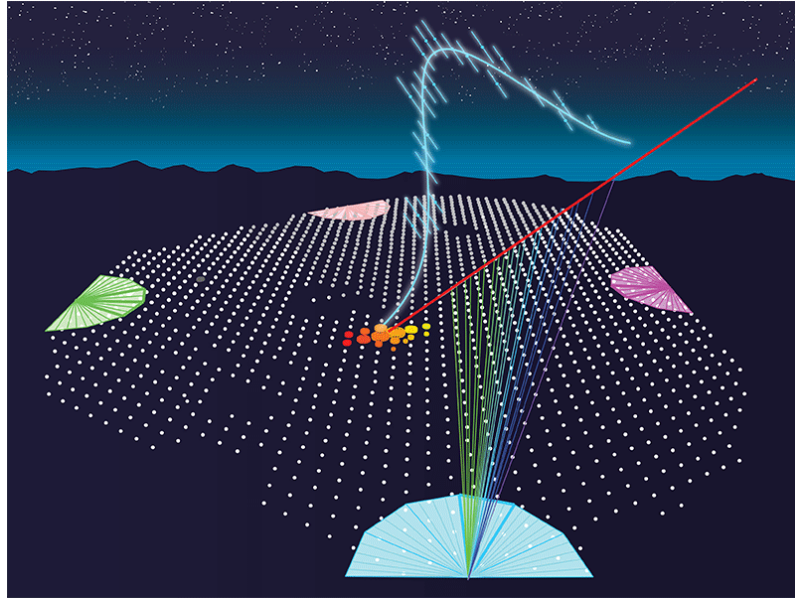


Figure 3.2: Representation of a hybrid event in the Pierre Auger Observatory. One of the FD sites detects the EAS using the fluorescence light emitted in the atmosphere while the SD stations measure the particle when they hit the ground. The red line represents the shower axis. Taken from [63].

allows for new cross-checks and calibrations between all the measurements. While in AERA an array of antennas detect the radio emissions of lower energy air showers, in AMIGA the muonic component of the EAS is measured using plastic scintillators buried 2.3 m underground.

3.1.1 Surface Detector

The SD [66] array of the Pierre Auger Observatory covers a total area of 3000 km². Such a massive area is required to accumulate meaningful amounts of data of UHECR in the lifetime of the Observatory. The 1660 WCD part of the array are 1500 m apart. In the left picture of figure 3.3 is shown a line of SD station in the typical landscape of the Observatory's site.

The WCDs are cylindric water tanks with a diameter of 3.6 m and a height of 1.2 m filled with 12 tones of ultra-pure water. Three photomultiplier tubes (PMTs) record the Cherenkov light generated by the passage of relativistic charged particles in the water. The tank is made of polyethylene liner creating a light-tight environment that reflects the light in the inner walls of the WCD. The PMTs, 9-inch Photonis XP1805/DI, and its housing are installed symmetrically on the top of the tank looking downwards into the water. The light produced is measured in Vertical Equivalent Muon (VEM) units. Each detector is calibrated so that 1 VEM corresponds to the signal produced by a muon traversing the tank on a vertical trajectory.

In the right image of figure 3.3 a station is pictured and the main components are shown. Each station is self-contained able to generate power and communicate through a radio

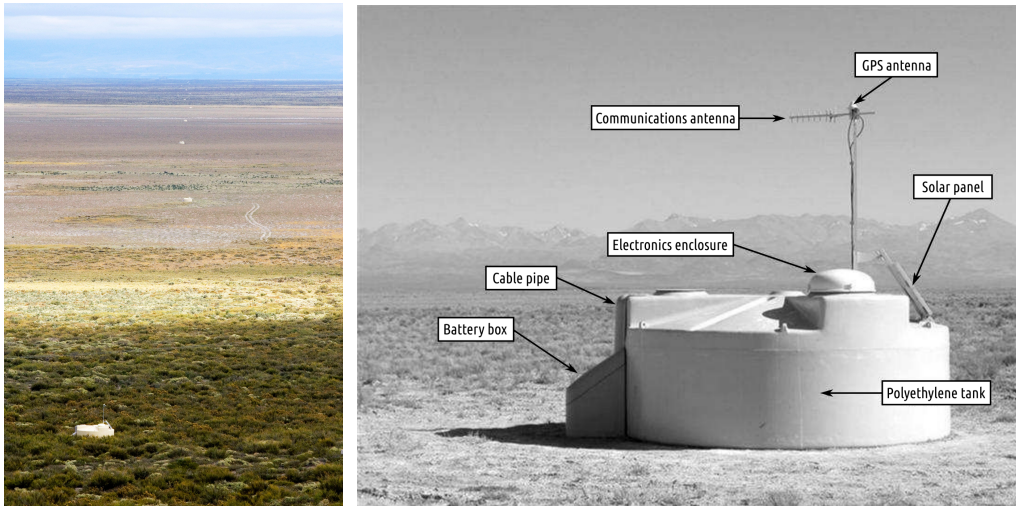


Figure 3.3: WCD part of the SD. Left: A line of SD stations in the typical landscape of the Observatory's site. Right: Picture of an SD station in the field and its main components. Taken from [1].

transceiver. Two solar panels, mounted on top of the tank, charge two 12 V batteries through a commercial charge controller. These are wired in series providing a total of 24 V and an average of 10 W to the station. The batteries are placed inside a box and isolated with foam so they are protected from the high temperature that can reduce their lifetime. Power is controlled by a Tank Power Control Board (TPCB) that monitors it and can hibernate a station in case of low battery charge. A bidirectional radio frequency telecommunication network is responsible for the communications between the stations and the central campus. A custom Wireless Local Area Network (WLAN) connects the antennas on top of the tank to a microwave backbone network that has five towers communicating between each other, four in the FD sites and a fifth one at the main campus. Inside the semi-spherical enclosure are placed all the electronics, including the data acquisition system that reads the PMTs signals and converts them to digital. The particularities of this system are addressed in section 3.2.

3.1.2 Fluorescence Detector

The FD [67] of the Pierre Auger Observatory consists of 24 telescopes, six in each of the four sites, overlooking the SD array. The telescopes are inside a clean climate-controlled building, like the one shown in the left picture of figure 3.4. The field of view of each telescope is $30^\circ \times 30^\circ$ in azimuth and elevation. The last has the minimum set at 1.5° above the horizon. This way, the total field of view of an FD site is 180° , combining the six telescopes. These were designed to measure air showers with primary energy of 10^{18} eV or above. Additionally, three extra telescopes are installed in the Coihueco site, forming the High Elevation Auger Telescopes (HEAT) [68]. These telescopes can be tilted changing the elevation range from 30° to 58° , extending down the energy of measured air showers to 10^{17} eV.

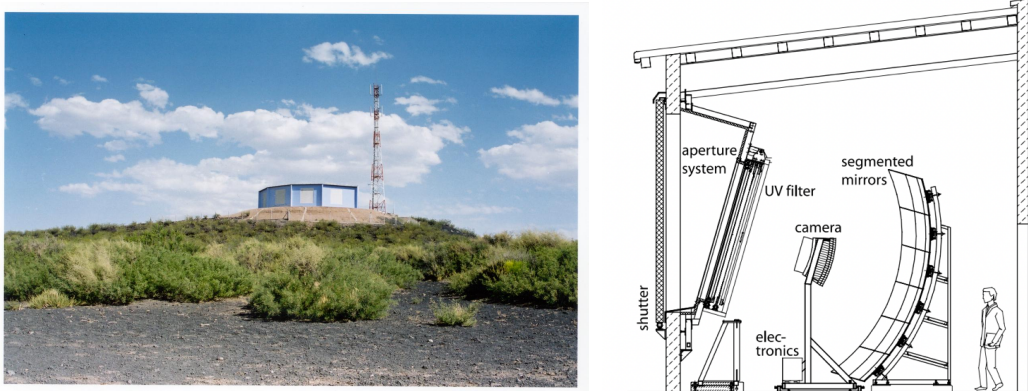


Figure 3.4: FD. Left: FD building and communication antenna at the Coihueco site. Right: Schematic view of the telescope with a description of its main components. Taken from [1].

The right diagram of figure 3.4 shows a schematic view of the fluorescence telescope. The fluorescence light emitted by the de-excitation of the atmospheric nitrogen when the EAS passes through, enters the circular diaphragm with a filter glass window. The filter transmits light in the UV band while absorbing the visible light, reducing the background that reaches the camera. The diaphragm also serves as a window over the aperture that keeps the building clean and climate-controlled. Corrector rings, placed in the outer part of the aperture, correct spherical aberration and eliminates coma aberration. Segmented spherical mirrors focused light that will then reach the camera. The camera is a matrix of hexagonal PMT tubes, Photonis XP3062 with a side length of 40 mm, arranged in 22 rows by 20 columns. The shutters protect the camera from sunlight during the day as well as rain and strong winds that might damage the equipment. Communication between the FD sites and the central campus is possible through the same microwave backbone network that serves the SD stations.

The atmospheric conditions during the FD operations are monitored using four LIDAR systems [69], one in each FD site. Balloon measurements of the atmospheric profile are performed using meteorological radiosondes attached to helium weather balloons, sent from the BLS. Two laser facilities, The CLF [70] and the XLF, located in the middle of the SD array, send laser test pulses to the telescope for calibration purposes.

3.1.3 Scintillator Surface Detector

The Scintillator Surface Detector (SSD), an upgrade to the Pierre Auger Observatory, consists of installing two $1.6 \times 1.2 \text{ m}^2$ scintillator modules on top of the existing WCD (as shown in figure 3.5). Each extruded plastic scintillator module is made of twelve 1.6 m long bars perforated with wavelength-shifting (WLS) fibers for light collection. The two modules are placed inside a $3.8 \times 1.3 \text{ m}^2$ aluminium box, with a Hamamatsu R9420 PMT in the middle connected to the 48 WLS fibers. When a particle crosses the scintillator bars it emits light that then travels through the WLS fibers to the PMT. With the addition of the SSD, the electronics of the WCD needed to be upgraded to accommodate the new

detector. The new electronics board is based on a Xilinx Zynq Field-Programmable Gate Array (FPGA) with built-in processors. A detailed description of the SSD can be found in [64]. The first SSD modules were installed at the end of 2016 and have been operational since then.

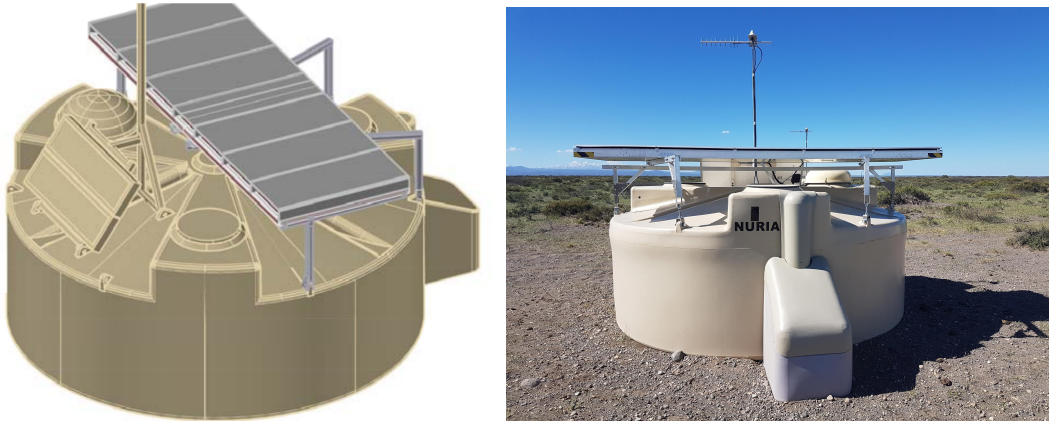


Figure 3.5: A SD station with an SSD scintillator on top. Left: Drawing of the tank and all its components with the new detector on top. Right: An SD station in the field with the scintillator installed. Taken from [64].

3.1.4 Other detectors

3.1.4.1 AERA

The Auger Engineering Radio Array (AERA) [61] comprises 153 autonomous radio stations distributed over an area of 17 km². It was designed to operate in coincidence with the other detectors of the Observatory to perform observations of EAS with primary energies in the 10¹⁸ eV range. Radio signals are sensitive to the development of the electromagnetic component of the air shower making radio detection a viable technique, as mentioned previously. Each station consists of two perpendicularly oriented antennas, aligned with the magnetic north and west, which are sensitive to emissions in the frequency range of 30 to 80 MHz. Various prototypes have been used since the beginning of 2009, first to understand the emission mechanisms. More recently, a first analysis of the radio emissions was published [71].

3.1.4.2 AMIGA

The Auger Muons and Infill for the Ground Array (AMIGA) [65] goal is to both lower the energy threshold of the SD array and to measure directly the muons part of the air showers. The objective of extend the SD energy threshold down to 10^{16.5} eV is possible by creating an array of closer WCDs in what is commonly known as the Infill. To measure the muonic content, an Underground Muon Detector (UMD) array is installed near the Infill WCDs. In it, scintillators with an area of 30 m² are buried underground at a depth of 2.3 m. The ground above the modules shields them from the electromagnetic component

of the shower, making sure the only particles detected are the muons. Each detector consists of 64 four meters long scintillator strips with WLS fibers. These are far enough from the SD station so that uniform shielding is guaranteed, without shadowing from the WCD. They are, however, close enough to the station so that both detectors can measure the same shower front. The UMD shares GPS time signal and triggers with the WCD while a new communication system was deployed to cope with the higher data rates. An engineering array of seven UMD stations has been installed and is taking data since 2017. The full-scale array is now being deployed in the field.

3.2 Data acquisition and triggers

The Central Data Acquisition System (CDAS), located in the main campus of the Observatory, was build to assemble the SD triggers, to control its detectors and to store data. It is designed to run continuously, with minimum intervention, and it is a mixture of commercial hardware with custom made, high level, software. While SD data is delivered directly to the CDAS, the FD data is recorded in each site locally and then transferred daily to the central campus. After the FD data is synchronized, it is merged with the SD events into hybrid coincidences. The data stored in the CDAS is mirrored every day to the IN2P3 Computer Center in Lyon, France.

In the SD stations, local triggers are essential to reduce the background signal rate (~ 3 kHz, mainly random single cosmic ray muons). Such a rate is not compatible with the limited communications bandwidth between the stations and the CDAS. Local triggers reduce the rate of events sent for analysis in the CDAS to 23 Hz. Upon receiving this information, the computers on the main campus will check for coincidences between stations. If a coincidence is verified, the CDAS will ask the stations in the area for the event's data. SD local and array level triggers are discussed in this section. The full details of the SD's trigger system can be found in [72].

In the FD stations, the data of each camera passes three trigger levels. Two are at hardware level, and the third one is a software trigger performed by the camera acquisition computer. These triggers, like the local SD ones, reduce unwanted and random events. After, if the event survives these filters, it is sent to a local station computer where the data of all the telescopes is reconstructed. A hybrid trigger is generated, sending a trigger to the array, via CDAS. A detailed description of the FD electronics can be found in [67].

The Observatory's data is analyzed using the Offline software framework. It was developed by the Pierre Auger Collaboration in C++ to read the different formats output by the detectors as well as files produced by the different simulation tools. Offline is built with a modular structure so that processing steps can be added or removed from the analysis. This way, this software allows performing events reconstruction using both the data from the Observatory and the simulation outputs. A full description of the software is given in [73].

3.2.1 SD signal digitization and triggers

Two signals are output by the WCD's PMTs: an AC coupled anode signal and the last dynode signal that is amplified by the PMT based electronics (32 times the charge gain of the anode). The PMT's outputs go the front-end board where noise filters are implemented before they are digitized using two 10 bits semi-flash 40 MHz ADC. The use of these two ADCs to read signals with different gains allows extending the dynamic range of the system to 15 bits. A Programmable Logic Device (PLD) monitors and controls the ADC, stores its data into a buffer memory and informs the station microcontroller when a trigger occurs. The digitized signals area (Q) and amplitude (I) are constantly monitored for trigger purposes. The front-end is interfaced with the main board of the SD electronics, the unified board (UB), that has the station controller (an IBM PowerPC) responsible for communications with the CDAS, among other things.

The SD local trigger has two levels of selection and records 768 samples ($19.2 \mu\text{s}$) of the flash ADCs. T1, the lower level trigger, has two main modes: threshold (TH) and time over threshold (ToT). TH mode requires a coincidence between all the PMTs when a simple threshold is applied. The threshold, usually around $1.75 I_{\text{VEM}}$, yields a rate of events of 100 Hz. ToT mode needs at least 13 bins in a 120 samples window to be over a threshold amplitude ($0.2 I_{\text{VEM}}$), allowing to select small signals spread in time. This condition has to happen in at least two of the three PMTs. The average rate of ToT triggers is 1.2 Hz. The second level trigger, T2, cuts the rate of T1s down to 23 Hz. While all T1-ToTs are considered to be a T2-ToT, the T1-THs need to pass a higher threshold ($3.2 I_{\text{VEM}}$) to become a T2-TH.

In 2013, two new T1 modes were installed in the SD, aiming to measure lower amplitude signals and so reducing the energy threshold of the array. The requirements for T1-TH and T1-ToT give a minimum signal of 1.75 VEM and 2.6 VEM, respectively. Moving to lower values, a typical background muon signal is 1 VEM by construction, requires the design of a trigger that can survive the high background in these ranges. The two algorithms, built on top of T1-ToT, are known as time over threshold deconvoluted (ToTd) and multiplicity of positive steps (MoPS). In the first, the signal exponential tail, that results of the diffusely reflected Cherenkov light, is deconvolved before applying the ToT conditions, reducing the effect of muons in the trigger. For the second, the number of positive-going steps is counted in a time window of $3 \mu\text{s}$. To reduce the influence of the muons and noise, the step needs to surpass the noise level and be lower than half the vertical muon step. If the number of steps is higher then four the trigger is accepted. Both modes require a signal greater than ~ 0.5 VEM and the conditions present in two out of three PMTs. Like in the case of T1-ToT, these complex T1s are automatically promoted to T2.

All T2's timestamps are sent to the CDAS for determination of the array-level trigger, T3. The generation of T3s takes into account a spatial and temporal combination of T2 triggers. The spatial coincidences are obtained by counting the number of stations outwards, from the central one, in terms of crowns. A crown is a hexagon around a central

station. The first crown is the six nearest stations, the second the 12 after and so on, as shown schematically in the right diagram of figure 3.6.

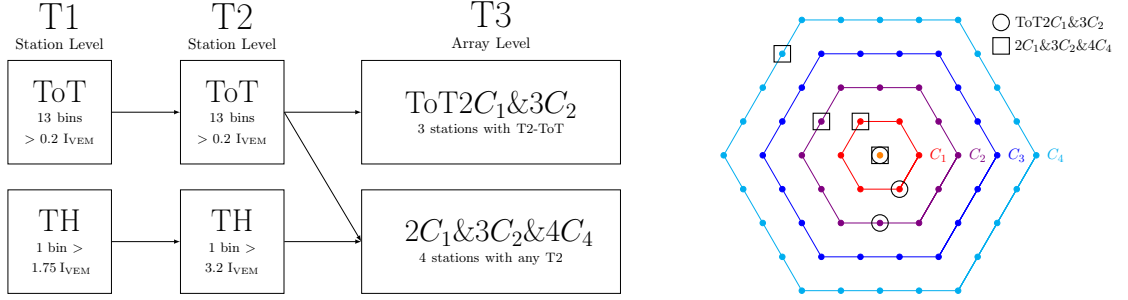


Figure 3.6: The SD local and array level triggers. Left: The 3 trigger levels of the surface array. T1 and T2 are station triggers and T3 is an array trigger generated by the CDAS. The two main types of T1s, ToT and TH are shown. The recently implemented T1 trigger, ToTd and MoPS, are not represented but follow the same sequence as the ToT. Right: The two T3 pattern, ToT2C₁&3C₂ (circles) and 2C₁&3C₂&4C₄ (squares). These figures are based on the ones presented in [1].

T2 triggers of the types ToT, as well as ToTd and MoPS, will generate a T3 with at least three stations. The pattern is called ToT2C₁&3C₂. It happens when two of the three stations are contained within a crown (2C₁), and all three are within two crowns (3C₂). An example of this T3 is represented using circles in the right diagram of figure 3.6. The timing criteria applied for this trigger is that each T2 must be $(6 + 5C_n)$ μ s of the one in the centre. Since this trigger has a low background, it selects mostly physics events. 90% of the events are real showers, being most efficient for showers below 60°. The second T3 mode is called 2C₁&3C₂&4C₄, a four-fold coincidence of any T2. At least two stations must be within one crown (2C₁), three of four in two crowns (3C₂), and all four within four crowns (4C₄). An example of the 2C₁&3C₂&4C₄ T3 is represented using squares in the right diagram of figure 3.6. The timing criteria applied are the same as in ToT2C₁&3C₂. This T3 is most efficient in horizontal showers, that are rich in muons. However, it accepts mostly background with only 5% of triggers being promoted to the next level. In the left diagram of 3.6 is shown a representation of the different level triggers discussed (ToTd and MoPS triggers follow the ToT pattern, as already mentioned).

Higher-level triggers, called physics triggers, are used during event reconstruction to identify the T3 events that are the result of an air shower. A description of these triggers is given in [72]. An example of a fourth level trigger, T4, is the 4C₁. This is a promotion of the 2C₁&3C₂&4C₄ T3 where 4 nearby stations were triggered. It is used to select horizontal showers.

3.2.2 FD signal digitization and triggers

The signals of all 440 PMTs channels in a telescope are digitized by a 12-bits ADC in a front-end board. Before sampling, the signals are processed by an anti-aliasing filter to match the 10 MHz digitization rate. The first level trigger (FLT) is implemented in the firmware of the front-end's FPGA. It applies an adjustable threshold that maintains the

pixel trigger rate at 100 Hz, to compensate for the different background conditions. The second level trigger (SLT), also implemented in the FPGA, looks for geometrical patterns in the data. Namely, it looks for at least five adjacent pixels in length compatible with a cosmic ray track. The SLT allows reducing the event rate from 100 Hz to a value between 0.1 Hz and 10 Hz, depending on the camera. After the two hardware triggers, data is collected by the camera's acquisition computer. In it, a software third level trigger (TLT) is implemented to reject fake shower events that survived the hardware trigger. It will reject events caused by lightning, cosmic muons impacts on the camera, and randomly triggered pixels without any time correlation.

The station's main PC, EyePC, reconstructs the data with all the telescopes information. This algorithm determines the preliminary shower direction and ground impact time, generating a hybrid trigger that is sent out to the CDAS. The CDAS will then send a request to the SD stations in the region impact, asking for signals recorded close to the time estimated. This trigger, FD-T3, allows recording low energy showers, below 3×10^{18} eV, where the array is not fully efficient.

All the information stored in each FD site is copied to the CDAS by the end of the night, when the acquisition is stopped.

3.3 Event reconstruction

3.3.1 SD reconstruction

The event reconstruction of the surface detector [74] allows determining the arrival direction of the incoming cosmic ray as well as estimate its energy. Both the deposited signals and the timing information given by the GPS are used in the reconstruction. The data is analyzed after the physics triggers are applied, cutting the number of events to guarantee a selection of good quality air showers. The reconstruction procedure described is used for vertical showers ($\theta < 60^\circ$) measured using the standard array (1500 m spacing).

The first step is the determination of the shower geometry. For events with enough triggered stations, this is possible using a concentric-spherical model to describe the shower front. The model, represented in the left picture of figure 3.7, describes the shower front evolution as a sphere inflating at the speed of light. The start time of the acquired signal, t_i , and the WCD position, \vec{x}_i , are used to compute the virtual origin of the shower in space, \vec{x}_{sh} , and time, t_0 :

$$c(t_i - t_0) = |\vec{x}_{sh} - \vec{x}_i|. \quad (3.1)$$

After the lateral distribution function (LDF) is fitted to the data. A modified NKG function is applied:

$$S(r) = S(r_{opt}) \left(\frac{r}{r_{opt}} \right)^\beta \left(\frac{r + r_1}{r_{opt} + r_1} \right)^{\beta+\gamma} \quad (3.2)$$

where $r_1 = 700$ m, β and γ are slope parameters that depend of the zenith angle, r_{opt} is the optimal distance, and $S(r_{opt})$ a estimator of the shower size. For the standard SD array,

the optimal distance is $r_{opt} = 1000$ m and thus the shower size is $S(1000)$. The right plot of figure 3.7 shows an example of an LDF fit that includes non-triggered and saturated stations. Its outcome is the shower impact point on the ground (\vec{x}_{gr}) and the shower size $S(1000)$.

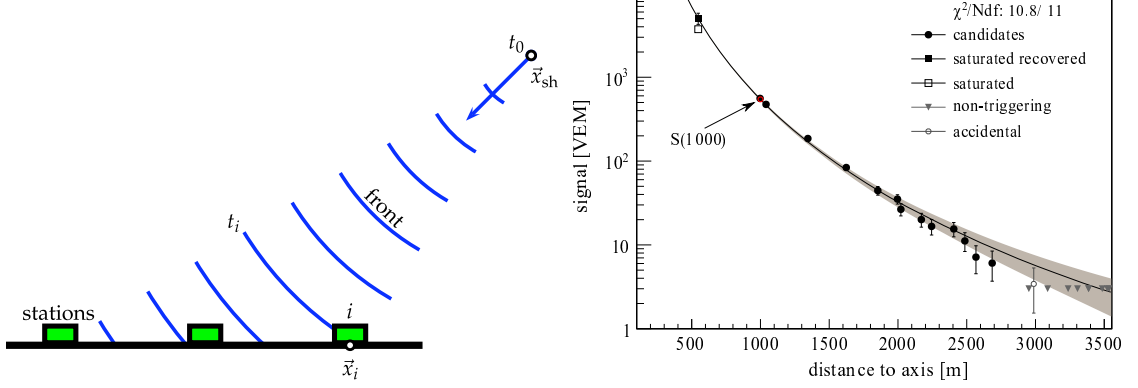


Figure 3.7: SD reconstruction. Left: Schematic representation of the evolution of the shower front. Right: Example of an LDF fit. The estimated value of the shower size $S(1000)$ is indicated. Taken from [1].

The shower axis \hat{a} is obtained using the virtual shower origin (\vec{x}_{sh} from equation 3.1) and the shower impact point (\vec{x}_{gr} from the LDF fit):

$$\hat{a} = \frac{\vec{x}_{sh} - \vec{x}_{gr}}{|\vec{x}_{sh} - \vec{x}_{gr}|}. \quad (3.3)$$

The angular resolution [75] of the reconstruction is better than 1.6° for events with 3 stations, and better than 0.9° for events with more than 6 stations.

Lastly, the energy can be estimated using $S(1000)$, and taking into account the shower attenuation with zenith angle θ and geometrical effects. The shape of the attenuation curve is obtained from data using the constant intensity cut (CIC) method [76]. In the SD, the attenuation curve $f_{CIC}(\theta) = 1 + ax + bx^2 + cx^3$ was fitted with $x = \cos^2\theta - \cos^2\bar{\theta}$. The most up to date results of the fit are presented in [77]. The median angle, $\bar{\theta} = 38^\circ$, is taken as a reference point to compute $S(1000)$:

$$S_{38} = \frac{S(1000)}{f_{CIC}(\theta)}. \quad (3.4)$$

S_{38} can be considered the signal a shower with an inclination of 38° and shower size $S(1000)$ would have produced.

Hybrid events¹ are used to obtain a correlation between the energy measured by the FD (E_{FD}) and S_{38} . The correlation is well described by the power law $E_{FD} = A(S_{38}/\text{VEM})^B$, where the parameters A and B are fitted to data. The latest results are shown in the left plot of figure 3.8, yielding $A = (0.186 \pm 0.003) \times 10^{18}$ eV and $B = 1.031 \pm 0.004$. Thus, the

¹3338 events collected between 1 January 2004 and 31 December 2017 [77].

SD energy can estimate as:

$$E_{SD} = A \left(\frac{S(1000)/f_{CIC}(\theta)}{\text{VEM}} \right)^B \quad (3.5)$$

The systematic uncertainty in the energy scale is 14% [78] and is dominated by the uncertainty in the absolute calibration of the FD telescopes. The SD energy resolution (see right plot of figure 3.8) is $\sim 21\%$ for 10^{18} eV and it decrease with energy, being $\sim 10\%$ at 10^{19} eV. This resolution was obtained from the distribution of the ratio $E_{SD}/E_{FD} = A(S_{38}/\text{VEM})^B/E_{FD}$ and fixing the FD energy resolution to 7.6%.

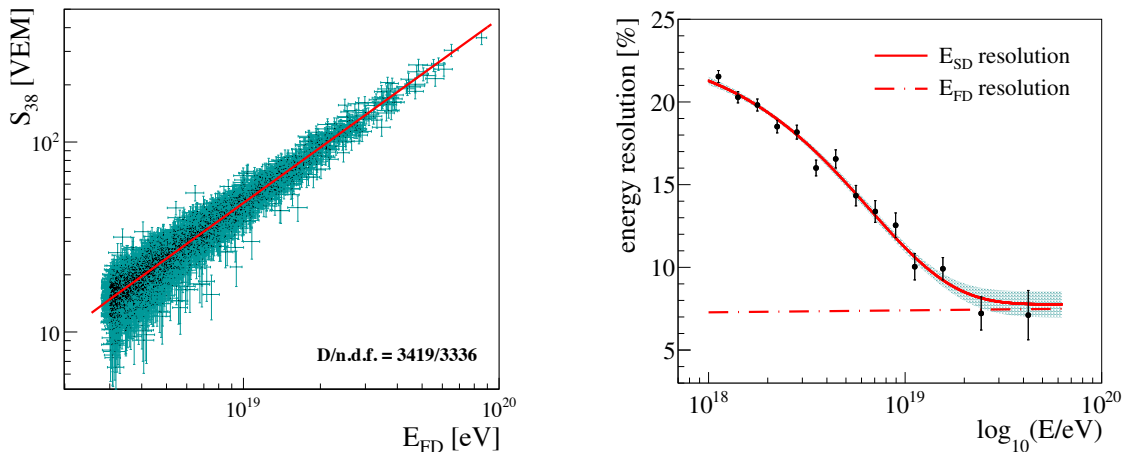


Figure 3.8: Left: Correlation between S_{38} and the FD energy. The data points are hybrid events. Right: Energy resolution of the SD estimated from hybrid events when the FD resolution is fixed to 7.6%. Taken from [77].

For inclined events, $\theta > 60^\circ$, a different reconstruction method is employed. Further information can be found in [79–81].

3.3.2 FD reconstruction

The FD event reconstruction can be divided into two steps: a geometrical reconstruction, which will determine the shower detector plane (SDP), and a reconstruction of the longitudinal shower development, which will evaluate the X_{\max} and the shower energy.

The shower detector plane (SDP) is the plane containing the shower axis and the triggered fluorescence telescope. It is obtained using the pointing direction of each pixel part of the event. A schematic view of the SDP is shown in the left diagram of figure 3.9. Thus, the shower axis can be determined using the time information of each pixel, which has an angle χ_i along the SDP. The arrival time of the shower light, $t(\chi_i)$, follows the equation:

$$t(\chi_i) = t_0 + \frac{R_p}{c} \tan \left(\frac{\chi_0 - \chi_i}{2} \right) \quad (3.6)$$

where R_p is the minimum distance between the shower axis and the detector, t_0 the time that corresponds to R_p and χ_0 the angle between the axis and the intersection of the

ground with the SDP (see the left diagram of figure 3.9). These three parameters are then determined by minimizing a function based on equation 3.6 that accounts for all the pixels (see [1]). In some trajectories, the timing information of a triggered SD station may be used to correct a degeneracy between R_p and χ_0 . This procedure is known as a hybrid reconstruction.

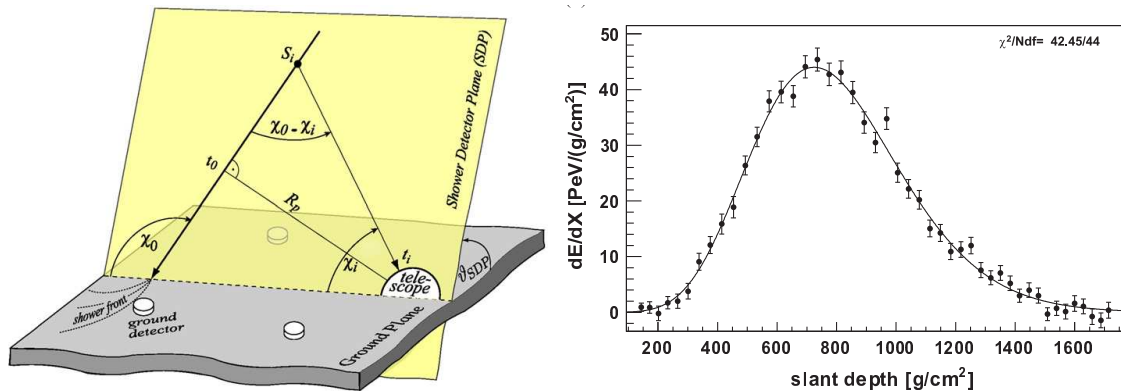


Figure 3.9: FD reconstruction. Left: Diagram of the geometrical shower reconstruction of the FD. Right: Reconstructed longitudinal profile: energy deposited as a function of the atmospheric depth. Taken from [67] and [1].

The signals recorded by the PMTs are converted into energy deposited as a function of the slant depth. The conversion takes into account the light attenuation in the atmosphere and disentangles the different light sources: fluorescence light, direct and scattered Cherenkov, as well as multiply scattered light. The proportionality between the fluorescence intensity and the energy deposit is given by the fluorescence yield². The data is fitted to the Gaisser-Hillas function (see equation 2.1):

$$f_{\text{GH}} = \left(\frac{dE}{dX} \right)_{\text{max}} \left(\frac{X - X_0}{X_{\text{max}} - X_0} \right)^{\frac{X_{\text{max}} - X_0}{\lambda}} \exp \left(- \frac{X_{\text{max}} - X_0}{\lambda} \right) \quad (3.7)$$

where $(dE/dX)_{\text{max}}$ is the energy deposited at depth X_{max} . The right plot of figure 3.9 shows the energy deposited as a function of the depth and the correspondent fit to equation 3.7.

The energy deposited in the atmosphere by the electromagnetic component of the shower is obtained by integrating the fitted Gaisser-Hillas. The primary cosmic ray energy is then estimated by adding the invisible energy, carried away by neutrinos and high energy muons. This is estimated to be 10 – 15% in the energy range of the FD measurement.

3.4 Selected results

The Pierre Auger Collaboration has published some of the most important experimental results in UHECR. In this section, select results are presented in what the energy spectrum,

²The fluorescence yield changes with atmospheric conditions, like air density, temperature, and pressure. Precise measurements [82] performed by the Airfly Collaboration are used to determine this variable.

mass composition, and arrival directions are concerned. The EAS muon contents results, the primary motivation for this work, are also shown.

3.4.1 Energy spectrum

The measurement of the flux of the highest energy cosmic rays has been one of the primary focuses of the Collaboration. With more than a decade of operation, the experimental data of the Pierre Auger Observatory was pivotal to confirm beyond doubt the existence of the *ankle* and the suppression in the energy spectrum [2, 83, 84].

The spectrum shown in the right plot of figure 3.10 is a combination of different analysis performed using data of the various detectors of the Observatory. These results were presented by the Collaboration in the 2019 edition of the International Cosmic Ray Conference (ICRC) and correspond to a total exposure that exceeds 77000 km² sr yr [77]. The left plot shows the results of each analysis: using the standard SD array (SD 1500 m) for vertical ($\theta < 60^\circ$) and inclined showers ($\theta > 60^\circ$), hybrid events, SD 750 m array to tap into a lower energies (with a threshold of 10¹⁷ eV), and Cherenkov light measured by the HEAT telescope (with a limit of 10^{16.5} eV).

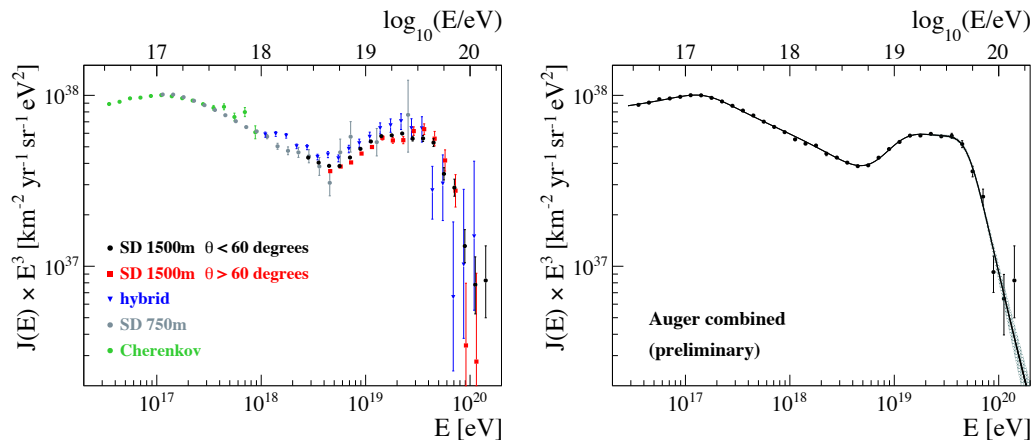


Figure 3.10: Energy spectrum measured by the Pierre Auger Observatory. Left: Spectra measured with different analysis techniques. Right: Combination of the several spectra in the left plot. Taken from [77].

The extension to lower energies allow to measure the *second knee*, an inflection before the *ankle*, that was observed by the KASCADE-Grande experiment [85]. Furthermore, a functional fit was performed to determine the energies of the inflection points and spectral indexes of different parts of the spectrum:

$$J \propto E^{-\gamma_0} \frac{1 + (E/E_{01})^{\gamma_0}}{1 + (E/E_{01})^{\gamma_1}} \frac{1 + (E/E_{12})^{\gamma_1}}{1 + (E/E_{12})^{\gamma_2}} \frac{1 + (E/E_{23})^{\gamma_2}}{1 + (E/E_{23})^{\gamma_3}} \frac{1 + (E/E_{34})^{\gamma_3}}{1 + (E/E_{34})^{\gamma_4}}. \quad (3.8)$$

The black line in the right plot of figure 3.10 represents the fit. Its results are presented in table 3.1. The number below each spectral index, represented with n in table 3.1, corresponds to the segments of the spectrum. 0 is the section of the spectrum before the *second knee*, 1 from the *second knee* to the *ankle*, 2 from the *ankle* until the point where

the spectrum flattens, 3 the "flat" section before the suppression and 4 the suppression. In [77], it is mentioned that the section of the spectrum before the suppression might indicate a further point of inflection.

| n | 0 | 1 | 2 | 3 | 4 |
|----------------------------------|-----------------|-----------------|---------------|---------------|---------------|
| $E_{(n)(n+1)} \times 10^{18}$ eV | 0.15 ± 0.02 | 6.2 ± 0.9 | 12 ± 2 | 50 ± 7 | – |
| γ_n | 2.92 ± 0.05 | 3.27 ± 0.05 | 2.2 ± 0.2 | 3.2 ± 0.1 | 5.4 ± 0.6 |

Table 3.1: Fit results of expression 3.8 to the data presented in the right plot of figure 3.10 [77].

3.4.2 Mass composition

Shower characteristics can be used to infer the primary particle composition in the UHECR range. The X_{\max} is usually chosen for this purpose, being the most robust mass-sensitive EAS observable. Namely, the mean value of the X_{\max} distributions as a function of the primary energy is compared with the predictions made by hadronic interaction models (mentioned in section 2.3).

Figure 3.11 shows the $\langle X_{\max} \rangle$ and $\sigma(X_{\max})$ as a function of the energy, in the UHECR range. These results, presented at ICRC2019 [86], were obtained using data from hybrid events, i.e., events registered by the FD and having at least one triggered SD station.

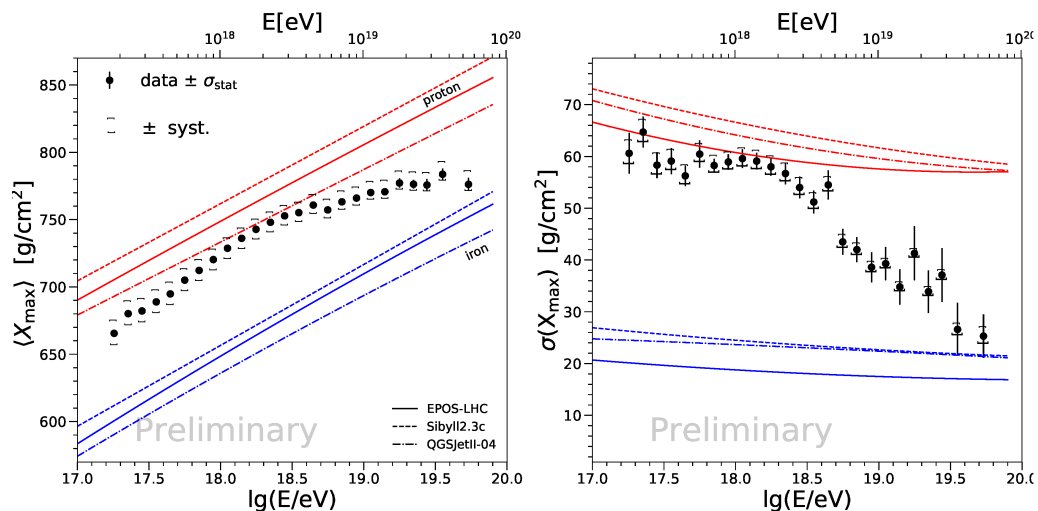


Figure 3.11: Measurements of $\langle X_{\max} \rangle$ (left) and $\sigma(X_{\max})$ (right) compared to the predictions for proton and iron nuclei of the hadronic interaction models EPOS-LHC, Sibyll 2.3c and QGSJetII-04. Taken from [86].

The results were compared with the predictions given by the hadronic interaction models EPOS-LHC, Sibyll 2.3c, and QGSJetII-04 for proton and iron-initiated showers. While below $10^{18.32 \pm 0.03}$ eV, the evolution of $\langle X_{\max} \rangle$ with energy (known as elongation rate) is 77 ± 2 g cm⁻²/decade, for higher energies this slope is significantly smaller: 26 ± 2 g cm⁻²/decade. The predictions give a constant elongation rate for the same primary composition (~ 60 g cm⁻²/decade). The measurement indicates that the mean primary

mass is getting lighter until $10^{18.32 \pm 0.03}$ eV, after which the trend inverts, and the composition becomes heavier. Furthermore, the narrowing of the X_{\max} distribution for energies above this threshold (see $\sigma(X_{\max})$ plot of figure 3.11) is in agreement with the composition behaviour mentioned above.

3.4.3 Arrival Directions

An analysis of the arrival directions can prove crucial information about the origin and nature of the UHECR. However, the interactions of cosmic rays with the galactic magnetic field, as well as the intergalactic one, make difficult the identification of sources. Such studies are, nonetheless, possible if taken into account that higher momentum and smaller charge (lighter mass) particles are less deflected from their original direction.

In 2017, the Pierre Auger Collaboration published results [3, 87] that found a statistically significant (5.2σ) dipolar large scale anisotropy for the highest energy cosmic rays, pointing to a direction in the sky. Figure 3.12 presents the flux of cosmic rays, for energies above 8×10^{18} eV, as a function of the position in the sky, in galactic coordinates, as seen by the Observatory's detectors. The maximum of the flux points towards galactic coordinates $(233^\circ, -13^\circ)$, represented with a cross, about $\sim 125^\circ$ from the galactic centre (the coordinates origin). The anisotropy observation supports the extragalactic origin hypothesis for UHECR rather than from sources within the galaxy.

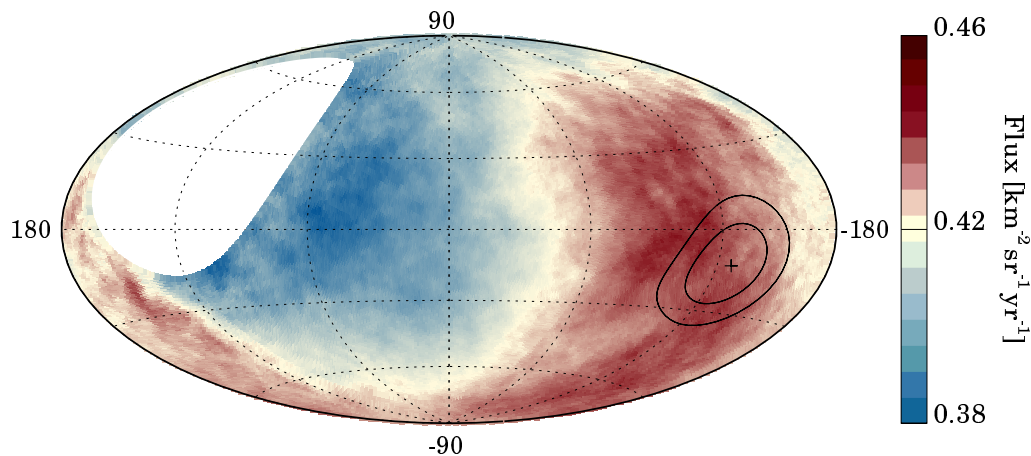


Figure 3.12: Sky map in galactic coordinates showing the cosmic-ray flux for energies above 8×10^{18} eV smoothed with a 45° top-hat function. The galactic centre is at the origin. The cross indicates the measured dipole direction; the contours denote the 68% and 95% confidence level regions. Taken from [3].

3.4.4 Number of muons

The study of EAS has been long seen as an opportunity to study the hadronic interactions at energy ranges far beyond the ones produced in modern colliders. Understanding these interactions would be of great importance to the large particle physics community. In what cosmic rays are concerned, it would be essential in the mass composition studies

as well as to understand the origin and propagation of UHECR. Furthermore, mass composition results rely on extrapolations of the hadronic interactions only measured up to the LHC energies. One could argue that undercover phenomena, e.g., an abrupt change on the hadronic interactions at higher energies, not yet accommodated by the models, could be another way to explain the composition results.

Muons constitute one of the best links to the hadronic interactions in the shower, because, as mentioned before, these are created in the decay of the shower hadrons. For that reason, several endeavours have been taken to understand their behaviour from the theoretical [88–90] and experimental [91–93] point of views. Recent studies [94] have shown using simulation that while the average of the muon distribution depends on the sum of all hadronic interactions, its shape depends mostly on what happens in the very first interaction of the shower.

The Pierre Auger Observatory has presented results of the number of muons and compared then to the predicted values given by the hadronic interaction models. Figure 3.13 show the average logarithmic muon content $\langle \ln R_\mu \rangle$ as a function of the average maximum shower depth $\langle X_{\max} \rangle$ at 10^{19} eV. The results fall outside the model predictions lines, making data and models incompatible. However, recent results [93] found that the fluctuations in the number of muons measured in data and the ones obtained in simulation, using the current hadronic interaction models, are compatible.

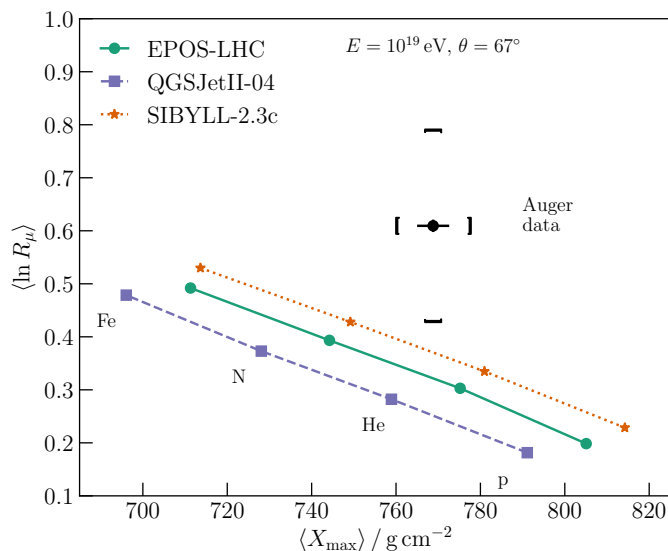


Figure 3.13: The Pierre Auger Observatory results for the average logarithmic muon content $\langle \ln R_\mu \rangle$ as a function of the average maximum shower depth $\langle X_{\max} \rangle$ at 10^{19} eV. The lines denote the distinct models' predictions for different primary compositions. Taken from [93] (updated).

Overall, the Observatory's results show a muon deficit in simulation (or muon excess in data) [91]. The fact that the muonic content is extrapolated indirectly from the WCD data analysis and the existing discrepancy between data and models, calls for an independent direct measurement of the muon content. MARTA [4] was designed to perform such measurement in Auger. Although, other independent experiments of the muonic content are

already part of the Observatory, i.e., AMIGA (section 3.1.4), and the soon to be installed SSD detectors (section 3.1.3) will improve the estimation of this component, another measurement of the muons directly below the WCD can be beneficial. A full description of MARTA is given in chapter 4.

4 The MARTA enhancement

The results presented in the previous chapter showed that the current muon measurements are not well described by models. Although this might point to the models not being able to describe interactions at the highest energies accurately, it can also be that the number of muons is not correctly estimated using the current techniques. Moreover, standard measurements of the air shower's particles at the ground, e.g., the Pierre Auger Observatory's WCD, measure a combination of the electromagnetic and muonic parts of the air shower. From that signal, the number of muons is obtained indirectly, introducing significant uncertainties in results like the estimation of the primary composition. A direct, independent, and accurate measurement of the muonic component of the EAS would allow to have composition sensitivity on a shower-by-shower basis, to study hadronic interactions at the highest energies, to improve the sensitivity to photon primaries, and to better understand and reduce the systematic uncertainties of many different measurements.

The Muon Array with RPCs for Tagging Air showers (MARTA) is an innovative concept that combines the measurement of the muons using Resistive Plate Chamber (RPC) [95] detectors and the one performed by the standard air shower detectors, that are sensitive to all detectable components. It was developed in the framework of the Pierre Auger Observatory to be installed in the SD stations. All the components of MARTA were this way, designed taking into account the specifications of the Observatory's SD stations, namely: the size of the detectors to be installed, the dimensions of the readout grid being used in the RPCs, the power consumption restrictions imposed by the station power system, the rate of events, the weather conditions that are expected in the Observatory's site, etc. The design was extensively studied using simulation, and the results were presented in [4]. An engineering array (EA) is starting to be installed in seven of the SD stations. It will be used to prove MARTA's concept and to help calibrate both simulations as well as other detectors.

In this chapter, the the concept of MARTA is introduced, and the station design described. Then a review of the simulation results with the expected performance is given, and the EA to be installed at the Observatory's SD is discussed.

4.1 Concept and design

In MARTA, four RPCs are placed under a WCD, as shown in figure 4.1. The detector's modules are installed inside a concrete structure that supports the WCD. This way, the WCD will remain unchanged and can continue operating as a standard detector in the SD array. The water, with a depth of 1.2 m, and the concrete structure, with a thickness of 15 cm, will act as shielding for the electromagnetic component of the shower. Thus, the RPCs will access the shower muons directly, most of which crossed and were measured by the WCD. It should be noted, that the materials above the RPC will also increase the energy threshold of the muon detection (a few hundred MeV). However, this effect should be small, given the typical muon energies in this phenomenon. With this setup, it will be possible to access the electromagnetic component in the tank by subtracting the number of muons measured by the RPC from the total signal given by the WCD ¹.

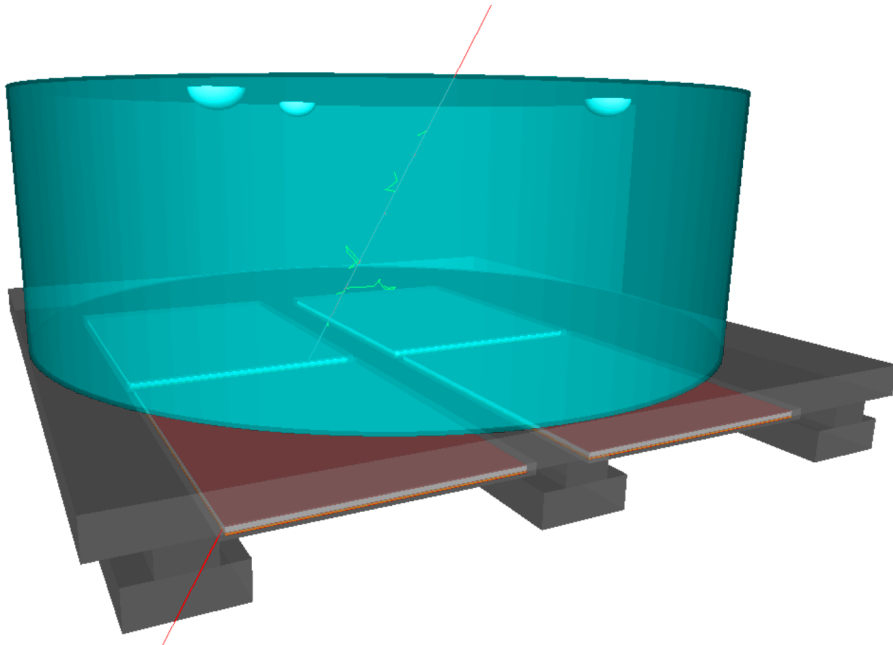


Figure 4.1: Representation of the MARTA station, illustrating its concept. Four RPCs (each with an area of $1.5 \times 1.2 \text{ m}^2$) are placed under a WCD. The top of the concrete structure is a square with side length of 3.6 m and a height of 15cm. The total height of the structure is 40 cm. The water inside the tank forms a cylinder with 1.2 m of height and 3.6 m of diameter. Taken from [4].

RPCs are widely used gaseous detectors of charged particles. They are known for being robust, low-cost, having high particle detection efficiency, and excellent spacial and time resolutions. The basic working principle is the following: a charged particle crosses a gas gap between two highly resistive parallel plates. Because high voltage (HV) is applied to the plates, after the first interaction of the particle with the gas, an avalanche of electrons

¹The WCD is sensible to all the detectable particles part of the shower, i.e., all but neutrinos. However, from the numbers presented in figure 2.3, it is possible to conclude that only a reduced number of hadrons will reach the ground. Furthermore, the hadrons who reach the ground already lost most of their energy in previous interactions in the air. Thus, their contribution to the WCD signal is negligible.

is created, that travel towards the anode, inducing a signal on the readout electrodes. A review on the RPC's state of art is given in section 5. These have meaningful advantages when compared to other detectors that perform the same kind of measurement, i.e., scintillators. Mainly, they have a lower-cost, which is key when covering large areas like in the case of UHECR arrays, and are easily build. Furthermore, the fact that the readout electrodes are physically separated from the gas volume, allows to have more complex readout patterns that are mostly constrained by the acquisition systems. It also allows to have a gas-tight sensitive volume with high-voltage isolation, making the detector more robust and less prone to failures. Although RPCs are mostly used in laboratory conditions (see section 5.2), much R&D has been done studying their ability to work in outdoors environments with low maintenance [5, 96–99].

The MARTA concept has many advantages when compared with other techniques used to measure muons in large EAS ground arrays, like the buried detectors. Firstly and as already mentioned, both the WCD and the RPC will measure essentially the same particles, allowing not only to have a full picture of the showers but also to cross-calibrate the detectors. The same cannot be said in the case of buried muon detectors. These need a constant mass over them so that particles above the same energy threshold can be detected in all directions. Thus, when pairing them with other instruments above ground, one has to guarantee the extra mass of the SD does not interfere with the measurement, i.e., avoid their shadow. Since they need to be further apart, both detectors will measure particles in the same shower front but not the same particles, making analyzing events more complex. Secondly, the energy of the muons measured in the RPC is mostly the same as in the WCD on top, while it differs considerably between the underground and SD. Finally, these detectors are easier to implement, taking less time and resources, and are also, consequently, easier to maintain.

MARTA takes advantages of communication, power and trigger systems of the SD of the Pierre Auger Observatory. An Offline implementation is being prepared so that MARTA's data and simulation can be analyzed with the other outputs of the Observatory [100].

4.2 Station description

A MARTA station combines the WCD and four RPC detectors, each inside an aluminium box that also hosts the electronics: power supply unit (PSU), HV, and data acquisition. Thus, a MARTA module is a sealed aluminium structure with gas, power, and communication connections. The aluminium box is divided into two compartments. The first compartment contains the RPC sensitive volume, the main component of the MARTA module, and the readout PCB, with 64 pads. The detector has an area of $1.2 \times 1.5 \text{ m}^2$ and two 1 mm gas gaps. Each pad has an area of $14 \times 18 \text{ cm}^2$ and these are distributed in 8×8 grid. A full review of the MARTA RPC's design and testing is presented in section 5.4. The second compartment, with an area of $0.447 \times 1.285 \text{ m}^2$, contains all the electronics.

Signal cables, HV, and gas connections are passed between the electronics and sensitive volume compartments. A schematic view² of the station with the four modules is presented in figure 4.2. Furthermore, the station has a Central Unit responsible not only for the management of the modules but also the interface with the WCD. A brief description of the MARTA's DAQ system is presented in [101].

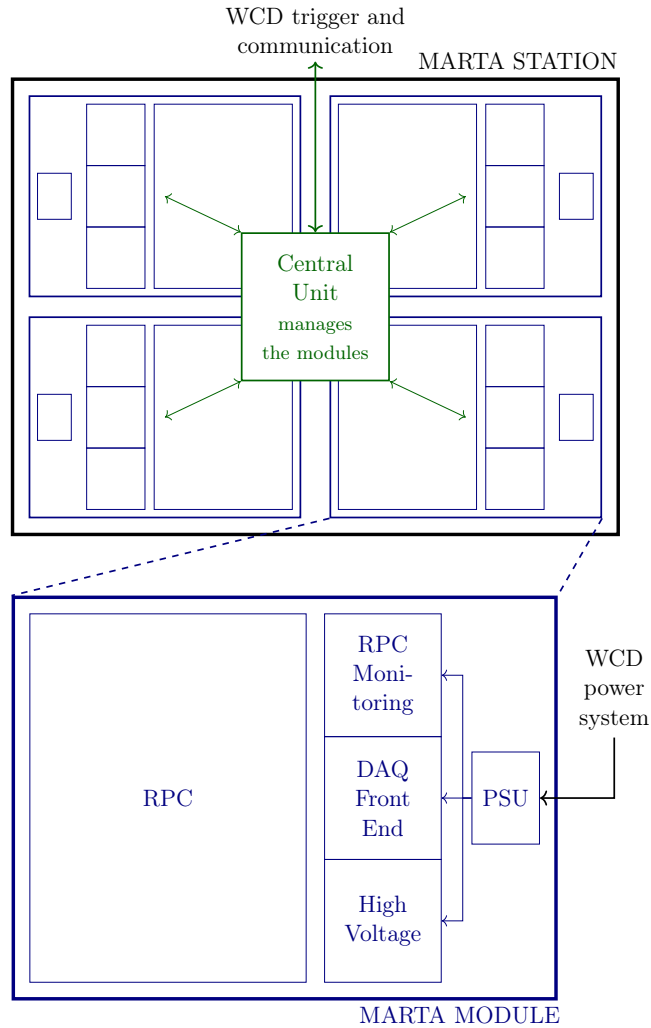


Figure 4.2: Schematic representation of the MARTA station. Four modules (blue), containing the RPC sensitive volume, readout grid, detector monitoring, data acquisition, power, and HV, are placed below the WCD. A Central Unit (green) manages the modules and works as an interface with the WCD.

The front-end board [102] is the primary component of the acquisition system. It will measure the 64 RPC signals using the MAROC 3 ASIC [6, 103, 104]. The RPC signal cables are soldered to a mezzanine board that is connected to the front-end. An FPGA is responsible for data and measurement management as well as communications via low-voltage differential signal (LVDS) with the Central Unit. The development of the front-end is the main focus of this thesis. In chapter 7 the front-end design is described while in

²Not to scale.

chapter 8 its performance is evaluated.

The HV board was developed from scratch since no commercially available options would fit MARTA's specifications. It was designed to be controlled and monitored via I²C, which allows adjusting the applied HV dynamically. Thus, it is possible to keep a constant reduced electric field (E/N) in the gas gaps, a quantity that is sensitive, among others, to the temperature and pressure of the environment. This is an essential feature since these RPCs are exposed to the harsh weather conditions of the Observatory's site.

The monitoring system is composed of a network of sensors that are placed strategically in the aluminium box. It can be divided into HV monitoring, already mentioned previously, gas monitoring, and weather monitoring. The humidity, air pressure, and temperature are measured inside the sensitive volume compartment. The gas flux is monitored using the bubblers that are installed before and after the detector gas input and output, respectively. Additionally, a pressure sensor is placed in the gas input. Measuring the gas flux will give hints about the RPC operation conditions, and help plan the replacement of gas bottles.

The power inside the electronics compartment is provided by a PSU. It was designed to get the 24 V given by the WCD power system and convert it to the required voltages of each component. The PSU is also controlled via I²C and allows to turn on and off individually every element inside the aluminium box.

A Central Unit per station controls all the electronics and act as a data concentrator. I²C and LVDS buses are available between the Central Unit and each module. Thus, it controls the different systems that use the I²C bus, e.g., HV, monitoring, and PSU, and use the fast LVDS lines to send commands to the front-end, as well as receive data and transmit triggers. It is based on an Intel Cyclone V SX SoC FPGA with a Hard Processor System (HPS) [105]. The FPGA and HPS share, among other things, memory. Hence, the FPGA can store the information received into the memory that will then be accessed by the processor. The data is this way stored in the Central Unit to be sent to the CDAS, if requested.

The trigger and communications systems of the SD (described in chapter 3) will be used by the MARTA station, as mentioned above. The Central Unit acts as the interface between the WCD and the RPCs' acquisition system. Whenever the WCD has a T1 or T2 trigger, of any type, the modules will acquire the data and send it to the Central Unit. It then waits to either keep the data in case the tank receives a T3 or erase it otherwise. In the EA, section 4.4, the communications between the station and the CDAS will be performed using the upgraded communication system, deployed by AMIGA, that can cope with higher transmission rates. It has the advantages of not interfering with the regular operation of the low bandwidth radio system of the SD and allowing for remote control using ssh.

All the parts of the MARTA station were designed to comply with the strict demands of outdoors operations. The stations are meant to be standalone: working for 24 hours a day with minimal maintenance in a hard to reach location. The harsh weather conditions of the Observatory also played an essential role when designing all parts of MARTA,

since the detectors need to work in different temperature conditions, that can vary from negative °C temperatures up to ~ 30 °C. Furthermore, the concrete structure will alleviate the significant temperature changes that can happen in a day and will interfere with the RPCs' operation. Another drawback of outdoors standalone operation is the limited power available. As seen before, in the Pierre Auger Observatory, power is generated using solar panels coupled with batteries, limited to a total consumption of about 10 W per station. Thus, the elements inside the station were designed having the low availability of power into consideration. Extra batteries and solar panels are installed in the EA stations, once again to not interfere with the normal operation of the SD array.

During the design process of MARTA, a different acquisition system was first made to prove that RPCs could be used outdoors. This system is called Prototype Readout Electronics for Counting particles (PREC) and uses analog electronics to read the RPC signals. While designing it, no concerns with power or space were taken into account. As an introduction to MARTA's DAQ systems, the first work of this thesis was to fully characterized the PREC system [106]. The results are presented in chapter 6.

4.3 Expected performance

A detailed simulation using the GEANT4 toolkit [107–109] was built to study the performance of MARTA in the Pierre Auger Observatory.

4.3.1 Station performance

In each station, the number of muons can be estimated as the number of hits in the RPC pads within a fiducial area. For the MARTA configuration, this area can be defined as the pads that have a mass overburden greater than 170 g cm^{-2} ³. The number of pads part of the fiducial area is a function of the shower geometry. While for a vertical shower, all pads below the shielding are in the fiducial area, for a shower with incident particles at 40° zenith angle, only 2/3 of the pads are part of the fiducial area (see the left plot of figure 4.3). The energy threshold was also studied for this mass overburden. The muon energy spectrum at 1400 m a.s.l. has its mean at ~ 1 GeV and about 15% of the those muons, with an energy lower than ~ 340 MeV, are absorbed after crossing the WCD and the concrete structure.

The simulated traces in the RPCs and the WCD are shown in the right plots of figure 4.3. The results take into account the RPC segmentation given by the spacial resolution of the pad grid, and a time resolution of 5 ns. These values correspond to a maximum particle density of $35.6 \text{ particles/m}^2$, assuming they all arrive at the same time. Such density is equivalent to that of muons 500 m away from the shower core in a $10^{19.5}$ eV proton shower with a zenith angle of 40° . In regions where the number of particles is higher, pile-up

³The value of 170 g cm^{-2} corresponds to the mass vertical particles cross when transversing the WCD and the concrete structure.

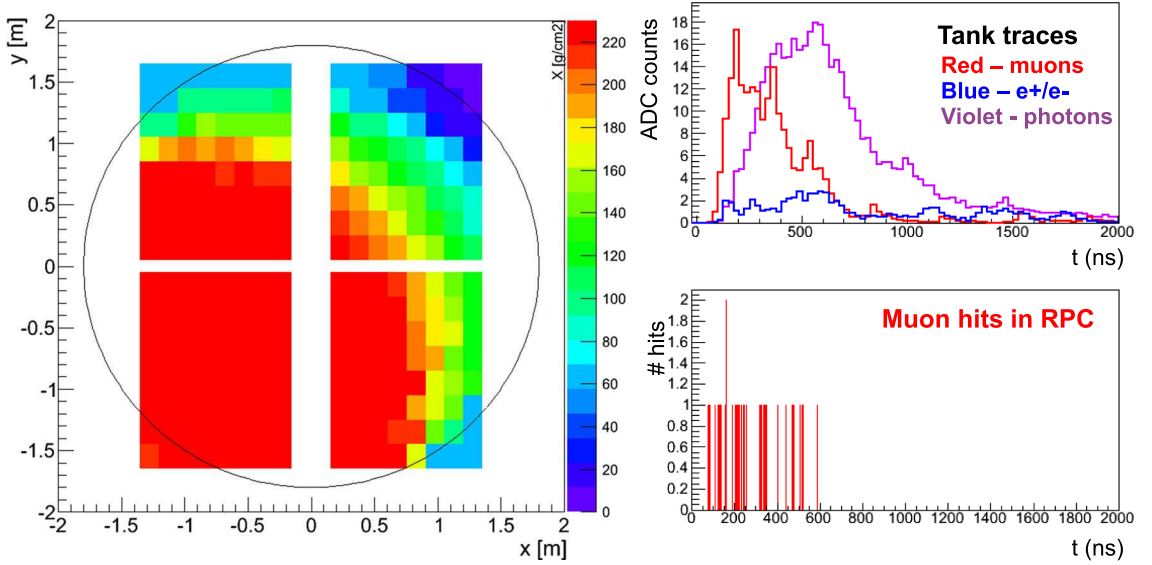


Figure 4.3: Left: Mass crossed by inclined particles, with a zenith angle of 40° , before hitting the RPCs. The circle indicates the area covered by the WCD. Right: Simulated traces of the WCD and the RPC signals. Taken from [4].

effects become relevant when the distance between particles is lower than the RPC spacial resolution. Dedicated algorithms, e.g., [110], can be used to recover the number of muons in these cases. Furthermore, a measurement of the charge induced in the RPC by the crossing particles can also help distinguish the number of hits in case of pile-up.

The atmospheric muon background flux was also simulated, at the Observatory’s altitude (1400 m a.s.l.), using primary cosmic rays with energies between 10^9 eV and 10^{15} eV. The number of atmospheric particles able to reach the RPCs was determined to be in the order of 5 – 7 Hz per pad. These particles can be used to monitor and calibrate the efficiency of the pads. With such a background rate, one can expect to reach a statistical precision of 1% every 30 minutes.

4.3.2 Array performance

An LDF can be obtained using the density of muons. In the example presented in the left plot of figure 4.4, a $10^{19.8}$ eV proton shower with a zenith angle of 38° was simulated. The LDF, density of particles (ρ) as a function of the shower core distance (r), was parametrized using the same equation described in section 3.3:

$$\rho_{\text{LDF}}(r, \beta) = \rho_{1000} \left(\frac{r}{1000} \right)^\beta \left(\frac{r + 700}{1000 + 700} \right)^\beta \quad (4.1)$$

where ρ_{1000} represents the normalization parameter, and β the shape parameter. The simulation procedure was repeated multiple times, obtaining a mean LDF for different primary cosmic rays compositions and energies. The results, when comparing the mean of ρ_{1000} and β of each composition, showed a clear separation between proton and iron.

These are shown in the right plot of figure 4.4. Although the results were obtained using a particular hadronic interaction model, QGSJetII-04, the simulations were repeated using EPOS-LHC, showing that the discrimination power was comparable. With the full SD array, less than half a year of exposure would be sufficient to reach the event statistics used. Lastly, one can fix the β as a function of the zenith angle and obtain the muon density 1000 m from the shower core ($\rho_{1000}^{\text{MARTA}}$). The bias of $\rho_{1000}^{\text{MARTA}}$ was compared with the true muon density, showing that it is mostly energy-independent and that it decreases as the zenith angle increases.

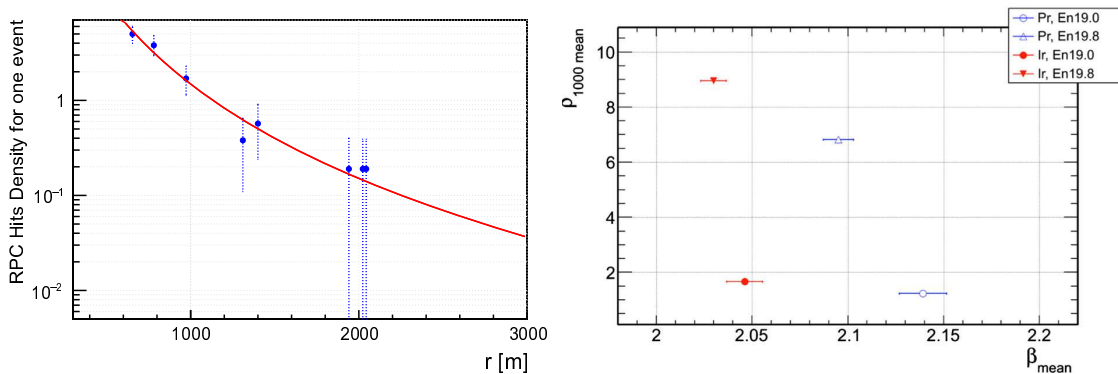


Figure 4.4: LDF of the muon density. Left: Simulated result of the RPC hits density as a function of the shower core distance. A proton shower with $E = 10^{19.8}$ eV and $\theta = 38^\circ$ was used. The RPC hit density is given in m^2 . Right: Results of the mean ρ_{1000} and β for different energy and composition showers. Multiple showers (~ 300) were simulated for each point. Taken from [4].

The Muon Production Depth (MPD) technique would also benefit from MARTA data. The MPD allows reconstructing the longitudinal profile of the muons production using the shower geometry and the arrival time of the muons [111, 112]. The maximum of this profile is known to be composition-sensitive [89]. A proper determination of this variable could add relevant information about the hadronic interactions in the shower. Although the reconstruction using MARTA is the same as the one using just the WCD, the direct detection of the muons would allow reducing the systematic uncertainties associated with the WCD response time. Furthermore, the separation of the shower components would make it possible to apply the MPD technique to stations close to the core as well as vertical showers, enlarging the energy and angular range of this technique. The angular dependence of the MPD can also give information about the EAS muon energy spectrum [113], which could be used to evaluate and constrain the hadronic interaction models.

4.3.3 Combined measurement

The use of the RPCs below the WCD allows detecting the same particles of the shower at consecutive depths. Systematic studies and cross-calibrations, that will help reduce the measurement uncertainties, are possible with this setup. Furthermore, the cross-analyses between the two detectors will increase the amount of reconstructed information, allowing,

e.g., to improve the sensitivity to photon primaries, which have a reduced muon content when compared with hadronic showers. The precision of the energy spectrum is also expected to benefit from a combined measurement, and the possibility to explore new shower variables is extended.

4.4 Engineering array

An EA of MARTA will be installed in seven of the SD stations. These stations are located in the 750 m array of the Infill. A hexagonal configuration will be used, with a station in the middle. A representation of the EA of MARTA is presented in the left picture of figure 4.5. The stations that will be part of the EA are represented with orange circles in the right map of figure 4.5. In it, the other tanks of the Infill are represented with blue circles, and the Coihueco FD site is shown using a yellow marker.

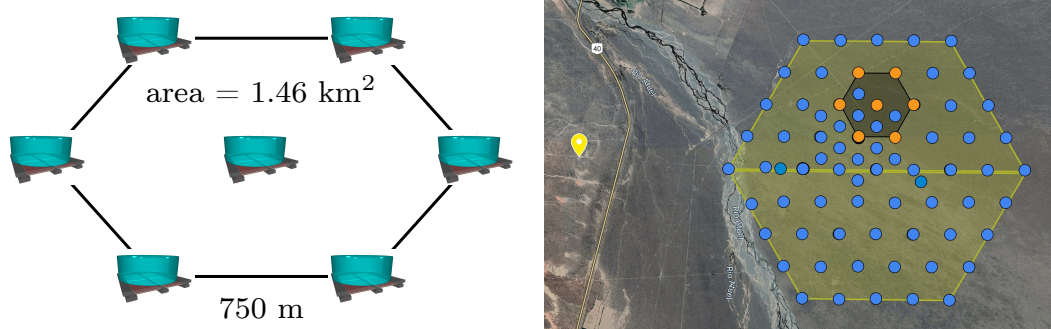


Figure 4.5: MARTA EA. Left: Representation of the EA. The seven stations are laid out in a hexagonal configuration with one in the middle. These are stations of the Infill array, meaning they are 750 m apart. The total area occupied is 1.46 km^2 . Right: Map with the stations where the EA will be installed. The MARTA stations are represented with orange circles. The other stations of the Infill are the blue circles. For reference, the yellow marker shows the Coihueco FD site.

The main goal of this small array is to study the MARTA concept performance, mainly how useful the combined measurement can be in the determination of the muonic content, and how the RPC detectors will perform in field conditions. The measurement proposed in the array performance subsection of section 4.3, average LDF slope at 10^{19} eV , is not feasible with an array of this size. However, it can still be performed at lower energies. The MARTA EA will measure mostly events in the *second knee* region of the spectrum, with energies between $10^{16.5} \text{ eV}$ and $10^{18.5} \text{ eV}$. In figure 4.6 is presented the number of events one should expect in the MARTA EA per month. The number of events where the shower core is expected to be inside the MARTA hexagon is also shown. Furthermore, the data that will be gathered from the EA can be used to cross-check the EAS physics in the region where there is accelerator data. The analysis proposed in the array performance subsection of section 4.3 will be done using mostly shower with energies around 10^{17} eV .

Several detectors are now in place in the same region of the array where MARTA will be deployed. While AERA antennas are already part of the Infill, SSD and AMIGA's

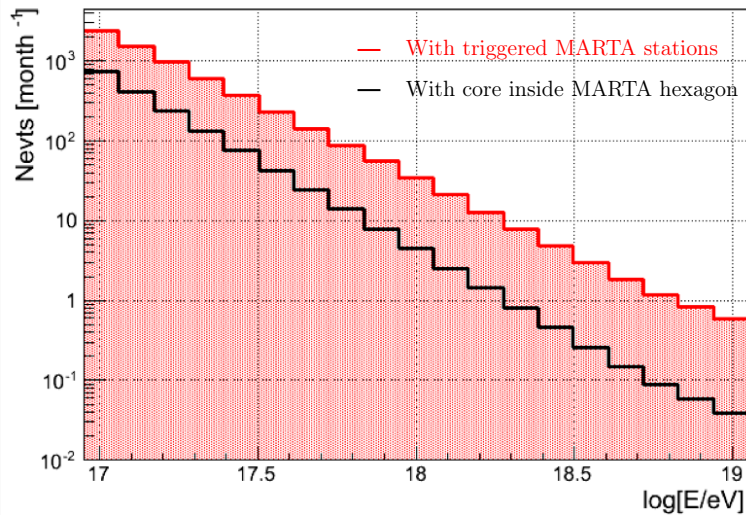


Figure 4.6: Number of events expected for different primary energy in the MARTA EA. The red line shows the events with triggered MARTA stations while the black line shows the number of events where the core of the EAS is expected to be inside the MARTA hexagon. Taken from [114].

UMD detectors will be installed in the tanks that are part of MARTA’s EA. Furthermore, the FD Coihueco and HEAT telescope are also looking at that array section. All these detectors will measure different shower components in the energy range of MARTA. Thus, cross-checks and cross-calibrations between the detectors are expected, which will allow improving analyses, simulations, and help reduce some of the uncertainties, as mentioned before. In particular, assessing the muons tracklength inside the WCD could be used to both determine their energy spectrum and evaluate the SD tank parameters. Some studies of the tracklength in the WCD have already been performed using an hodoscope of MARTA RPCs [115].

The installation of the EA is on its way, as of the time of this thesis writing. The first RPCs are already installed in the concrete structure, underneath the WCD. As already mentioned, extra batteries and solar panels are installed in the EA stations to not interfere with the power system of the tank. Furthermore, the array will be connected to the CDAS using the new AMIGA network to not saturate the low bandwidth of the standard SD radio system. Figure 4.7 shows the first installed MARTA station in the Peter Mazur tank, on the southeast corner of the MARTA hexagon (see figure 4.5). The two extra solar panels (the ones to the right) and batteries were deployed. The bootle that supplies the gas to the RPC is buried underground inside a plastic box. Other than the AMIGA UMD detector, this station also has an SSD scintillator already installed⁴.

⁴The scintillator can be seen on the top of the tank.



Figure 4.7: Peter Mazur SD station in the Infill with MARTA RPCs installed inside the support concrete structure. Extra solar panels and batteries were mounted to not interfere with the standard operation of this WCD.

5 Resistive Plate Chambers

RPCs are gaseous detectors of charged particles that were developed in 1981 by R. Santonico and R. Cardarelli [95]. The original detector was based on the same principles as the Parallel Plate Spark Chamber [116] and was presented as an alternative to the localized discharge spark counters developed in 1971 by Y. N. Pestov and colleagues [117]. The introduction of the RPC was seen as a simplification of the previously developments. Moreover, the absence of high-pressure gas, the low requirements of mechanical precision, and the use of plastic materials instead of glass would simplify the construction and operation of the detector, as well as reduce its cost, widening the range of possible applications. The original RPC was a single gas gap detector that was operated in streamer mode (see section 5.1 for more on the RPC operation modes). A gas gap of 1.5 mm is sandwiched between two resistive plates, made of bakelite, a high resistivity material ($10^{10} \Omega\text{cm}$). The gap was filled with a mixture of 50% argon and 50% iso-butane at atmospheric pressure. HV was applied to one of the electrodes, while the other was connected to ground, creating a uniform electric field. In the left picture of figure 5.1 is presented a diagram with the cross-section of this single gap RPC. The design described has an efficiencies of 97% and a time resolution of 1.2 ns^1 . The development of RPCs, created a more affordable alternative to plastic scintillators (lower cost and simple to construct).

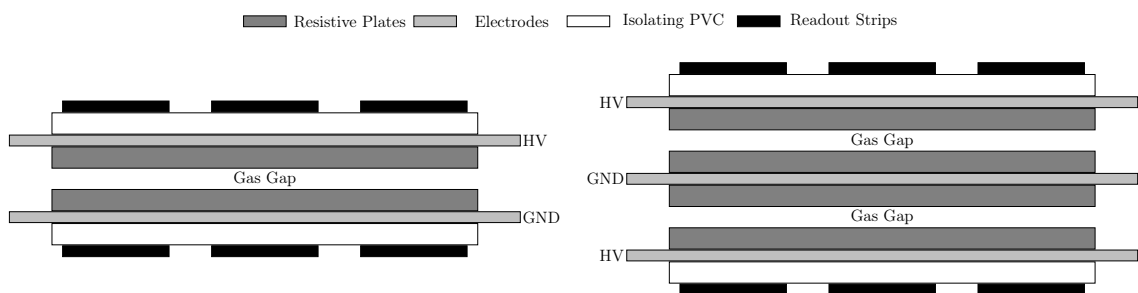


Figure 5.1: Cross-section of the original single gap RPC (left) and the first RPC configuration with two gaps (right). In both cases bakelite was used as resistive plates. Based on the drawings presented in [95] and [118].

Since its introduction, many improvements were made to the original RPC design. In 1988, a new configuration was presented [118], where three resistive plates were used to separate two gaps. A diagram of this configuration is presented in the right image of figure

¹This value corresponds to the Full Width at Half Maximum (FWHM) of the Gaussian distribution.

5.1. This setup can be interpreted as two single gap RPCs, stacked on top of each other. The measurements presented better efficiency results, and a time resolution of around 1 ns. In [119], the first results with an RPC in avalanche mode were shown. The primary purpose of this development was to increase the rate capabilities of this detector by reducing its dead time that can be significant when working in streamer mode. The consequent decrease in induced charge had, however, to be compensated by introducing dedicated electronics for signal amplification. Multi-gap RPCs were later introduced in 1996 [120], where three 2 mm gaps were used with four resistive layers. In this case, HV is only applied to the outer plates leaving the inner plates electrically floating. Such configuration allows having the excellent time resolution characteristic of narrow gas gaps and the high efficiencies typical in wider gaps [121]. In the early 2000s, four thin gas gaps (0.3 mm) were used to achieve time resolutions as low as 50 ps in what is known as timing RPC (tRPC) [122, 123].

The developments continued into the 21st century, with a variety of configurations, materials, and gas mixtures being used to improve performance as well as tune the detector characteristics to the different applications. However, until the introduction of MARTA, very few progress was made trying to use RPCs in outdoor field conditions. Furthermore, the fact that RPCs were almost only used in laboratory conditions, with controlled temperature and humidity conditions², led to believe that this kind of detectors was not suited for field operations. The work performed in the development of RPCs MARTA showed otherwise: RPCs can be operated in harsh weather conditions with low maintenance while having good and stable efficiencies [5, 96–99]. Combining that fact, with their low cost, easy manufacturing, and the spatial resolution given by the readout plane³, makes RPCs an excellent solution to be used in large EAS arrays.

In this chapter, a review of the signal generation in the RPC gas gap is given. Some applications of RPCs in astroparticle and particle physics are mentioned. Typical RPC readout systems are then discussed. Lastly, the MARTA RPC configuration is described.

5.1 Signal generation

Whenever a charged particle crosses the detector, there is a chance that it ionizes the gas creating electron-ion pairs. The number of ionizations (primary clusters) per unit of length follows a Poisson distribution, assuming the probability of an ionization is independent of the previous collision. The average number of clusters, given by $\bar{n} = g/\lambda$, with g the length traveled by the particle inside the gas and λ the mean free path, varies with the gas mixture used. It can range from less than one per millimeter to up to about 10 clusters per millimeter [124]. One should also note that more than one electron can be ejected in a single collision, meaning the cluster size is represented by a distribution. Simulation results for a tRPC configuration using a typical gas mixture show that more than 80% of

²These variables will influence the effective electric field applied in the gas gap, changing the working conditions of the detector.

³Detectors like the large area scintillators that are used to measure air showers cannot, in most cases, determine the position where the particles crossed.

the clusters have a size of one [124].

Due to the strong applied uniform electric field, the free electrons will drift towards the anode and the ions towards the cathode. The drifting electrons will, on a microscopic level, gain a kinetic energy proportional to the electric field strength. Whenever an electron collides, it loses some kinetic energy due to recoil and excitation, slowing down. Then it is accelerated again by the electric field, and the process repeats. On a macroscopic level, a drifting velocity can be measured over a large number of collisions. This multiplication is known as a Townsend avalanche and is commonly used in particle detectors. It presents in a first approach an exponential growth of the number of electrons in the detector. The distribution of the total number of electrons, for avalanches initiated by a single ionization evenly distributed on the gas gap, can be modelled after an exponential. However, the first measurements of the charge spectrum of RPCs in avalanche mode showed otherwise [125]. In fact, it was observed that the distribution would evolve from an exponential shape to a Landau to a Gaussian as the HV was increased. At high electric fields, the space charge effect contributes to a modification of the avalanche dynamics [126]. The avalanche can grow until it reaches a critical number of electrons, where the electric field created by the free particles is comparable to the one created by the applied HV. This growth results in an overall reduction of the electric field in the centre of the avalanche, modifying its propagation and multiplication. This effect is fundamental in the study of the RPC avalanche physics. Furthermore, it makes the modelling of the electrons' behaviour a non-trivial problem that is still not totally understood.

Since the introduction of the avalanche mode in RPCs, several of these models have been proposed. The models presented are, in some cases, simple approximations that neglect some of the processes that are known to occur in the gas. However, they seem to reproduce experimental data, and some of them have been used as functional parameterization of the data.

The basic processes taking place in RPCs have been described in [127], and it can successfully describe some data. A Polya distribution was used to model the avalanche, that assumes unphysical parameters making its interpretation unclear. This model was later extended, adding a simplified approach to the space charge effect: the avalanche growth would stop at the critical number of electrons [128].

A logistic function, originally used to describe the evolution of biological populations, was introduced to model the saturated growth result of the space charge effect [129]. A constant-coefficient non-linear differential equation connected to the logistic function is used to model the creation of new electrons that replace the ones that are left in lower regions of the electric field. Using this model, the charge measured for different electric fields was successfully fitted to the function:

$$Q(V) = K \ln(1 + e^{a(V-V_0)}) \quad (5.1)$$

with Q the charge, V the voltage applied and K , a and V_0 the fitting parameters. The left plot in figure 5.2 shows the measured charge for different applied voltages fitted to the

function presented in [129].

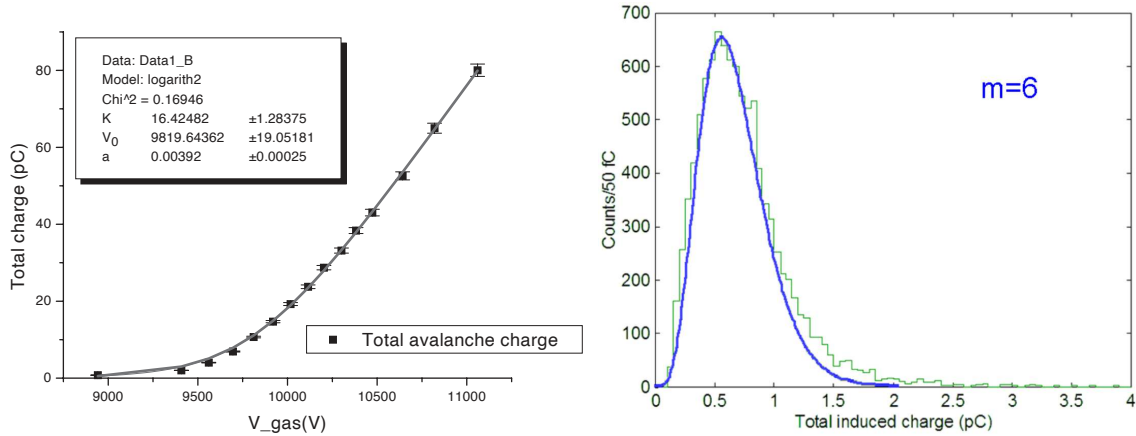


Figure 5.2: RPC avalanche models applied to detector data. Left: Charge versus applied voltage fitted to the logistic model function presented in equation 5.1. Taken from [129]. Right: Charge spectrum of the RPC signals (data from [130]) fitted to the gamma distribution presented in 5.2. Taken from [131].

A simulation of the RPC physics was presented in [124, 132] that was able to reproduce data successfully. Detector gas parameters entirely based on theoretical predictions and physical models were used for both the avalanche development and the space charge effects. Furthermore, the space charge effect was simulated in time steps, calculating at each time the electric field distribution within the avalanche, and finding the gas parameters locally.

Lastly, in [133], a comprehensive treatment of the RPC modeling is presented. In it, a gamma distribution was obtained to describe the charge distribution of the avalanche RPC signals:

$$P(\mathcal{N}_e) = \frac{e^{\frac{\mathcal{N}_e}{G/r}} \mathcal{N}_e^{m-1} (G/r)^{-m}}{\Gamma(m)} \quad (5.2)$$

where $P(\mathcal{N}_e)$ is the probability distribution function of the final charge of the avalanche (\mathcal{N}_e), $G = e^{\alpha^* g}$ is the maximum average gas gain with $\alpha^* = \alpha - \eta$, α ionizations, η attachments and g the gap size. r is the ratio α^*/α and $m = \lambda r/\alpha^*$, where λ is the average cluster density. Although this result was obtained using some approximations that include not considering the space charge effect, it was later shown [131] that the distribution agrees with detector data. An example of such an agreement is shown in the right plot of figure 5.2. The fit results are hard to interpret and, in some cases, unphysical, which can be due to the several approximations used. Though no physical interpretation can be gained from using the gamma distribution, it was found to be an excellent functional parameterization of the detector data.

The movement of charges inside the gas gap induces a current signal in the readout electrodes. The small drift velocities of the ions make it so the signal induced by them is much slower than the signal produced by the electrons. One should also note that only a fraction of the current created by the electrons and ions is induced in the readout electrodes.

At very high electric fields, a new phenomenon can occur distinct from the avalanche multiplication. It is known as streamer, and its result is a fast increase of the charge. An avalanche can be transformed into a streamer by two different generation mechanisms [134–136]. The first is a slow mechanism where the initial avalanche emits UV photons that will knock electrons out of the cathode. These electrons will generate new avalanches that will later transform into a streamer. In this case, one can observe both the avalanche signal and the streamer signal dozens of nanoseconds later (see in figure 5.3). In the second mechanism, electrons in the enhanced electric field (tip of the avalanche when the space charge effect is present) will be accelerated quickly and form new avalanches. The old avalanche will merge with the new ones forming a streamer. This is a rapid process when compared to the photon emission mechanism. In the case of RPCs, the streamer will never evolve in any discharges or sparks. These phenomena require a considerable current flow that is suppressed by the high resistivity of the electrodes.

Figure 5.3 shows RPCs signals measured for different HVs using the single 2 mm gap configuration presented in [137]. For the lower voltage (top left), the signal presented corresponds to an avalanche. As the HV is increased (top right), both the avalanche and streamer signals are shown and well separated. Then, the delay between signals starts to decrease (bottom left), and eventually, these end up merging (bottom right).

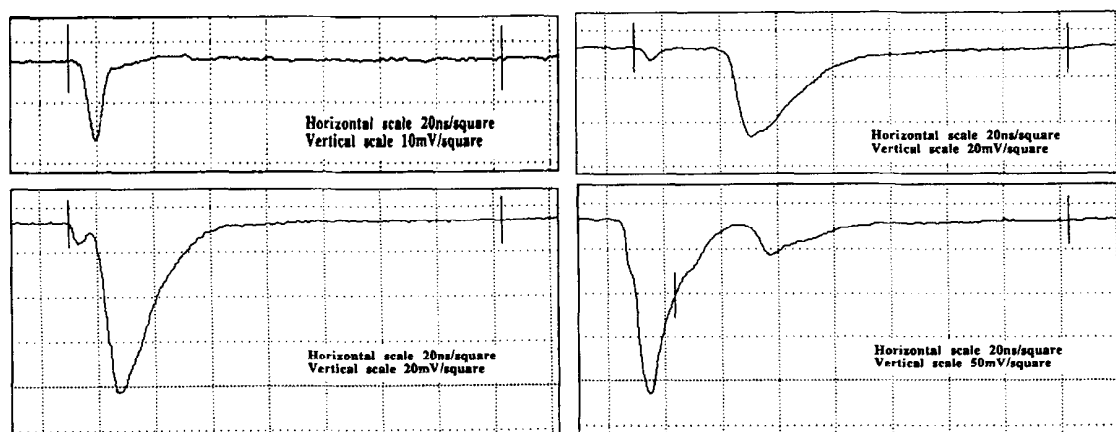


Figure 5.3: RPC signals for a single gap detector with different HVs applied. Top left: 9.4 kV applied. Avalanche signal. Top right: 9.6 kV applied. Avalanche and streamer signal separated. Bottom left: 10.2 kV applied. Avalanche and streamer signal closer together. Bottom right: 10.2 kV applied. Avalanche and streamer signal merged. Taken from [137].

While in streamer mode RPCs, streamer formation is desired, in avalanche mode, the big signals are an unwanted side-effect. Furthermore, the larger signals produced in streamer mode (~ 0.5 nC to a few nC [138, 139]) allow having simpler readout electronics with no amplification and direct discrimination. However, the big charges create blind spots in the detector, limiting its operation rate to a few hundred Hz/cm² [138]. In the long term, this will also increase the degradation of the detector and significantly reduce its lifetime. In avalanche mode, the signals (few pC [132]) need low noise amplification electronics. Nevertheless, the operation is more stable, leading to a longer lifetime as well

as a higher maximum particle rate (few kHz/cm² [138])⁴.

5.2 Applications

RPC based detectors have been extensively used in particle physics, and are an emerging technology astroparticle physics. Furthermore, imaging techniques with RPCs, like Positron Emission Tomography (PET) and even muon tomography to create images of three-dimensional (3D) structures, have shown promising results. Their flexibility in design and construction, make RPCs tunable to a wide range of applications and environments. RPCs can be broadly qualified into two different categories: trigger and timing.

Trigger RPCs are usually RPCs with one or two gaps, working in either avalanche or streamer mode, used to trigger and detect minimum ionizing particles (MIP), like muons. This type of detector has efficiencies as high as 98% and a time resolution of ~ 1 ns. Trigger RPCs working in streamer mode have been implemented in high energy particle physics experiments like L3 [140] and ALICE [141]⁵ at CERN, BELLE [143] at KEK, BESIII [144] at IHEP, OPERA [145] at LNGS, and BaBar [146] at SLAC. Astroparticle physics experiments like COVER_PLASTEX [147] at Haverah Park, and ARGO-YBJ [148] have used streamer mode trigger RPCs to detect EAS, while MONOLITH [149] at LNGS and ICAL [150] at INO measure atmospheric neutrinos using this detector configuration. Avalanche mode trigger RPCs are used in high energy particle physics experiments like LHCb [151], ATLAS [152] and CMS [153] at CERN and PHENIX [154] at RHIC. An example of trigger RPCs are the ATLAS muon spectrometer placed in the outer part of the detector. These have a 2 mm single gap, cover an area of 3650 m², and have more than 350 thousand independent readout channels. They provide information on the presence and arrival time of the muons that travel through the detectors after the collision. Figure 5.4 shows the position of the RPCs in the ATLAS detector.

Timing RPCs are, as mentioned previously, most of the time multi-gap detectors working in avalanche mode with gaps as small as 0.2 mm. This configuration can achieve efficiencies of 99% and time resolutions of 50 ps and are usually used for Time of Flight (TOF) [122] measurements. Timing RPCs have been implemented in high energy particle physics experiments like ALICE [156] and HARP [157] at CERN, STAR [158] at RHIC, HADES [159] and FOPI [160] at GSI, BGO-EGG [161] at LEPS2, BESIII [162] at IHEP, NICA [163] at JINR, and CBM [164] at FAIR. The ALICE TOF, along with two other systems, are used for particle identification (PID)⁶ by getting their velocity and using the momentum measured with the tracking detector [165]. These RPCs are based on a double-stack design: two stacks of five gas gaps. They cover an area of 141 m², and have 160 thousand readout channels, each connected to a pickup pad with an area of

⁴These are typical for bakelite resistive plates.

⁵ALICE trigger wall RPCs were later modified to work in avalanche mode [142].

⁶The ALICE particle identification system operates in the range of momenta between 0.15 GeV/c to 20 GeV/c. The RPC TOF provides charged-particle PID in the intermediate momentum section (below 2.5 GeV/c).

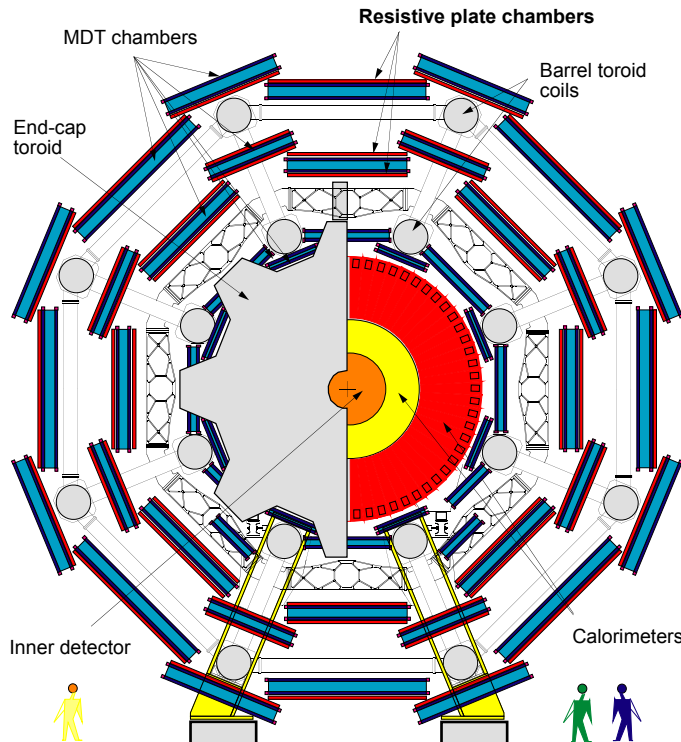


Figure 5.4: Transverse view of the ATLAS muon spectrometer. RPCs are indicated. Taken from [155]

$3.5 \times 2.5 \text{ cm}^2$. Lastly, one should note that the TRAGALDABAS [166] experiment has been using MARTA-like RPCs to measure cosmic rays induced EAS.

RPCs have found some applications outside of the high energy particle and the astroparticles fields. Muon tomography to create 3D images of structure using air showers muons has been successfully performed using RPCs. While the TOMUVOL group has used single gap RPCs in avalanche mode to study a volcano in the south of France [167], a group in the United Kingdom has proposed to use single gap RPCs in streamer and avalanche mode to scan cargo containers for nuclear materials [168]. Moreover, recent developments have been presented, showing the intention to use multi-gap RPCs in muon tomography [169]. Medical imaging is also possible using RPCs. A PET scan has been performed in small animals, with a multi-gap RPC accomplishing a resolution of 0.4 mm FWHM [170, 171]. Another project tested multi-gap RPCs for in-beam PET in proton and carbon ion therapy [172]. A different group has recently also presented studies of feasibility of PET imaging with RPCs [173].

5.3 Signal readout

Since RPCs are mainly used to measure particle hits and their timing, most of the front-end electronics developed are quite simple in concept. They frequently consist of an amplifier if the signal needs amplification, i.e., in avalanche mode, followed by a discriminator/comparator that is controlled by a threshold. Charge measurements are essentially

used to study the detector physics, control the signal integrity, or correct the measured time, and can be performed using integrator circuits, part of charge-to-digital converter (QDC).

5.3.1 Avalanche mode

Several Application Specific Integrated Circuits (ASIC) chips were designed to measure the RPC outputs. The development of custom ASICs, instead of conventional integrated circuits (IC), allowed reducing the cost and power consumption of the readout systems.

Custom ASICs were designed in the late 90s to be installed in the ATLAS and CMS experiments. The ATLAS chip [174], has eight channels, each with three stages of amplification that were followed by a comparator. The minimum detectable signal had a peak before amplification of $150 \mu\text{V}$, and the power consumption per channel was 50 mW. The CMS chip [175] has six channels, each with two stages of amplification and a discriminator. The discriminator includes a zero-crossing comparator to decouple the logic pulse width from the signal amplitude. It has a minimum threshold of 10 fC, and power consumption of 30 mW per channel.

The NINO ASIC [176] has eight input channels, and it was developed for the ALICE TOF detectors. Signal amplification is performed by four identical cascade amplifiers, optimized for the delay and slew rate. The amplifiers provide sufficient gain to operate as a discriminator. The threshold is set by a voltage difference applied to two symmetrical inputs. Each channel has a peaking time of 1 ns with a resolution of 20 ps rms. It has a minimum detection threshold of 10 fC, and the charge can be obtained by measuring the pulse width. The ToT of the pulse is measured using a time-to-digital converter (TDC). This ASIC has a power consumption of 27 mW per channel. NINO has found some applications outside of ALICE: it was used to test the CBM TOF detectors [177].

The PADI ASIC [178] was designed to be used with the CBM TOF RPCs. The design was initially derived from the NINO architecture, and it had several redesigns since its introduction in [179]. This means that the concept is similar, a fast amplifier followed by a discriminator. These redesigns allowed to tune the ASIC to the detector characteristics, as well as reduce noise and increase amplification. The PADI is used together with a TDC chip to get a precise TOF measurement. It can achieve a time resolution as low as $\sigma = 20$ ps. The version PADI-8 has eight input channels and power consumption of 17 mW per channel.

The HARDROC [180] is a 64 input channel ASIC that was initially developed to be used in the SDHCAL of CALICE [181]. Figure 5.5 shows the block diagram of analog part of the HARDROC. After the pre-amplifier, the signal goes into three fast shapers and one slow shaper. A discriminator is placed after every fast shaper, each tuned for a different charge range. The outputs are then sent to a two-bit encoder that is stored into a digital memory. The slow shaper signal follows to a track and hold to provide a multiplexed analog charge output. Its power consumption per channel is 2.5 mW, and the minimum threshold measured is 10 fC. The most recent version of this ASIC will also be installed

in the front-end electronics of the INO-ICAL RPCs. The HARDROC is an ASIC of the ROC family by OMEGA [182]. These ASICs, for the most part, share the same amplifier architecture, and the subsequent electronics are configured according to the detector type for which the chip will be used. As mentioned before, the MAROC (described in section 7.2), part of the ROC family, is used to read the MARTA RPC signals. Although it was not specifically designed to be used with RPCs, there is at least one other case where the MAROC was used with these kinds of detectors [183]. Other OMEGA ASICs, like the SKIROC [184] and PETIROC [185], are also listed as RPC compliant.

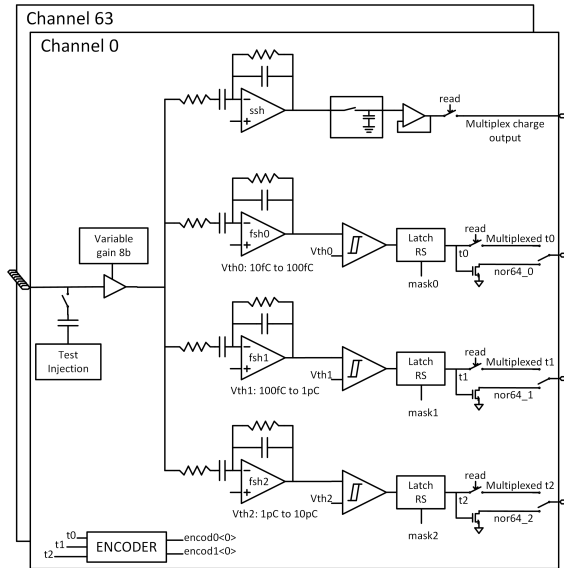


Figure 5.5: Block diagram of the HARDROC 3B analog part. Taken from [186].

The FEERIC [187] is an eight input channels ASIC developed for the ALICE muon trigger RPCs. It is part of the upgrade that coincides with the change of operation mode from streamer to avalanche. The block diagram of a FEERIC channel is presented in figure 5.6. The signal is first amplified by a transimpedance amplifier. Then it goes to a zero-crossing discriminator that gives a logic signal whose timing is amplitude independent. Lastly, a one-shot circuit will output a differential signal (LVDS) with a width of 23 ns, while preventing re-triggering for 100 ns. The minimum threshold above noise is 8 mV and it has a power consumption of 70 mW per channel.

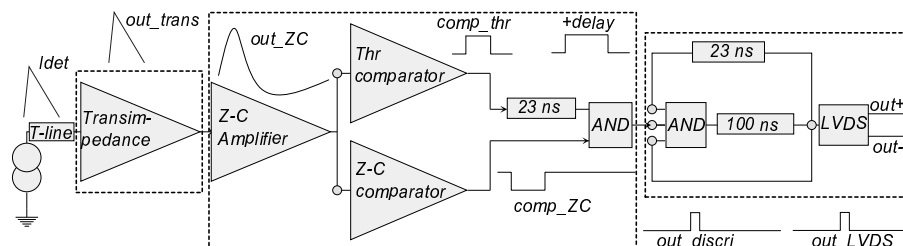


Figure 5.6: Block diagram of a FEERIC channel. Taken from [188].

Though ASICs have many advantages over conventional IC, in some instances, these

are still preferred. That is the case of the HADES front-end electronics (HADES FEE) for the tRPC wall [189]. A block diagram of a HADES FEE channel is presented in figure 5.7. An NXP BGM1013 amplifier [190] followed by a Maxim Integrated MAX9601 comparator [191], form the amplifier discriminator pair. While the discriminator triggers using a conventional threshold, its width is given by a charge to width integrator circuit that uses an OPA690 operational amplifier by Texas Instruments [192]. The logic signal is lately converted to LVDS. The physical threshold of the HADES FEE was estimated to be at about 30 fC, which corresponds to 1 mV. It has a power consumption of < 0.5 W per channel and a time resolution, including RPC, of $\sigma = 73$ ps measured in-beam tests. Other examples of the use of conventional IC are the HARP front-end [193], and the FOPI front-end [194]. The first prototype of MARTA readout electronics, the PREC (see chapter 6), was also designed using conventional IC.

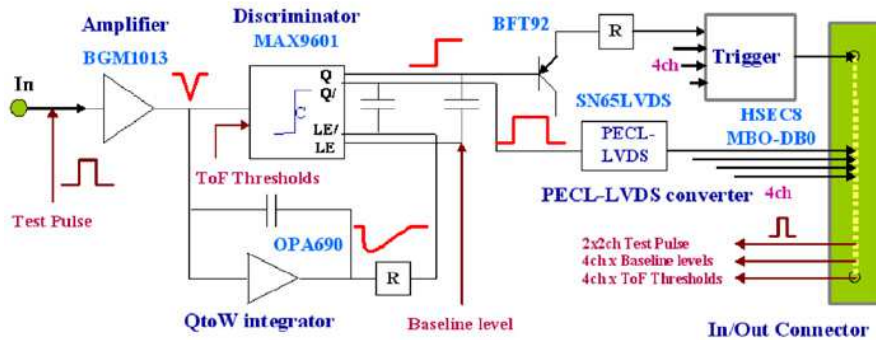


Figure 5.7: Block diagram of a HADES FEE channel. Taken from [195].

A summary of the different readout systems presented in this section is shown in table 5.1.

| Experiment | Type of electronics | Chip name | Channels per chip | Minimum threshold* | Consumption per channel (mW) |
|---------------|---------------------|-----------|-------------------|--------------------|------------------------------|
| ALICE Trigger | ASIC | FEERIC | 8 | 8 mV | 70 |
| ALICE TOF | ASIC | NINO | 8 | 10 fC | 27 |
| ATLAS | ASIC | - | 8 | 150 μ V | 50 |
| CALICE | ASIC | HARDROC | 64 | 10 fC | 2.5 |
| CBM | ASIC | PADI | 8 | 10 fC | 17 |
| CMS | ASIC | - | 6 | 10 fC | 30 |
| HADES | Conventional IC | - | - | 30 fC | < 500 |

* some values are before amplification, others after. More details in the text above.

Table 5.1: Summary of the present front-end systems used for readout of avalanche RPC signals.

5.3.2 Streamer mode

The front-end electronics used to read RPC streamer signals are, as already mentioned, mostly composed by a discriminator. This is possible because the signal induced by a

streamer is enough so that no amplification is needed. The Front-End Card (FEC), 16 channels, designed for the BaBar RPCs [196] is an example of that. The signals that come from the readout strips are directly connected to a discriminator controlled by a threshold. While a fast OR of the discriminators' outputs is available to get a fast trigger, every single discriminated signal is sent to a monostable and then to a shift register. After, the serial output of the register is read by a FIFO memory. In the OPERA experiment, an LVDS line receiver (Texas Instruments' SN75LVDS386 [197]) was studied and validated as a good differential analog discriminator [198]. This development came out of the necessity to have an inexpensive differential discriminator that is available in large scale integration packages. Like in the BaBar FEC a fast OR of all the channels is available to get a fast trigger. The discriminated output also follow to a event latch that will wait for the fast OR to store the data into a register. In this case, all the digital electronics after the discriminator are programmed into an FPGA.

5.4 MARTA RPC

The MARTA RPCs were designed to count the number of particles under the Observatory's WCD. Thus, the two main focuses of the development were:

- to have a reliable and robust detector, with good and stable efficiency and able to sustain the harsh conditions of field operation;
- to have a spatial resolution that was a good compromise between the number of readout channels, keeping the power consumption to a minimum, and the expected rate of particles, to avoid pile-up effects in the pads.

The requirement presented mean that theses detectors fall into the trigger RPC category since a precise timing measurement is not needed.

The configuration chosen was a detector with two 1 mm gas gaps separated by three 2 mm thick glass plates. The glass plates have an area of $1.2 \times 1.5 \text{ m}^2$ and are separated by Nylon monofilaments. HV is applied to the outer glasses by means of a layer of semi-conductive resistive acrylic paint [199]. The glass stack is enclosed by a gas-tight acrylic box defining the sensitive volume. The detector operates with a mono-component gas R-134a, at a flow rate of 4 cc/min. Figure 5.8 shows a schematic drawing of the first prototype developed for the study of the feasibility of MARTA. One should note that the gap and glass dimensions are different from the ones chosen for the production version. Nonetheless, the other characteristics of the sensitive volume were kept unchanged. This configuration assures efficiencies above 90% and time resolution of around $300 \text{ ps } \sigma$ [97].

The readout plane has 64 pickup electrodes distributed in an 8×8 pad grid and is placed on the top of the sensitive volume. The pads have an area of $14 \times 18 \text{ cm}^2$ and are separated by a 1 cm guard ring making the readout area 90% of the total area. The left picture of figure 5.9 shows the readout PCB, with the 64 pads and the guard ring around them. As mentioned previously, the sensitive volume, readout planes, and the

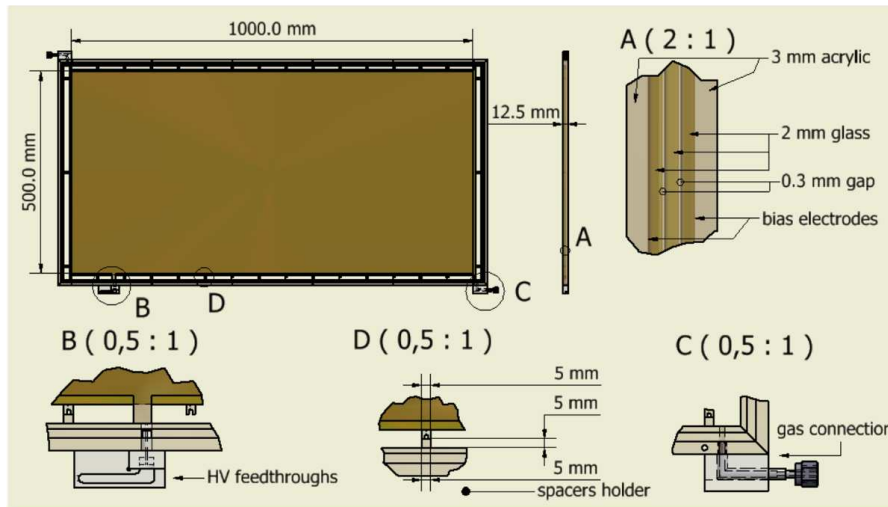


Figure 5.8: Schematic drawing with the dimensions of the first MARTA prototype. The gas gap and glass dimensions are different from the ones chosen for the production version (1 mm gas gap and $1.2 \times 1.5 \text{ m}^2$ glasses). Taken from [96].

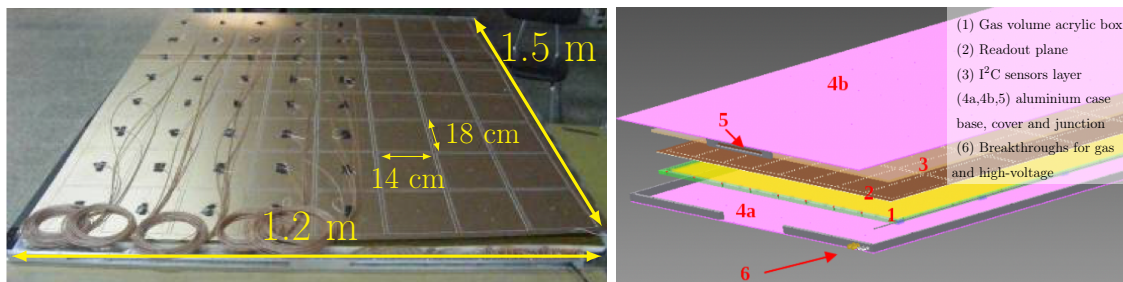


Figure 5.9: MARTA RPC. Left: Readout plane configuration and detector dimensions. Right: Schematic of the detector aluminium box, readout plane, sensors layer, and detector volume. Taken from [4] and [98].

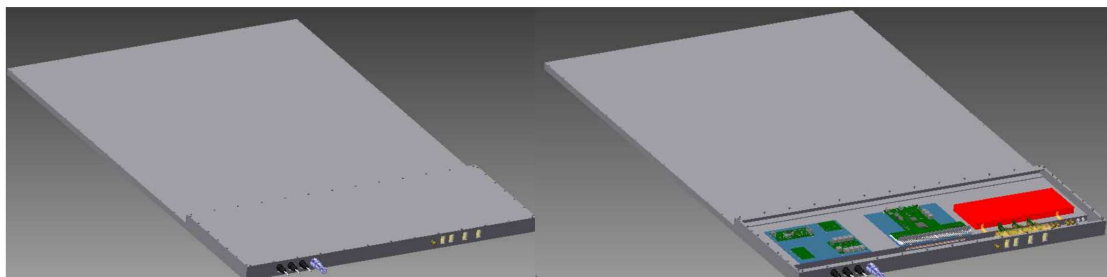


Figure 5.10: 3D CAD of the aluminium box where the sensitive volume and the readout pad plane are placed. The small extra compartment houses the electronics subsystems: HV (red), gas monitoring bubbler block (yellow), front-end board (centre green board), PSU, and other monitoring (left green boards). Taken from [5].

environmental monitoring I²C sensors are placed inside an aluminium box. A schematic view of the detector module, which includes the aluminium box, readout plane, sensitive volume, and monitoring layer, is presented in the right picture of figure 5.9. In figure 5.10 is shown a CAD view of the final detector, where the second compartment, that hosts all the electronics is visible. The dimensions of the detector box are $1.76 \times 1.285 \text{ m}^2$, with a height of 6 cm in the region of the electronics' compartment and 2.5 cm otherwise. The electronics' box is $0.447 \times 1.285 \text{ m}^2$ and is visible in the right picture of figure 5.10. On the right is the HV (shown in red), in the centre the front-end electronics, and on the left the PSU and other monitoring electronics. The detector has three RJ45 communication inputs, one power input, and gas input.

The RPCs were designed to work in avalanche mode. The typical avalanche signal is a negative pulse that develops in a few nanoseconds. It presents a fast rise ($\sim 1.5 \text{ ns}$) followed by a RC-discharge-like fall ($\sim 6 \text{ ns}$). There is, however, a small fraction of avalanche that will be converted into streamers. This fraction is of $\sim 1\%$ for usual operation voltages. An avalanche and a streamer signal are shown in figure 5.11. The avalanche signal (left) has a peak of a few mV while the streamer signal (right) has a minimum at around -70 mV . In the case of the streamer signal, one can see the initial avalanche about 100 ns before.

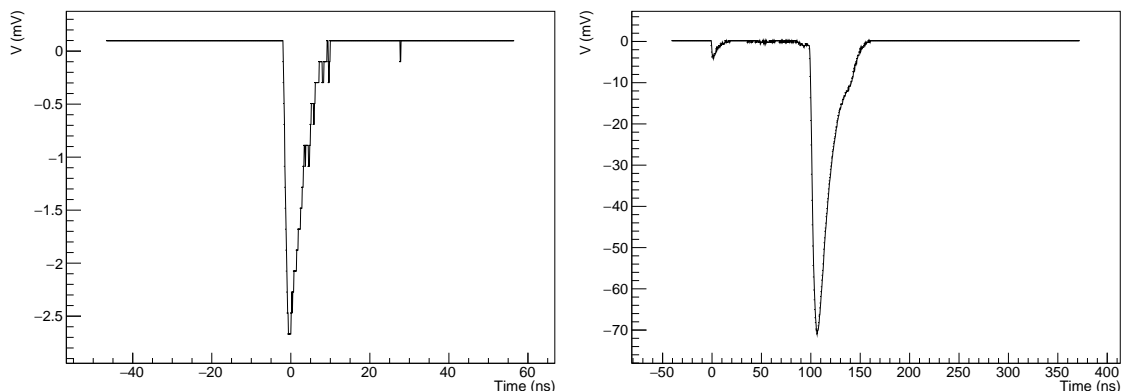


Figure 5.11: Avalanche (right) and streamer (left) signals measured with a Rhode & Schwarz RTO 1014 oscilloscope [200].

Several charge spectra were acquired during the laboratory tests performed to the final RPC configuration [97]. The results are shown in figure 5.12. Two distributions can be distinguished: with lower charge the avalanche spectrum that follows the gamma shape, mentioned previously, and on the right the streamer spectrum. Due to the distance between the gaps and the pickup electrodes, it is estimated that only $\sim 10\%$ of the total charge will be induced in the pads [97]. Furthermore, in the spectrum presented, only the fast component, the free electrons of the avalanche, was measured. The reason for this is that the ions are much slower than the electronics used for the measurement.

In MARTA, the variations in temperature, humidity, and pressure in the environment need to be taken into account. Thus, the electric field applied to the gaps is expressed as the reduced electric field (E/N), a quantity proportional to the detector gain that can change

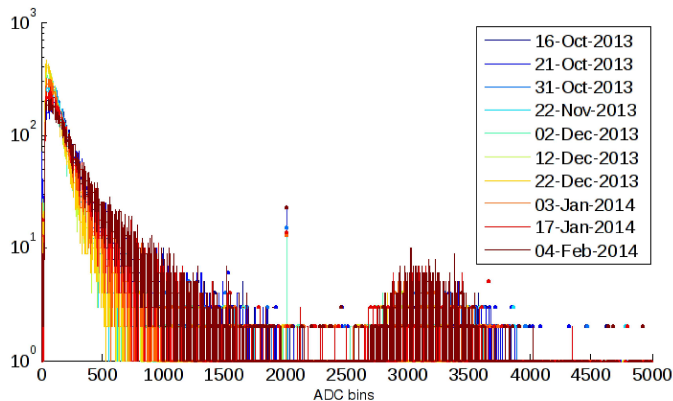


Figure 5.12: The charge spectrum of MARTA RPCs measured in the laboratory for four months. There is a clear separation between the avalanche spectrum (left) and the streamer spectrum (right). Taken from [97].

with the weather conditions⁷. The E/N can be calculated using the following expressions [97]:

$$E/N = 0.0138068748 \frac{V_{\text{eff}}}{d} \frac{T + 273.15}{P} \text{ [Td]}$$

$$V_{\text{eff}} = V_{\text{app}} - R_{\text{cm}^2} I_{\text{cm}^2} \quad (5.3)$$

$$R_{\text{cm}^2} = \rho(T) \times t \times l$$

with d the gap thickness in cm, T the temperature in degree Celsius and P the pressure inside the detector in mbar. The effective potential V_{eff} is calculated using the applied voltage (V_{app}), the current drawn by the detector per square centimeter (I), and the resistance per square centimeter (R). The last is then dependent on the volume resistivity, $\rho(T) = 10.5 \times 10^{12} \times 10^{(20-T)/24.3}$, the amount that the gas plates contribute to each gap, t , and the glass thickness, l . In the particular case of the MARTA RPCs $d = 0.1$ cm, $l = 0.2$ cm and $t = 1.5$. This variable is used to monitor the detector behaviour, as well as adjust the HV accordingly. Therefore, the conditions of operation can be constant despite the variable environmental conditions.

The charge median, streamer fraction, and efficiency were studied in the laboratory as a function of E/N measured over 9 months [97]. Furthermore, three different gas fluxes were used in these measurements. The results are presented in the top plots of figure 5.13. The efficiency as a function of the charge induced is also shown. The charge distribution shows the expected exponential dependence that is also presented in the left plot of figure 5.2. The streamer fraction increases with the E/N , and for the highest electric field studied is $\sim 10\%$. The efficiency is very well correlated with the E/N , with a plateau at about 90%, the maximum value expected since only 90% of the readout plane is covered with pads, the other 10% being the guard rings. One should, however, note that ionizations taking place under these rings can spread to the neighboring pads, increasing the observed efficiency. Lastly, the efficiency as a function of the charge also has the expected shape

⁷ E is the applied electric field and N is the gas numerical density.

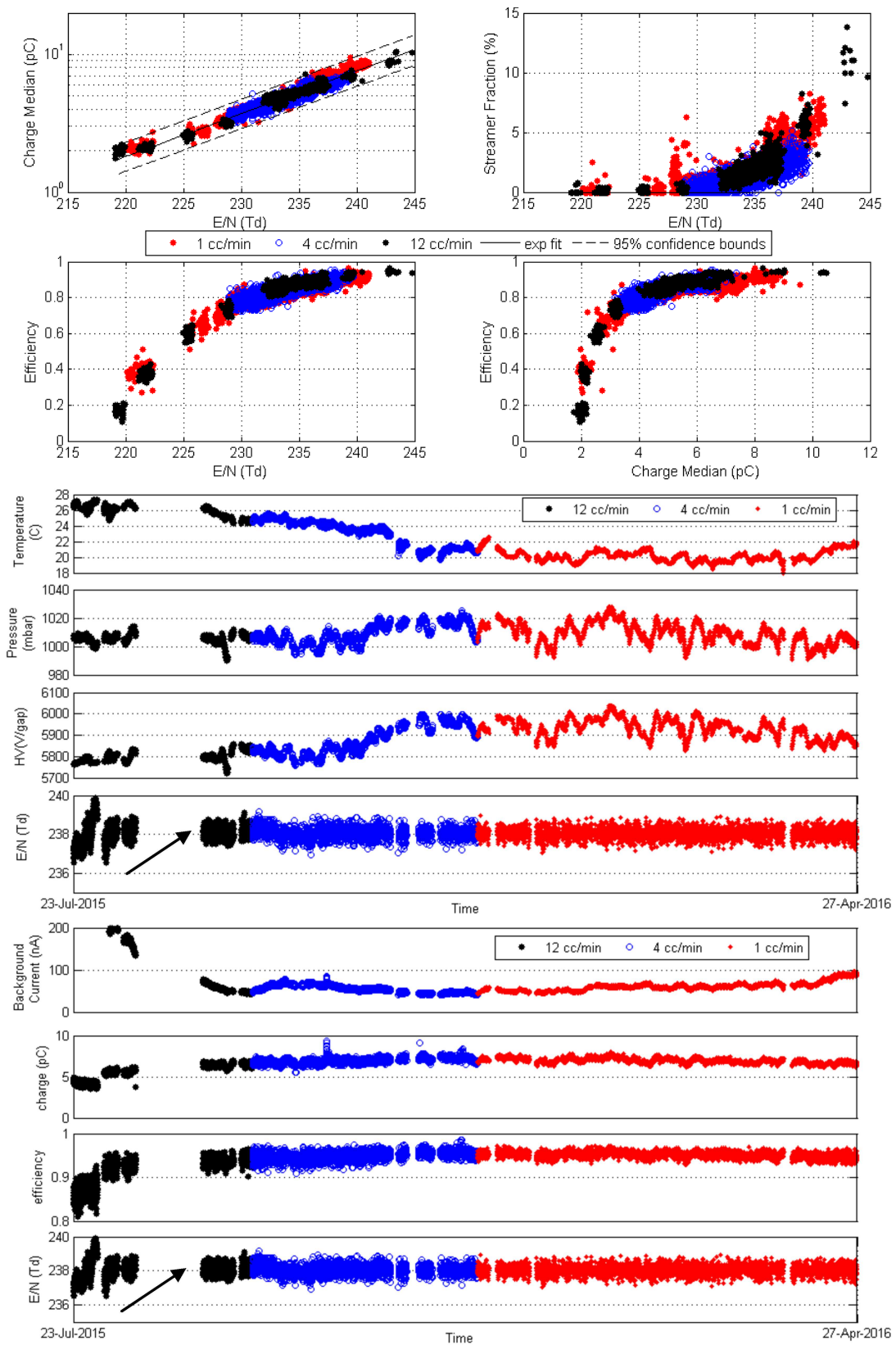


Figure 5.13: Laboratory test of MARTA RPCs. The top four plots show the efficiency, charge and streamer fraction as a function of the E/N as well as the efficiency vs the charge. The middle and bottom plot show the results of the dynamic HV adjustment. Taken from [97] and [98].

and it is independent from the gas flow rate.

The dynamic HV adjustment was a necessary step to ensure that the working conditions of the detectors would not change with the variation of the temperature and pressure. Indoor laboratory tests were performed, where the HV was adjusted every 15 minutes according to the conditions measured inside the sensitive volume [98]. Pressure variations, other than the small daily changes, were not studied as a hypobaric chamber would be needed and was not available. The algorithm used to regulate the HV neglects the contribution of $R_{\text{cm}^2} \times I_{\text{cm}^2}$ (see equation 5.3) to compute V_{eff} . This way the electric field that will be applied to the gas gap is calculated as $V_{\text{app}} = V_{\text{ref}} \times T_{\text{ref}}/T_{\text{measured}} \times P_{\text{measured}}/P_{\text{ref}}$ [201]. The reference value to get a $E/N = 238$ Td, according to the results shown in [97], are $V_{\text{ref}} = 5800$ V, $T_{\text{ref}} = 25$ °C and $P_{\text{ref}} = 1000$ mbar. The data used for the adjustment are the averages values since the last change.

The results of the adjustment are presented in the bottom two plots of figure 5.13. The arrow indicates the start of the adjustment. The data was measured during 8 months, and one can see that this method was enough to keep the E/N constant during this period. In the middle plot, it is possible to see how the HV changes with the pressure and temperature variations. The bottom plot shows that the charge and the efficiency are stable over the 8 months of constant E/N . Finally, one should point out that the results are independent of the gas flux. These measurements show that the adjustment described is sufficient to guarantee the stable operation of the detectors.

Outdoor field tests were performed at the Pierre Auger Observatory's site [5, 99]. Namely, two RPCs were placed on top of each other underneath one of the Infill WCD. The RPCs were installed inside the same concrete structure used in MARTA's EA. The plots of figure 5.14 show that it is feasible to operate these detectors in the field with a constant E/N .

The results present the seasonal temperature and pressure variations through a period of more than a year and a half. The evolution of the HV in this particular detector, to keep the E/N constant, is also shown. In this case, the E/N reference value was chosen to be 255 Td. The daily temperature variations inside the concrete structure are much smaller (by a factor of 10) than the gradient that is expected in the deployment site⁸. These temperature conditions, combined with small variations in pressure, will make the HV adjustments very small, enabling to use the algorithm presented above. For higher variations (e.g., more than 10°C), it would be impossible to neglect the glass resistivity in the E/N calculation.

This setup was also used to study the efficiency of these detectors in the field. A trigger between the WCD and one of the RPCs was defined to measure the second RPC. The results are shown in figure 5.15, where a mean efficiency of 86.2% is measured. The discrepancy between these results and the ones shown above can be explained by the variation in pressure between the laboratory and the field (15% lower in the field). The difference can not be compensated by increasing the HV, since the pressure also affects

⁸The daily temperature variations in the Observatory's site can be as large as 30°C per day.

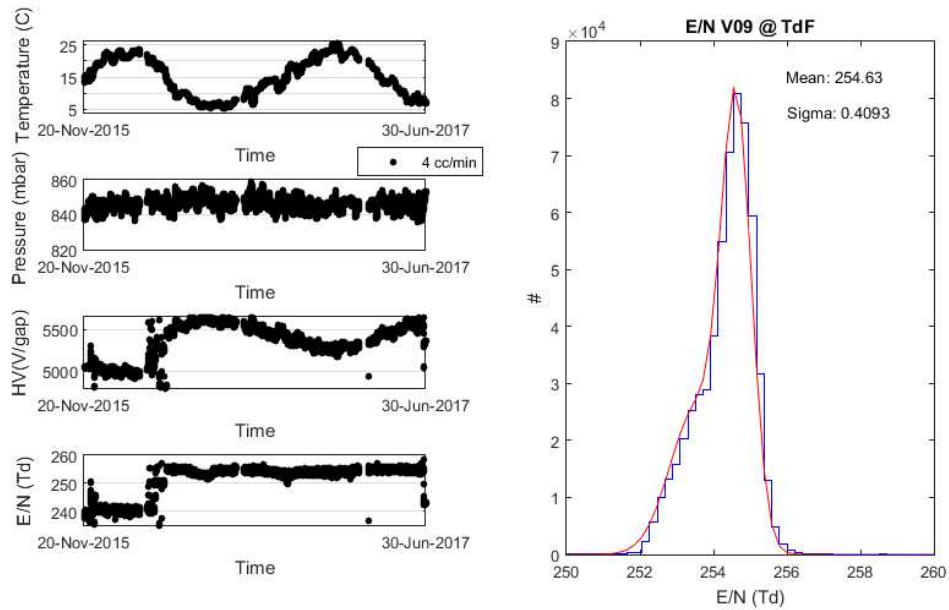


Figure 5.14: Performance of an RPC in the field, operating at 4 cc/min, for more than a year and a half. The temperature and pressure inside the aluminium box are shown, as well as the HV, adjusted to keep the E/N constant (left). On the right is shown the distribution of E/N since March 2016. Taken from [5].

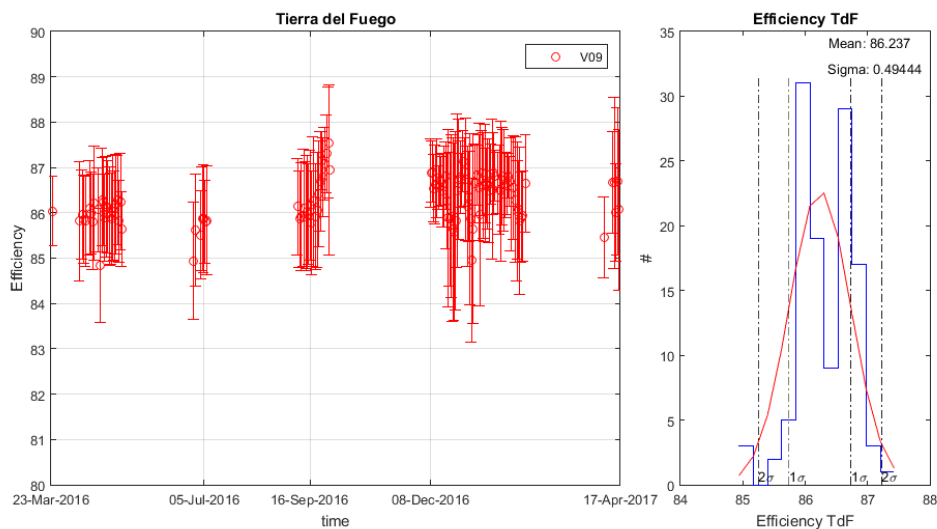


Figure 5.15: Detector efficiency measured in the Observatory's site. Data taking suffered several interruptions during the one and a half year period due to readout system malfunctions. The efficiency was kept stable over time, with an average of 86.2%. Taken from [5].

the gas density, reducing the number of primary ionization and, consequently, the charge distribution favours smaller charges. Lastly, one should note that the readout system in this setup, the PREC (chapter 6), was designed as a proof of concept and is not suited to work in the harsh outdoor conditions. For that reason, the data taking suffered several interruptions.

While the RPC sensitive volume and electronics for the EA were built in Portugal, these are then assembled in Brazil and shipped to the Observatory's main campus, where they are fully tested before deployment. More than twenty detectors have been entirely produced and are already in the Observatory site ready to be installed. The remaining detectors are in the final steps of production.

6 Prototype readout electronics for MARTA

The first step in the development of the readout system for the MARTA RPCs was the design of a prototype system using conventional ICs. Thus, the Prototype Readout Electronics for Counting particles (PREC) was designed to count hits in RPC detectors. As seen in the examples given in section 5.3, the systems that use discrete electronics not only consume more power than their ASIC counterparts but are also usually bulkier, making them unsuitable for a detector like MARTA. Nonetheless, the simplicity and ease of operation made the design of this system a fundamental part of the development of MARTA, namely in the first tests performed with RPCs in the field.

The PREC consists of a very low noise front-end (PREC-FE) board, with an amplifier followed by a comparator, that is coupled to a digital motherboard (PREC-MB) that controls the acquisition and aggregates data. The PREC-MB is then connected to an acquisition computer for data storage and human interface. Although the PREC was designed to measure RPC signals, it can be used with other detectors that also present fast negative voltage pulses, such as PMTs and silicon PMTs [202].

Even though the R&D of this system is not part of this thesis, its characterization was an essential first step in this work. It consists of the measurement of different parameters in laboratory conditions, e.g., gain, noise, crosstalk, etc., that allows to estimate the performance of the DAQ.

In this chapter, this system is firstly described, then its characterization is presented. Lastly, some of the PREC applications are highlighted. Most of the work presented in this chapter is published in [106].

6.1 Description

A block diagram of the PREC is presented in figure 6.1. As mentioned above, the PREC is composed of the PREC-FE, that digitizes the signals, and the purely digital PREC-MB. The eight channels PREC-FE amplifies and discriminates the RPC outputs, before sending the digitized signal to the PREC-MBs via LVDS. The PREC-MB can be connected to 13 PREC-FEs, making it responsible for 104 acquisition channels. It has 13 peripheral FPGAs, one for each PREC-FE, as well as a central FPGA. While the former

receives the differential signals and stores data in case of a trigger, the latter controls all the peripheral FPGAs, aggregating the data from them. The central FPGA is also responsible for the communication via USB with the acquisition computer using an FTDI chip (FT2232H [203]). Although the system was initially thought to operate with an external trigger, that is distributed to all the peripheral FPGAs, a self-trigger mode is also available.

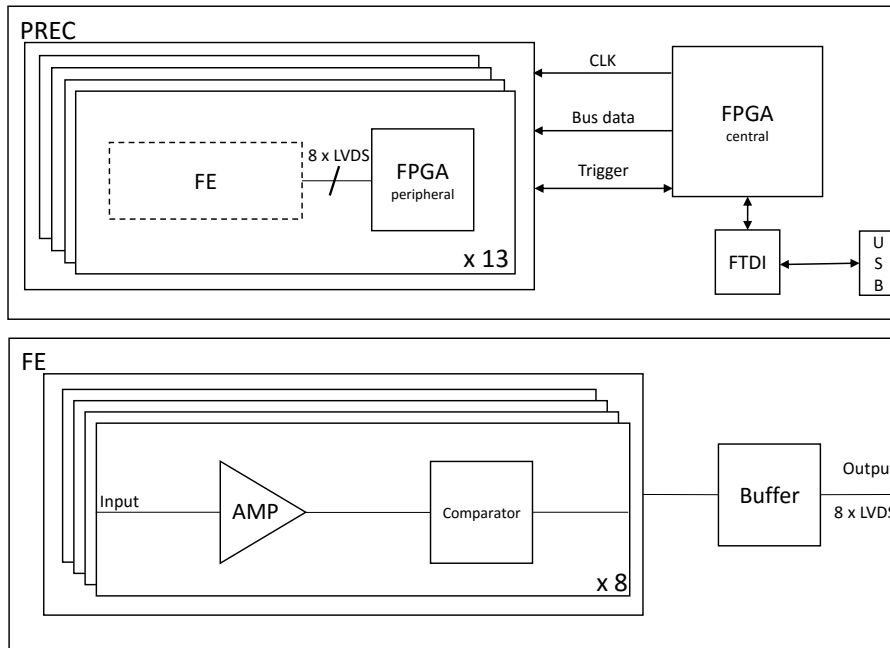


Figure 6.1: Block diagram of the PREC system. In the top rectangle, each one of the 13 peripheral FPGAs is connected to a PREC-FE via LVDS and to the central FPGA using the data, clock, and trigger lines. In the bottom rectangle, the PREC-FE is detailed, with the digitization stage followed by a buffer that drives the differential signal through long cables.

6.1.1 Front-end

Each of the eight PREC-FE channels can be divided into four stages: input, amplification, discrimination, and output. The input stage uses MMCX connectors, and the PCB was designed to guarantee that the line has a 50Ω characteristic impedance. Schottky diodes were placed after the input to protect the amplifier from large overvoltage signals. The amplification stage relies on the MAR-8ASM+ amplifier by Mini-Circuits [204]. The design follows the recommendations from Mini-Circuits closely: the input and output are AC coupled by capacitors. The amplifier is powered by a nominal voltage supply of 12 V, and it presents a gain of ~ 31 dB at a frequency of 50 MHz. The amplifier output is fed to the comparator through a track designed to have 50Ω impedance. The discriminator stage is performed by an ADCMP604 comparator from Analog Devices [205]. This chip is a fast comparator with an LVDS output to minimize pickup noise. The threshold is set by a DAC, DAC7578 by Texas Instruments [206], that is controlled by the slow control

via I²C. Applications like particle counting require a DAC where a good resolution is more crucial than having a wide dynamic range. Therefore, a DAC with a maximum input voltage of 400 mV and a resolution of 12 bits was chosen. The comparator's outputs are made available in two RJ45 connectors by differential and equilibrated lines. LVDS buffers were introduced to drive the signal through long cables and to isolate the components from subsequent electronics. A picture of the PREC-FE board is presented in figure 6.2.

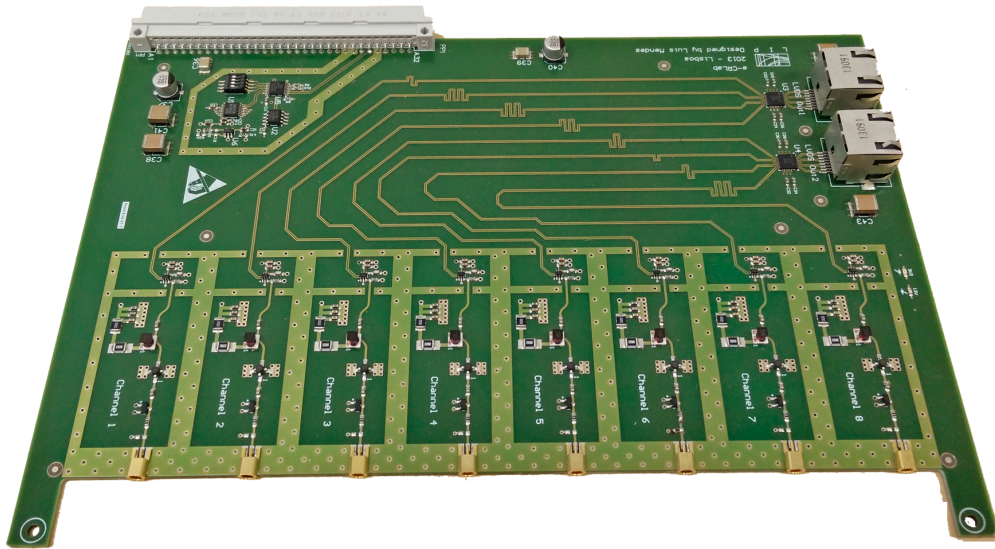


Figure 6.2: PREC-FE picture.

6.1.2 Motherboard

The PREC-MB concentrates the data generated by up to 13 PREC-FE boards. The digitized differential signals are fed into the PREC-MB by means of UTP cables through RJ45 connectors. For each PREC-FE, the eight signals (two cables) are input into one of the small peripheral FPGAs. The 13 FPGAs (Intel Cyclone III, model EP3C5F256C6N [207]) are then connected to a more powerful central FPGA (Intel Cyclone III, model EP3C40Q240C8N [207]) by two differential equilibrated lines used for clock and a synchronization signal: trigger most of the time. Thus, it is assured that all peripheral FPGAs receive these signals at the same time. Furthermore, a bus of 13 individual direct lines, used for data communication, connect the central FPGA to the peripheral ones. As mentioned above, the system was initially designed to operate using an external trigger. However, self-triggering is possible by introducing a mode in which the data bus is also a trigger bus. This way, relevant signals measured by the PREC-FE, can be used to generate a trigger inside the central FPGA. The peripheral FPGAs are continually recording data into a memory with a depth of 100 positions using a 100 MHz clock (PREC-MB master clock). Once these detect a trigger, the data in the memories is stored. An FTDI chip connected to the central FPGA allows extracting the data to an acquisition computer via USB. The computer software will loop through the peripheral FPGAs to collect the data and store

it into a text file. The PREC-MB power supply is 12 V, which is then regulated to the values needed by each component. FPGA programming is possible using a USB-Blaster. General-purpose I/Os and an external clock input are available, increasing the flexibility of the system.



Figure 6.3: PREC-MB picture.

6.2 Characterization

The PREC system was characterized by performing measurements that are typical when accessing the performance of DAQ systems [188, 208, 209]. Most of the tests were done to the PREC-FE with a major focus on its amplifier. The quantities measured were the following:

- **Gain:** the gain and charge gain of the system was measured between PREC-FE input and the amplifier output. Several points were obtained using different power supply values and temperatures. Determining the gain in different settings allows understanding how the PREC behaves in outdoor field conditions.
- **Noise:** the noise was also measured with different power supply and temperature conditions. The standard deviation of the amplifier's baseline was taken as the noise, allowing to determine the minimum threshold that can be set, to avoid random events.
- **Crosstalk:** two adjacent channels were monitored at the same time to determine if the signal propagation through one of them would induce a signal in the other. Thus, it is possible to estimate the percentage of fake signals one should expect.
- **Trigger efficiency:** the trigger efficiency was taken as the number of signals after the comparator over the number of input signals. The s-curve¹ for the trigger efficiency against the set threshold was studied for three different charge values.

¹Step curve where the trigger efficiency goes from 1 to 0.

- **Propagation time:** the time a signal takes to travel from the PREC-FE input to the PREC-MB peripheral FPGA was determined (the fraction correspondent to the propagation in the UTP cable was subtracted). This quantity can have a strong influence when using the PREC in situations where a precise time of the particle crossing is needed, e.g., timing and coincidence measurements.
- **Power consumption:** the power consumption was studied for the PREC-FE analog circuitry, the PREC-FE digital part, and the PREC-MB. These quantities were measured in three different situations: no channels triggered, one channel triggered, and all channels triggered. Moreover, the power consumption was determined for different power supply voltages, in the case of the PREC-FE analog circuitry. As previously mentioned, the power consumption is of extreme importance when setting up an experiment, especially in the conditions of MARTA where the power is limited.

6.2.1 Test bench description

The test bench used to characterize the system consisted of a Tektronix AFG3252 signal generator [210], an injector board, a PREC-FE, a PREC-MB, and a Rohde & Schwarz RTO 1014 oscilloscope [200]. In figure 6.4 is shown a representation of the test setup. LEMO cables connect the small injector to the signal generator and the PREC-FE. In the cases where temperatures control was needed, a freezer chamber instrumented with a thermometer was used.

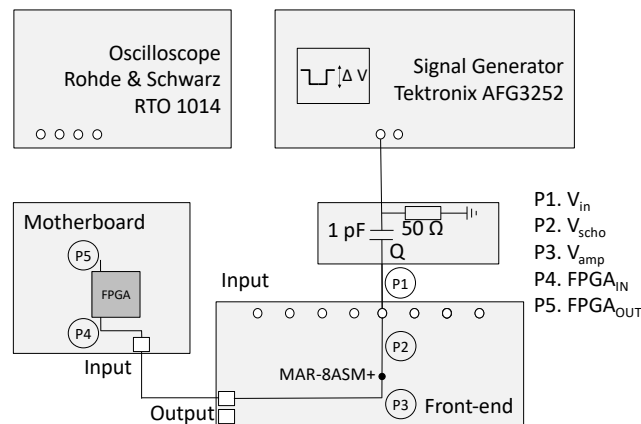


Figure 6.4: Representation of the test setup. The signal generator outputs a negative square wave into a small injector board with a 1 pF capacitor. The signal is then input into the PREC system. P1 to P5 shows the points where measurements were performed using the oscilloscope.

The generator sends a negative square wave with ΔV amplitude and a frequency of 100 kHz. Thus, the injector board creates a pulse with charge $Q = C\Delta V$, when the square wave goes from $-\Delta V$ to 0. The pulse generated is a fast signal with a width of around 4 ns, a typical value for particle detectors (e.g., see the avalanche RPC output presented in figure 5.11). The signal from the injector is input into the PREC-FE, and it goes through

the different components until it reaches the PREC-FE's output. After that, the signal is sent to the PREC-MB, where it arrives at one of the peripheral FPGAs. In its path, five points were measured using the oscilloscope (see P1 to P5 in figure 6.4):

- **P1** is the signal to be input in the PREC-FE (with amplitude V_{in});
- **P2** is the signal after the Schottky diode (with amplitude V_{scho});
- **P3** is the amplifier's output signal (with amplitude V_{amp});
- **P4** is the input of the peripheral FPGA;
- **P5** is the output of the peripheral FPGA.

P2 and P5 were measured using a regular oscilloscope probe, P3 using a soldered LEMO cable to minimize pickup noise, and P4 a differential probe (RT-ZD30). P1 was measured connecting the injector output directly into the oscilloscope, whenever a measurement of the peak value was required. Although the value measured in P1 (V_{in}) is negative, in the results presented, its absolute value is used. Lastly, one should note that the measurement of V_{amp} in P3 using the LEMO cable introduces an unwanted attenuation. For that reason, a calibration constant was obtained: the same signal was measured using the LEMO cable ($V_{amp\ uncalibrated}$), and a calibrated oscilloscope probe ($V_{amp\ real}$). The signal used has a charge of 1000 fC and was measured in the following conditions: $T = 24.7\ ^\circ\text{C}$ and $V_{analog} = 12\ \text{V}$ ². The measurement yield a calibration constant of:

$$\frac{V_{amp\ real}}{V_{amp\ uncalibrated}} = \frac{0.507\ \text{V}}{0.300\ \text{V}} = 1.690. \quad (6.1)$$

6.2.2 Gain

The gain³ and charge gain of the system were obtained using the measurements performed in P1 and P3. While the gain was determined by doing the ratio between the measured values of V_{amp} and V_{in} , the charge gain was computed doing V_{amp}/Q with the charge (Q) determined indirectly using the equation mentioned above.

These quantities were measured for ten different charge values, eight different V_{analog} values, and five temperatures. The charges used are presented in the top left plot of figure 6.5. The correspondent V_{in} was measured and plotted as a function of Q . The points were fitted to a linear function yielding a slope of 0.019 mV/fC, which was applied as a conversion factor between Q and V_{in} in the measurements presented. The temperatures used are 24.7 °C, -1 °C, -16.4 °C, -19.8 °C and -27.3 °C and the V_{analog} values are 10 V, 11 V, 11.5 V, 11.75 V, 12 V, 12.25 V, 12.5 V and 13 V. The points where the temperature was changed were measured with constant $V_{analog} = 12\ \text{V}$ and the points with different V_{analog} were acquired with a constant temperature at $T = 24.7\ ^\circ\text{C}$.

² V_{analog} denotes the power supply voltage of the PREC-FE analog part.

³Voltage gain.

For each charge, several values of V_{in} and V_{amp} were measured using the oscilloscope. The values were then plotted into an histogram and fitted using a Gaussian distribution. The mean value of the fit was taken as the measurement result and the σ as the error. An example of an histogram is presented in the top right plot of figure 6.5 for the case $Q = 300$ fC, $T = 24.7$ °C, and $V_{analog} = 12$ V.

The measurement results are presented in the middle and bottom plots of figure 6.5.

In the middle plots are shown the measurements of V_{amp} as a function of the charge, for each temperature (left) and V_{analog} (right). The data was fitted to a linear function, $y = a + bx$, and the charge gain for each temperature and power supply voltage taken as the slope. The same study was performed for the V_{amp} as a function of V_{in} to obtain the gain. The fit results are presented in table 6.1.

| $V_{analog} = 12$ V | | | | |
|---------------------|----------------|-------------------|----------------|------------------|
| | Charge Gain | | Gain | |
| T (°C) | a (mV) | b (mV/fC) | a (mV) | b |
| 24.7 | 15.5 ± 0.6 | 0.499 ± 0.001 | 11.1 ± 0.6 | 26.29 ± 0.05 |
| -1 | 17.1 ± 0.7 | 0.517 ± 0.001 | 12.4 ± 0.7 | 27.15 ± 0.06 |
| -16.4 | 16.8 ± 0.7 | 0.527 ± 0.001 | 12.1 ± 0.7 | 27.77 ± 0.06 |
| -19.8 | 17.1 ± 0.7 | 0.529 ± 0.001 | 12.4 ± 0.7 | 27.79 ± 0.06 |
| -27.3 | 17.1 ± 0.6 | 0.539 ± 0.001 | 12.4 ± 0.7 | 28.31 ± 0.05 |

| $T = 24.7$ °C | | | | |
|------------------|----------------|-------------------|----------------|------------------|
| | Charge Gain | | Gain | |
| V_{analog} (V) | a (mV) | b (mV/fC) | a (mV) | b |
| 10 | 19.5 ± 0.5 | 0.404 ± 0.001 | 15.6 ± 0.6 | 21.26 ± 0.05 |
| 11 | 17.5 ± 0.6 | 0.454 ± 0.001 | 13.4 ± 0.6 | 23.84 ± 0.05 |
| 11.5 | 17.5 ± 0.6 | 0.475 ± 0.001 | 13.1 ± 0.6 | 24.98 ± 0.05 |
| 11.75 | 16.4 ± 0.6 | 0.488 ± 0.001 | 12.1 ± 0.6 | 25.61 ± 0.05 |
| 12 | 16.1 ± 0.6 | 0.499 ± 0.001 | 11.5 ± 0.6 | 26.21 ± 0.05 |
| 12.25 | 15.6 ± 0.6 | 0.507 ± 0.001 | 11.0 ± 0.6 | 26.65 ± 0.05 |
| 12.5 | 15.2 ± 0.6 | 0.518 ± 0.001 | 10.7 ± 0.7 | 27.19 ± 0.05 |
| 13 | 14.8 ± 0.6 | 0.535 ± 0.001 | 10.1 ± 0.7 | 28.10 ± 0.06 |

Table 6.1: Fit results for charge gain and gain for different temperatures (top) and different V_{analog} (bottom).

The bottom plots show the charge gain and the gain as a function of the temperature (left) and V_{analog} (right). In both cases, a linear function was fitted to the data points. The results show that the charge gain and gain decrease with temperature and increase with the power supplied. The calculated slope are -7.36×10^{-4} mV/(fC K) and -0.03845 K $^{-1}$ for charge gain and gain versus temperature, respectively, and 4.411×10^{-5} fC $^{-1}$ and 2.3165 V $^{-1}$ for charge gain and gain as a function of V_{analog} , respectively. These dependencies are in line with the ones presented in the amplifiers datasheet [204]. Moreover, the datasheet shows the gain going down with temperature and going up with the current, which is by construction proportional to V_{analog} .

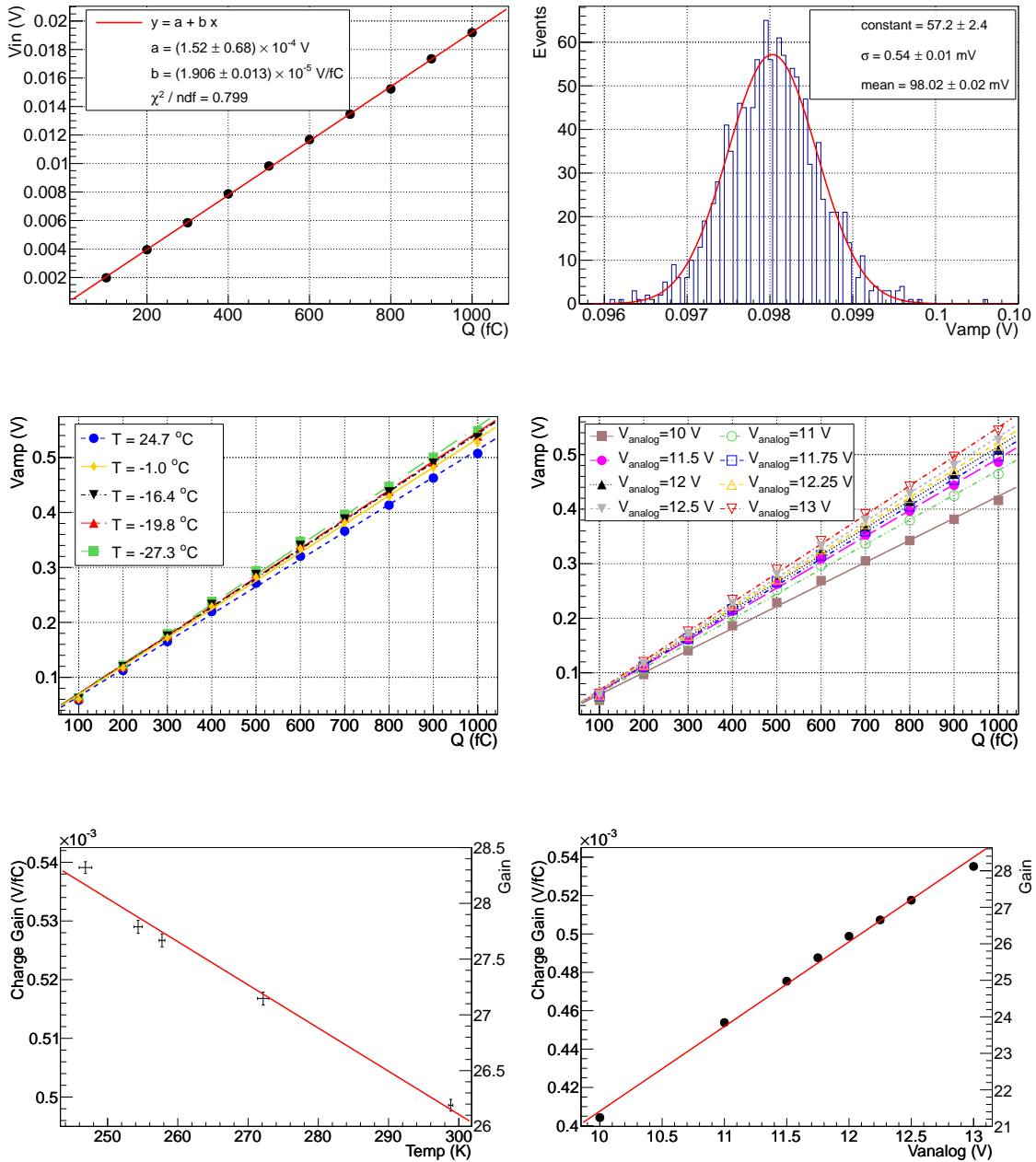


Figure 6.5: Measurement results of the gain and charge gain. Top left: V_{in} as a function of charge. The experimental points were fitted to a linear function. Top right: Histogram and Gaussian fit for the case $Q = 300$ fC, $T = 24.7$ °C and $V_{analog} = 12$ V. Middle: V_{amp} as a function of the charge. For each temperature (left) and V_{analog} (right) ten charges were measured and fitted to a linear function. The fit results are presented in table 6.1. Bottom: Variation of the charge gain and gain with the temperature (left) and V_{analog} (right). The data was again fitted to a linear function. In all the plots, except for the bottom left one, the data errors fall within the marker used for each data point.

6.2.3 Noise

The noise was taken as the standard deviation of the amplifier output's baseline. Different conditions of V_{analog} : 10 V, 11 V, 11.5 V, 11.75 V, 12 V, 12.25 V, 12.5 V, and 13 V, and temperatures: 30.75 °C, -1.3 °C, -16.15 °C, -19.75 °C, and -26.95 °C, were used.

In the left picture of figure 6.6 is presented as an example of a baseline measurement. It shows a noise sample on a $10 \mu\text{s}$ window, as well as the histogram acquired by the advanced measurement function of the oscilloscope. For all conditions mentioned, a histogram like the one presented was acquired and fitted to a Gaussian distribution. The σ of each distribution was obtained, and 3σ taken as the noise level. In the particular case of the picture shown in figure 6.6 the fit results yield: constant = 1.48×10^7 , $\sigma = 0.449$ mV, and mean = 0.197 mV.

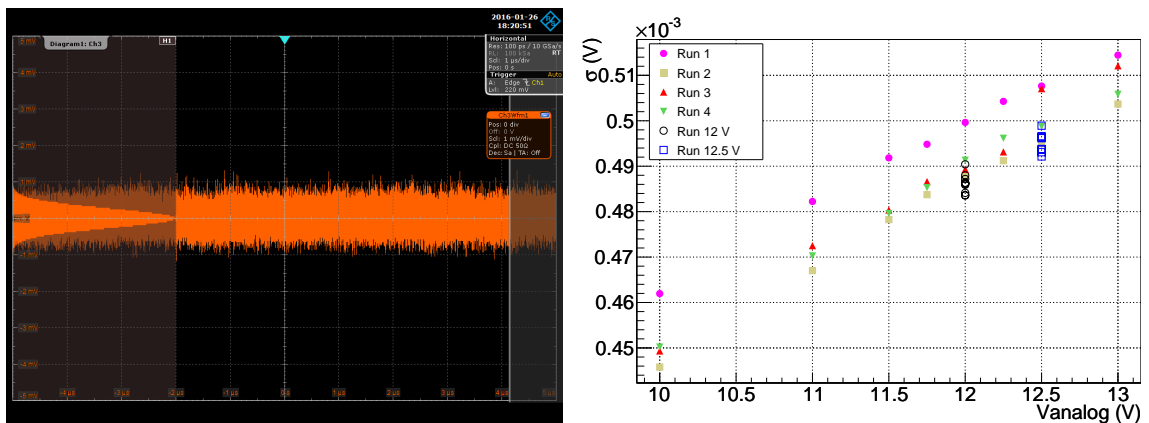


Figure 6.6: PREC noise measurement. Left: Example of a baseline sample in a $10 \mu\text{s}$ window. A histogram was acquired using an oscilloscope measurement option, at room temperature and with the power supply at 10 V. The histogram was then fitted to a Gaussian distribution yielding $\sigma = 0.449$ mV, and mean = 0.197 mV. Right: σ results of the Gaussian distributions for different V_{analog} values. Four runs (full marker points) were performed for each power supply, and an extra ten runs for the values 12 V and 12.5 V (open marker points). The data errors fall within the marker used for each data point.

The measured values for different temperatures with constant V_{analog} did not show any significant variations (less than 0.5%). The same can not be said for different V_{analog} where the σ varied between 0.446 mV and 0.515 mV, for 10 V and 13 V respectively. The results are presented in the right plot of figure 6.6. Four different runs were performed for each value of power supply, and an extra ten runs for the points 12 V and 12.5 V. Thus, one can conclude that the noise level, defined as 3σ , is always lower than 1.545 mV, setting that value as the limit at which a threshold should be used.

6.2.4 Crosstalk

Potential crosstalk between channels was evaluated by input a signal in one channel and measuring the amplifier output of the adjacent one. High amplitude signals were applied to maximize the chance of crosstalk. Furthermore, a capacitor with 330 pF was

used instead of the 1 pF shown in figure 6.4. The effect of the Schottky protection diode was also studied by measuring its output with the large signals. The test was performed at room temperature and with a power supply voltage of $V_{\text{analog}} = 12$ V.

The left picture in figure 6.7 shows the crosstalk test performed with an input signal with $V_{\text{in}} = 2$ V. It also shows the signal at P2 (V_{scho}) of the channel with an input and P3 (V_{amp}) of the adjacent one. The strong attenuation of the input signal by the Schottky, to protect the amplifier input, is seen in the image. Furthermore, the amplifier output of the neighbor channel does not seem to be influenced by the big input signal. Although this can be easily seen in the image presented, a further test was performed. Possible crosstalk was evaluated by acquiring two histograms of the baseline: one for the region without ($t \leq -10$ ns) and the other for the region with signal ($t \geq -10$ ns). The results are shown in the right plot of figure 6.7. The width of the Gaussian does not change significantly to assume that there is any crosstalk. Furthermore, the σ is no more than 0.5% higher after the arrival of the input signal. Similar outcomes were obtained with a V_{in} of 0.4 V. The results presented allow concluding that crosstalk in these conditions is undetectable. If there is any, it is below the noise level.

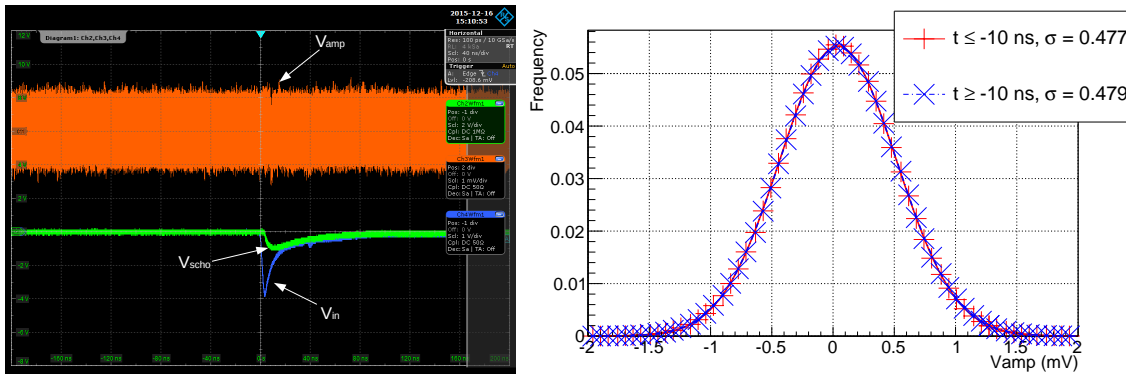


Figure 6.7: Crosstalk measurement results. Left: Screenshot of the oscilloscope measurement for the signals in P1 (V_{in}) and P2 (V_{scho}) of the channel with an input, and P3 (V_{amp}) of the adjacent one. In this case, the amplitude used was 2 V. Right: Histograms of the amplifiers output's baseline for the adjacent channel and respective Gaussian fits before and after the arrival of a signal.

6.2.5 Trigger efficiency

The trigger efficiency was obtained as the ratio between the number of signals that would be detected in P5 (peripheral FPGA output) and the number of signals sent by the generator, P1, in the same time period. The two outputs of the generator were set to send the same signals: one to the PREC-FE input and the other to the oscilloscope. By counting the number of peaks in the oscilloscope during a 200 ms time window, it was possible to determine the trigger efficiency as $n_{\text{peaksP5}}/n_{\text{peaksP1}}$. An example of such measurement is presented in the left screenshot of figure 6.8. In this case, the efficiency is almost 0, as only one of the 19999 peaks input is detected in the FGPA output. The PREC-FE

threshold was swept in steps of 1 mV in the region where the efficiency transitions from 1 to 0 (defining an s-curve). For this test three charge values were considered: $Q = 300$ fC, $Q = 335$ fC and $Q = 370$ fC. The measurement was performed at room temperature and using $V_{\text{analog}} = 12$ V.

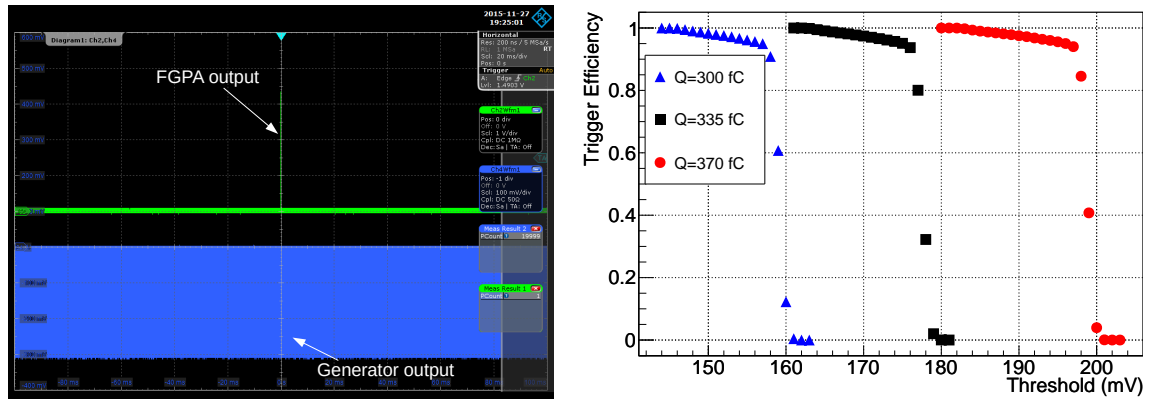


Figure 6.8: Threshold efficiency measurement results. Left: Example of the measurement of the number of peaks in both the generator and peripheral FPGA output, over a time window of 200 ms. Right: Trigger efficiency s-curves for the three charges measured, at room temperature and with $V_{\text{analog}} = 12$ V. The data errors fall within the marker used for each data point.

In the right plot of figure 6.8 are presented the results obtained for the three charges. They all followed the same trend: the efficiency drops from 1 to 0.94 in about 15 mV, and then it goes to 0 in 3 mV. The mid point of the s-curve, where the efficiency is 0.5, is 159.2 mV, 177.7 mV and 198.8 mV for $Q = 300$ fC, $Q = 335$ fC and $Q = 370$ fC, respectively. The width of the s-curve drop corresponds mainly to the fluctuations of the peak of the signal. Furthermore, the value 3 mV is of the order of the baseline fluctuations measured before.

6.2.6 Propagation time

The propagation time of a signal through the PREC-FE was studied. The time difference between the signal at P1, the system input, and P4, the respective peripheral FPGA input on the PREC-MB, was measured using the oscilloscope. To neglect the influence of the travel time in the cable between boards, two cables with different lengths were used, allowing to estimate the time if this value was null. The measurement was performed at room temperature, with $V_{\text{analog}} = 12$ V, and to minimize trigger delay, a low threshold of 10 mV was set.

Since two types of probes were used, a regular one for P1 and a differential one for P4, possible time differences between them were also determined. In fact, when connecting these to the same place in the board, it was found that the standard probe is 1 ns slower than the differential one. In the results presented, that time difference is accounted for.

The results are shown in figure 6.9, where screenshots of the oscilloscope acquisition are presented. In it, the signals at the PREC-FE and peripheral FPGA input are visible. In the left image, a 1 m cable was used, while in the right picture, the cable was 42 cm. The

former had a time difference between signals of 10.72 ns, while in the latter, this difference is 7.88 ns. Thus, it is possible to conclude that for a null-length cable, the propagation time would be 5.82 ns.

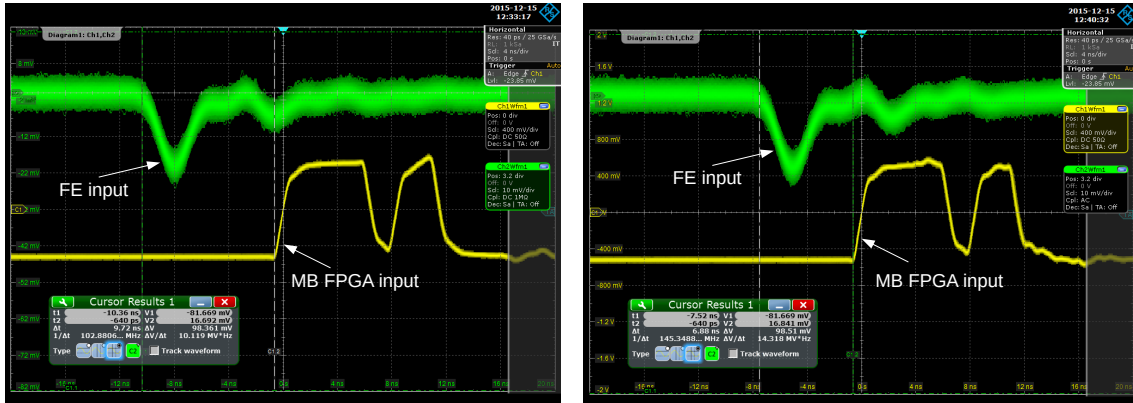


Figure 6.9: Propagation time measurement results. The time measured between the PREC-FE input and the correspondent peripheral FPGA input in the PREC-MB is shown, using a cable of 1 m (left) and 42 cm (right) to connect the boards.

Furthermore, the time dispersion between channels was tested. Two pulses were injected in different channels, and the time difference acquired in the oscilloscope at the FPGA outputs (P5). The measurement showed a deviation lower than 1 ns.

6.2.7 Power consumption

The power consumption of the PREC was measured by determining independently the values for the three different parts of the system: the analog and digital part of the PREC-FE, and the PREC-MB. This was performed at room temperature, with $V_{\text{analog}} = 12 \text{ V}$, and by reading the voltage and current information provided by the power supply.

To test the influence of signals flowing through the board, three cases were measured: normal, null, and high trigger rate. In the first, the threshold was set at 100 mV, ensuring only the channel with an input would trigger. In the second, no signal was input and thus nothing triggered. In the last, the threshold was lowered to 1 mV so that the system would trigger on the baseline. The power consumption of the PREC-MB, 3.372 W, and the analog part of the PREC-FE, 3.576 W, were found to not change with the different trigger rates. The digital part of the PREC-FE changed from 1.403 W in the first two cases to 1.442 W in the last case. This change can most likely be justified by the high switching frequency of the comparators and LVDS buffers.

Taken into account the values presented above and 13 possible PREC-FE connected to a PREC-MB, accounting for a total of 104 acquisition channels, one can conclude that the power consumption is always lower than 660 mW per channel. Although this value is higher when compared to the examples given in section 5.3, it is still in the same order of magnitude as the conventional IC system presented.

Lastly, the power values for different V_{analog} were measured at room temperature. The

results, presented in table 6.2, show that the consumption increases from 2.28 W to 4.33 W, when V_{analog} is 10 and 13 V respectively. Using $V_{\text{analog}} = 10\text{V}$, would lower the PREC power consumption per channel to less than 500 mW.

| | | | | | | | | |
|-------------------------|-------|-------|-------|-------|-------|-------|-------|-------|
| V_{analog} (V) | 10.00 | 11.00 | 11.50 | 11.75 | 12.00 | 12.25 | 12.50 | 13.00 |
| Power (W) | 2.280 | 2.904 | 3.232 | 3.408 | 3.576 | 3.761 | 3.950 | 4.329 |

Table 6.2: Power consumption for 8 values of V_{analog} , at room temperature.

6.2.8 Summary

The characterization of the PREC system was done by measuring some quantities that are essential to assess DAQ systems performances: the gain, noise, crosstalk, trigger efficiency, propagation time, and power consumption.

- The gain and charge gain were measured in various temperatures and using different power supply values in the PREC-FE analog part. The results show that gain is proportional to the power supplied and inversely proportional to the temperature. For nominal working conditions (12 V power supply and room temperature), the charge gain and gain are respectively 0.51 mV/fC and 26.3.
- The noise was measured as the standard deviation of the amplifier output's baseline, allowing to set a threshold as low as 1.6 mV.
- Crosstalk between channels was undetectable above the detection line limited by noise.
- The trigger efficiency was characterized by its s-curve when this quantity goes from 0 to 1. The curve showed a steep drop with a width of 3 mV, which corresponds to the fluctuations of the signal.
- The propagation time between the PREC input and the respective peripheral FPGA was measured at 5.82 ns for a null-length cable.
- The system's power consumption was independently determined for the three parts that require a power supply, in different trigger rate conditions. The results yield a power consumption of 660 mW per channel in nominal operating conditions. However, this value can be lowered to 500 mW per channel by using 10 V in the PREC-FE analog part, which also reduces the amplifier gain.

6.3 PREC applications

The development of a simple and easy to use system like PREC, with only an amplifier followed by a discriminator, allowed performing a number of necessary tests to the RPCs while the final DAQ was being developed. Thus, although PREC was never thought to be

the acquisition system to be used in the MARTA stations, mostly due to its high power consumption and bulkiness, it was the perfect prototype and proof of concept DAQ. PREC also found some applications outside of MARTA: it used in other RPC systems, and even with silicon PMTs.

The tests performed in one of the Observatory's Infill array stations, presented in section 5.4, were done using PREC. The two RPCs on top of each other were instrumented with this system. The efficiency of one of them was studied, which involved programming a trigger into the PREC-MB between the second RPC and the station WCD. In this setup a total of twelve PREC-FE boards were used with a PREC-MBs. The electronics were buried inside a box by the station, as shown in figure 6.10.

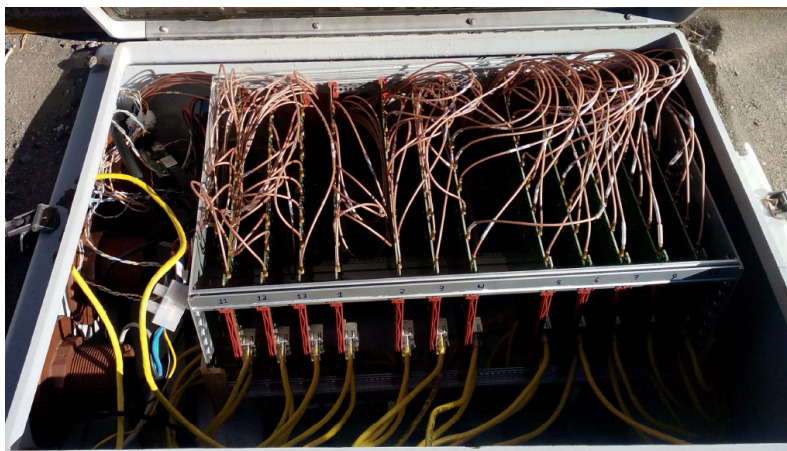


Figure 6.10: PREC installed in the Observatory's site during the RPC tests under a WCD. Picture courtesy of Luís Mendes.

This system was also used to study the WCD response to muons [211, 212]. Namely, a tank was sandwiched between two RPCs, and the coincidence trigger of the RPCs was used to acquire the tank data. Therefore, the track length of the muon inside the tank could be calculated, by knowing where the particle crossed the RPCs. Thus, it was possible to plot, the signal measured in the PMTs (in VEM, see section 3.1.1) with the distance the muon traveled through the tank. The results were compared with simulation, showing to be in accordance, which helped validating the Observatory's WCD simulation. In this setup, each RPC was instrumented with PREC. The coincidence trigger, sent to the tank, was generated by the PREC-MB, showing the flexibility of the system.

A TOF-tracker based on multi-gap RPCs was also instrumented with the PREC-FE. The device is described in [213] and is composed of three detector layers with readout strips. It provides accurate time and bi-dimensional space coordinates for the particle crossing. In this case, the PREC-FE was used as a timing circuit paired with a TDC. Additional charge sensing amplifiers were utilized to measure the signal's charge and determine the particle's crossing position. This telescope presented a position resolution of $1.33 \text{ mm } \sigma$, and time resolution of $150 \text{ ps } \sigma$.

One other use of PREC was to study a prototype detector developed for academic

purposes. It was designed to be used during classes in secondary schools [214]. The device is composed of scintillators connected to silicon PMTs, Hamamatsu's MPPC S12572 [215]. In this project, the PREC-FE was part of the test bench utilized to determine some of the system's parameters, like the scintillators' dark current. This example shows once again the flexibility of PREC, and that it can be used with detectors other than RPCs.

7 MARTA front-end

The successful design and operation of PREC, along with the indications that RPCs could be operated in the field, prompted the development of the second and final acquisition system. This time the system needed to comply with the power and space restrictions of MARTA stations. Unlike PREC, the new front-end was required to not only measure particle hits but also the charge induced by the avalanche in the signal readout plane. Thus, it will be possible to get the number of particles whenever pile-up effects are present¹.

The MAROC ASIC [6, 103, 104] was chosen to digitize the RPC signals. Although it was not designed to read these detectors, there is at least one other example where this chip was used with RPCs [183]. Furthermore, the multi-anode PMTs signals, for which the MAROC was designed, share some characteristics with the RPC signals, namely its negative polarity. After initial testing using OMEGA's development board [216] it was shown that the RPC signals can be measured using this ASIC [217].

Many reasons lead to choosing the MAROC over other chips from OMEGA, namely the HARDROC, which was specifically designed to work with RPCs. The fact that there was previous experience in the laboratory with this ASIC (see [202]) made it the obvious candidate to begin with. Moreover, it has 64 input channels, which match the 8 by 8 pad grid of the RPCs, it is compact, with an area of 16 mm², and low power with consumption of 3.5 mW per channel. Unlike the HARDROC in the MAROC the 64 discriminated outputs can be directly accessed outside the chip. The MAROC also has a slow shaper circuitry followed by an internal ADC to measure charge, while the HARDROC only has the slow shaper, which is output to be read outside the ASIC.

The ASIC outputs follow to an FPGA that is responsible for all the digital electronics, which include the MAROC management, and communication with the Central Unit or an acquisition computer². Three different versions of the front-end were prototyped and tested, and the final one produced to be used in the field.

The development of the MARTA front-end is the main focus of this thesis. Mainly, the firmware and software implementations, debugging, deployment, and integration with the rest of the MARTA module. The description of this system has been published in [102]. In this chapter, first, the front-end's requirements are discussed, and then the design of its three prototypes is presented. After, the MAROC ASIC is described, and lastly, the

¹As mentioned in section 4.3, pile-up effects are expected near the core of showers initiated by the most energetic cosmic rays, where the density of particles is higher than 35.6 particles/m².

²Moving forward, these will be mention as "acquisition machine".

firmware and software are detailed.

7.1 Requirements

There are not many examples where RPCs were deployed in self-sufficient stations like the ones from the Pierre Auger Observatory. RPCs are mostly used in laboratory conditions (see applications in section 5.2), where the requirements are different from field operation. Although space and power are always a concern, usually, there is enough available so that it is not as much of a limiting factor as in cosmic ray arrays' stations. Thus, MARTA has some technical challenges that were not present in other RPC related projects. These challenges also apply to the development of the RPC readout system. Considering that, a list of requirements for the front-end was put together:

- **Fast signal digitization to deal with the fast RPC pulses.**

The MARTA RPC signals are negative pulses with small amplitude of a few mV, a fast rise and an RC-discharge-like fall, with a total width of about 7.5 ns. Amplification is a requirement for such small signals, as mentioned previously. The MAROC ASIC has a pre-amplifier and several shapers that are designed to read small signals.

- **Estimate the number of particles for both the high and low particle density regions of the shower: a complementary charge measurement is necessary.**

The system needs to be able to measure not only particle hits but also the charge induced. In RPCs, the charge is not directly proportional to the number of particles crossing, since it depends mostly on the avalanche's development phenomena, mentioned in section 5.1. This characteristic makes the determination of the number of particles a non-trivial problem, that needs to be carefully studied either whenever data-taking is started or using simulation. It is expected that with enough data, patterns start to emerge in the high-density regions that might help determine this number.

Other applications of the charge measurement in RPCs should also be mentioned. Particularly, the fact that a fast charge spectra acquisition can give valuable information about the detector behaviour. Factors like the gas flux and purity, as well as, weather conditions can influence the detector performance and therefore change the spectrum. A baseline charge spectrum can be performed for each RPC, and then periodical control acquisition, can be used to flag any problem with the detector. Moreover, this measurement can help distinguish crosstalk from real hits, since in a crosstalk signal, considerable less charge should be measured.

The MAROC fits this requirement since it has a dedicated ADC preceded by a slow shaper used to measure charge.

- **Low power of a few watts per RPC.**

All components of the board needed to be carefully picked to comply with these restrictions. The average 10 W given by the station battery should not be exceeded, with the risk of power cutdowns that will stop the acquisition. The ASIC and FPGA combo that was chosen for the front-end helps alleviate the power consumption, since only one of each chip is needed per RPC. Furthermore, in both cases, low power versions were picked, and the same happened with all other essential components. In some cases, parts were put in for debugging and even to increase the flexibility of the board, which can be disconnected during data taking, reducing power consumption to a minimum necessary.

- **Stable and reliable for low maintenance operation.**

The location of the Observatory's SD stations is isolated, hard to reach, and exposed to variable weather conditions. Thus, the board has to be able to recover from possible crashes without any human interaction. All possible causes of failure have to be accounted for and mechanisms put in place to try and solve them online. Only in extreme cases where possibly a fatal failure is present, the station should be visited. Lastly, the front-end has to be stable in the different temperature conditions that will be present in the field.

- **Compact design due to space limitation inside the aluminium case.**

A small electronics compartment is part of each MARTA module. The compartment has an area of $0.447 \times 1.285 \text{ m}^2$, and a height of a few cm. It has to fit not only the front-end but also HV, monitoring, and PSU. Thus, the space is extremely limited, having much less than 0.1 m^2 to fit the front-end in. The fact that only one ASIC and FPGA are needed per RPC will help to cope with this restriction. They both have an area that does not exceed the dozens of mm^2 making it possible to design a compact system.

- **Trigger inputs and outputs.**

Trigger lines directly connected to the FPGA are necessary to synchronize the data measurement with other detectors in the system. The fact that these are linked to the FPGA gives the system flexibility, with the possibility of a trigger being generated in the front-end board. The primary trigger mode in MARTA's stations will be using SD's T1 and T2 from the WCD and routed through the Central Unit. The trigger lines between the Central Unit and the FPGA's front-end are differential (LVDS). Nonetheless, single-ended lines are also present, through SMA or LEMO connectors.

- **Fast lines for communication and data transfer.**

Two communication links were projected to be part of the front-end. The first, through LVDS, is used to communicate and transfer data to the Central Unit. A custom protocol was designed and implemented in both the front-end and Central Unit's FPGA, which uses three differential lines in each direction. The second is standard USB communication using the same FTDI chip as the PREC-MB. This link

is mostly used for the development and debugging of the board with any computer that can run the custom C++ software (including the standard FTDI drivers). Once again, having the USB communication increases the board flexibility, since any computer, including single-board computers (with a USB port), can be used to manage acquisitions.

- **Power fail safe mechanism.**

A power fail mechanism helps prevent any damage to the system in case of a sudden spike of power. Such protection was also installed in the PSU, which is connected directly to the station’s batteries. However, having it on the front-end assures that in case of anything going wrong, which includes human error, the board components are safe. Once again, this feature will be valuable if the system’s uses expand outside of the context of MARTA in a not so controlled environment.

7.2 MAROC

The Multi Anode Read-Out Chip (MAROC) 3 ASIC [6, 103, 104], developed by OMEGA, fills MARTA’s criteria. As mentioned above, it is low power, compact, has 64 input channels each with a pre-amplifier, 64 discriminated outputs, and can perform charge measurements up to ~ 15 pC. A block diagram of the MAROC³ is presented in figure 7.1.

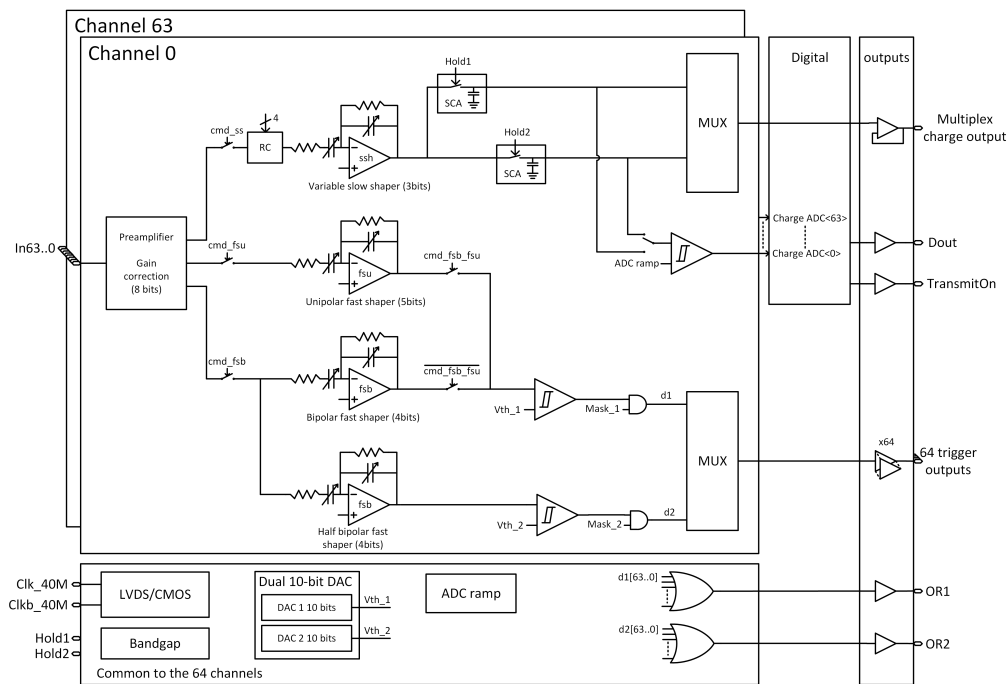


Figure 7.1: MAROC 3/3A block diagram. Taken from [218].

³The diagram shown is for version 3A. However, the only difference between version 3 and 3A is the chip packaging.

The MAROC can be customized using a collection of 800+ bits, which will configure the ASIC. These will set parameters like the discriminator's threshold, the amplifier's gain, the switches shown in the block diagram, etc. The list of parameters is shown in appendix A. Detailed information about these can be found in the ASIC's datasheet [103, 104].

The input signal first goes through a pre-amplifier. Each of the 64 channels has its own amplifier with a gain correction from 0 to 4. The gain is set with an eight bits word: word = 1 corresponds to gain = 1/64, word = 64 to gain = 1, and word = 255 to gain = 255/64 \approx 4. In this work, the gain used is always word = 64, unless stated. After being amplified, the signal follows to three different branches: fast shaper branch, slow shaper branch, and sum branch (not represented in figure 7.1).

In the sum branch, a direct output of the pre-amplifiers signal is available. There are eight analog outputs, each consisting of the sum of up to eight channels. Which channels are summed can be set using the configuration parameters.

The fast shaper branch is responsible for the discrimination of signals. First, the signal goes through one of three variable fast shapers: unipolar, bipolar, and half-bipolar. These are characterized by their rise time between 20 and 25 ns [103, 104]. Each shaper has a set of configurable resistors and capacitors that can change this time. Two discriminators follow the shapers, one is after the unipolar and bipolar, and the other after the half-bipolar. The discriminators' thresholds are set by a programmable 10-bit DACs that are common to all channels. The configurable parameters set both which of the shaper are used and the threshold values. The output of the discriminators follow to a MUX that output both, none or just one of the discriminated signals. An OR of the discriminator's outputs is also available.

The tests performed during the early development of this system focused on determining whether or not the MAROC would be able to measure the RPC signals [217]. Namely, the ASIC's development board was used to determine how the fast shaper branch would behave in the presence of real RPC signals. Of the three possible shaper choices, the bipolar ones were chosen over the unipolar to avoid the baseline undershoot that is characteristic of the latter. Between the two other shapers, the half bipolar is known to be used with higher charges, making the bipolar fast shaper the chosen one. Figure 7.2 shows an oscilloscope screenshot, where one MAROC channel was tested connected to an RPC. In yellow is presented the RPC signal after the pre-amplifier, in blue the bipolar fast shaper output and in lilac the discriminated signals. From these results, it was possible to conclude early on that the MAROC was able to measure the RPC signals.

The slow shaper branch is responsible for the charge measurement. First, the amplified signal goes through a variable RC circuit followed by a variable slow shaper. In both cases, the values of the capacitors part of the circuits can be changed in the programmable bits. It produces a slow signal with rising time, which can vary between 50 and 150 ns depending on the configuration used. The charge is obtained by acquiring the peak value of the slow shaper signal, which are known to be proportional.

After the signal is shaped, two sample and hold circuits are used to sample the baseline

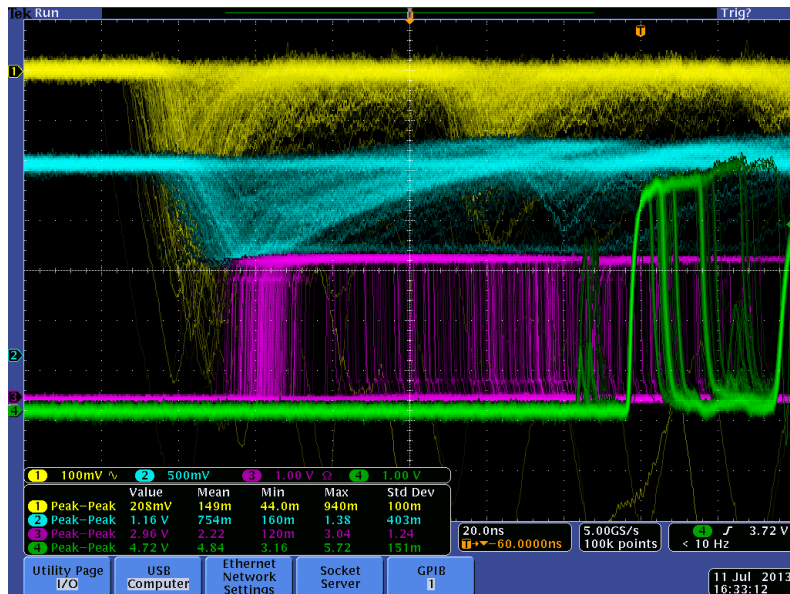


Figure 7.2: Oscilloscope screenshot of the first measurement of RPC signals being read by the MAROC. Yellow: RPC signal after the internal ASIC amplification. Blue: bipolar fast shaper output. Lilac: discriminator output. Taken from [217].

and peak. The moment the signal is held is determined by two inputs of the ASIC, Hold1, and Hold2. These are common to all 64 channels and, in the case of MARTA's front-end, generated by the FPGA. The held signal of the peak then follows to a Wilkinson ADC to be digitized. The ADC can be 8, 10, or 12 bits, depending on the application. In this work, the 12 bits option was chosen, increasing the resolution of the measurement. Wilkinson is a ramp type ADC, which means that a counter will measure the number of clocks (with a frequency of 40 MHz) between a reference and the held peak value. Since the ramp slope is constant, the number of clocks is proportional to the value input in the ADC. Lastly, the 64×12 ADC bits are output in a serial line. The dead time of this measurement is significant since it has to wait for the ramp to reach the peak value. Thus, the maximum dead time of the ADC is $\sim 100 \mu\text{s}$ per event.

Both the fast shaper and slow shaper output are available outside the ASIC. In the case of the slow shaper, it can be measured by an external ADC. However, these signals are multiplexed, meaning only one channel can be output at a time. An example of typical responses of the shapers to RPC signals are presented in figure 7.3⁴. The bipolar fast shaper (left) configurations used were $R_{\text{fs}} = 150 \Omega$ and $c_{\text{fs}} = 150 \text{ fF}$, while for the slow shaper (right) the configurations were $c_{\text{RC}} = 2250 \text{ fF}$ and $c_{\text{ss}} = 2100 \text{ fF}$.

A test input, Ctest, is available and can simulate an input charge through a 1 pF capacitor. The Ctest can be turned on and off for each channel using the configuration parameters. Lastly, crosstalk between channels in the MAROC is known to be less than 1% [103].

⁴The ringing present in the right image is due to the oscilloscope measurement. The signal was not measured in the ideal conditions that would minimize such effect.

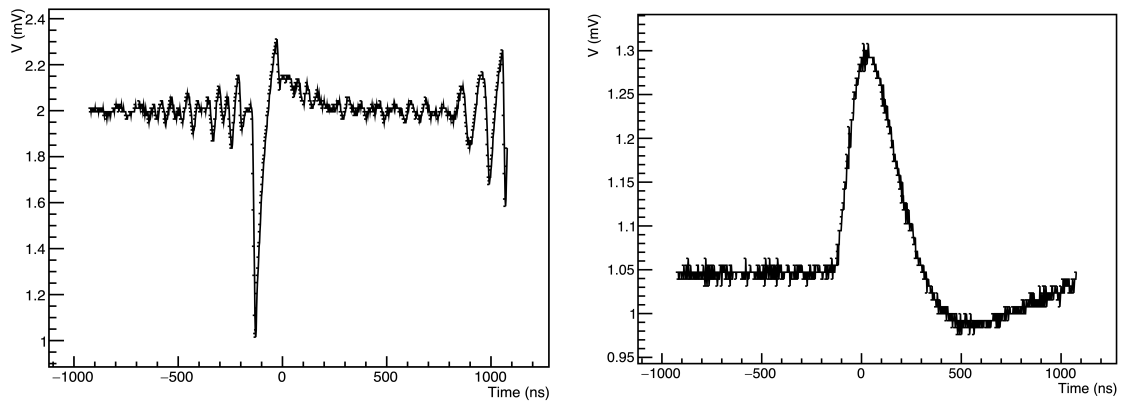


Figure 7.3: Fast shaper (left) and slow shaper (right) response to a typical RPC signal.

7.3 Design and prototypes

The MARTA front-end had several iterations during its design process. Through the four years of development, five PCB layouts were drawn, of which three were produced. In each new layout, improvements were made on the previous one with the experience and knowledge acquired from the testing and debugging process. Furthermore, as the MARTA station outline was getting finalized, new features were added. The process concluded when the final design was delivered covering all the requirements and ready to be installed. The board's production name is MARTA DAQ, and it was drawn by Miguel Ferreira at LIP's e-CRLab [219].

The first prototype, MARTA DAQ I, started being developed in late 2013, and a small batch of about ten boards was produced in 2014. It follows closely the concept of the MAROC development board with the same FPGA being used, an Intel Cyclone (model EP1C6Q240C6N) [220]. While the MAROC is managed by the FPGA, the latter is controlled by an acquisition computer via USB, with an FT2232H chip by FTDI [203]. Test points, to measure the signals between the FPGA and the MAROC, as well as LEMO/SMA connectors routed directed to the FPGA, were added to facilitate the development process. A new input stage was also introduced in this prototype. The RPC cables are attached to a pair of mezzanine boards that are connected to the front-end using MICTOR connectors [221]. Two versions of the mezzanine boards were produced. In the first, designed to be used during the development process, MMCX connectors were installed to match the RPC cables. In the second, designed to be used in the MARTA module, the RPC cables are directly soldered to the mezzanine board. Pictures of the MARTA DAQ I (top) and the two mezzanine boards (bottom) are shown in figure 7.4. The crucial measurement modules of firmware and software were developed using this version. Furthermore, the initial test benches that validated the board's concept were performed using this prototype.

Almost two years of accumulated experience with this prototype led to a redesigning of the system much closer to MARTA's requisites. In the meanwhile, two new PCB layouts were drawn, MARTA DAQ II and III, where bugs were corrected and new features

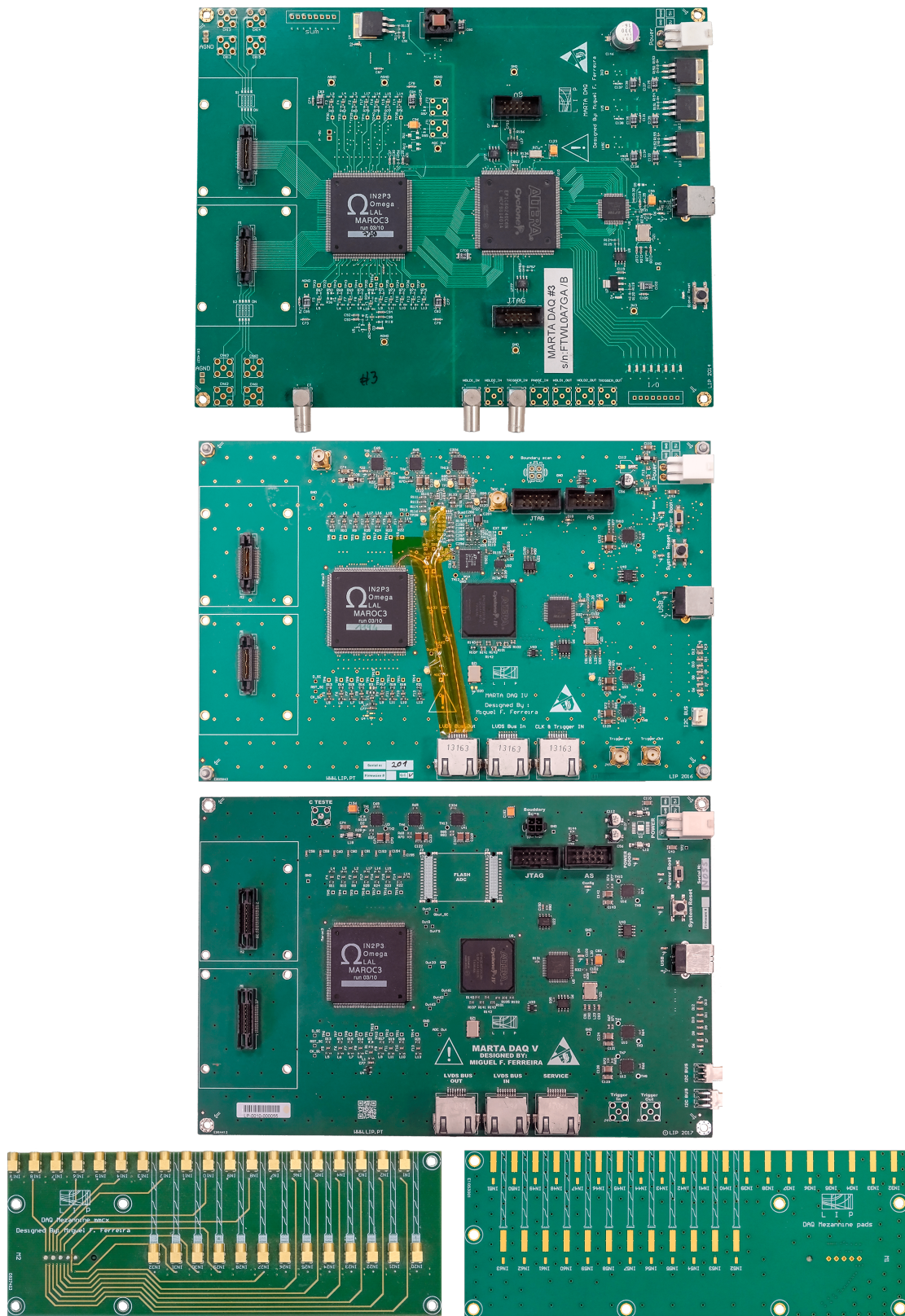


Figure 7.4: MARTA DAQ first prototype (top), second prototype (second from the top), production version (third from the top), and both mezzanine input boards (bottom). Bottom left: mezzanine with MMCX connectors, used for development. Bottom right: mezzanine without connectors, the signal cables are soldered.

added. Although these were never produced, they were important stepping stones in the development process, since the improvements would be part of the second prototype.

The second prototype, MARTA DAQ IV, is shown in the second picture from the top of figure 7.4. It was produced in 2016, with about four boards being fully put together. Major improvements were implemented, with the most significant one being the new FPGA. This upgrade was necessary because the firmware implemented on the original FPGA was maxing out the devices' memory. Furthermore, the FPGA was an old product that is now discontinued. The chosen replacement was an Intel Cyclone IV FPGA (model EP4CE30F23C8L) [222]. It is an up to date device, with the right balance of PLLs and I/Os, enough true-LVDS pins, and a good speed grade for this application. Unlike the previous FPGA, this one is packaged in a ball grid array (BGA) configuration, which meant all the routing had to be redone. Firmware programming is done using a USB blaster through Active Serial, connected to an erasable programmable read-only memory (EPROM), or using JTAG. The EPROM saves the firmware and programs the FPGA each time the system is started. The JTAG interface allows for firmware debugging using Quartus' SignalTapII [223].

USB communication was mostly kept unchanged, and new differential communication and trigger lines were routed to three RJ45 connectors. An I²C bus was added with temperature and humidity sensors to monitor atmospheric conditions. The LEMO/SMA connectors were reduced to the essential ones: two connected directly to the FPGA, for additional trigger interface, and a third one for the Ctest input. A watchdog system, Texas Instruments' TPS3825 [224], was included as a power fail-safe mechanism. Thus, whenever the power supply goes below or above a threshold voltage, the system is turned off making sure none of the components are affected. Another addition was boundary-scan, allowing to do production quality control. Namely, it tests the connectivity between devices, like the FPGA, and the ASIC.

The last change was the addition of an external flash ADC. It was put in with the intention of measuring the sum of all 64 RPC signals, after the MAROC's amplification. This measurement would mostly be used for calibration purposes and to have a quick estimation of the total charge induced in the RPC. The sum outputs of all channels would be enabled, and the eight pulses externally summed. Then, the summed signal would go through a shaper before entering the external ADC. The chosen chip, an LTC2242-12 flash ADC by Analog Devices [225], can reach sampling speeds of 250 MHz, enough to measure the shaped signal. The ADC is then connected to the FPGA, for management and data storage. Preliminary tests performed showed the potentiality of the concept, but the circuitry needed some rearrangement. This is not critical since this feature is not fundamental for the operation of the front-end in MARTA's context. Furthermore, an ADC like the one chosen consumes too much power and would not be turned on during field operation.

The firmware and software development continued in this version, with the code already developed ported to the new FPGA. Small routing bugs were found that required a patch

on each of the boards produced. For that reason, the design of the final production version started right after these problems were found, and the lifetime of this prototype was reduced significantly.

The production version of the front-end is MARTA DAQ V that was delivered in 2017. Compared to the second prototype, other than the bug fixes, the main difference is that the external ADC was moved to a piggy board. Thus, its redesign would not interfere with the development schedule of the front-end for the EA. As of the writing of this thesis, almost no effort was put into that part of the system. Two reasons led to that decision: the focus needed to be put into finishing other designs related to MARTA, and the fact that the ADC's price skyrocket due to the high demand for this device by the industry. As this is the production version, a fuse was also added, at the power input of the board, to protect the system from human mistakes like reversing the input's polarity.

A total of 55 boards were produced, of which about 30 will be installed in the MARTA's EA (not including spares). The final firmware and software developments were done with this board, including LVDS communication. The validation tests show in chapter 8 were mostly performed using the production version. All working setups, most of which are mentioned in chapter 9, use this board. Detailed documentation that includes information about connections, block diagrams, and the bill of materials can be found in [226]. A block diagram of MARTA DAQ V is presented in figure 7.5. All the main components are represented, and it is shown how these interact with each other.

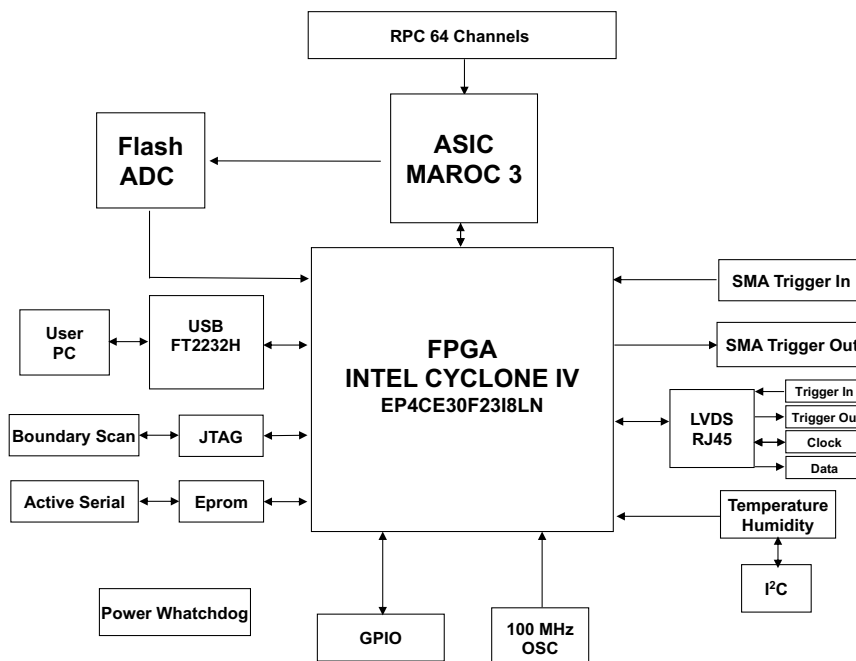


Figure 7.5: MARTA front-end block diagram.

The design was implemented in an eight layers PCB, where the bottom and top layers

are ground planes to shield the analog signals. Furthermore, to avoid ground loops, the PCB was stitched with ground vias. The power supply voltage is 5 V that is then regulated to five different values: 3.3 V for logic, 1 V for the FPGA core, 2.5 V for LVDS lines, 1.5 V and 3.5 V for the MAROC. The MAROC bias is also filtered to guarantee a clean and stable supply. Equilibrated lines are possible from the RPC pad to the MAROC due to the MICTOR connectors that allow matching the cable impedance, and the transmission lines with $50\ \Omega$ impedance that drive the signal to the MAROC input, avoiding reflexions. Lastly, power boot and system reset switches are available to reset and reboot the front-end manually. The MARTA DAQ V has an area of $21.6 \times 14.4\ \text{cm}^2$ and a total power consumption of 1.43 W (excluding external ADC). It is under the limit of a few watts per RPC and corresponds to a consumption of 22 mW per channel.

All the versions of the front-end were designed using the MAROC 3. However, the ASIC was repacked into a BGA configuration (MAROC 3A), and the variant 3 of the chip is no longer produced. For that reason, a new PCB layout is being prepared where all the routing will be redone to accommodate the new chip. Moreover, among other new features, the FPGA will be switched to a chip part of Intel's new range of low power devices, a Cyclone 10 LP [227].

7.4 Firmware and software implementation

The firmware programmed in the FPGA and the software running in the acquisition machine manage all the processes in the front-end. These are closely linked since the software's job is to control the firmware that will then interact with all the devices part of the system.

After some experience modifying the code installed in the MAROC's development board, the firmware was written from scratch. It was written with Intel's design software, Quartus Prime, and using the hardware description language Verilog. The software was in a first instance developed in C# and run exclusively in Windows. It was later rewritten in C++ to be executed in computers running Linux, including the Central Unit. Since some data is stored in ROOT [228] trees, this analysis framework is needed to compile and run the code. The same happens with the FTDI library, required when a computer is connected to the board via USB.

The firmware and software can be divided into modules. The four primary modules are: communication, ASIC configuration, hit measurement, and charge measurement. The first is responsible for the interaction between the firmware and the software. The configuration module programs the 800+ variable bits into the MAROC. The hit and charge measurement modules, manage the acquisitions, and store the data in the FPGA before it is transmitted to the acquisition machine for posterior analysis. Other small elements should also be mentioned: a rate module that measures the signal rate of each RPC pad, and a trigger module that allows changing the trigger used in the acquisitions.

7.4.1 Module 1: Communication

In the communication chain, the front-end's FPGA and its firmware are always slaves, while the software and the devices that run it are the masters⁵. This way, each acquisition machine can control more than one front-end. The communication between the software and firmware can be divided into two types: write and read. In the first, data is sent to be written in a particular address of the FPGA, e.g., memories, registers, etc. In the second, the master device requests the slave for information, like temporarily stored data, the state of a particular flag, etc. The FPGA responds with the requested words, and communication is ceased until the software initiates it again.

A submodule was created for each type of communication: USB and LVDS. These interpret the protocols in the case of incoming communications and build them in outgoing ones. After the data is decoded and before it is sent out, the rest of the firmware behaviour is independent of the communication type. Since, the LVDS links were added in the later stages of the development, most of the firmware design was done with the USB communication module.

7.4.1.1 USB

The USB chip is an FT2232H by FTDI [203], as mentioned before. The chip has two parallel channels and several communication styles that can be configured. In this development, only one channel was used, A, and the "FT245 Style Asynchronous FIFO Interface" communication was chosen (see [203] for details). This style uses parallel transmission over eight bidirectional lines and is controlled by four more, all connected directly to the FPGA. Although this is a largely used configuration, and both software and firmware modules are easily found online, custom code was written for this project. In what software is concerned, the standard FTDI drivers and libraries were used as a starting point. These are available in most Linux's package management command-line utilities, e.g., apt and yum.

The communication protocol chosen is, however, not custom. It was designed by LAL [229] and used in the MAROC's development board with a different FTDI chip. The write, read request and read sequences are presented in table 7.1. All the sequences start with the header, '10101010', and finish with the trailer, '01010101'. The write transmission, in the direction PC -> front-end, sends the number of bytes to be written, the address, and the data. Both the address and 'number of bytes - 1' words are composed of eight bits each, limiting of data transmitted per communication to 256 bytes. The first bit of the address is always '0' when writing and '1' when reading. The read request, in the same direction, has a similar sequence. However, the 'number of bytes - 1' that can be requested are sent in 16 bits, reaching up to 65536 words. The sequence is the eight least significant bit (LSB) of 'number of bytes - 1', the address, and the most significant bit (MSB) of 'number of bytes - 1'. The response, in the direction front-end -> PC, starts with the LSB

⁵In a master/slave configuration, communication is always started by the master. The slave can only send data after being requested by the master.

of 'number of bytes - 1', the address, and then data to be sent.

Write: PC -> Front-end

| Header | Number of bytes - 1 (N-1) | Address | Data | Trailer |
|----------|---------------------------|---------|-------------------|----------|
| 10101010 | 8 bits | 8 bits | $N \times 8$ bits | 01010101 |

Read request: PC -> Front-end

| Header | Number of bytes - 1 (N-1) | Address | Number of bytes - 1 (N-1) | Trailer |
|----------|---------------------------|---------|---------------------------|----------|
| 10101010 | 8 bits - LSB | 8 bits | 8 bits - MSB | 01010101 |

Read: Front-end -> PC

| Header | Number of bytes - 1 (N-1) | Address | Data | Trailer |
|----------|---------------------------|---------|-------------------|----------|
| 10101010 | 8 bits - LSB | 8 bits | $N \times 8$ bits | 01010101 |

LSB - Least significant bits

MSB - Most significant bits

Table 7.1: USB communication protocol. Based on [229].

The smallest transmission possible, comprised of 5 bytes, takes a total of 1 μ s, while the longest, a total of 65540 bytes, takes 13 ms. When data is transmitted, this time is considered dead time since the acquisitions are interrupted.

7.4.1.2 LVDS

LVDS communications are performed between the front-end's FPGA and the Central Unit's FPGA using two UTP cables: one in each direction. The four lines of each cable are used for data, clock, enable, and trigger. In what the communication is concerned, only data, clock, and enable are relevant. Enable is idle at high and goes to low in case of transmission. The data line follows a custom protocol that was designed to be compatible with the firmware code already written for USB. The clock speed chosen was 40 MHz that is half the speed of the most used clock inside the front-end. However, this value can vary as long as it respects the FPGA's speed grade.

As mentioned before, the Central Unit's FPGA includes a processor (HPS), where a Linux operating system is installed. Since these two parts of the device share memory, the data to be sent out and read by the FPGA can be accessed by the software directly. Thus the drivers, needed for USB communication, are replaced by memory access functions.

The LVDS communication protocol is presented in table 7.2. Unlike the USB, where eight lines are used for data (parallel transmission), to communicate with the Central Unit only one line is used (serial transmission). Nevertheless, the same information is sent out or received: the address, the number of bytes to be sent or requested, and the data itself. Additionally, a checksum was added that is verified after each communication. Its value is equal to the number of '1s' part of the transmission, using 16 bits. The receiving device will verify it and compare the result with the checksum bits. In case of a mismatch, an internal counter register of the front-end's FPGA is increased. This register can be accessed by the master from time to time, to check if the communication is performed correctly.

Write, in the direction Centra Unit -> front-end, and read, in the opposite direction, share the same sequence. The first eight bits are the address, where the MSB is '0' if

Write: Central Unit -> Front-end

| Address | Number of bytes - 1 (N-1) | Data | Checksum |
|---------|---------------------------|-------------------|----------|
| 8 bits | 16 bits | $N \times 8$ bits | 16 bits |

Read request: Central Unit -> Front-end

| Address | Number of bytes - 1 (N-1) |
|---------|---------------------------|
| 8 bits | 16 bits |

Read: Front-end -> Central Unit

| Address | Number of bytes - 1 (N-1) | Data | Checksum |
|---------|---------------------------|-------------------|----------|
| 8 bits | 16 bits | $N \times 8$ bits | 16 bits |

Table 7.2: LVDS communication protocol.

writing and '1' if reading. The next 16 bits are the number of bytes to be sent ('number of bytes - 1'). This way, although the communication is serial, the number of bits sent is always a multiple of eight. After, the data bits are sent, followed by the last 16 bits of the transmission, the checksum. The maximum number of bytes allowed per communications is 65536. The smallest communication possible, where only a byte of data is sent, would correspond to a total of six bytes, which with the standard 40 MHz clock, takes 1200 ns. The longest, a total of 65541 bytes, would take more than 13 ms considering the same clock.

The read request, in the direction Central Unit -> front-end, is always three bytes. The first corresponds to the address, with the most significant bit always '1'. The other two are the number of bytes to be requested. Lastly, one should note that since an enable line is part of the transmission, there is no need to use a header nor a trailer byte, like in the USB.

An example of a read transmission is shown in figure 7.6 using the SignalTap connected to a front-end. In the lines, LVDS_in are the three read request bytes, while in the LVDS_out is the front-end's response. In both directions, line '0' is the trigger, not used for communication, '1' the enable, '2' the data, and '3' the clock. The request was one byte, $N - 1 = 0$, making the 16 bits word '0000000000000000', from address 129 '10000001'. The response was the byte '01111111', making the total number of ones nine, and the checksum bits '0000000000001001'.

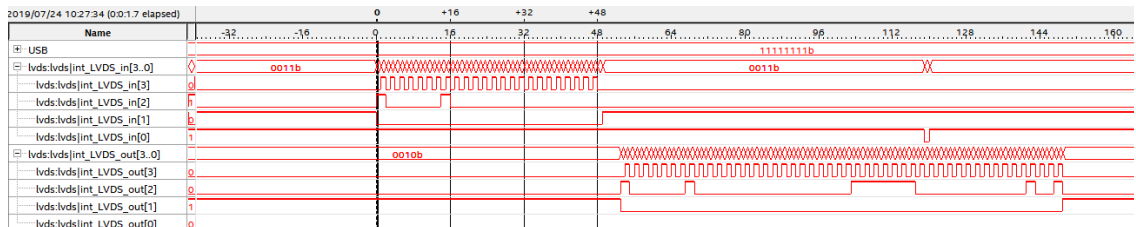


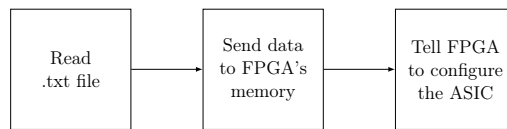
Figure 7.6: Example of an LVDS transmission seen using SignalTap. A request is received in the lines LVDS_in and a response sent in LVDS_out. In both directions, line '0' is the trigger, not used for communication, '1' the enable, '2' the data, and '3' the clock.

7.4.2 Module 2: ASIC configuration

A block diagram of this module's firmware and software is shown in figure 7.7. The first step is for software to send the 829 configuration bits to the FPGA. The configuration is set in a .txt file, where each line corresponds to a different parameter (see appendix A's table). Having the configuration in an external file, not only simplifies the process of changing any parameters but also allows having multiple files prepared with different settings. The .txt file is read by the software that converts the 363 lines to a binary word. That word is then sent to the FPGA via USB or LVDS, where it is stored into a memory.

The configuration is sent to the ASIC using three slow control lines: D_SC, RST_SC, and CLK_SC. These correspond, respectively, to a data, reset, and clock line. Their sequence are described in [103, 104]. Thus, after the parameters are stored in the FPGA memory, the next step is to transform them into the three slow control lines. Namely, whenever the software tells the FPGA to program the ASIC, a submodule is started, which will read the stored data and convert it into the three lines.

Software



Firmware

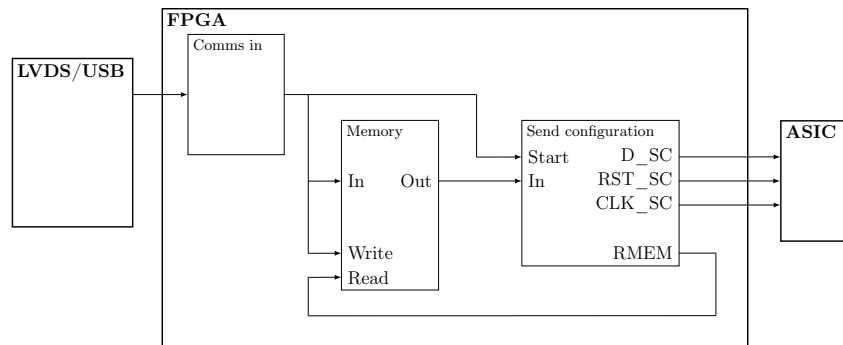


Figure 7.7: Block diagram of the software and firmware module to program the ASIC's configuration.

The configuration should be sent out before every acquisition for two reasons. The first is that when the ASIC is turned on, it does not recover its old state: all parameters are set to 0, which is a not working configuration. To solve this, a default word could be added to the FPGA memory and programmed as soon as the board is booted without any software interaction. Although not implemented, it would allow getting the MAROC in working condition as soon as the board is turned on. However, this solution would not guarantee that the right configuration is set, as to change the default boot configuration, the FPGA needed to be reprogrammed, which is not practical. And that is the second reason why the MAROC should be reprogrammed before an acquisition. By sending the slow control every

time, it is ensured that the right configuration is set, and that way, the acquisition will run as expected.

A similar module is used to configure the fast shaper as slow shaper multiplexed outputs, with the lines `D_R`, `RST_R`, and `CLK_R` (see [103, 104]). In MARTA's front-end, these outputs are only used for debugging purposes, e.g., to acquire the signals shown in figure 7.3 with an oscilloscope.

7.4.3 Module 3: Hit measurement

The hit measurement is based on storing the state of the ASIC's 64 discriminated outputs before a trigger. For that, a FIFO memory was implemented in the FPGA, where the output states are recorded every 12.5 ns. The memory's depth is 128 words corresponding to a time windows of 1.6 μ s. Thus, this value is the maximum time difference allowed between the RPC signals, after being digitized, and the acquisition trigger. It also assumes that the discriminated outputs are faster than the trigger. This is true in all the applications where this system was implemented. A block diagram of the hit measurement module, for both software and firmware, is shown in figure 7.8.

Whenever the acquisition is started, the software tells the FPGA to begin filling the memory. The FIFO gets quickly filled at which point it starts dumping the oldest state to clear space for the newest one. Thus, the 128 words of 64 bits are at every moment the latest states of the discriminated lines. Once the acquisition trigger is detected, the memory is stopped. While in MARTA's stations, the trigger is provided by the WCD's electronics via the Central Unit, other signals can be configured to perform this role. This range from external triggers that are input via the LEMO/SMA connectors, to signals generated inside the FPGA like an OR of the 64 outputs.

In a typical event, where only a channel has signal⁶, three to six of the 8192 bits are '1'. Thus, instead of sending the raw data directly to the acquisition machine, a zero suppression submodule was implemented. It will read the data stored and convert all the '1' into its position in the FIFO. This module is started as soon as the acquisition trigger stops the memory.

After the zero suppression, each '1' will corresponds to two bytes, the first with the channel information and the second with the time information. The time corresponds to the position inside the FIFO memory, with 0 the furthest from the trigger, and 127 the closest. Thus, an event with four '1' will send eight bytes instead of the 1024 bytes the raw data has. This will reduce the dead time of the data transfer (200 ns per byte in case of LVDS), as long as the number of '1' is lower than 512, which corresponds to eight '1' in each of the 64 channels.

Meanwhile, the software starts looping a three-stage state machine. The first step is asking the firmware if the data is ready to be sent by requesting two bytes from an FPGA register. The data is considered ready after the zero suppression analysis is concluded, at

⁶Measurements performed with the acquisition in self-trigger mode have shown that in 90% of the events only one pad has signal.

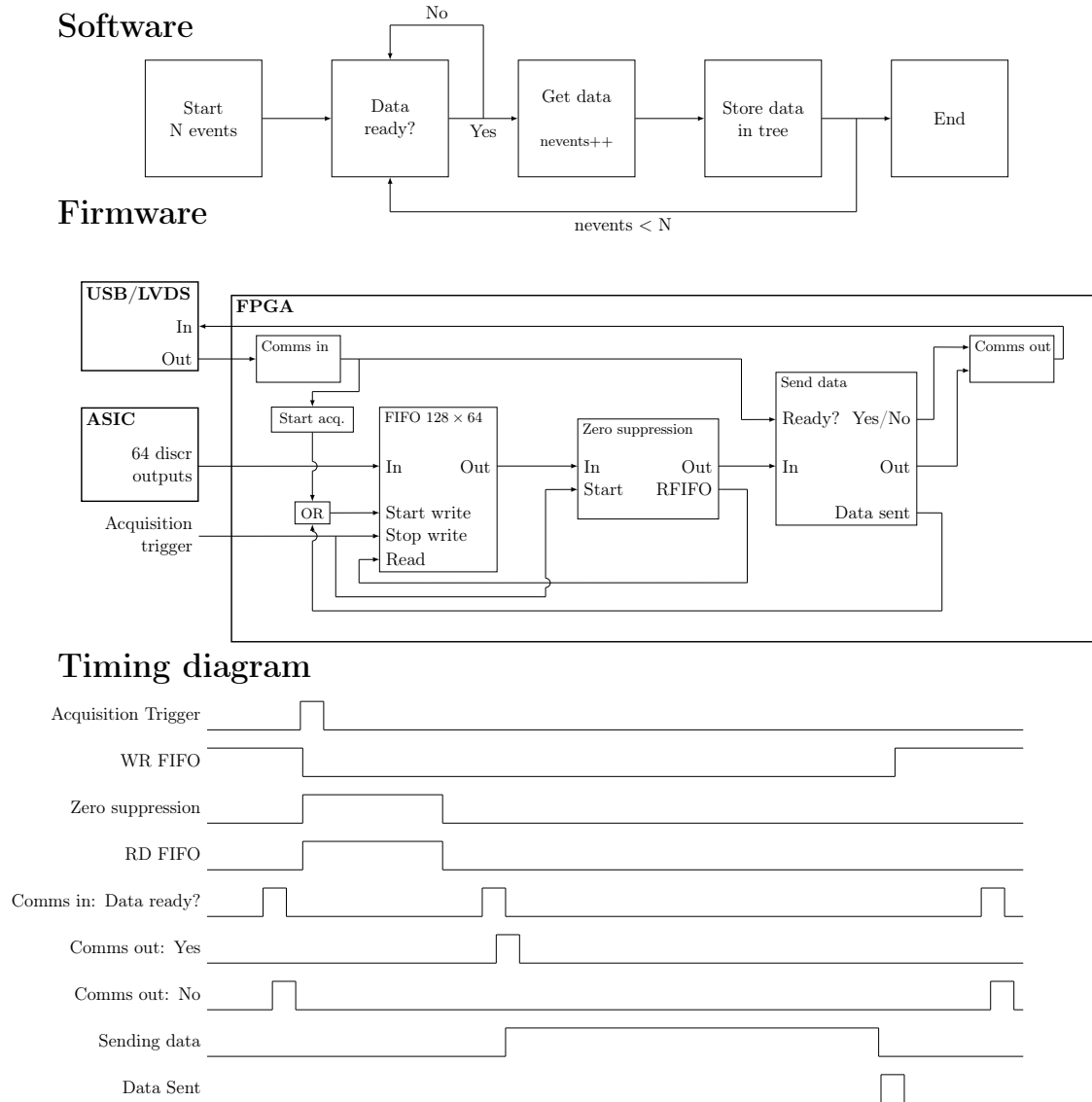


Figure 7.8: Block diagram of the software and firmware module that controls the hit measurement. A timing diagram is also shown (not to scale).

which point the FPGA will respond with the number of '1s' the event has. If asked during any other time, the answer will be 'no', and the 16 bits will be set to the decimal value 65535, which is higher than the maximum number of '1s' allowed. The software will receive the answer and either proceed to the second step in case of 'yes' or repeat the question in case of 'no'. In the second stage, the computer will request the data from the FPGA. Finally, in the last stage, it will store it in a ROOT tree.

The ROOT tree, where data is stored, was designed using the following configuration: time \rightarrow channel \rightarrow RPC \rightarrow station \rightarrow event. An event has at least one station, an identifier, to match data with other detectors in the system, e.g., WCD, and a timestamp given by the acquisition machine. Each station can then have multiple RPCs, each RPC has 64 channels, and each channel can have up to 128 times.

The state machine will loop enough times until it gets to the number of events request by the user. In case of a setup with multiple detectors, like the four RPCs in a MARTA station, all the front-ends are acquired one after the other, before moving into the next event. The measurement's dead time is largely due to the time taken by the data transfer, which can vary, as mentioned above. However, even in the worst-case scenario (every bit '1'), where the data transfer would take more than 3 ms is faster than 100 Hz T1 rate.

The sequence of actions inside the FPGA for an event is summarized in the timing diagram of figure 7.8. The FIFO stops being written as soon as the FPGA detects the acquisition trigger. At that point, the memory starts being read and the zero suppression submodule processing the data. The software is continuously asking if data is ready, and the answer is only yes after the zero suppression module is done. Then, data is requested by the acquisition machine and sent. As soon as it is sent, the FIFO starts getting filled again, waiting for the next trigger. One should note that every trigger detected whenever the memory is not being written, i.e., when data is being either processed or sent, is ignored.

7.4.4 Module 4: Charge measurement

The charge measurement module manages the acquisition, sending the necessary signals to the ASIC, and storing the ADC output before transferring it to the acquisition machine. Although the main branch in this measurement is the slow shaper, the fast shaper also plays an important role. Namely, in setting up both hold signals, one for the baseline (Hold2) and the other for the slow shaper peak⁷ (Hold1). The holds are controlled by the OR of the 64 discriminated outputs that is generated inside the FPGA. They are idle if high and send to low to activate the sample and hold circuitry. The sample and hold output is unchanged as long as the hold signal is kept at low. While Hold2 is triggered as soon as the discriminated signal goes to high, Hold1 is sent to low later. The time between the discriminated output and Hold1 is essentially the rise time of the slow shaper. This variable is known as hold delay and is set by the user before starting a new run of events. It is configured by sending an eight bits word to a register. Hold1 will be set to

⁷Proportional to the charge.

low after a counter (with a 240 MHz clock) reaches the value written in that register. This makes the maximum hold delay about $1 \mu\text{s}$ and its resolution 4.167 ns. A diagram with the relevant signals used to set up Hold1 is presented in figure 7.9. It is also shown how the slow shaper output looks like after the sample and hold. The optimal hold delay was studied for different ASIC configurations inputting a signal with a generator followed by a capacitor, and then using with real RPC signals. The results are presented in chapter 8.

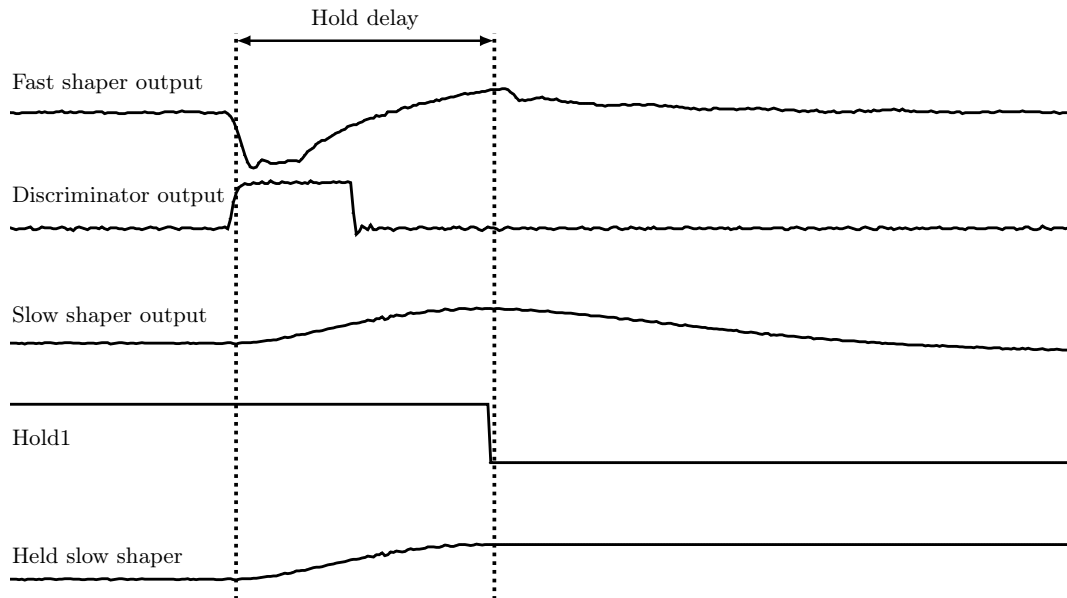


Figure 7.9: Hold1 setup with all relevant signals. The discriminator output starts a counter that will send Hold1 to low when the hold delay value is reached. The sample and hold will keep the peak held so that the ADC can read its value.

The ASIC's ADC is controlled by three lines: reset, start and clock. These are fully described in [103, 104]: after the peak is held, the ADC can be reset and then started. Once the ADC is on the conversion will begin, and the ramp rises until it reaches the held value. At that point, the ADC starts transmitting data using two lines: transmission on, and data. The first is high when data is being sent and the second has the 768 serial bits. The clock is input into the ASIC using a differential line, and its value is 40 MHz. These five lines are connected to the front-end's FPGA and are controlled by an ADC's interface submodule.

A block diagram of the charge module, for both software and firmware, is presented in 7.10. The software starts by setting up the hold delay and starting the measurement. Next, the firmware will wait for the OR of the discriminated outputs to hold the peak and baseline of the shaper signal. Two measurement types are programmed into the FPGA: self-trigger and using a validation trigger. In self-trigger mode, after Hold1 is set to low the ADC is started, while in validation mode, a time window is open after the discriminated output's OR. If in that time, an external signal is detected, the ADC will be reset and started. If not, the holds will be set back to high and the process is restarted. This validation trigger, like the acquisition trigger in the hit measurement, can be set to different signals.

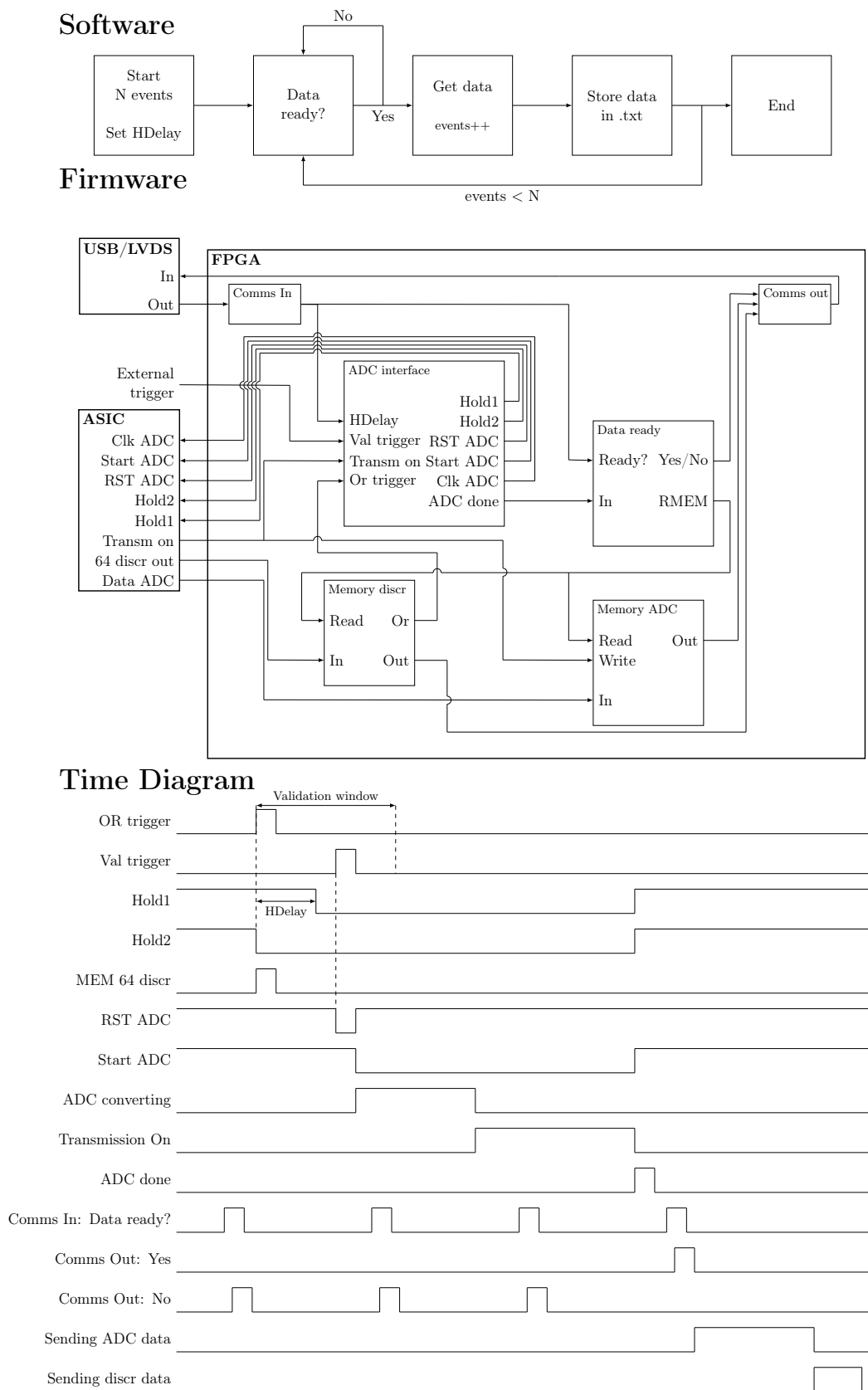


Figure 7.10: Block diagram of the software and firmware module that controls the charge measurement. A timing diagram is also shown (not to scale).

In this measurement, two memories are used. The first will receive the ADC lines, storing its data before sending it out. The second will save the state of the 64 discriminated outputs used to hold the slow shaper baseline and peak. Thus, it is possible to know which channels triggered the measurement, allowing to expand the analysis of this data.

Meanwhile, the software is asking the FPGA if the event data is ready. Once the ADC is done, and everything is stored in the memories, the data is ready to be read. The acquisition machine, will first read the ADC data and then the discriminator data, before storing it in a .txt file. Each event corresponds to a line with 832 bits where the first 12 are the ADC data of channel 0 (in Gray binary), the second 12 correspond to channel 1, and so on. The last 64 bits are the discriminator data, where the first bit is the state of channel 0, and the last the state of channel 63. Like in the case of the hit measurement, this procedure will be looped until the number of events asked by the user is reached. Most of the dead time is due to the ADC conversion time that can take up to 100 μ s, while the data transfer will take around 21 μ s.

The sequence of actions inside the FPGA for an event is summarized in the timing diagram of figure 7.10. As the OR of the discriminated outputs is detected, the ADC interface submodule sends Hold2 to low immediately, and Hold1 after the counter reaches the hold delay value. Simultaneously, the memory for the discriminator outputs stores its current state. Since the validation trigger was detected in its time window, the ADC is reset and then started. Conversion goes on, and when it is done, the data is transmitted to the FPGA. The software has been asking if data is ready, and after it is successfully stored in the memory, the answer is yes. Then, it first requests the ADC data and after the discriminator data. Once again, while the measurement is being processed, all incoming triggers are ignored.

7.4.5 Other modules

Smaller modules were also added to the firmware and software of the front-end. These can either be complementary to the main four modules: PLL and trigger modules, perform secondary measurements: rate module, or be used to test specific parts of the system.

The PLL module converts the 100 MHz clock generated in the oscillator crystal to the values required by the different elements of the firmware. The PLL Megafunctions part of Quartus was used to perform this task [230]. The output includes the 40 MHz used in the ASIC's ADC, the 80 MHz for the hit measurement's FIFO, and the 240 MHz needed to generate the hold delay.

The trigger module is used to manage the signals, that will be routed to the acquisition trigger of the hit measurement, and the validation trigger of the charge measurement. As already mentioned above, an eight bits register is set via USB or LVDS to choose one of the pre-programmed triggers. These include the WCD trigger (default), other LVDS triggers, the self-trigger, external triggers via LEMO/SMA connectors, e.g., when using a signal generator, and even triggers produced inside the FPGA. An example of the latter case is the logical combination of the discriminated outputs, e.g., AND or OR of particular channels.

Furthermore, in setups, where two front-end are connected to detectors in coincidence, one of them was tasked to create the trigger (see section 9.2.1). It received the OR output of the other board, and whenever a coincidence is detected, it sends out an acquisition trigger. For setups with more than two detectors in coincidence, not enough lines are available to and from the FPGA, meaning a dedicated trigger board is required, e.g., the Central Unit.

In the MARTA station, event identifiers are not a concern for the front-end, since these are managed by the Central Unit. However, for setups where the Central Unit is not used, the firmware is programmed to send a 24 bits id after every event. This word can either be generated inside the FPGA or be received after the trigger from an external source.

A rate measurement module was also added. It can either measure the rate of every single channel or one of the programmed triggers. When requested by the software, it will count the number of times a signal is detected in a fixed time interval. The data is then sent back to the computer where it is stored.

Lastly, two tests modules were added: one to test the LVDS links and the other to use the external ADC. A cable was connected to the LVDS input and output, to test the links. Pulses would be sent out and counted on the other side of the cable, allowing to measure the number of signals lost in the cable (see section 8.3). For the external ADC, the firmware was successfully developed to manage the acquisition, as well as, store and send out its data to the acquisition computer.

8 Performance and test results of the front-end

The studies of the front-end's performance were focused on the two first requirements mentioned in section 7.1: being able to read the fast RPC signals using the hit and charge measurement. While most of the other requirements, e.g., compact and low power, having trigger and communication lines, etc., were solved with design decisions, the response of the system, mainly of the ASIC, to the RPC signals needed to be carefully investigated and understood. However, the processes that occur during the avalanche's propagation in the gas gap, described in 5.1, make the distribution of signals induced in the readout plane not trivial and hard to control when testing and debugging a new system. For that reason, in the earlier stage of this work, laboratory test benches were fundamental in the development of the front-end, as well as, in the understanding of its behaviour. Namely, a signal generator was used to send pulses into the MAROC, either through a capacitor or connecting it to the ASIC's Ctest, allowing to have an input with a known charge and constant frequency. Like in the tests described in chapter 6, the signal generator was a Tektronix AFG3252 [210], and the pulse's charge computed as $Q = C\Delta V$, with C the capacitor's capacitance and ΔV the amplitude of the generated negative square wave. After ensuring that the measurements were working as expected with generated pulses, real RPC signals were tested. While in some cases, the results were compared with the ones obtained using a different acquisition system, in others, the observations were analyzed and tested with models proposed in the literature. The tests carried out to assess the measurements' performance were the following:

- **RPC efficiency:** A hodoscope of RPCs was used to measure the efficiency of a MARTA RPC. The latter was placed in the middle of the hodoscope, and some of its outputs were instrumented with the front-end and a second reference RPC data acquisition system (HADES FEE). A trigger given by the hodoscope would prompt the simultaneous measurement of different channels with the two systems, making it possible to measure the efficiency of the MARTA RPC.
- **Trigger efficiency:** Several charge values were input in one of the ASIC's channel, and the trigger efficiency was measured in different temperature conditions. Thus, it was possible to determine if the temperature changes expected in the field will affect

the hit measurement.

- **Charge measurement with generated pulses:** The charge measurement in self-trigger mode was first tested with pulses from the signal generator, using a representative channel. The slow shaper output curve was obtained measuring the ADC output with different hold delay values. Multiple configurations of the variable capacitors in the slow shaper circuitry were tested, and the optimal one chosen. Using that configuration, the hold delay correspondent to the peak was determined. Finally, two calibration curves were obtained: one for the full ASIC range, and another for the range where most of the RPC events are expected to be.
- **Charge measurement with RPC signals:** Using the capacitor configuration determined above, the optimal hold delay was again obtained, this time with RPC signals. The influence of the threshold on the charge measurement was studied. Furthermore, a coincidence trigger of two scintillators (muon trigger), one above and the other below the pad being measured, was used to test the validation trigger mode and compare the charge spectrums when using self-trigger and muon trigger. Lastly, the same validation trigger was used to measure the charge distribution for six different E/N. The results were compared with some of the models mentioned in section 5.1.

The differential lines used for communication with the Central Unit were also tested. Namely, pulses were sent out through the LVDS output and then reinjected in the input. Two counters were used to determine the number of pulses that would leave the FPGA and the ones that would come back. The results were compared, using two clock speeds and two cable lengths.

In this chapter, first, the studies related to the hit measurement are presented, and then the ones to do with the charge measurement are shown. After, tests performed to other parts of the system are discussed, and lastly, a summary of the front-end performance is given. The work presented in this chapter related to the hit measurement and charge measurement using the signal generator has been published in [102]. The measurement of the MARTA RPCs' charge is being prepared for publication [231].

8.1 Hit measurement

8.1.1 RPC efficiency

The first validation test performed after the development of the hit measurement was to determine the RPC efficiency. A representation of the setup used is presented in figure 8.1: a test RPC was placed between a hodoscope. Each of the hodoscope planes is composed of two RPC detectors on top of each other, with an area of $2 \times 0.5 \text{ m}^2$, and 60 readout strips. By measuring the deposited charge and time information, on both sides of the strip, it is possible to determine the position (with a resolution of 1 cm) where the particle crossed.

From the position information in the planes, one can obtain the particle's trajectory. The hodoscope is triggered when simultaneous signals appear in the top and bottom planes. A full description of the hodoscope's RPCs is presented in [232, 233].

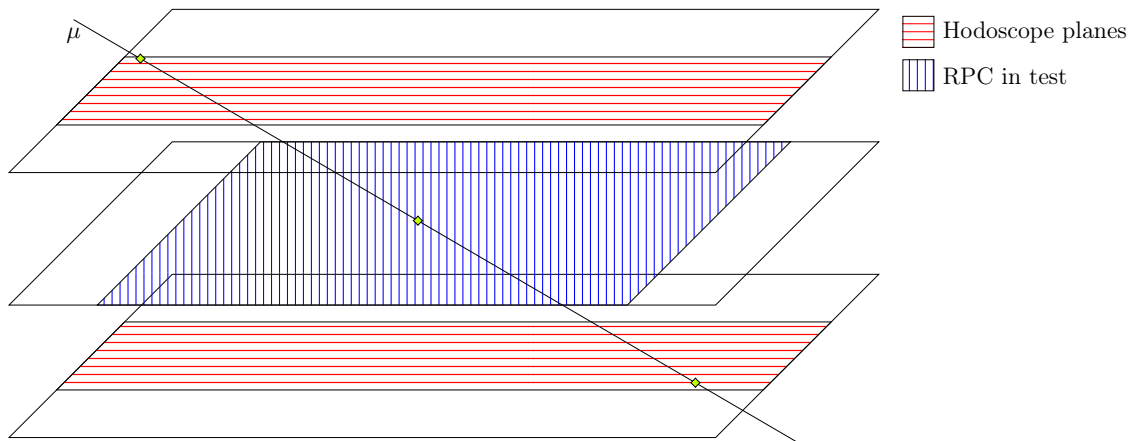


Figure 8.1: Representation of setup used to measure the efficiency: a test RPC was placed in a hodoscope that allowed to track the crossing particles' trajectory.

The test RPC where the front-end was connected was an early version of a MARTA RPC. This meant that the detector used was not fully optimized, and its efficiency was not maximized. For that reason, it was decided not to compare the result obtained with the expected efficiency. Rather, an established RPC DAQ system was connected to some of the outputs and their efficiency measured with it. Thus, the front-end performance was evaluated by comparing the results obtained with the ones measured using the HADES FEE, described in [189] and mentioned in section 5.3. This comparison is possible because the efficiency measured is a product of the detector's efficiency and the DAQ's efficiency. Measuring it with both systems at the same time ensures that detector efficiency is the same during this study.

The coincidence of the hodoscope's planes was used as the acquisition trigger in the front-end's hit measurement. A 24 bits event identifier was sent along with the trigger, allowing to match the events measured with the different systems. For this measurement, the MAROC was programmed with the default MARTA configuration shown in appendix A. While the test RPC's top half was fully instrumented with the front-end, the bottom half was instrumented in a chessboard configuration with both DAQs. That can be seen in the left plot of figure 8.2. In it, each point corresponds to the position a particle crossed the test RPC plane, and the colour shows which system measured the event¹. Over the data are overlapped the hodoscope and test RPC's positions, as well as the latter's pad positions. Due to the setup's geometry, only 16 of the instrumented pads, 12 with the front-end and four with HADES FEE, were in the field of view of the hodoscope. This corresponded to two rows, represented in the right diagram of figure 8.2. In this diagram, the number of the pads and to which of the acquisition system each pad was connected is shown.

¹Using only single pad events.

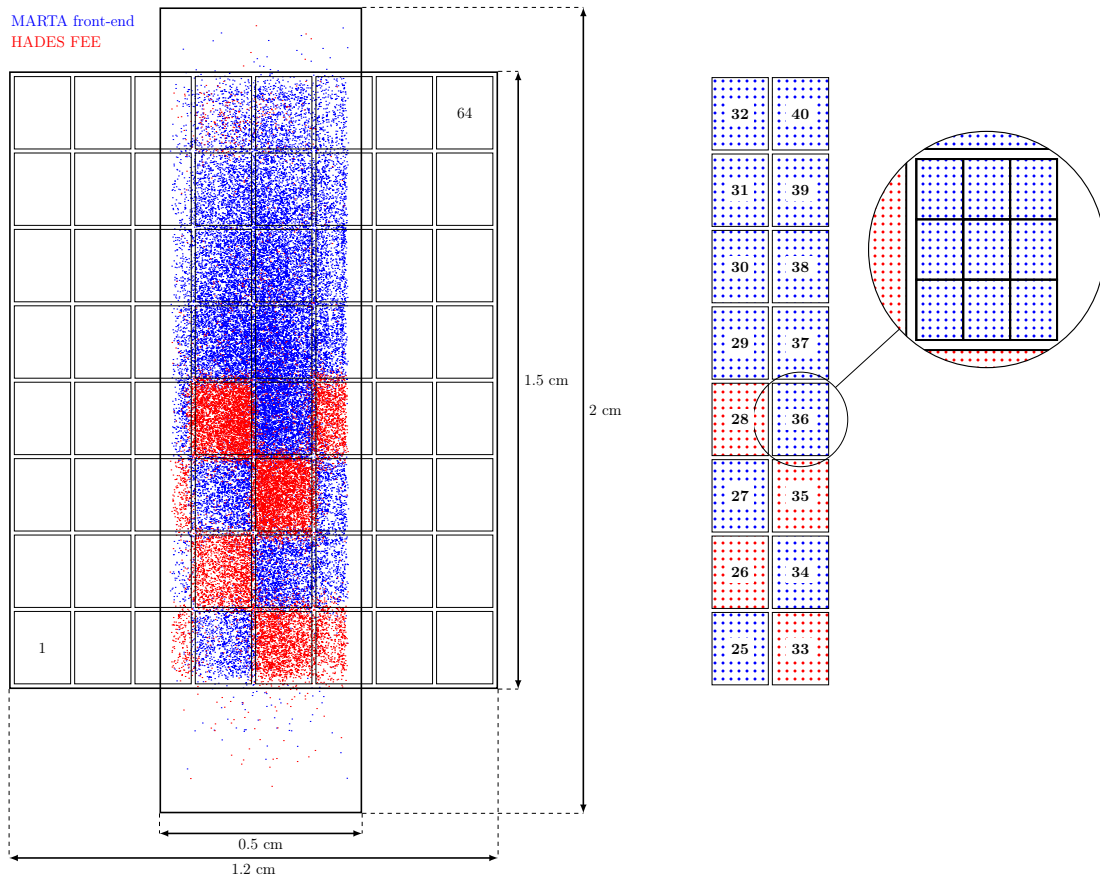


Figure 8.2: Left: Measurement data: position the particles crossed the test RPC versus which of the acquisitions systems registered the event. The readout pads position and the hodoscope dimensions are drawn over the data (red for the HADES FEE and blue for the MARTA front-end). For reference, pads 1 and 64 are identified. Right: The 16 pads used for the efficiency measurement. The distribution of pads per DAQ is given. A zoom of one of them is presented, showing the division in nine equal parts. The efficiency was determined using events that crossed the central division of the pad.

In the efficiency calculations, each pad was divided into nine equal parts (as shown in the right diagram of figure 8.2), and only the events that crossed the central region were taken into account. Furthermore, events where more than one channel was triggered were not considered. The efficiency was defined as the number of events detected in the test RPC divided by the number of events foreseen by the hodoscope. The plot in figure 8.3 shows the measurement results: for each pad number, the efficiency is represented. The error bars were calculated as in [234], with the number of events being dominant. Furthermore, the setup's geometry created an inequality in the number of events per pad, with a higher number of particles crossing the middle ones.

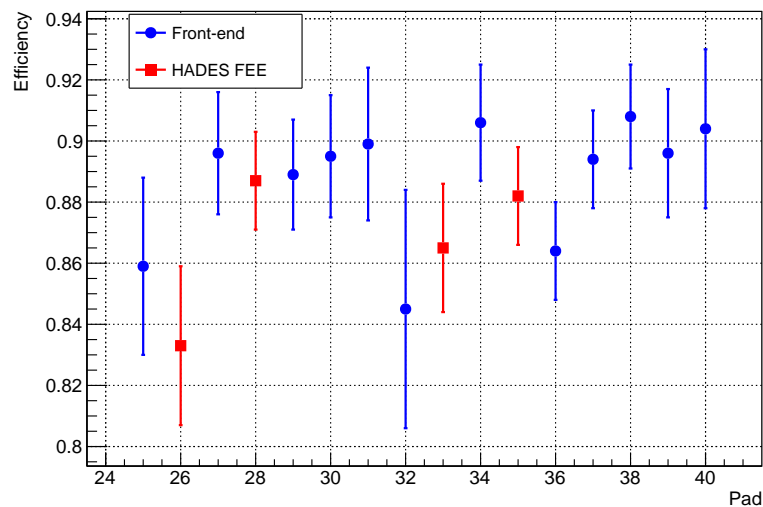


Figure 8.3: Measured efficiency versus pad number. The pad distributuinn can be found in figure 8.2.

The average efficiency measured by the front-end and by the HADES FEE were compared. To minimize the geometrical inefficiencies, the average of the front-end was computed only using pads 25, 27, 34 and 36. The results for the pads instrumented with MARTA's readout have an average efficiency of 0.881 ± 0.011 , while the ones measured with HADES FEE yield an average of 0.867 ± 0.010 . The number of standard deviations between the two averages is approximately 1. This result shows that the efficiencies are compatible, with the average efficiency values higher for the front-end.

The test presented validates the MARTA front-end as a good acquisition system for RPC detector. It shows that this DAQ is able to read the signals without introducing any unwanted inefficiencies. The results of this test were a critical first step in showing that the design decisions were correct, namely that the components chosen would fit the job.

8.1.2 Trigger efficiency

The trigger efficiency was studied to test how the hit measurement behaves in different temperature conditions. Namely, the ratio between the number of signals detected by the

front-end and the signals input was estimated using different temperatures. Pulses with small charges were generated in the Tektronix AFG3252 and sent to the front-end so that an s-curve could be obtained. The s-curve was measured in the charge region where the efficiency transitions from 0 to 1.

A representative channel was tested for seven temperatures in the range of $-22\text{ }^{\circ}\text{C}$ to $25\text{ }^{\circ}\text{C}$. Low temperatures were achieved using a freezer and measured with the I²C sensor installed in the front-end. Once again the MAROC ASIC was programmed with the default MARTA configuration (see appendix A), and the threshold set at 210. The charge range from 35 to 60 fC was swept obtaining a clear curve for each of the temperatures. The results are presented in figure 8.4. While in the left plot are shown the full s-curves for the seven temperatures, in the right one a zoom of the data points near the maximum efficiency is given (in the range of 47.5 to 50.5 fC).

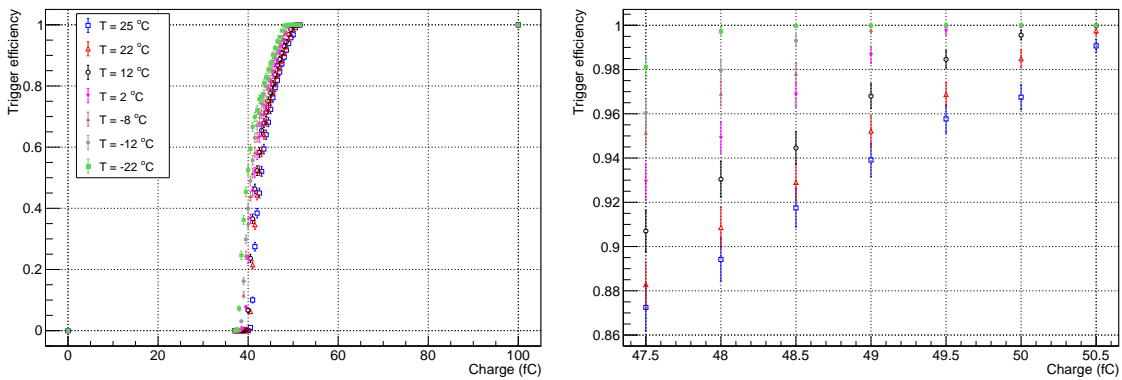


Figure 8.4: Trigger efficiency of the hit measurement versus the input charge for seven different temperatures. The charge was swept in the region where the efficiency transitions from 0 to 1. In the right plot is presented a zoom-in of the data points near the maximum efficiency.

The results show that for charges higher than 37 fC the trigger efficiency is no longer null while for values greater than 52 fC the threshold used is 100% efficient. The s-curves for the different temperatures have similar shapes, and as the temperature increases, the curves move to higher charges. However, the difference between the lowest and highest temperatures is never bigger than 3 fC. This way, it is possible to conclude that the temperature variations in the field² will not affect the stability of the system. Furthermore, one can also state that the minimum detectable charge is one order of magnitude lower than the average value given by an RPC avalanche signal (see figure 8.5 in section 8.2 for reference). Although it was already previously shown that the front-end did not introduce any unwanted inefficiencies in the detection of particles, these results reinforced that statement.

²Considering the concrete structure thermal protection, the expected temperature swing during the year is $30\text{ }^{\circ}\text{C}$, while during the day is $1\text{ }^{\circ}\text{C}$ (see figure 5.14).

8.2 Charge measurement

The charge measurement was studied in two stages. In the first, generated pulses with known charge were input into the front-end, allowing to tune the system. In the second, real RPC signals were acquired, to understand if the measurement yields the expected results. Throughout the tests presented in this section, the same representative channel of the ASIC was used.

Before any signals were injected in the front-end, a reference charge distribution of a MARTA RPC was obtained. RPC signals, like the ones shown in figure 5.11, were acquired with the Rhode & Schwarz RTO 1014 oscilloscope [200]. Since the charge is the currents integral in a time interval, for each waveform the charge was computed as:

$$\sum_n \frac{V_n}{50 \Omega} \Delta t \quad (8.1)$$

where n are the points of the oscilloscope signal that are not baseline. V_n its amplitude, and Δt the oscilloscope horizontal resolution, i.e., time. The voltage was converted into current using Ohm's law: V_n was divided by the 50Ω input resistance of the oscilloscope. The results are presented in figure 8.5.

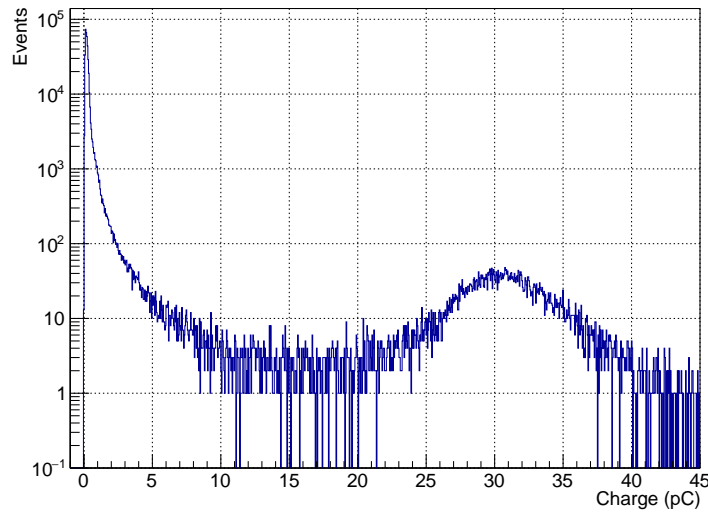


Figure 8.5: MARTA RPC charge distribution acquired with a Rhode & Schwarz RTO 1014 oscilloscope.

The measured signals present an average charge of 0.86 pC, and 95% of the events have a value lower than 1 pC. The spectrum has two distinguished regions: avalanche signals from 0 to 5 pC and streamer signals from 25 to 35 pC. The percentage of streamers in this distribution is about 1.6%, which is in accordance with the results shown in the top right plot of figure 5.13. Since the stated charge range of the ASIC is 0 to 15 pC [103, 104], the first conclusion that can be taken from this spectrum is that the ASIC will not be sensible

to the charge given by the streamer signals.

Although this distribution can give a good indication of the MARTA RPC's charge spectrum, the oscilloscope configuration used made it so smaller charges were not measured. This is because a compromise had to be made in the vertical scale of the measurement window so that higher voltage signal would not saturate, making the smaller ones undetectable by the trigger set.

Before going into the assessment of the charge measurement, it is necessary to mention its pedestal. Since all 64 channels are measured simultaneously, the baseline of the slow shaper will be acquired whenever some of these have no signal. This is the measurement's pedestal, which in the MAROC ASIC has the particularity of not being centred around the value of 0 ADC units, and varying from channel to channel and even from chip to chip. An example of such measurement is given in the plots of figure 8.6. The pedestal distribution is Gaussian, and for the case of the MAROC used, its mean varies between 150 and 180 ADC units. This variation is standard according to the ASIC's datasheet [103, 104]. In the example presented, channel 27 has only a few baseline events since this was the channel where signals were being input.

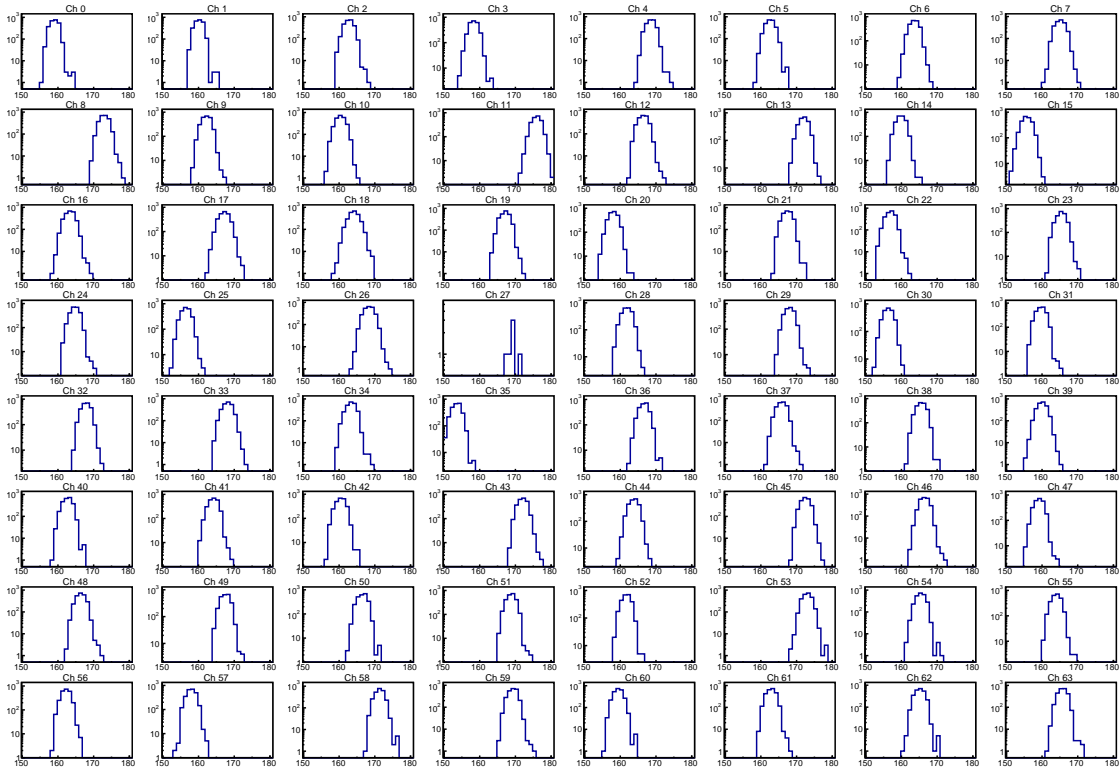


Figure 8.6: Charge measurement pedestal. In all plots, the x-axis corresponds to the ADC output (ADC units) and the y-axis to the number of events. Since signals were only being input into one channel of the ASIC, number 27, in all the others, the baseline of the slow shaper was measured.

In this section, the standard MARTA configuration of the ASIC, presented in appendix A, was used with some exceptions. While the gain and fast shaper bits were kept unchanged, the threshold and the slow shaper capacitors were changed to determine the

optimal configuration. One should also note that all the measurements presented were performed in self-trigger unless stated.

8.2.1 Using generated signals

To find the optimal slow shaper configuration and hold delay to measure the charge of generated signals, a series of acquisitions were performed. The hold delay was swept from zero to 60 using a constant charge. The results yield the slow shaper waveform. The curves for some of the configurations tested are presented in the left plot of figure 8.7. One should note that in the measurements presented, the clock that controlled the hold delay was set at 320 MHz. This clock was later found to create timing issues due to the size of the signal paths inside the FPGA, and so it was reduced to the 240 MHz mentioned in section 7.4. In these measurements, the threshold set to discriminate the fast shaper was 210.

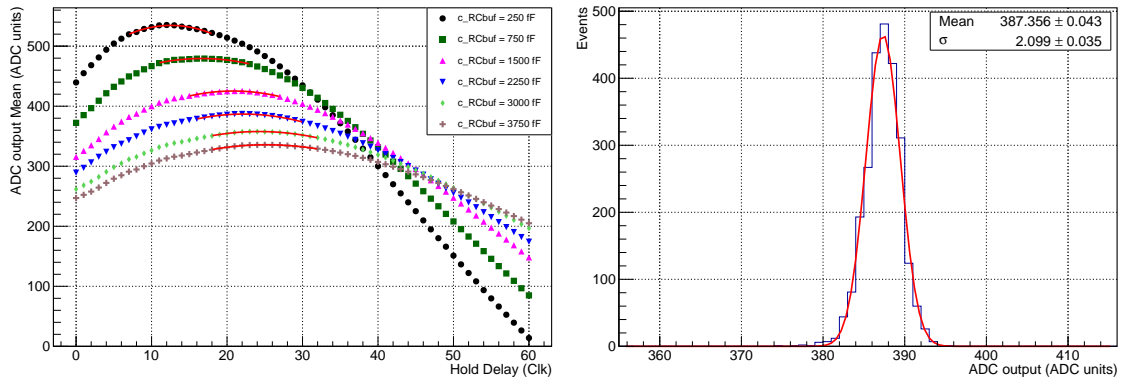


Figure 8.7: Left: ADC output versus hold delay for different slow shaper configurations: c_{fc} was kept constant at 2100 fF, and six c_{RCbuf} values were used. The slow shaper waveforms were obtained. For each, the peak was extracted by fitting a Gaussian to the point near the maximum. The data errors fall within the marker used for each data point. Right: Histogram for the point $c_{fc} = 2100$ fF, $c_{RCbuf} = 2250$ fF, and hold delay = 23, on the left plot. The mean of the Gaussian fit was taken as the measurement result.

The curves shown in the left plot of figure 8.7 were obtained with the slow shaper’s feedback capacitor (c_{fc}) at a constant value of 2100 fF, and using six different RC buffer capacitor (c_{RCbuf}) configurations: 250, 750, 1500, 2250, 3000 and 3750 fF.³ The input charge used was 0.5 pC. Smaller values of the c_{fc} were tested. However, in most cases the slow shaper peak would come before hold delay = 0. These results are consistent with the ones obtained in [217], where the slow shaper output was measured, and it was shown that the waveforms for lower c_{fc} have a shorter rise time.

For each of the waveforms’ points, a charge measurement of 2500 events was performed. The results were plotted into a histogram that presented the expected Gaussian distribution. For all histograms obtained, a Gaussian fit was performed, and the mean taken as

³The variable feedback capacitors correspond to the bits 178-180 of the ASIC configuration (0 to 2100 fF), while the RC buffer capacitors are set using bits 182-185 (0 to 3750 fF). For more details check appendix A and the ASIC’s datasheet [103, 104].

the measurement result. An example of such histogram is shown in the right plot of figure 8.7. The configuration used was $c_{fc} = 2100$ fF, $c_{RCbuf} = 2250$ fF, and hold delay = 23. The fit results yield mean = 387.36 ± 0.04 ADC units and $\sigma = 2.10 \pm 0.04$ ADC units.

To estimate the slow shaper's maximum for each configuration, a Gaussian was used to fit the points near the maximum region and its mean was taken as the hold delay that corresponds to the peak. The results for the configurations tested are presented in table 8.1.

| c_{RCbuf} (fF) | 250 | 750 | 1500 | 2250 | 3000 | 3750 |
|------------------|----------------|----------------|----------------|----------------|----------------|----------------|
| Maximum (clk) | 12.6 ± 0.2 | 16.7 ± 0.4 | 20.8 ± 0.3 | 22.2 ± 0.3 | 24.3 ± 0.4 | 25.2 ± 0.4 |

Table 8.1: Fit results of the slow shaper peak for the six curves shown in the left plot of figure 8.7.

In the following measurements of this section the blue configuration of figure 8.7 ($c_{fc} = 2100$ fF, $c_{RCbuf} = 2250$ fF) was used. Of the six capacitors combinations tests, this one is a good compromise, between the rise time, having the maximum well after hold delay = 0, and how defined its shape is. Namely, because for the two configurations with higher c_{RCbuf} the peak becomes flatter.

With the slow shaper configuration chosen, the same test was performed now using different input charges. The results are shown in the plot of figure 8.8, for six charge values: 0.25, 0.5, 0.75, 1, 2, and 4 pC. The same Gaussian fit as before was performed to the maximum region, allowing to extract the peak of each waveform. The mean of the Gaussians and correspondent ADC outputs are presented in table 8.2.

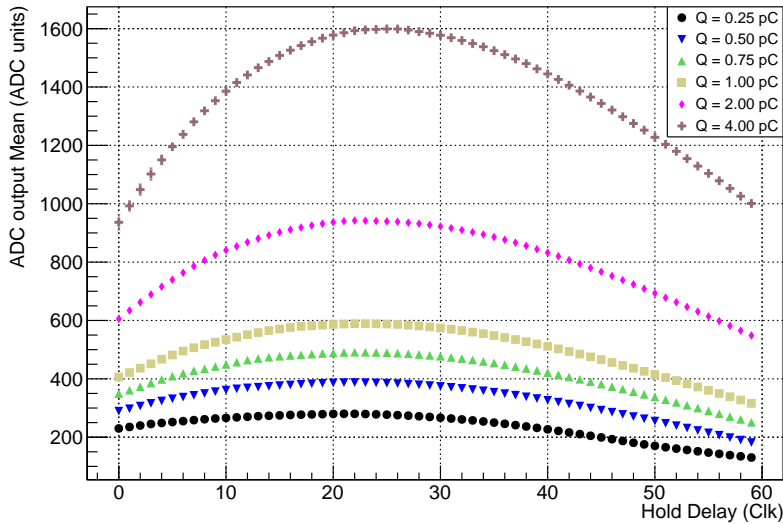


Figure 8.8: ADC output as a function of the hold delay for six input charges using $c_{fc} = 2100$ fF, $c_{RCbuf} = 2250$ fF. The data errors fall within the marker used for each data point.

As the charge goes to higher values, so does the hold delay that corresponds to the peak. However, these delays are all within ~ 2 clk of their average: 23 clk. Furthermore, if we get the ADC output for this average (see the last row of table 8.2), it is possible to conclude that the values are all close to the maximums obtained. The difference is never

| charge (pC) | 0.25 | 0.5 | 0.75 | 1 | 2 | 4 |
|------------------------------------|-----------------|-----------------|-----------------|-----------------|-----------------|------------------|
| max hold delay (clk) | 21.0 ± 0.3 | 22.2 ± 0.3 | 22.7 ± 0.4 | 22.8 ± 0.3 | 23.7 ± 0.4 | 25.2 ± 0.4 |
| max (ADC units) | 280.2 ± 2.1 | 387.4 ± 2.1 | 491.0 ± 2.1 | 589.0 ± 2.2 | 941.9 ± 2.2 | 1598.8 ± 2.3 |
| at hold delay = 23 clk (ADC units) | 279.4 ± 2.1 | 386.9 ± 2.1 | 491.0 ± 2.1 | 589.0 ± 2.2 | 941.9 ± 2.2 | 1598.8 ± 2.2 |

Table 8.2: Maximum of the curves shown in figure 8.8. For each charge, the ADC output at hold delay = 23 clk is also presented.

larger than 3 ADC units, which corresponds to a bias of about 1% in the worst case. This way, the value 23 clk was chosen as the optimal hold delay. Furthermore, the ADC outputs measured with this delay are taken as the charge measurement for generated signals. One should also note that tests performed to higher charge values showed that the peak would keep moving to bigger hold delays.

Lastly, 15 input charges were measured using the chosen configuration and hold delay, in the range of 0 to 20 pC. The results were plotted as a function of the input charge. These are presented in the left plot of figure 8.9, along with an interpolation of the points. The data has an approximately linear dependence until 4 pC. At that point, it stops being linear and starts to curve until about 12 pC. From 12 to 20 pC, the line is constant, meaning the measurement does not have sensibility in that region.

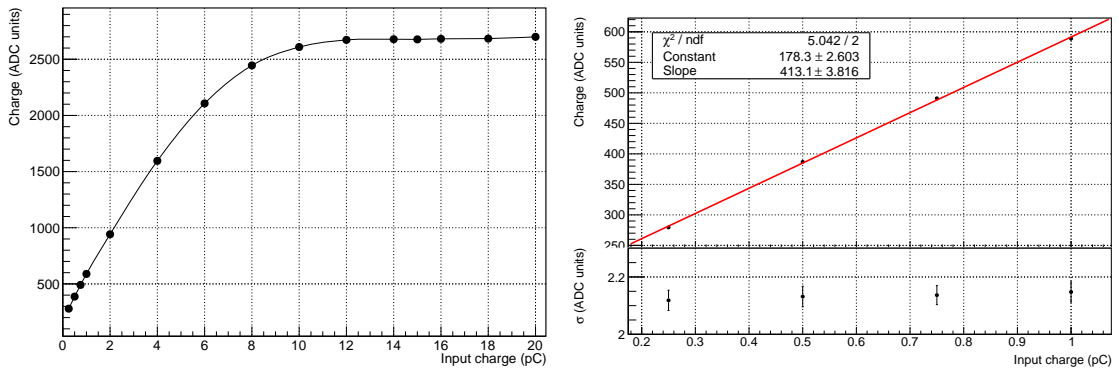


Figure 8.9: Measurement of known input charges with the optimized configuration and hold delay. The data errors fall within the marker used for each data point. Left: Results in the charge range of 0 to 20 pC. An interpolation was obtained for the data points. Right: Zoom-in and linear fit for the region from 0 to 1 pC. The standard deviation of the Gaussian fit for each of the data point is presented in the bottom.

The region with input charge up to 1 pC, 95% of the events in figure 8.5, has a clear linear dependence. This part of the curve was zoomed-in in the right plot of figure 8.9, and a linear function, $y = a + bx$, fitted to it. The fit yield $a = 178.4 \pm 2.6$ ADC units and $b = 413.2 \pm 3.8$ ADC units/pC. In the bottom are shown the standard deviations (σ) of the Gaussian fits for each of the points. The average σ is 2.13 ± 0.02 ADC units which corresponds to a charge of 5.16 ± 0.06 fC. These results are comparable with the values presented in the ASICs datasheet [103, 104].

The interpolation and linear dependency obtained can be used as a calibration for the particular channel and board tested. These allow converting the ADC outputs into real values in Coulombs. For the rest of the channels and boards, such calibration needs to be

performed individually. This can be shown by the results presented in figure 8.10. In this plot are shown measurements for different channels using the same input charge (0.5 pC). These values are once again compatible with the ASIC’s datasheet [103, 104], with the data distributed around a central value.

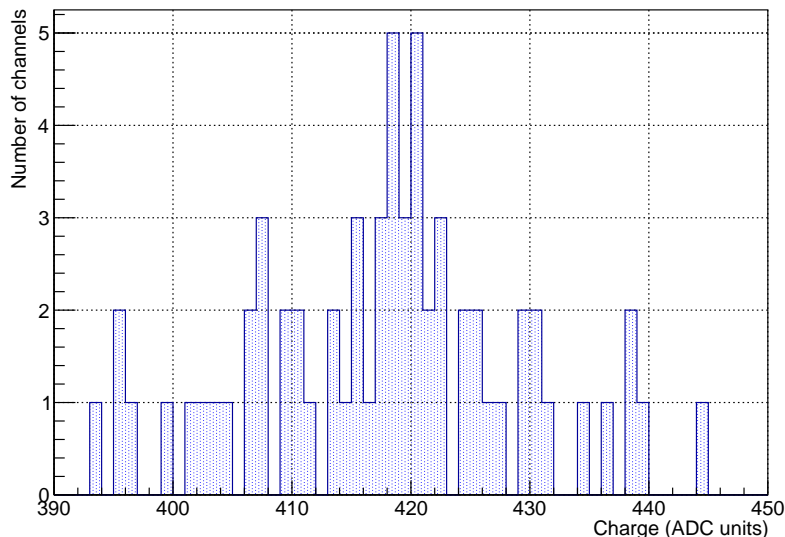


Figure 8.10: Charge measurement for different channels using the same input charge.

The results showed that with the parameters chosen, the system should be able to read the charge of the RPC avalanche signals. Furthermore, it also proves that the streamer signals are out of the range of the front-end, with the measurement saturating after 12 pC. Changes in the configuration might allow measuring the larger signals, namely, by reducing the gain of the pre-amplifier. However, this will also reduce the sensitivity to avalanche signals, which are the majority of events in the MARTA RPCs. For that reason, and although it might seem possible to measure the charge spectrum of streamers, no effort was put into studying this possibility.

8.2.2 Using RPC signals

The charge measurement using real RPC pulses was performed with a representative pad of a MARTA RPC connected to an input of the front-end. The optimal hold delay was measured for these signals, and four discriminator threshold were tested. The slow shaper configuration used was the one determined with generated signals: $c_{fc} = 2100$ fF and $c_{RCbuf} = 2250$ fF. Firstly, the self-trigger measurement was utilized, and after the results with this acquisition mode were compared with the ones obtained using a validation trigger: the coincidence of two scintillators placed above and below the pad. Lastly, the charge distribution was acquired for different E/N, and the outcome studied according to the models published in the literature.

8.2.2.1 Hold delay and threshold optimization

The hold delay range was swept, using RPC signals, for four different discriminator threshold values: 210, 240, 270, and 300. In the plot of figure 8.11, are shown the results for the case where the threshold was 240. For each value of hold delay, a distribution was obtained. Thus, the coloured scale represents the normalized number of events. The spectrum for the case hold delay = 29 clk is shown in the inset of this figure. Once again, the shape of the plot seems to follow the slow shaper output waveform. Note that a few pedestal events are visible in the first hold delay values, at around 160 ADC units.

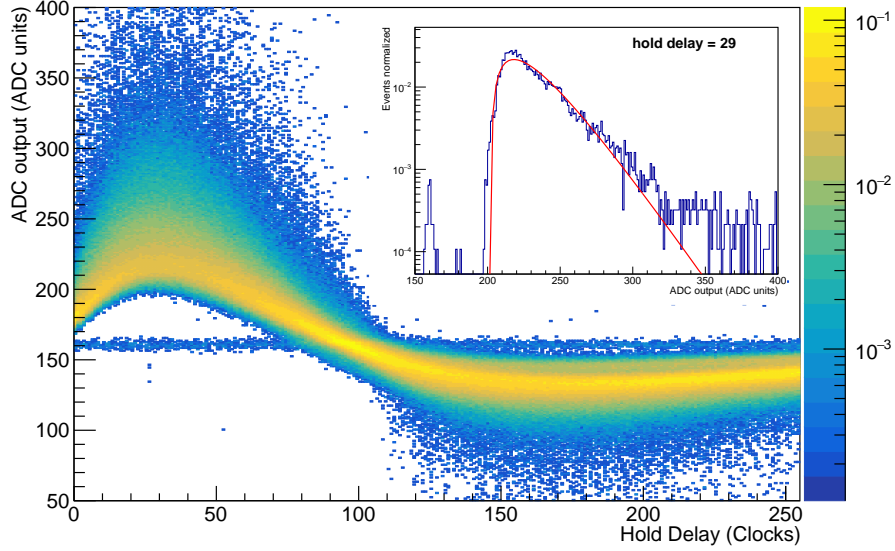


Figure 8.11: ADC output as a function of the hold delay for real RPC signals. The coloured scale shows the normalized number of events. The plot shape follows closely a slow shaper signal typical waveform. The insert shows the measurement for hold delay = 29 clk and the fit to the gamma distribution (expression 8.2).

To get the hold delay correspondent to the slow shaper peak, the maximum of the first 80 distributions was determined. For that the following function was fitted to each spectrum:

$$y(x) = c \frac{e^{-\frac{x-x_0}{a}} (x-x_0)^{b-1} a^{-b}}{\Gamma(b)} \quad (8.2)$$

where x_0 , a , b and c are the fitting parameters and Γ the gamma function. This is the gamma distribution mentioned in section 5.1 and equation 5.2. As shown before, this equation can successfully describe the charge spectrum data of RPCs. In the inset of figure 8.11, the fit result for that particular distribution is shown. Two reasons led to only determining the maximum of the first 80 distributions: firstly because these are enough to get the slow shaper peak, that is clearly in the 20 to 40 range, and secondly because after that value the shape of the distributions changes and the gamma fit stops giving good results.

After, the maximum of the 80 distributions were plotted and fitted using an expression

that was found to successfully fit slow shaper waveforms in the past [217]:

$$y(x) = c + (1 - e^{-ax+d})e^{-bx+f} \quad (8.3)$$

where a , b , c , d and f are the fitting parameters. The results of the fits for the four thresholds used are presented in the top four plots of figure 8.12. In them are also shown the distributions and the maximum obtained for each hold delay in the range 0 to 80 clk. Furthermore, the maximum points and their fits were compiled and drawn in the bottom plot of figure 8.12.

In all four cases, the peak value appears to be in the same hold delay region. Moreover, the fit results yield that the hold delay correspondent to the waveform peaks are 31.3, 29.6, 28.4 and 27.2 clk for the discriminator thresholds 210, 240, 270, and 300 respectively. The average of the four values is 29.2, which rounded to an integer is 29 clk. Like in the case of the generated signals, the difference between the ADC output for slow shaper maximum and the one using hold delay = 29 clk is always less than 2 ADC units. This value corresponds to a bias of less than 1%. This way, 29 clk was found to be the hold delay correspondent to the slow shaper peak when measuring the MARTA RPCs pulses.

The spectra for the four thresholds at the slow shaper peak are presented in the plot of figure 8.13. All four histograms were first normalized using the number of events of each acquisition. After, the distributions for 240, 270, and 300 were scaled so that their peak would match the correspondent point in the lower threshold spectrum. As expected, the distributions measured with higher thresholds are part of the ones obtained with lower thresholds. Moreover, it is also visible that in the distributions with 270 and 300, the cut imposed by the discriminator to the left side of the spectra is not as steep as in the other cases.

Next, two scintillators, one below and the other above the RPC pad, were used to generate a validation trigger for the charge measurement. Namely, the coincidence of the scintillators would create a signal (muon trigger) that was sent to one of the SMA inputs of the board. This trigger ensures that most of the events that will be read by the system are atmospheric muons. Only the discriminator thresholds 210 and 240 were tested since it was shown in the previous results that with higher values to many events would be lost. The results were compared to a self-trigger measurement that was redone after the coincidence run. This way, it was possible to guarantee that the RPC had the same working conditions. The top plots of figure 8.14 show the self-trigger and coincidence distributions for the threshold values 210 (left) and 240 (right). While for the latter the shape of the distributions is almost identical, the same can not be said about the former. Namely, the self-trigger spectrum has more events in the peak region, making it narrower than the coincidence one. This might indicate that rising the discriminator threshold to 240 eliminates some noise and unwanted events that are being picked up with the lower value. To test this, the distributions of the top left figure were re-plotted. However this time the coincidence spectrum was scaled such that the distributions' right side would match. The results are shown in the bottom plot of figure 8.14.

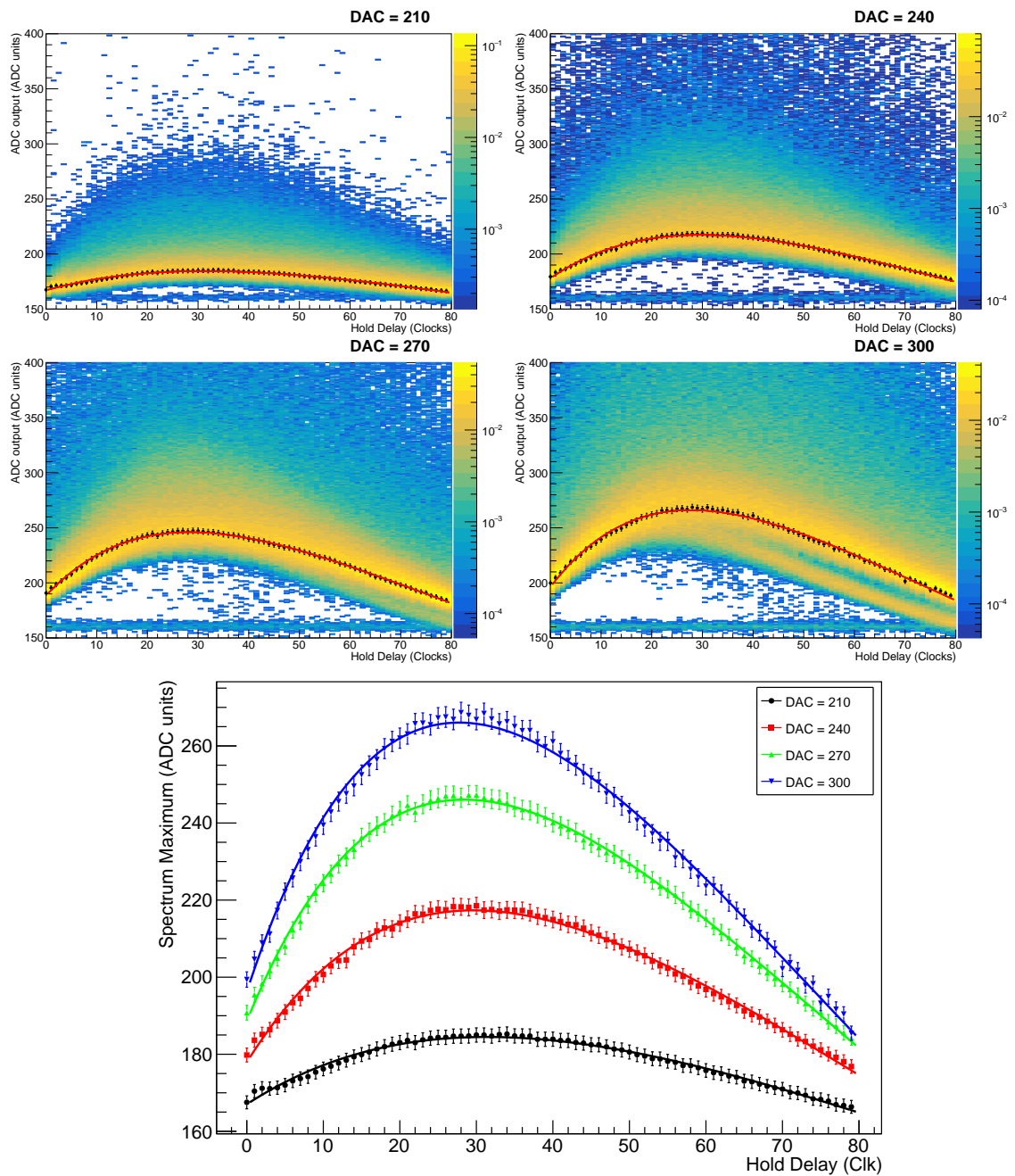


Figure 8.12: Top: ADC output as a function of the hold delay in the range of 0 to 80 clk for the four discriminator threshold values tested. The coloured scale shows the normalized number of events. The maximum of each distribution was obtained using function 8.2, and after these were fitted to expression 8.3 to get the slow shaper peak. Bottom: Maximums of the distributions as a function of the hold delay for the discriminator threshold values used. The fits for each curve are also shown.

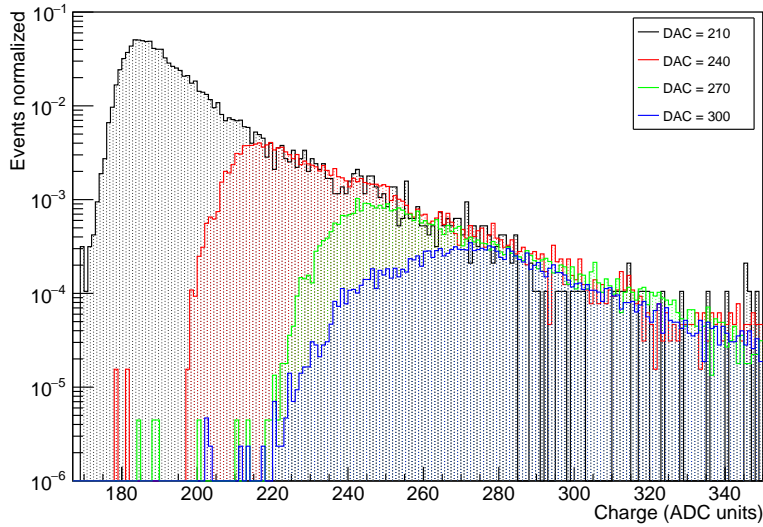


Figure 8.13: Distribution for the slow shaper peak (hold delay = 29 clk) using the four discriminator threshold values tested. The three higher threshold spectra were scaled so that their peak would match the correspondent point in the 210 distribution.

The self-trigger distribution of figure 8.14 was fitted using a function that is the sum of a Gaussian (in blue) and the expression in equation 8.2 (in green). The overall fit (in red) is in accordance with the data, having a χ^2/ndf of 2.45. Moreover, the gamma fit of equation 8.2 (in green), seems to follow the data of the coincidence histogram. These results further the hypothesis stated above: at threshold 210 the self-trigger spectra is the sum of the muon spectrum with a Gaussian component that disappears when the threshold is increased. The results of this test allow concluding that while a threshold at 240 should be used with the self-trigger measurement, 210 seems to work well when a validation trigger is part of the setup.

8.2.2.2 Charge distribution for different reduced electric fields

The electric field applied in the RPC's gas gaps drives the avalanche towards its anode, inducing a signal into the readout pad (see section 5.1). This way, it is expectable that whenever the electric field applied is modified the avalanche gain also changes, and so does the signals' charge distribution. Thus, the RPC charge spectrum was measured using six different HVs values. Like in previous MARTA measurements, the electric field is expressed as the E/N (see section 5.4 and equation 5.3). For this acquisition, the coincidence of the two scintillators (see above) was used as the validation trigger. The discriminator threshold was set at 210 and the hold delay at 29 clk. The six charge spectra were measured in the E/N range of 215 to 240 Td. The results are presented in the plot of figure 8.15.

As E/N gets higher, the spectra get wider and the peak moves to bigger charges. This trend is in accordance with the conclusion of [125], mentioned in section 5.1. The authors observed the changes in the distribution of the charge as the HV was increased. First, it had

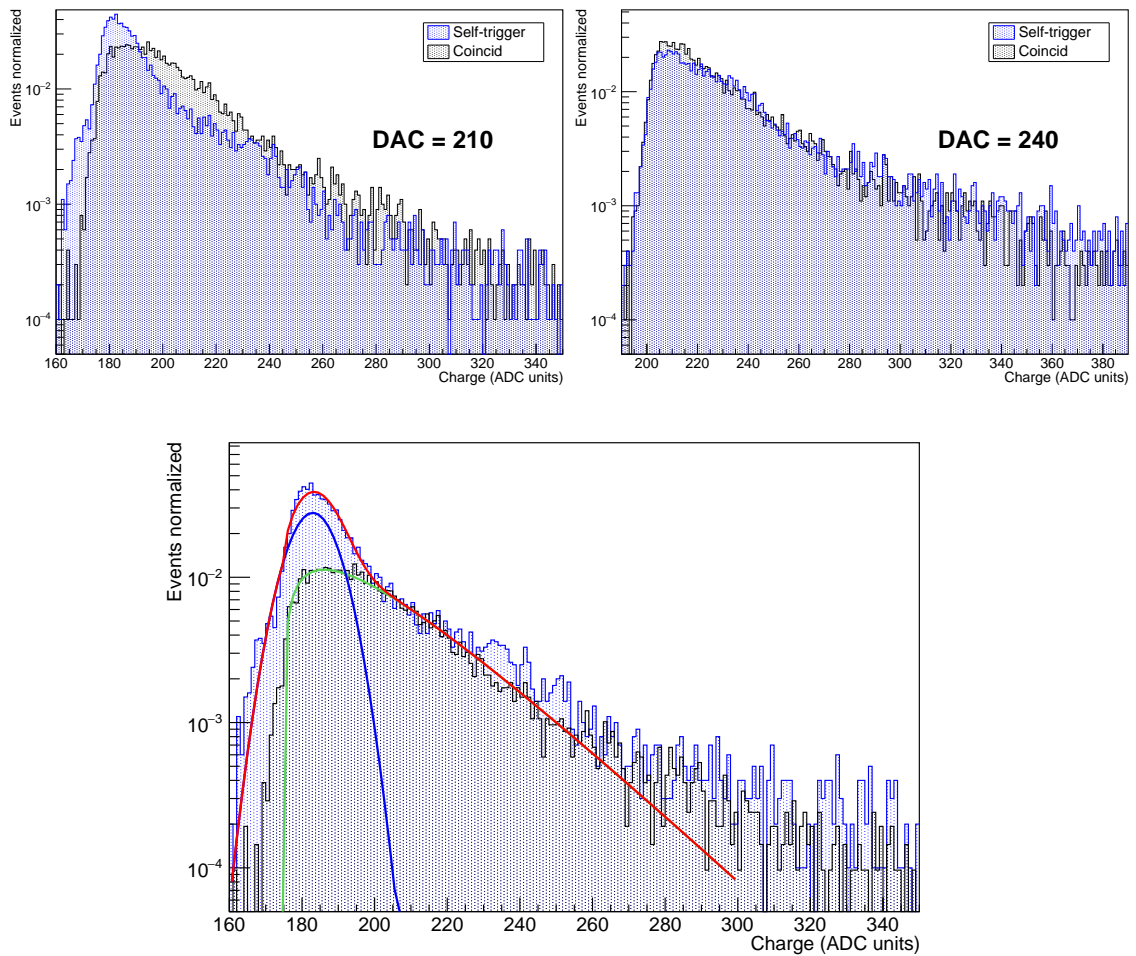


Figure 8.14: Top: Self-trigger (blue) and coincidence trigger (black) charge spectra using two discriminator thresholds: 210 (left) and 240 (right). Bottom: Same distributions as the top left plot, but this time the coincidence histogram was scaled so that the fall of the spectra would overlap. The self-trigger distribution was fitted to a function (red line) that is the sum of a Gaussian (blue line) and equation 8.2 (green line).

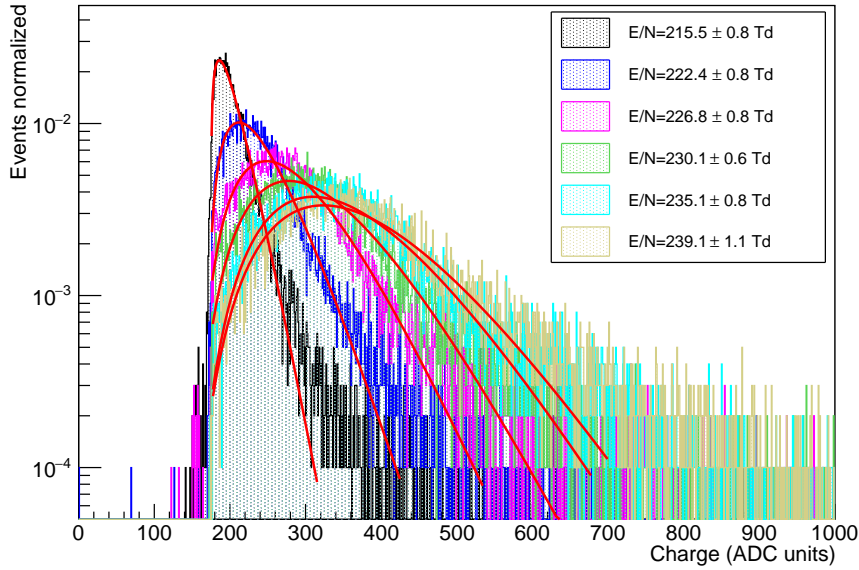


Figure 8.15: Charge spectra for six different E/N. Each of them was fitted to the gamma distribution of equation 8.2.

a exponential shape, then a Landau and lastly, it would have a Gaussian-like distribution. Furthermore, when fitting the histograms to equation 8.2, there is exceptional accordance between data and the function. Namely, the fits have a χ^2/ndf results between 1.3 and 1.7. As also mentioned in section 5.1, this function was found to be an excellent functional parameterization of detector data [131, 133].

References like [97, 129, 235] have presented results where the evolution of the charge, either total or mean, was studied as a function of the electric field. While in all of them an exponential-like evolution is present, in the last two, the data was successfully fitted to the logistic function mentioned in equation 5.1. In figure 8.16, this analysis was performed to the mean of the spectra shown in figure 8.15. The trend is confirmed with the results yielding a χ^2/ndf of 1.96.

The results obtained for the charge distribution as a function of the E/N were compared with three distinct models that were previously used to describe the RPC's charge spectrum. The data acquired in this test seems to agree with the models, showing that the front-end can measure the charge of RPC signals correctly.

8.3 Differential lines

A test was prepared to assess the reliability of the LVDS lines. These are run directly from the FPGA into two RJ45 connectors, one with four inputs, and the other with four outputs. The test consisted of having three lines out of the FPGA and then input again, using a cable with one end connected in the LVDS input and the other in the LVDS output. The three lines were data, clock, and enable. The clock is continuously on, and whenever the test is running the enable line is set to high. Data consisted of periodically changing the line state to high for a clock cycle. Two 64 bits counters, one on each side of the cable,

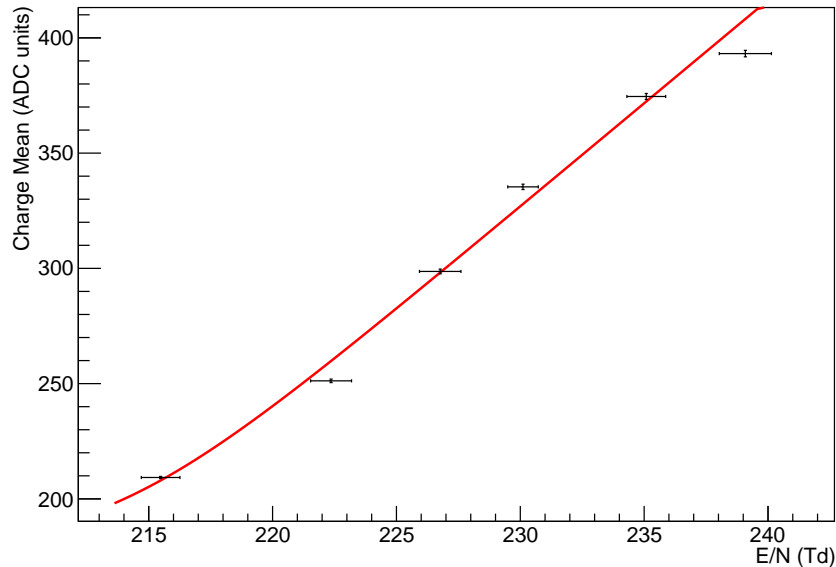


Figure 8.16: Charge distribution average versus the E/N. The data points were fitted to the logistic function of equation 5.1 yielding a χ^2/ndf of 1.96.

increase any time the data was detected at '1'. A representation of this setup is shown in figure 8.17.

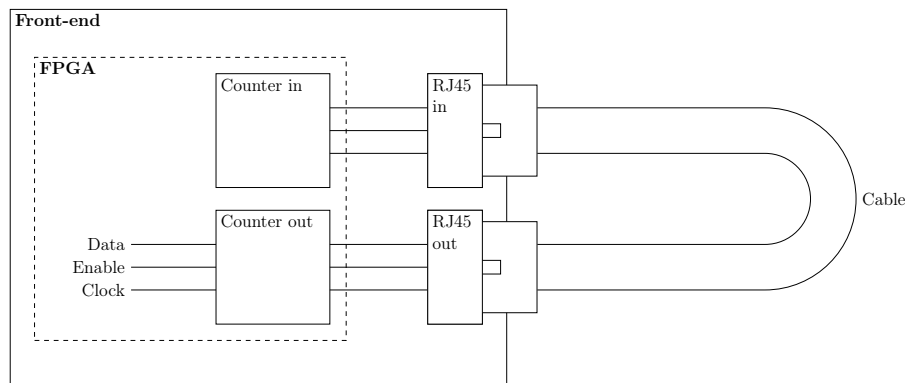


Figure 8.17: Representation of the setup used to test the front-end's LVDS links.

By comparing the counters' outputs, it is possible to know if any signals were lost in the way. This test was done for two clock frequency: 40 MHz, the speed used in the standard LVDS communications, and 320 MHz, the highest clock generated by the FPGA's PLL. Two cables, with lengths 0.62 m and 6.2 m, were connected. Thus, a total of four acquisitions were performed, each of them for about a day. The results are presented in table 8.3.

The results show that the lines are reliable at high clock speeds, especially at the speed of the LVDS communication protocol. Only in the case of clock = 320 MHz and cable = 6.2 m events were lost: 2 in 3.46×10^{12} . Although this value is insignificant when compared to the total number of events, it shows that the lines are not 100% efficient and that some data loss should be expected. This highlights the importance of having a mechanism like the checksum used to manage communication errors.

| Clock frequency | Cable length | Events sent | Events lost |
|-----------------|--------------|-----------------------|-------------|
| 40 MHz | 0.62 m | 4.32×10^{11} | 0 |
| | 6.2 m | 4.32×10^{11} | 0 |
| 320 MHz | 0.62 m | 3.61×10^{12} | 0 |
| | 6.2 m | 3.46×10^{12} | 2 |

Table 8.3: LVDS links test results for the four acquisitions performed.

8.4 Summary

In this chapter, the performance of the front-end was assessed. First, the efficiency of the RPC was measured, and the results compared with the ones obtained by another established RPC DAQ. The efficiencies that both systems got were compatible, showing that the front-end does not introduce any unwanted inefficiencies. After, s-curves of the trigger efficiency (transition from 0 to 1) as a function of the input charge were acquired for different temperatures in a range of about 50 °C. The influence of temperature in the results was found to be negligible, with the charge difference between the lowest and highest temperature never higher than 3 fC. Then, the charge measurement was tested, using generated negative square pulses through a capacitor, and real RPC signals. In both cases, the optimal ASIC parameters and hold delay were determined. For generated signals, the ASIC charge range was tested and compared to the expected range of RPC signals. The conclusion was that the MAROC is not able to get streamer signals' charge with the chosen configuration. Moreover, for the lower charge signals, in the avalanche region, a calibration curve was obtained. With RPC signals, the self-trigger measurement was compared with the validation trigger one. The latter was the coincidence of two scintillators placed above and below the pad being tested. Moreover, it was possible to determine which discriminator threshold should be used with each measurement type. The charge spectra of the RPC signals were acquired with different electric fields and the results tested against models presented in the literature. The distributions obtained followed the expected patterns, concluding that the charge spectrum was being read correctly. Lastly, the LVDS lines efficiency was evaluated, showing that although very few events were lost in the lines, this number was not null. Error detection mechanisms had already been put in place in the communication protocol, expecting this loss to happen.

Overall, with the results presented, it is possible to conclude that this system is capable of measure the fast avalanche RPC signals, including their charge, and that the weather conditions in the Observatory's site should not influence the acquisition. Furthermore, the differential communication lines showed to be reliable, with an efficiency of almost 100%.

9 Applications

In this chapter, some applications of the front-end and the MARTA modules are described and discussed. It includes the MARTA EA, the motivation of this development, a hodoscope build to test the new Observatory’s scintillators, and a smaller detector to study the rock profile of an decommissioned mine, used as a public science center, with muon tomography.

9.1 Engineering array

The production of MARTA modules for the EA was divided into two stages. In the first, most of the parts were developed and built at LIP: the sensitive volumes (gas-tight acrylic box), all the electronics and gas systems. In the second, the components were then shipped to São Carlos, Brazil, where the MARTA modules were put together. This included the production of the aluminium boxes, the readout PCBs and all the cabling. A picture of the front-end inside the aluminium box, with all the cables, is presented in figure 9.1. The 64 RPC outputs are soldered to the mezzanine boards. The differential communication lines are connected to the Central Unit using the blue cables. The power is coming from the PSU through the connector in the top left corner of the board. Lastly, the I²C cable, in the top right, part of the slow control network connected to the Central Unit, gets the data from the board’s temperature and humidity sensors. The EA is composed of seven stations, meaning a total of 28 MARTA modules will be deployed. Thus, more than half of the board’s production run will be used in the EA, not including spares.

A quality control test was put together to screen any errors in the detector construction, like outputs not correctly connected. It is performed after every module is built and it consists of a charge acquisition of the 64 channels in self-trigger mode. This measurement has the advantage of being easy and quick to perform while giving a good indication of the detector status. Moreover, for each test, only a computer that can run the acquisition software via USB is needed, and each run takes about 20 minutes. A script was written that performs the measurement and plots the spectra as soon as the acquisition ends. This way, the test can be run by the technicians building the detectors, by only pressing a button.

Two examples of the RPC quality control charge measurement are presented in figure 9.2. In the charge spectra of the top plot, the results are the expected ones, with the

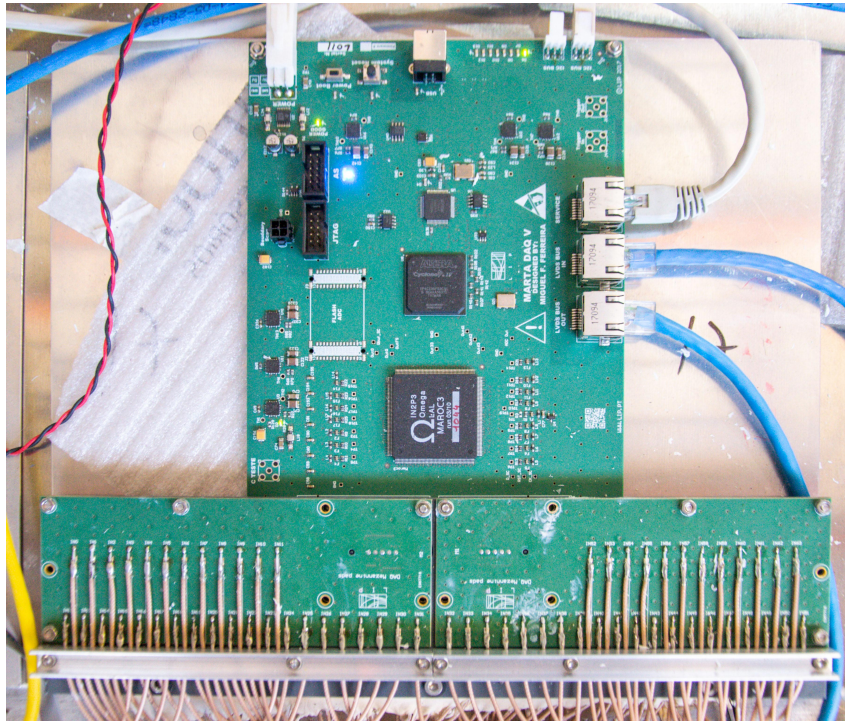


Figure 9.1: Front-end connected inside the MARTA module’s aluminium box. The 64 RPC cables are soldered to the mezzanine boards, the differential communication lines are connected using the two blue ethernet cables, power is coming through the connector on the top left, and a I²C cable allow to read the temperature and humidity sensors.

pedestal signal overlapping in some cases the peak of the signal distribution. However, in the bottom plot, the same can not be said. Most of the signal is to the left of the pedestal, which indicates that something is wrong in the RPC construction. It was later found that this RPC had the HV wrongly applied. The positive plane was switched with the negative one, making the polarity of the output signal inverted.

The first batch of 22 MARTA modules was shipped to the Observatory’s site, in mid-2019. While some of these were employed in other setups, i.e., the hodoscope (see section 9.2), four of the modules are already installed in the Peter Mazur station, as mentioned in section 4.4. These were prepared for deployment in the Observatory’s assembly building, which included checking all connections, gas system, and lastly a measurement of the charge distribution. The last batch of RPCs is still, as of the writing of this thesis, being put together in Brazil. These are expected to arrive at the Observatory before the deployment of the first four stations is completed.

Data runs with the first station should have started in the end of last year. However, a technical problem with the slow control chain, already solved in the laboratory, prevented the remote operation of the detector. Furthermore, the fix is yet to be implemented in the field, due to station’s being isolated and hard to reach. Thus, data taking was postponed until the solution is fully installed, most likely in the second semester of 2020.

In an initial stage, the standard acquisition will only use the hit measurement to count muons. Periodical quick charge spectra are planned, interrupting the standard acquisition,

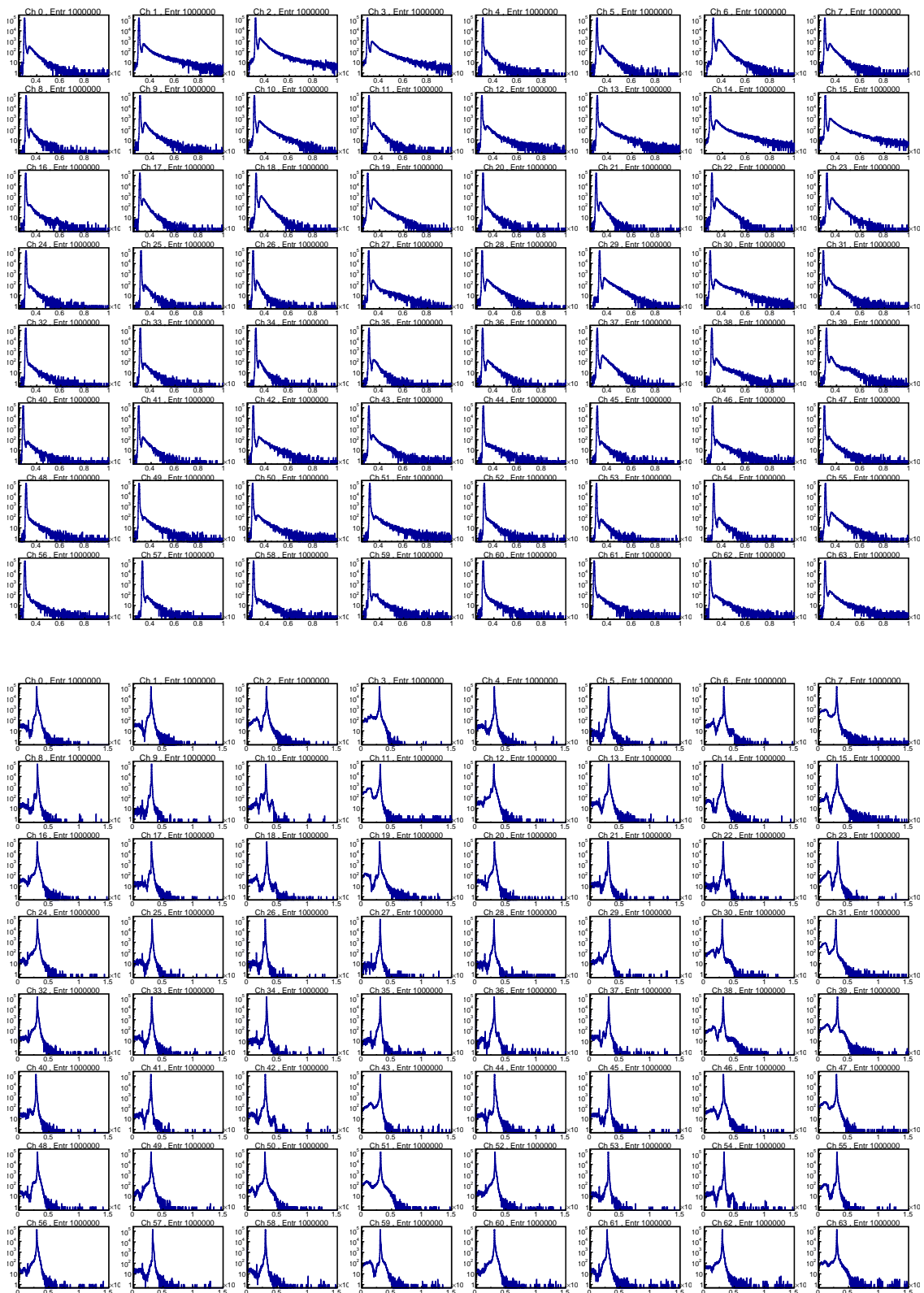


Figure 9.2: Quality control measurement of the charge distribution for two RPCs after they are assembled. Top: The results are the expected ones, with the pedestal overlapping the spectra peak. Bottom: Most of the events are to the left of the pedestal, showing something went wrong in the construction process.

to help assess the health of the RPC. After the analyses of the first data, it will become apparent when charge measurement will be needed as a complement of the standard acquisition. In principle, due to the high dead time of the this measurement, it can not be run in parallel with the muon counting, and so it is crucial to study in what situations it would be beneficial to use it. Furthermore, in this first phase of the acquisition, all T1 events will be acquired and stored in the Central Unit. Once per day, these events will be sent to the CDAS. Afterwards, the MARTA data will be matched with the T3 triggers and combined with the SD data for posterior analysis.

9.2 Hodoscope

A hodoscope of MARTA RPCs was installed at the Pierre Auger Observatory to study the new scintillators part of the SSD upgrade (see section 3.1.3). The scintillators were all built in different institutions in Europe and tested before they were shipped to the Observatory's site in Argentina. This way, the hodoscope will be used with three different purposes:

- have a standardized test of the scintillators before installation;
- look for any possible parts failure during shipping;
- investigate any malfunction in the detectors after these start taking data.

The MARTA RPCs will also be tested in this setup before these are deployed in the field.

The concept of the hodoscope as a test bench for the SSD detectors was first assessed using a small 30×30 cm² scintillator. In this first version only two RPCs, one above and another below the scintillator were used. However, as mentioned previously, each SSD module has two 160×120 cm² scintillators side by side inside a sealed aluminium box. This means that with only one RPC per hodoscope plane, the system would only be able to cover one of the scintillators of the SSD. Thus, the final setup was installed in the Observatory's assembly building with a total of four RPCs: two on top, alongside each other, and another two on the bottom, also side by side.

In this section, the results of the prototype setup are shown. Then, the final system is presented, along with a GEANT4 simulation. As of the writing of this thesis, the hodoscope is still to be used, meaning no data will be shown. The work in this section was presented to the collaboration in two internal notes [236, 237], and in multiple meetings.

9.2.1 Prototype setup

The prototype setup of the hodoscope consisted of two RPCs placed on a stand, as shown in the top of figure 9.3. While one of the RPCs was placed on the higher shelf, on top of a wooden pallet (top RPC), the other (bottom RPC) was on the lower shelf inside a shipping crate. The RPCs were aligned in the x and y coordinates and 1.07 m apart in

the z coordinate. The small scintillator was inside a wooden box that can be seen in the middle shelf of the stand. Although the box was $87 \times 35 \text{ cm}^2$ and had a height of 18 cm, the $30 \times 30 \text{ cm}^2$ square test scintillator was installed all the way to the right. The PMT occupies the rest of the box. The test scintillator was placed precisely in between the RPCs, which means its plane is 54.75 cm away from each of the RPC planes. A representation of the side (left) and top (right) views of the setup, with all the dimensions, is shown in the bottom pictures of figure 9.3.



Figure 9.3: Top: Hodoscope prototype stand in the Observatory’s assembly building. The RPCs are placed on the higher and lower shelf, separated by 1.07 m. On the middle shelf, inside a wooden box is the small scintillator. Bottom: Representation of the side (left) and top (right) views of the prototype hodoscope setup. The scintillator used to assess the system’s performance is also shown.

While the RPCs were read using the front-end, the scintillator signals were measured

with a PicoScope 3206D MSO oscilloscope [238]. The RPCs' coincidence was generated inside one of the front-end's FPGA and sent to the other and to the PicoScope to be used as the trigger. A delay of $1.125 \mu\text{s}$ was added to the coincidence trigger, to ensure the signal in the PicoScope would come before the trigger. Event identifiers are also created and sent out with the trigger, to match the data of the different detectors. In this setup, the hit measurement was used and the data stored in a ROOT tree similar to the one described in section 7.4.

For each event, the data will be the pad the particle crossed in both RPCs and the waveform measured in the PicoScope. Thus, it is possible to compute the particle's trajectory, as shown in appendix B, and get where it crossed in the scintillator's plane. In all calculations the distance between RPCs, z , was considered to be 1.095 m which corresponds to the distance from the middle of the top to the centre of the bottom RPC. The spatial resolution in the scintillators' plane depends not only on the RPC pad size but also on its position between the RPCs. In the case of a detector placed precisely in between the RPCs, like the small scintillator, a matrix of 15×15 is covered, where each rectangle has an area of $7.5 \times 9.5 \text{ cm}^2$.

The acquisition to test the system took about 7 hours and had an event rate of 39.9 Hz. While on the top RPC three pads were not instrumented, on the bottom detector one pad was not connected. Data where more than one pad was triggered per RPC was not considered, making the data set used $\sim 89\%$ of the events acquired. In the PicoScope, 625 points were acquired per event to measure the scintillator's waveform. The configurations used included an 8 ns time resolution and a window of $\pm 200 \text{ mV}$. The test scintillator was connected to one of the channels with a 50Ω termination, while the trigger was input into the digital channel of the PicoScope. For debug purposes, the trigger was also connected to the second acquisition channel (without termination).

The distribution per pad and time for both RPCs is presented in the top plots of figure 9.4. The time corresponds to the hit's position in the FIFO memory, i.e., the time between the detection and the coincidence trigger. The middle left plot of figure 9.4 shows a zoom of that time difference for pad 36 of the bottom RPC. Most of the events are between $-1.4625 \mu\text{s}$ and $-1.5 \mu\text{s}$, which is compatible with the time the coincidence trigger takes to be created, and the delay applied. The middle right plot of figure 9.4 has the event distribution per pad for the bottom RPC. As expected, due to the system's acceptance, pads in the centre of the RPCs have more events than the ones in the borders. The angular distributions of the reconstructed trajectories are presented in the bottom two plots of figure 9.4. The azimuthal distribution (left) shows that the most common angles are 0° , 90° , 180° , and 270° , which corresponds to a coincidence between pads in the same row or column. The zenithal distribution (right) has angles between 7.8° and 57.1° not including the vertical trajectories (0° , 3.6% of the events).

The data distribution in the scintillator plane is shown in the left plot of figure 9.5. The coloured scale represents the normalized number of hits, and as expected, there is a higher density of coincidence events away from the borders. The red rectangle represents

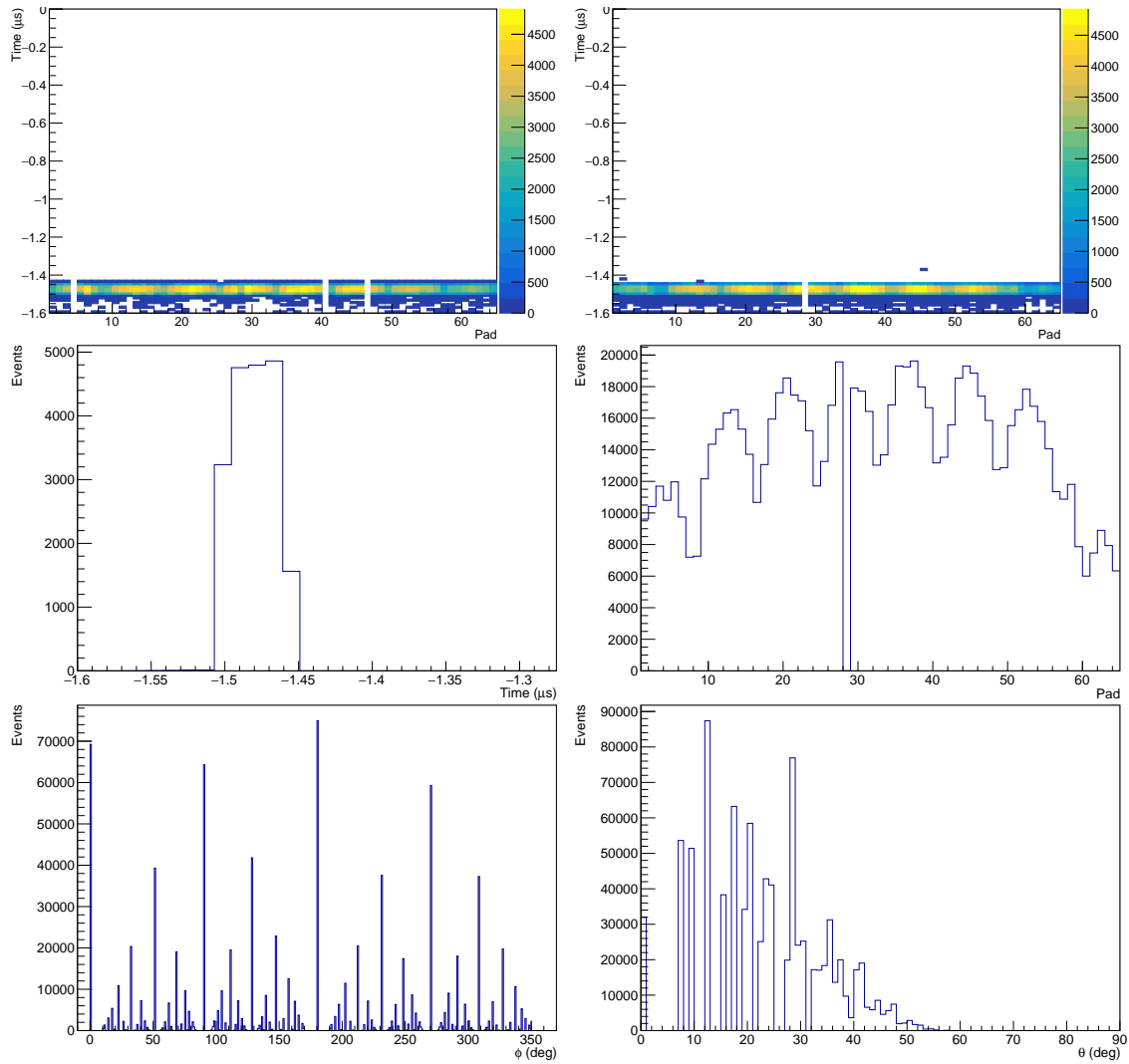


Figure 9.4: Events distribution per RPC on the prototype hodoscope. Top: Pad and time distribution of the coincidence events in the top (left) and bottom (right) RPC. Middle left: Time distribution of coincidence events that crossed pad 36 of the bottom RPC. Middle right: Pad distribution of the coincidence event in the bottom RPC. Bottom: Angular distributions of the particles' trajectories. The azimuth (left) and zenith (right) angles are shown.

roughly the region where the small scintillator is.

In the right plot of figure 9.5 is shown a typical PicoScope event, with the signals collected in both channels. In black is the small scintillator signal while in red is the coincidence trigger sent by the front-end's FPGA. The distance between the peak of the scintillator waveform and the rising edge of the trigger is $1.45 \mu\text{s}$ which is compatible with the time shown in the top plots of figure 9.4. With this plot, it is possible to conclude that the delay added to the coincidence trigger was excessive and can be reduced.

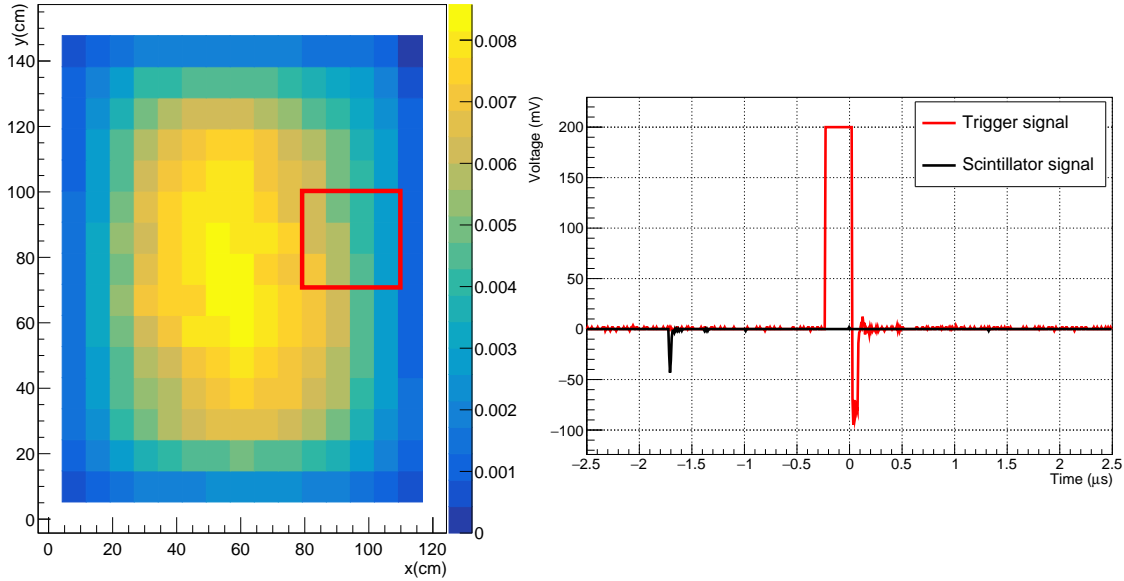


Figure 9.5: Left: Coincidence event distribution in the scintillator plane. The coloured scale represents the normalized number of events. The red line roughly denotes the test scintillator's position. Right: Typical event acquired by the PicoScope. In black is the test scintillator waveform, while in red is shown the trigger sent by front-end's FPGA.

Two studies were performed with the data acquired. In the first, the threshold efficiency was measured. It was done by considering that the scintillator was active when its signal was in the time region of $-2.1 \mu\text{s}$ to $-1.3 \mu\text{s}$ and it would cross a threshold set at -5 mV . The results are shown in the left plot of figure 9.6. The position of the small scintillator is clearly seen, with efficiencies as high as 90%. Furthermore, the 4 by 3 region where this value is higher cover an area of $30 \times 28.5 \text{ cm}^2$, which is close to the scintillator size. 68.3% of the events are in that region, where the average efficiency is 82.4%. If considering the neighbour positions of this area, the percentage of events is 91.7%. It should, however, be mentioned that choosing the centre of the pad as the point where the particle crosses the RPC introduces uncertainties, of the order of the pad size, in the position estimation. In the second approach, the absolute value of the small scintillator's signal peak was determined. For that, the minimum value measured between $-2.1 \mu\text{s}$ and $-1.3 \mu\text{s}$ was obtained for each event. For all the positions in the test scintillator plane, these values were summed and divided by the number of events, obtaining the average peak signal. The results are shown in the right plot of figure 9.6. Once again the placement of the scintillator is well determined, with the larger signals being obtained in the region near the PMT (left centre).

Lastly, it should be referred that some spots to the left of the scintillator have more signal than the rest of the area without a detector. It corresponds to the region where the PMT is placed.

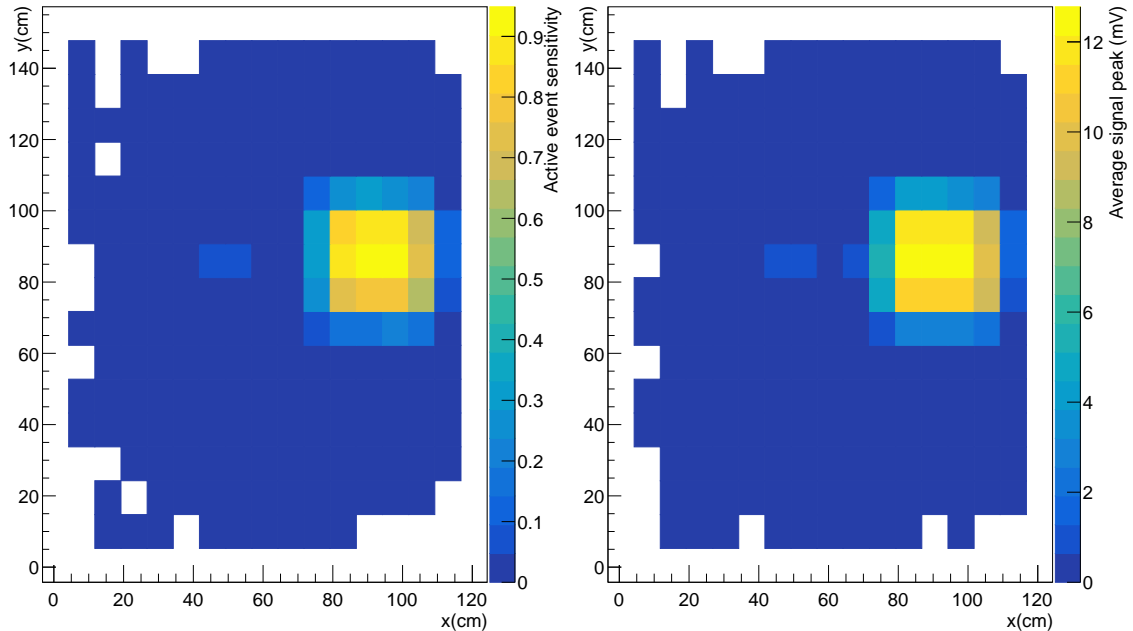


Figure 9.6: Results of the measurement of the small scintillator with the prototype hodoscope. Left: Efficiency as a function of the position. The scintillator was considered active when the signal was in the time region of $-2.1 \mu\text{s}$ to $-1.3 \mu\text{s}$ and crossed a threshold of -5 mV . Right: Average test scintillator signal peak. The absolute value of each signal was obtained and its average per position plotted.

In both approaches, the test scintillator position is well identified. It shows that the hodoscope is able to characterize the scintillator and determine where a malfunction might be, e.g., a broken fiber. This test can also be considered an assessment of the RPC's data acquisition system. It was the first time the front-end was used to measure the RPCs in a non-validation/debugging setting. The results were the expected ones, with the system, including the front-end, working as intended.

9.2.2 Final setup

After the successful operation of the first hodoscope, the second setup started being put together. A new stand was custom built by the Observatory's staff to fit two RPC detectors side by side on each of the hodoscope planes, and an SSD in between them. A picture of the final setup, with all the detectors installed, is presented in the top of figure 9.7. The stand is organized in the following from the bottom to the top: lower RPC hodoscope plane, SSD module, top RPC hodoscope plane, and electronics. In the bottom diagram of the same figure is shown a representation of the system, with all relevant dimensions. The stand was built so that the SSD modules could be easily put in and taken out of the shelf, using, for example, a forklift. It was also foreseen to test more than one module at

a time, stacked on top of each other. For that reason, the distance from the scintillators to the top RPCs is bigger than to the bottom RPCs. In both the picture and diagram presented, a total of 8 RPCs are shown. However, only four of them will be used as part of the hodoscope. The others are detectors being prepared and tested to be installed in the MARTA stations. The top RPCs of the pairs were used as part of the hodoscope.

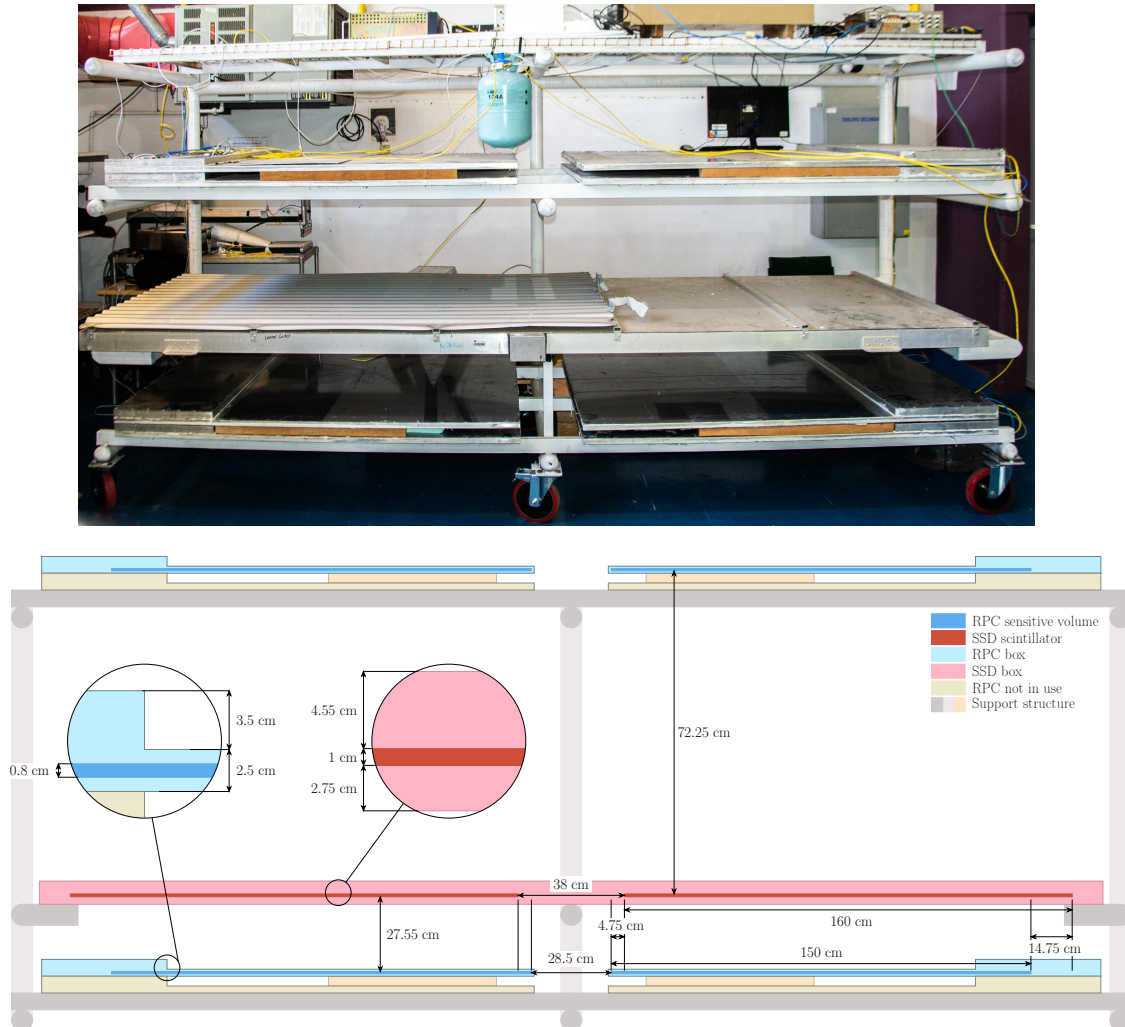


Figure 9.7: RPC hodoscope final setup. Top: Picture of the setup installed in the Observatory’s assembly building. Electronics are placed on the top shelf, RPCs on the second from the top and bottom shelves, and the SSD module on the second shelf from the bottom. Bottom: Representation of the setup. All relevant dimensions are shown.

The system’s electronics, other than the ones that are inside the MARTA module, are placed in the stand’s top shelf. It includes the Central Unit that controls the four RPCs of the hodoscope, the SSD electronics (the upgraded UB or UUB, mentioned in section 3.1.3), power supplies, etc. In this setup, the trigger generation is no longer a responsibility of one of the front-end’s FPGA, instead it is done in the Central Unit. Each of the four RPC’s front-ends sends an OR of the 64 discriminated outputs to the Central Unit that will look for a coincidence. Such an event happens when one of the top plane’s RPCs is in coincidence with one of the bottom plane’s RPCs. The trigger is then sent to the four

front-ends and to the UUB with an event identifier.

As of the writing of this thesis, the four RPCs and electronics were fully tested, and the Central Unit is generating the coincidence trigger. However, coincidence events have yet to be acquired, so no data was measured. Nevertheless, a simulation was prepared to study the setup.

9.2.2.1 Simulation

A simulation using the GEANT4 toolkit [107–109] was prepared following the geometry presented in the bottom diagram of figure 9.7. The SSD module was extracted from the `Offline` simulation software. A full description of the scintillator’s simulation is presented in [239, 240]. As mentioned previously, each SSD module has two sets of twelve scintillator’s bars perforated with 24 fibers. The fibers, each with 5.85 m, transverse the length of the bars and are then reinjected in the scintillator. Thus, both ends of the fiber are connected to the PMT. A representation of the SSD is presented in figure 9.8. In the left picture are shown the right and left modules, each with the twelve scintillator bars, separated by a gap that host the fibers travelling to the PMT. In the right picture is represented the path of a fiber inside the scintillator. The simulation takes the energy deposited by the crossing particle and converts it into the number of photoelectrons produced at the PMT’s photocathode. Position-dependent signal loss is included in the simulation having into account the attenuation length and a decreased yield that is observed for particles close to the edge of the scintillator bars [239].

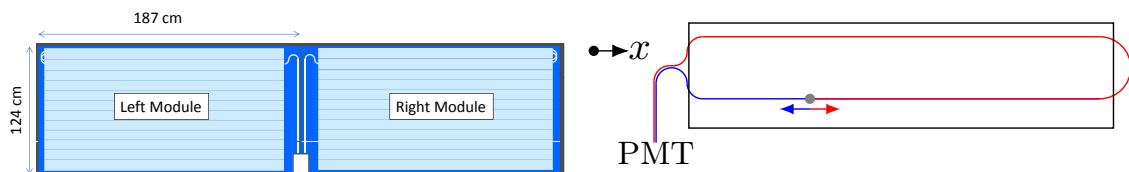


Figure 9.8: Representation of the SSD. Left: The two modules are shown, each with twelve scintillator bars. The gap that divides them will host the fibers connected to the PMT. Taken from [64]. Right: Diagram of a fiber inside the scintillator. A particle crossing is represented in grey. The two paths the particles can go through are shown in red and blue. Based on the drawings presented in [239].

The RPC simulation is the same one that has been recently added with the MARTA’s module to `Offline`. This implementation is described in [100]. The RPC structure is fully detailed, including the aluminium case, acrylic box, glass plates, and gas composition. The signal generated in the gas is simulated using a parameterization that takes into account the particle inclination relative to the RPC plane. Lastly, signal digitalization using a simple threshold is also included in the simulation chain.

The simulation data was stored in a ROOT tree, similar to the one described in section 7.4. The position the particles crossed the RPCs was turned into a pad number that was stored with the hit’s time information. The output of the SSD module was the signal’s charge, i.e., the number of photoelectrons produced at the PMT. The simulation was

performed injecting 100 GeV muons in a plane with an area of $4.4 \times 1.6 \text{ m}^2$ that was placed 1 m above the SSD. The particles angular distribution was constrained to zenith angles between 0° (vertical) and 75° with all possible azimuth allowed. A picture with the simulation geometry and a particle crossing the detectors are shown in figure 9.9.

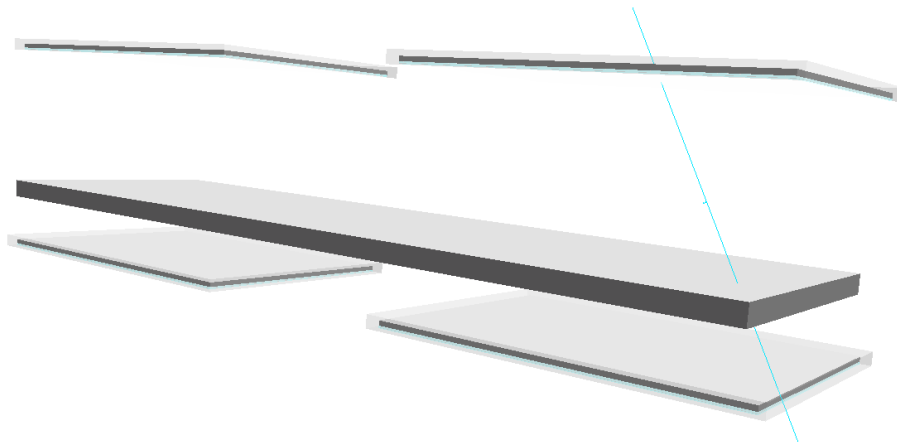


Figure 9.9: Simulation’s visualization of a particle going through the setup.

The simulation output was analysed, with about 8% of the events generated, hitting one pad on the top plane of the hodoscope and another one in the bottom plane. These events were the ones used in the results that follow. The average charge was plotted as a function of the position the particle crossed the SSD plane. Like in the case of the prototype hodoscope, the particle’s trajectory was obtained using the geometric centre of the RPC’s pads. The results are presented in the plot of figure 9.10. The bin size was obtained as the maximum distance between muon hits in the SSD plane. The coloured scale represents the average charge, i.e., the number of photoelectrons.

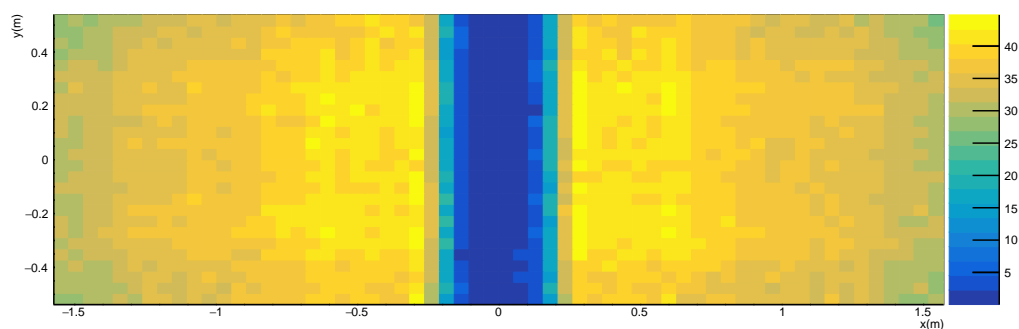


Figure 9.10: Simulation results: average charge (number of photoelectrons) as a function of the position the particle crossed the SSD.

The results show that as the position the particle crossed the scintillator gets closer to the centre of the SSD, the charge collected also gets higher (excluding the gap). Such variation is expected in the x coordinate, where the further the particle is from the centre, the more attenuation the signal has. However, these fluctuations can also be observed in the y coordinate, where it should not happen. This difference is because of the zenith

angle of the particle that can vary from bin to bin. Results presented in [239, 240], show that there is a dependency of the charge generated and the direction of the particle. The same study, charge as a function of the zenith angle was done. The data is presented in the top plot of figure 9.11. The points were fitted to the function $a/\cos(\theta)$, with a a free parameter, and scaled so that the charge at 35° is 1. The same fit and normalization were performed in [239, 240] and the results are, as expected, the same. The large error bars for bigger angles are due to the limited number of events that cross the top and bottom layer of the hodoscope with such a high zenith. To remove the angular dependency from the plot of figure 9.10, the charge of each event was divided by $a/\cos(\theta)$. The value of a used was not the one obtained for the fit of the top plot of figure 9.11. Instead, the result of the fit to data not normalized to the charge at 35° was used. Thus, the average charge corrected with the angle as a function of the position in the SSD plane is shown in the bottom plot of 9.11. Since a variation in the y coordinate is no longer visible, one can conclude that this effect was in fact, due to the angular differences from bin to bin.

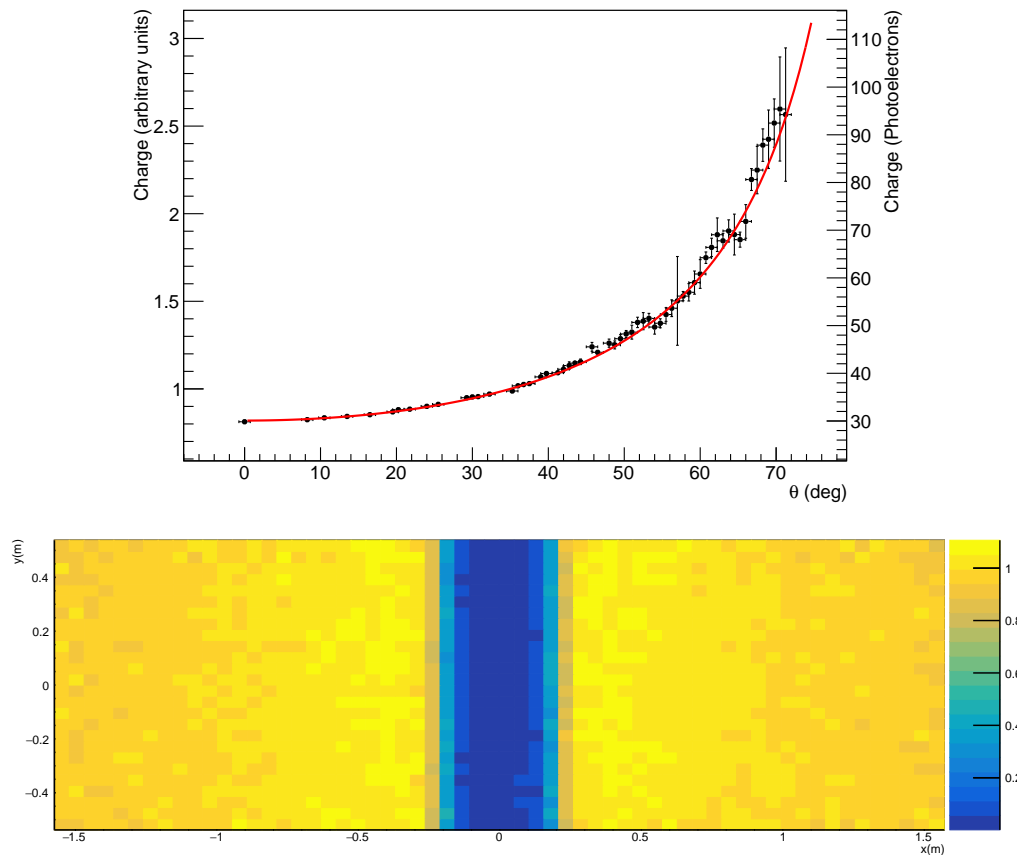


Figure 9.11: Top: Charge (number of photoelectrons) as a function of the zenith angle. The data points were scaled so that at 35° the charge would be 1. The results were fitted to the function $a/\cos(\theta)$. Bottom: Charge corrected with the particle's zenith angle as a function of the position.

The simulation results show that with this geometry, some of the scintillator's length is not observed. Namely only about 1.4 m of the 1.6 m long scintillators is covered in the x axis. To test a configuration where all the scintillator is visible, each RPC was moved 20 cm away from the origin of the x axis. The simulation was re-run, and the results are

presented in the plot of figure 9.12. Once again, the charge (coloured scale) was corrected with the zenith angle. Although it is still visible the decrease of signal with the increase of $|x|$ and now both ends of the modules are measured, there is a decrease in statistics in the area of the scintillators near the centre of the SSD. This is due to this region's events being more inclined particle with a trajectory that would hit, for example, the top left and bottom right RPCs. The effect is visible in the region $|x| < 0.5$ m where the bins are not as homogeneous as for the rest of the scintillator. Acquiring more data will help to blend the bins better.

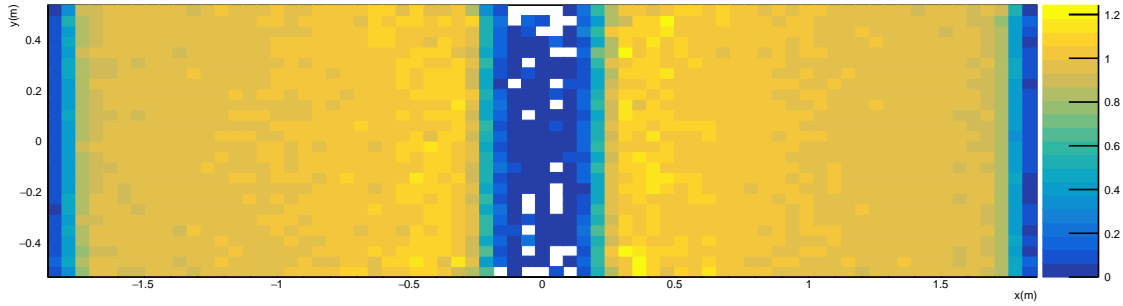


Figure 9.12: Charge (number of photoelectrons) corrected with the particle's zenith angle as a function of the position, with the RPCs of each plane 0.685 cm apart.

For both configurations of the RPCs, the mean charge for each x bin was obtained. The results are presented in the plot of figure 9.13. In blue are shown the point for the first configuration: figure 9.7 with the RPCs 0.285 m apart; and in red for the second one: the RPCs were 0.685 m apart. Lines with the same colours show the RPCs positions, while a black line represents the SSD scintillators placement. The results were fitted to the function that computes the signal loss in the simulation [240]:

$$\text{att}(x) = c \times A(x) \times L(x)$$

$$A(x) = e^{-l_{\text{long}}(x)/\lambda_f} + e^{-l_{\text{short}}(x)/\lambda_f} \quad (9.1)$$

$$L(x) = (1 - \alpha e^{-d_{\text{long}}(x)/\lambda_b})(1 - \alpha e^{-d_{\text{short}}(x)/\lambda_b})$$

where $A(x)$ is the attenuation along the fiber and $L(x)$ the decrease yield near the edge of the bars, mentioned before. c is a scaling constant, λ_f the attenuation length in the fiber, λ_b the attenuation length of the boundary effect, and α corresponds to the maximum loss. l_{long} is the long length of the fiber shown in red in the right diagram of figure 9.8, and l_{short} the shorth length of the fiber shown in blue in the same picture. d_{long} is the long distance between the crossing particle and the bar's end, and d_{short} the correspondent short distance. This four variables are only dependent of the hit's x coordinate in the scintillator: $l_{\text{long}}(x) = 4.7935 - |x|$ m, $l_{\text{short}}(x) = 5.85 - l_{\text{long}}(x)$ m, $d_{\text{short}}(x) = 0.19 - |x|$ m, and $d_{\text{long}} = 1.6 - d_{\text{short}}(x)$ m. The fit to the data point of the second configuration was performed fixing $\lambda_f = 3.12$ m, $\lambda_b = 0.046$ m, and $\alpha = 0.18$, and letting the parameter c free. As expected, the fit describes well most of the data of both RPC configurations.

However, in the scintillator borders, the points are below the curve. If events with corrected charge smaller than 0.1 are taken out of the average, the data point will match the fit. This indicates that what is moving these points to lower values is the contribution of particles that did not hit the scintillator, where the charge collected would be 0, or secondaries that generate less signal.

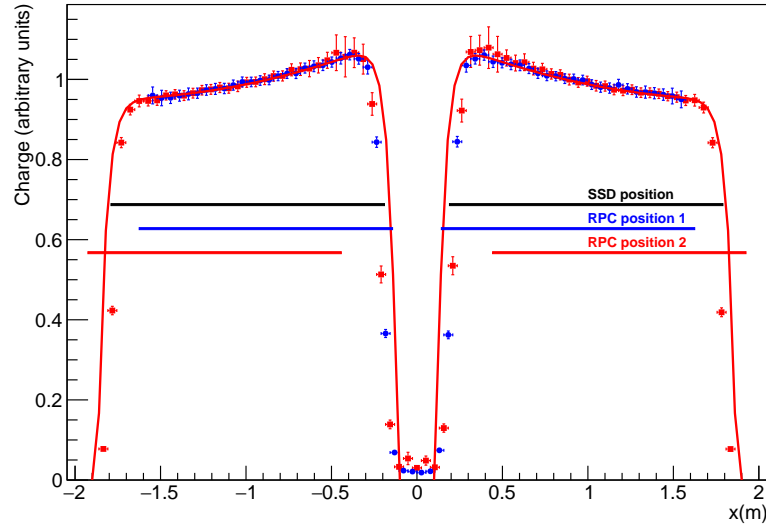


Figure 9.13: Charge (number of photoelectrons) corrected with the particle's zenith angle as a function of the x coordinate in the SSD. The results of the two studied configurations are presented. While for the blue points the RPCs were 0.285 m apart, for the red ones these were 0.685 m from each other. A fit was performed to the red data using the expression of equation 9.1. The position of the RPCs for each configuration and of the scintillator is also shown.

The last test performed was to simulate broken fibers inside the scintillator. To achieve this effect, the code's photoelectrons generation was modified: the particles that would go through the point where the fiber is *broken* are not accounted for. Two scenarios were tested: a fiber was *broken* in the right scintillator close to the gap, and four fibers next to each other were *broken* in the left scintillator near the gap. The results are presented in figure 9.14: for the first case, the data is shown in the top plot, while for the second one, it is drawn in the bottom plot. In both cases, the coloured scale represents the charge corrected with the zenith angle. The position of the *broken* fibers is mentioned in the caption of figure 9.14. The expected decrease in charge is visible in the region where the *break* is, affecting all scintillator's length.

For each scenario and the case of no *broken* fibers, shown in figure 9.11, the average charge of the x bins was computed for every y bin. The results are shown in the plot of figure 9.15. A noticeable decrease in the charge produced is evident in the region where the fibers were *broken*. In the scenario with a *broken* fiber, the scintillator bars that see a decrease in charge are the ones where that fiber is going through: from $y = -0.2$ m to $y = 0$ m. In the second scenario it influences the bars from $y = -0.2$ m to $y = 0.2$ m. For the first case, the total signal decrease is 1.1%, and for the second, it is 4.5%. Although these results indicate what to expect, they have to be compared with real data of a detector

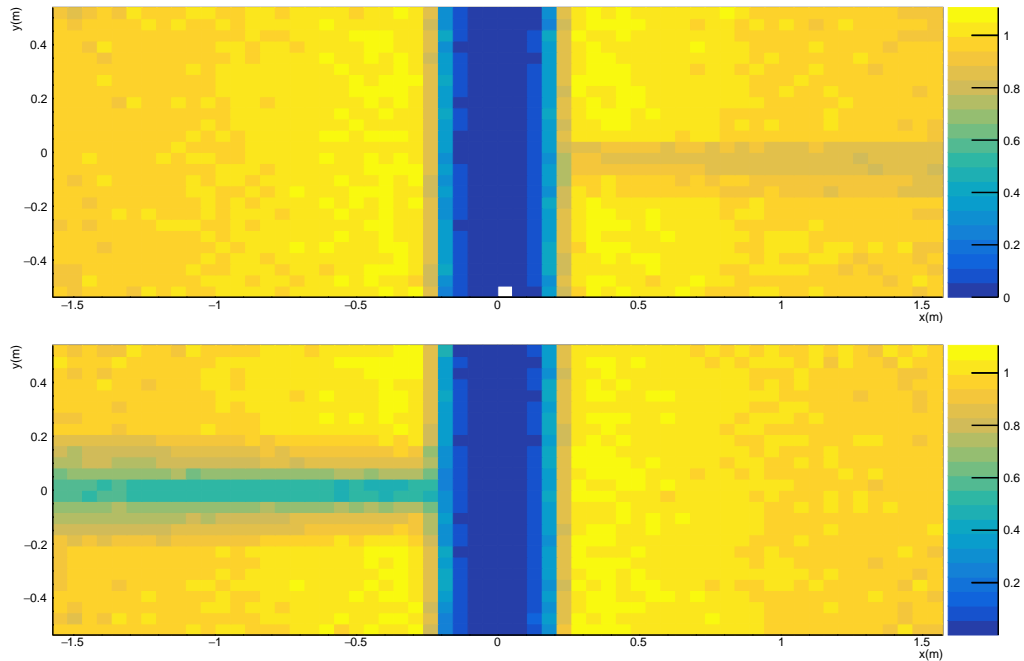


Figure 9.14: Charge (number of photoelectrons) corrected with the particle’s zenith angle as a function of the particle’s position for the two scenarios where fibers were *broken*. Top: One fiber was *broken* at $(0.24, -0.125)$ m. Bottom: Four fibers were *broken* at $(-0.24, -0.375)$ m, $(-0.24, -0.125)$ m, $(-0.24, 0.125)$ m, and $(-0.24, 0.375)$ m.

with a broken fiber to be validated.

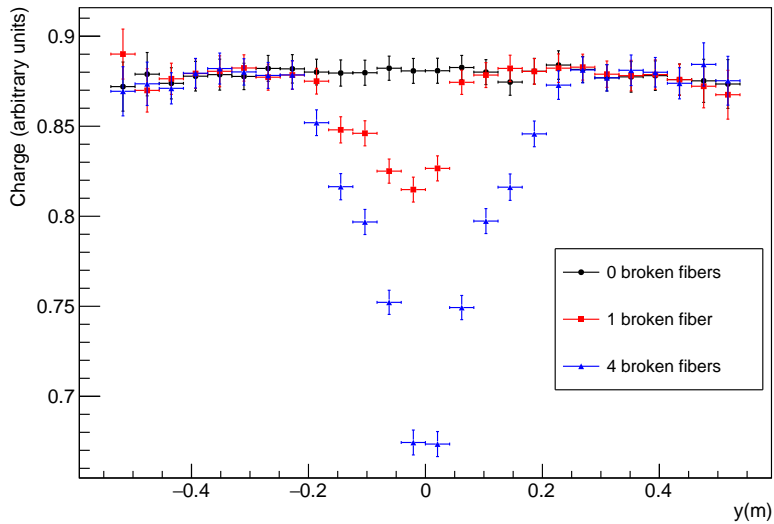


Figure 9.15: Average of the charge (number of photoelectrons) corrected with the particle’s zenith angle as a function of the y coordinate. The cases of no *broken* fibers (black), one *broken* fiber (red), and four *broken* fibers (blue) are plotted.

The simulation of the RPC hodoscope to test the SSD modules was built and tested. With the results, it was possible to determine the angular dependency of the collected charge and to see the signal’s variation along the scintillator’s length. The latter was successfully correlated with the attenuations that occur in the fibers. Two configurations

were studied by changing the distance between RPCs in the hodoscope plane. While in the first the scintillators' length was not fully covered, in the second it was. However, in the latter configuration, the number of events that would cross the scintillators' region near the centre decreased significantly. Lastly, fibers were *broken* and a cut in the signal produced was observed in the region of the malfunction. All the analysis shown in this section can be done with the data that will come out of the hodoscope.

9.3 Muon tomography

Muon tomography [241] is a non-invasive imaging technique, that measures the flux of air shower's muons to determine the density of a material. Namely, the reduction of the number of particles when transversing it is used. One of the first applications of this technique was in 1969 to find hidden chambers inside the Pyramid of Khafre in Egipt [242]. Since then, the application of this technique has been extended to volcanology, geophysics, archaeology, homeland and nuclear security, etc. [241, 243].

In 2018, a partnership between LIP and ICT was started to use muon tomography in the context of geophysics. Namely, the pilot detector will be installed at the Lousal mine, in Alentejo, Portugal (38°02'10.5"N 8°25'35.6"W), with the support of Centro de Ciência Viva do Lousal, Mina de Ciência [244]. In a first phase the main goal will be to create a map of the galleries, and later to distinguish the density of the different types of rocks above the mine. Furthermore, geophysical techniques, e.g., gravimetry, will also measure the density of the materials, allowing a precise reconstruction of the ground. The detector will also be used for outreach and education since the mine is now a museum that has daily visits.

The detector developed for this purpose was a spinoff of the ones built for MARTA. In this case, four small RPCs, are going to be installed in a stand that can be moved around the mine. The planes have an area of $1 \times 1 \text{ m}^2$ and are instrumented with most of the electronics used in the MARTA modules. This includes the front-end presented in this work. In early 2019, a small prototype was installed in the mine, that was used to test the detector's operation. In the meanwhile, the final four detectors started to be built. As of this thesis' writing, the detectors are operational and being tested in LIP's facilities before they are moved to the field, later this year. A picture of the detectors during testing is shown in figure 9.16. Like in the case of MARTA, the four detectors and their electronics are placed inside an aluminium box. In the picture, these are separated by styrofoam sheets and supported using pieces of wood. A single-board computer controls the front-ends through USB. A trigger board is used to generate coincidences between the planes. Each front-end will send the OR of the 64 discriminated outputs through the differential lines. The trigger board generates the trigger with a 24 bits event identifier that is distributed to the four detectors.

For this project, it was decided to use the charge measurement as the primary acquisition mode. The signal coming from the trigger board will be used as the validation of



Figure 9.16: Picture of the four detectors being tested in the laboratory, before they are moved to the mine.

the self-trigger. Having the charge of each channel allows for more analysis, than simply having which of the signals crossed the discriminator threshold. For example, it will be possible to determine the output that has more signal in case multiple channels are triggered. Furthermore, as the RPCs are smaller, so is the expected rate of events, making the dead time of the charge measurement less of a concern. The rate will also drop because the RPCs will be underground, and will use a trigger that will reduce the zenith angle's aperture.

The spatial resolution of each detector, i.e., the readout PCB, was designed with different pads and strips arrangements. This way, it will be possible to study the different configurations. Namely, in three of the RPCs, a central core with a grid of 7×7 small pads, each with $3.8 \times 3.8 \text{ cm}^2$, was implemented. Around it, 15 other pads and strips were added to have in total the 64 channels that each front-end can read. Thus, four big pads, some covering as much as 0.269 m^2 , were added, as well as, 11 strips with different length and width. In this layout, pads and strips were separated by guard rings of 3 mm. For the fourth RPC, it was decided to have a readout plane with 64 strips, that would cover the entire length of the PCB, and have a width of about 10 mm. A representation of the readout PCBs' layouts is shown in figure 9.17. The top RPC of the stack presented in figure 9.16 has the layout shown in the right picture the figure, while the other three have the left one.

A preliminary study with the data coming out of the laboratory tests was performed. In the case of the results presented, the trigger was the coincidence of the first and third plane counting from the bottom. Furthermore, in this analysis, the data of the top plane, with the 64 strips readout, was not used.

The first step in the analysis was to determine which channels had signal. For that, it was necessary to study the position of the pedestals. The charge distribution of each channel was obtained, and the pedestal peak fitted to a Gaussian. This way, a channel was considered active if its charge was above the mean $+ 3\sigma$, where the mean and σ were

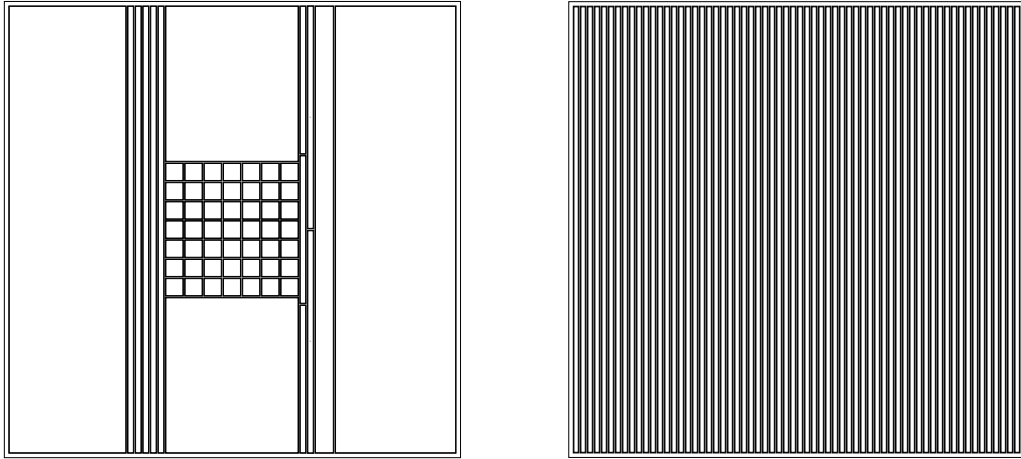


Figure 9.17: Layout of the PCB readouts. While three of the RPCs use the left layout with a mix of pads and strips, the fourth one has 64 strips with the length of the PCB, shown in the right diagram.

taken of the fit results. An example of a pedestal and its fit is shown in figure 9.18.

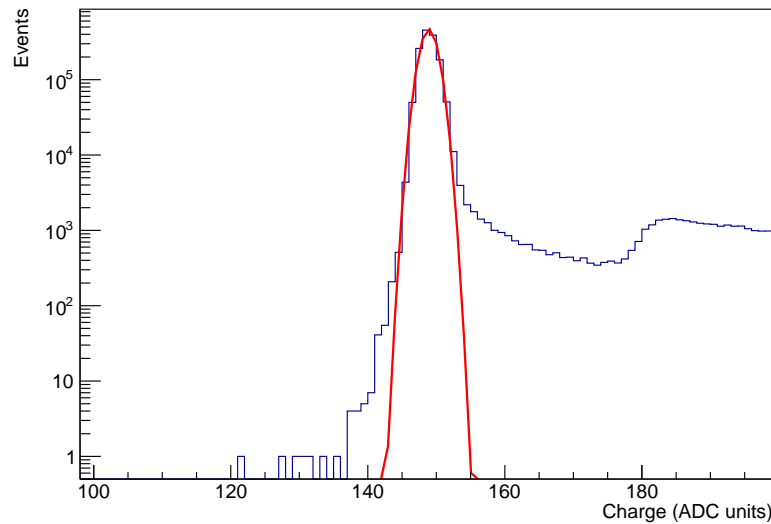


Figure 9.18: Pedestal of a channel's charge distribution. The data was fitted to a Gaussian, and the results used to determine if a particle crossed the detector. In this case, the results yield mean = 148.912 ± 0.001 ADC units, $\sigma = 1.181 \pm 0.001$ ADC units, and constant = $(4.703 \pm 0.005) \times 10^5$ events.

The next step was to study the particle trajectory using the position it crossed the detectors. Events, where only one of the channels had signal per RPC, were chosen, and some of them plotted in figure 9.19. Painted in red is the position crossed in the bottom detector, in yellow in the middle one, and in blue in the top detector. In all cases presented, as well as, other events studied, the trajectories are viable, with the yellow pad/strip in the way of the red and blue. This visualization is possible because the middle RPC is halfway between the other two detectors¹.

¹The distance between two consecutive detectors is 145 mm.

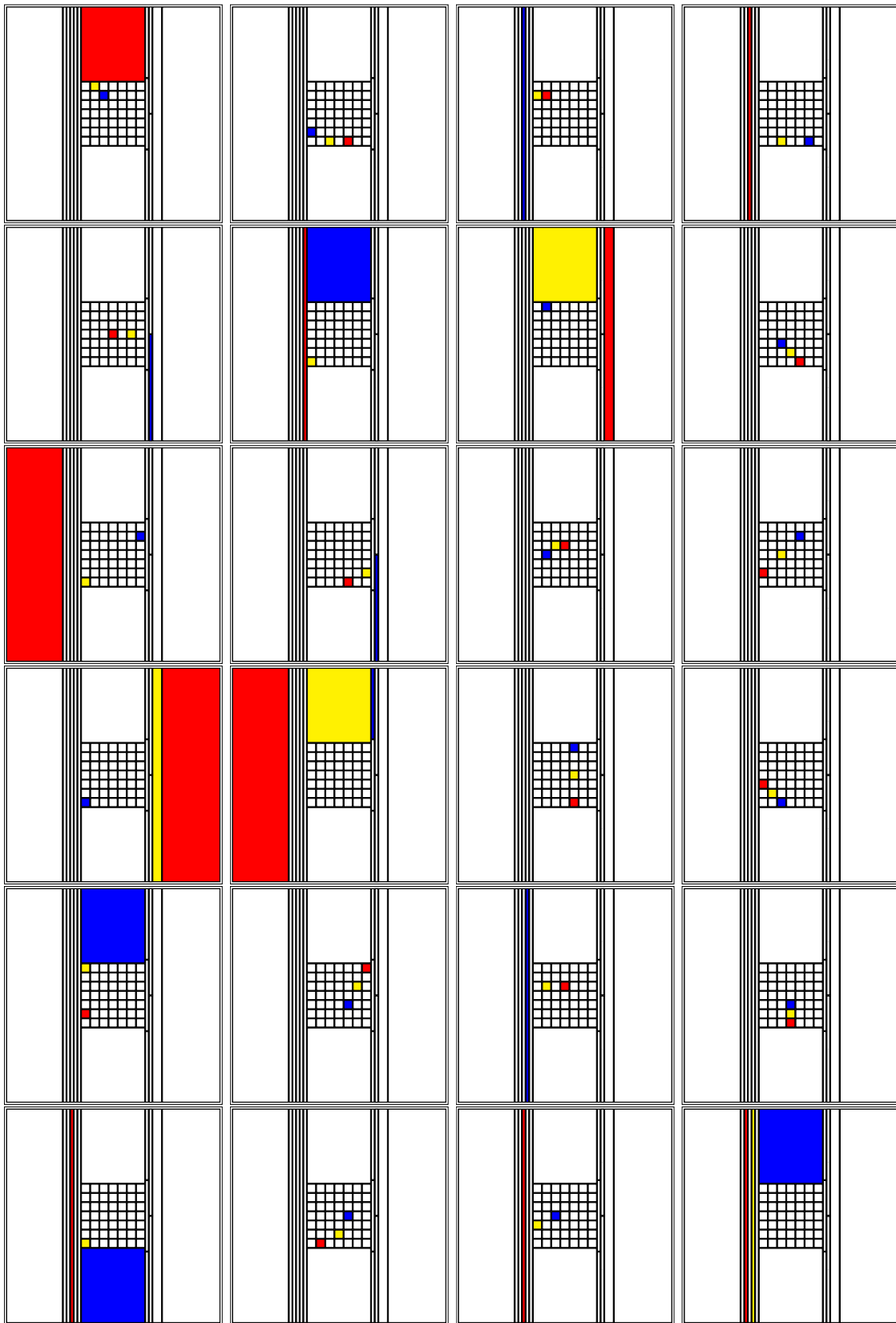


Figure 9.19: Position particle crossed the three bottom RPC of the tomography detector. The trajectory of the particle is visible, with the position painted in red corresponding to the bottom RPC, in yellow the middle one, and in blue the top one.

Then, the particle's trajectories were computed for events that crossed one pad of the central core, in the top and bottom RPC. This sample amounts to less than 10% of all measured events, with zenith angles between 0° and 53° . The efficiency of the middle RPC was obtained using only the vertical ($\theta = 0^\circ$) events of this sample. If in the middle RPC more than one channel has a signal, the chosen was the one with a higher charge. The results are presented in the plot of figure 9.20. An insert that indicates the location of each pad was added. The average efficiency is $77.54 \pm 2.49\%$, with one row, from pad 22 to 28, having a clear drop. The fact that, during these tests, the detector's applied HV is still not in its nominal value, might justify the values being lower than expected. However, it is essential also to take in consideration potential inefficiencies introduced by the front-end and the data analysis. In what the first is concerned, the ASIC parameters used were the ones optimized for the MARTA RPCs. The optimization measurement should be redone for these detectors, to guarantee that the slow shaper peak is being properly acquired. The cuts performed in the data analysis can also introduce inefficiencies since some real signals may have a charge below the pedestal's Gaussian. Lastly, one should also mention that in the data presented, the 64 discriminated outputs part of the charge measurement were not available due to a bug. Once this problem is fixed, it will be easier to determine if a signal is present or not, even if its charge is in the pedestal.

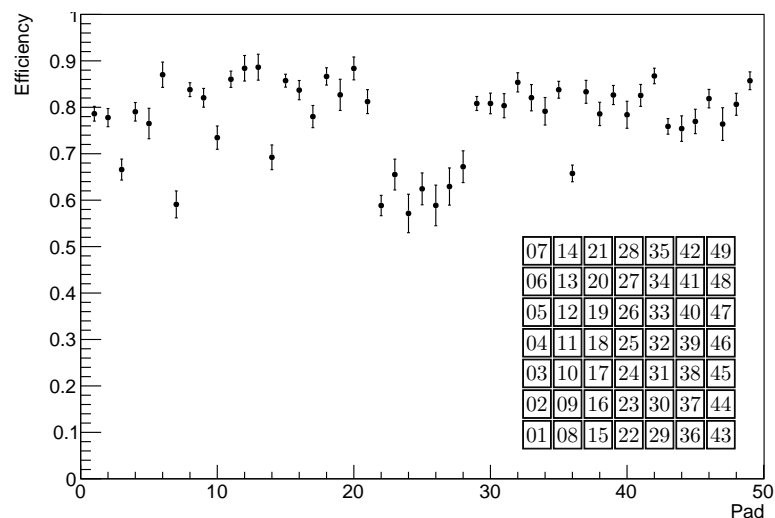


Figure 9.20: Efficiency of the pads in the central core, using vertical events. An insert was added, showing the position of each pad.

The results show, once again, that the front-end is measuring the RPC signals correctly. Furthermore, the limited analysis presented shows the potential of these detectors. However, this system is still in the process of being optimized, including some bugs that were already found in the software/firmware. More studies need to be done so that the data coming out of the RPCs is totally understood before the detector is moved to the field. For example, detailed studies for each channel need to be performed to see if the differences between these RPCs and the MARTA ones, e.g., the readout, change the signal charge distribution or even the position of the optimal hold delay.

9.4 Summary

In this chapter, the applications of the MARTA front-end were presented. The status of the deployment of the EA was given, with the first station already deployed. Due to a slow control bug, data is yet to be acquired, and it should start in the second semester of 2020. It was also shown that the charge measurement was successfully used to quality control and validate the RPCs after construction. It will be used again in the Observatory's assembly building before the detectors are moved to the field.

Two hodoscopes were put together using MARTA modules. These were built to test the SSD detectors before they are installed in the field. the hodoscope will also be used with the MARTA RPCs. The first setup was built as a prototype and a proof of concept. With it, it was possible to determine the position and efficiency of a small test scintillator. The second hodoscope is ready to test the new scintillator, although it has not been used yet. It was built so that multiple SSDs can be fully tested at once, optimising the process. A simulation of the latter setup was prepared using the SSD and RPC modules implemented in Offline. Its outcome was analysed: the dependency of the charge given by the PMTs with the particle's trajectory was the expected one. Furthermore, it was also possible to see the attenuation of the signal in the fibers. Broken fibers were also simulated, and the outcome presented, although real data still needs to be compared with the results obtained. The simulation showed the type of analyses that can be done with this hodoscope, and what are the expected results.

A detector for muon tomography was built with the front-end as the readout system. It will be installed in an decommissioned mine, used as a public science center, to study the rock profile above it. Unlike, the two previous cases, here, the charge measurement was used as the primary acquisition mode. The final detector has been built and is in testing, before it is moved to the field. Testing data shows that the system is able to compute the particles' trajectories correctly. However, it still needs to be debugged and optimised. Furthermore, data has to be understood before the detector is installed in the mine.

Lastly, one should mention that the front-end was installed in two other setups in the Pierre Auger Observatory. In both cases, it replaced the PREC system. In the Tierra del Fuego WCD, where the field performance of the RPCs (presented in section 5.4) was studied, the front-end was installed to test the system using the WCD trigger. In the Gianni Navarra WCD, where the tank performance studies were made (mentioned in section 6.3), the front-end is also installed and ready to be used to continue these tests, now with an SSD on top of the tank.

Although not much real data has come out of the applications presented in this chapter, the few that has indicates that the front-end is performing well. In the next year, when most of the detectors start measuring actual events, the performance of the front-end in all of these setups can be fully assessed. This is also true for the MARTA module itself.

10 Conclusions

The work in this thesis was developed in the framework of the Portuguese participation in the Pierre Auger Observatory. It focused on the development, validation, and deployment of a new data acquisition front-end for the MARTA upgrade. With MARTA, the goal is to have an independent and direct measurement of the air shower's muonic content, and this way determine the number of muons. This work is concluded, as the first detectors are being installed in the field, and with data taking expected to be started in the next few months.

This project, started in [217], was in a first phase about whether or not the MAROC ASIC, a chip designed to be used with multi-anode PMTs, was able to digitize the RPC avalanche signals. Being able to use this chip would allow having a compact board that can measure 64 channels at once while being low power. These are some of the most important requirements when measuring air showers in large array experiment. The stations are usually small, isolated, hard to reach, and power relies on batteries and solar panels. The initial results with the MAROC were promising, and the development of the MARTA front-end started with this ASIC as its central piece.

Two prototypes were designed and produced that consist of, among other things, the MAROC, an input stage, an FPGA for all the digital electronics, and communication links. Most of the software and firmware were developed with these prototypes, including measurement management, data storage, ASIC configuration, and communication with an acquisition computer or the Central Unit, part of the MARTA station. Moreover, two main types of measurements were implemented: hit measurement, the primary acquisition mode of MARTA, used to determine if a particle crossed the detector; and charge measurement, that acquires the charge induced in the RPC's readout plane. Having a charge measurement was another requirement of the development because this acquisition mode is planned to be used to get the number of particles in case of pile-up in the detector's pads. Furthermore, it can also be used to study the behaviour and health of the RPCs.

The final production version of the MARTA front-end was designed, tested and produced. In the end, the board consisted of an eight layers PCB, with equilibrated input lines that avoid reflections, the MAROC ASIC to digitize the RPC signals and an FPGA that manages all components and interfaces with the rest of the acquisition system outside of the front-end. All the initial requirements and the ones added during development were fulfilled. Namely, the production version has an area of $21.6 \times 14.4 \text{ cm}^2$ and power con-

sumption of 1.43 W in its field configuration (no external ADC). This value is under the limit of a few watts per RPC and corresponds to a consumption of 22 mW per channel. A total of 55 front-ends were produced, of which more than half will be installed in the MARTA EA.

The validation process of the two measurement types was mostly done in parallel with the development of the system. The first test was to determine the efficiency of the detector and front-end to muons, using the hit measurement. The acquisition was performed with a hodoscope and the RPC in testing placed in the middle. The results were obtained and compared with the ones acquired simultaneously with an established RPC DAQ (HADES FEE), showing that the front-end was as efficient as the other system. This validation test was an essential milestone in the development process because it showed that the MAROC could, in fact, be used to read the RPC signals, without introducing any inefficiencies. The next step was to understand how the hit measurement would behave in different temperature conditions. The threshold efficiency's s-curve was measured for different temperatures in a range of 50 °C, showing a negligible dependence, that will not influence data taking.

With the primary acquisition mode validated, the charge measurement was optimized and tested. The optimal ASIC configurations were determined using both generated signals through a capacitor and real RPC signals. The former worked as a trial of the measurement before the real signal could be acquired. With it, it was also possible to confirm the charge limits of the ASIC, and that the RPC avalanche signals were in that range. In the latter, after optimization as well as tests with different triggers, spectra were acquired in various detector conditions. Namely, the HV applied was changed, changing the E/N of the RPC. The results presented follow tendencies previously observed in the literature. This confirms that the front-end can measure the charge induced in the readout plane by the avalanche.

Some applications of the front-end were presented. First, the status of the EA was given, including results of the charge measurements used to quality control the RPCs' production. A hodoscope using MARTA RPCs was also put together to test the Observatory's SSDs before deployment. An initial prototype was installed and tested with a small scintillator showing that the system was working as intended. This hodoscope version was another important milestone in the development and validation of front-end since it was the first setup that acquired data outside of the assessment tests. Then a final version, that covers the full area of the SSD was built. This last hodoscope is ready to use, however, acquisitions are yet to be performed. To study the latter setup, a simulation in GEANT4 was put together, that showed what kind of analysis can be done and what are the results expected with the hodoscope. A detector for muon tomography was also assembled, using smaller RPCs with the DAQ described in this work. Unlike the hodoscope previously mentioned, this time, the charge measurement was used as the main acquisition mode. Early results of laboratory tests were presented, showing that the detector is working correctly. Debugging, testing and optimization are now ongoing and soon the detector will be ready to do muon tomography.

Lastly, it is also important to mention the work done characterizing the PREC acquisi-

tion system. This system is the predecessor of the front-end developed, and it was designed to help determine if RPCs could be used outdoors. The PREC was fully characterized, with its gain measured for different temperature conditions. The results also show that its noise level is low, and that crosstalk above this level is not detectable. This DAQ was important not only, in testing the RPCs, as mentioned above, but was also part of the setup that helped validate the simulation of the Observatory's WCD. Furthermore, it has also been used with other detectors, namely silicon PMTs.

With the first of seven MARTA stations already installed, it is now time to start doing physics with these detectors. An LDF of the number of muons should be possible with the events that will be acquired by the Peter Mazur station. As important as the first physics results, are not only the experience already gained during this development but also the one that will be obtained, running these detectors, studying their performance and analyzing the data. It will certainly open the door to apply the MARTA concept in other situation, already done for the muon tomography, and even for the development of new ideas.

To end, it should be mention that the MARTA front-end's development does not end here. The board is being redesigned to accommodate the updated ASIC version and a different FPGA with new features that will expand the flexibility of the front-end.

Appendices

A - MAROC configurable parameters

| Name | Bit number | .txt line | .txt input | MARTA configuration | Comment |
|------------------|------------|-----------|------------|---------------------|---|
| DacOnOff | 0 | 1 | 0 or 1 | 1 | - |
| OtagOnOff | 1 | 2 | 0 or 1 | 1 | - |
| SmallDac | 2 | 3 | 0 or 1 | 0 | Smaller DAC1 slope |
| DAC1 | 13 - 22 | 4 | 0 to 1023 | 210 - 300 | D1 threshold value |
| DAC2 | 3 - 12 | 5 | 0 to 1023 | 0 | D2 threshold value |
| EnOutAdc | 23 | 6 | 0 or 1 | 0 | Enables ADC output ('0' for enable) |
| InvStartCmptGray | 24 | 7 | 0 or 1 | 0 | Inverts the start ADC polarity ('0' for enable) |
| Ramp8bit | 25 | 8 | 0 or 1 | 0 | 8 bits ADC |
| Ramp10bit | 26 | 9 | 0 or 1 | 0 | 10 bits ADC |
| Mask1_ch0 - 63 | 27 - 154 | 10 - 73 | 0 or 1 | 0 | Enables D1 outputs (channel 0 to 63,'0' for enable) |
| Mask2_ch0 - 63 | | 74 - 137 | 0 or 1 | 1 | Enables D2 outputs (channel 0 to 63, '0' for enable) |
| CmdCKMux | 155 | 138 | 0 or 1 | 0 | - |
| D1D2 | 156 | 139 | 0 or 1 | 0 | Trigger output choice ('0' for D1) |
| InvDisAdc | 157 | 140 | 0 or 1 | 0 | Should be off |
| PolarTrig | 158 | 141 | 0 or 1 | 0 | Discriminator polarity ('0' for active high) |
| EnTriState | 159 | 142 | 0 or 1 | 1 | Enables triggers tri-state output buffer |
| ValidDcFsb2 | 160 | 143 | 0 or 1 | 0 | Enables half-bipolar fast shaper DC measurement |
| FC50fFsb2 | 161 | 144 | 0 or 1 | 0 | Half-bipolar feedback capacitor (50 fF) |
| FC100fFsb2 | 162 | 145 | 0 or 1 | 0 | Half-bipolar feedback capacitor (100 fF) |
| FR100kFsb2 | 163 | 146 | 0 or 1 | 0 | Half-bipolar feedback resistor (100 k Ω) |
| FR50kFsb2 | 164 | 147 | 0 or 1 | 0 | Half-bipolar feedback resistor (50 k Ω) |
| ValidDcFs | 165 | 148 | 0 or 1 | 1 | Enables bipolar and unipolar fast shaper DC measurement |
| CmdFsbFsu | 166 | 149 | 0 or 1 | 0 | Choise between unipolar and bipolar fast shaper ('0' for bipolar) |
| FC50fFsb1 | 167 | 150 | 0 or 1 | 1 | Bipolar feedback capacitor (50 fF) |
| FC100fFsb1 | 168 | 151 | 0 or 1 | 1 | Bipolar feedback capacitor (100 fF) |
| FR100kFsb1 | 169 | 152 | 0 or 1 | 1 | Bipolar feedback resistor (100 k Ω) |
| FR50kFsb1 | 170 | 153 | 0 or 1 | 1 | Bipolar feedback resistor (50 k Ω) |
| FR100kFsu | 171 | 154 | 0 or 1 | 0 | Unipolar feedback resistor (100 k Ω) |
| FR50kFsu | 172 | 155 | 0 or 1 | 0 | Unipolar feedback resistor (50 k Ω) |
| FR25kFsu | 173 | 156 | 0 or 1 | 0 | Unipolar feedback resistor (25 k Ω) |
| FC40fFsu | 174 | 157 | 0 or 1 | 0 | Unipolar feedback capacitor (40 fF) |
| FC20fFsu | 175 | 158 | 0 or 1 | 0 | Unipolar feedback capacitor (20 fF) |
| H1H2C | 176 | 159 | 0 or 1 | 1 | Hold signal to be input into the ADC ('1' for Hold1) |
| EnWilkiAdc | 177 | 160 | 0 or 1 | 1 | Enables ADC conversion |
| FC1200fSS | 178 | 161 | 0 or 1 | 1 | Slow shaper feedback capacitor (1200 fF) |
| FC600fSS | 179 | 162 | 0 or 1 | 1 | Slow shaper feedback capacitor (600 fF) |
| FC300fSS | 180 | 163 | 0 or 1 | 1 | Slow shaper feedback capacitor (300 fF) |
| SSOnOff | 181 | 164 | 0 or 1 | 1 | Slow shaper power supply |
| CBuf2pSS | 182 | 165 | 0 or 1 | 1 | RC buffer capacitor (2000 fF) |
| CBuf1pSS | 183 | 166 | 0 or 1 | 0 | RC buffer capacitor (1000 fF) |
| CBuf500fSS | 184 | 167 | 0 or 1 | 0 | RC buffer capacitor (500 fF) |
| CBuf250fSS | 185 | 168 | 0 or 1 | 1 | RC buffer capacitor (250 fF) |
| CmdFsb | 186 | 169 | 0 or 1 | 1 | Enables signals at the bipolar and half-bipolar fast shaper input |
| Cmdss | 187 | 170 | 0 or 1 | 1 | Enables signals at the slow shaper input |
| CmdFsu | 188 | 171 | 0 or 1 | 1 | Enables signals at the unipolar fast shaper input |
| Gain_ch0 - 63 | 198 - 764 | 172 - 235 | 0 to 255 | 64 | Pre-amplifier gain correction (channel 0 to 63) |
| Sum_enable0 - 63 | | 236 - 299 | 0 or 1 | 0 | Enables sum output (channel 0 to 63) |
| Ctest_ch0 - 63 | 765 - 828 | 300 - 363 | 0 or 1 | 0 | Enables ctest input (channel 0 to 63) |

Table A.1: MAROC configuration bits. The table includes the bit's name, number, line, and possible input in the .txt file, the default MARTA configuration, and comments on each parameter. For more information, refer to the ASIC datasheet [103, 104]. '1' is 'enable' unless stated.

B - Hodoscope trajectory calculations

The position (x, y) in meters where the RPC was crossed is calculated using the following expressions:

$$\begin{aligned} x &= 0.15 \times \text{column} \\ y &= 0.19 \times \text{row} \end{aligned} \quad (\text{B.1})$$

where column and row vary from 0 to 7. Column is calculated as the closest integer to $(\text{pad} - 1)/8 - 0.5$ and row is calculated as $(\text{pad} - 1) - 8 \times \text{column}$. This way position $(0,0)$ corresponds to the center of pad 1.

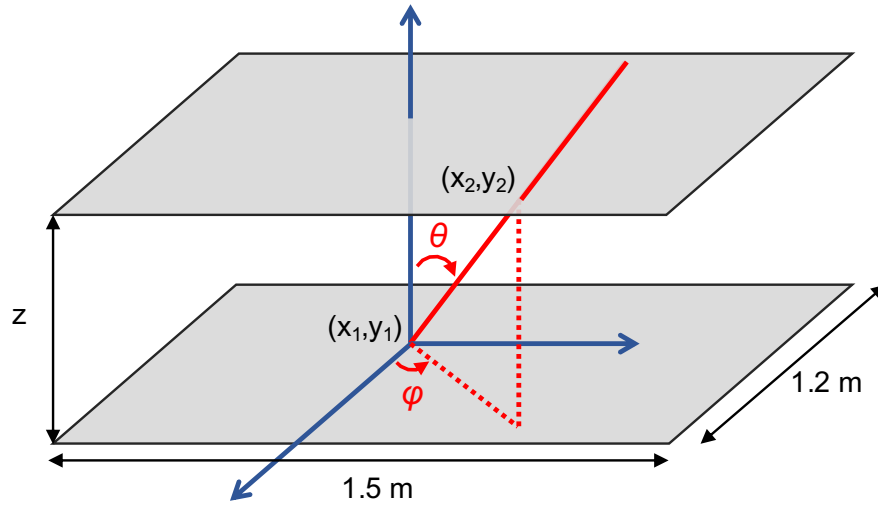


Figure B.1: Angles representation. ϕ is the azimuthal angle and θ the zenithal angle.

Knowing the position $(x_1, y_1, 0)$ in the bottom RPC and (x_2, y_2, z) in the top RPC, as shown in figure B.1, it is possible to get the trajectory of the crossing particle by calculating the azimuthal (ϕ) and zenithal (θ) angle:

$$\begin{aligned} \phi &= \arctan\left(\frac{y_2 - y_1}{x_2 - x_1}\right) \\ \theta &= \arccos\left(\frac{z}{\sqrt{(x_2 - x_1)^2 + (y_2 - y_1)^2 + z^2}}\right) \end{aligned} \quad (\text{B.2})$$

Using these angles and the position the particle crossed one of the RPCs, it is possible to determine every point in its trajectory.

Bibliography

- [1] A. Aab *et al.*, “The Pierre Auger Cosmic Ray Observatory,” *Nucl. Instrum. Methods A*, vol. 798, p. 172, 2015.
- [2] J. Abraham *et al.*, “Observation of the suppression of the flux of cosmic rays above 4×10^{19} eV,” *Phys. Rev. Lett.*, vol. 101, p. 061101, 2008.
- [3] A. Aab *et al.*, “Observation of a large-scale anisotropy in the arrival directions of cosmic rays above 8×10^{18} eV,” *Science*, vol. 357, no. 6357, p. 1266, 2017.
- [4] P. Abreu *et al.*, “MARTA: a high-energy cosmic-ray detector concept for high-accuracy muon measurement,” *The European Physical Journal C*, vol. 78, no. 4, p. 333, 2018.
- [5] L. Lopes *et al.*, “Long term experience in Autonomous Stations and production quality control,” *Journal of Instrumentation*, vol. 14, p. C07002, 2019.
- [6] S. Blin *et al.*, “MAROC, a generic photomultiplier readout chip,” *Journal of Instrumentation*, vol. 5, no. 12, p. C12007, 2010.
- [7] T. Wulf, “Beobachtungen über die Strahlung hoher Durchdringungsfähigkeit auf dem Eiffelturm,” *Phys. Z.*, vol. 11, p. 811, 1910.
- [8] D. Pacini, “La radiazione penetrante alla superficie ed in seno alle acque,” *Il Nuovo Cimento*, vol. 3, no. 1, p. 93, 1912.
- [9] A. Gockel, “Luftelektrische Beobachtungen bei einer Ballonfahrt,” *Phys. Z.*, vol. 11, p. 280, 1910.
- [10] V. F. Hess, “Über Beobachtungen der durchdringenden Strahlung bei sieben Freiballonfahrten,” *Phys. Z.*, vol. 13, p. 1084, 1912.
- [11] T. H. Johnson, “The Azimuthal Asymmetry of the Cosmic Radiation,” *Phys. Rev.*, vol. 43, p. 834, 1933.
- [12] L. Alvarez and A. H. Compton, “A Positively Charged Component of Cosmic Rays,” *Phys. Rev.*, vol. 43, p. 835, 1933.

- [13] B. Rossi, "Directional Measurements on the Cosmic Rays Near the Geomagnetic Equator," *Phys. Rev.*, vol. 45, p. 212, 1934.
- [14] B. Rossi, "Misure sulla distribuzione angolare di intensita della radiazione penetrante all' Asmara," *Supplemento a la Ricerca Scientifica*, vol. 1, p. 579, 1934.
- [15] P. Auger *et al.*, "Extensive Cosmic-Ray Showers," *Rev. Mod. Phys.*, vol. 11, p. 288, 1939.
- [16] C. D. Anderson, "The Positive Electron," *Phys. Rev.*, vol. 43, p. 491, 1933.
- [17] S. H. Neddermeyer and C. D. Anderson, "Cosmic-Ray Particles of Intermediate Mass," *Phys. Rev.*, vol. 54, p. 88, 1938.
- [18] D. H. Perkins, "Nuclear Disintegration by Meson Capture," *Nature*, vol. 159, no. 4030, p. 126, 1947.
- [19] J. Linsley, "Evidence for a Primary Cosmic-Ray Particle with Energy 10^{20} eV," *Phys. Rev. Lett.*, vol. 10, p. 146, 1963.
- [20] R. Engel *et al.*, "Extensive Air Showers and Hadronic Interactions at High Energy," *Annual Review of Nuclear and Particle Science*, vol. 61, no. 1, p. 467, 2011.
- [21] T. Antoni *et al.*, "KASCADE measurements of energy spectra for elemental groups of cosmic rays: Results and open problems," *Astroparticle Physics*, vol. 24, no. 1, p. 1, 2005.
- [22] K. Greisen, "End to the Cosmic-Ray Spectrum?," *Phys. Rev. Lett.*, vol. 16, p. 748, 1966.
- [23] G. T. Zatsepin and V. A. Kuz'min, "Upper limit of the spectrum of cosmic rays," *JETP Lett.*, vol. 4, p. 78, 1966.
- [24] J. J. Beatty, J. Matthews, and S. Wakely, "Review of Particle Physics: Cosmic Rays," *Phys. Rev. D*, vol. 98, p. 424, 2018.
- [25] P. K. F. Grieder, *Cosmic rays at earth*. Bern, Switerland: Elsevier Science, 2001.
- [26] T. Gaisser and A. M. Hillas, "Reliability of the method of constant intensity cuts for reconstructing the average development of vertical showers," *Proceedings, 36nd International Cosmic Ray Conference (ICRC 1977): Plovdiv, Bulgaria*, 1997.
- [27] K. Kamata and J. Nishimura, "The Lateral and the Angular Structure Functions of Electron Showers," *Progress of Theoretical Physics Supplement*, vol. 6, p. 93, 1958.
- [28] K. Greisen, "Cosmic Ray Showers," *Annual Review of Nuclear Science*, vol. 10, no. 1, p. 63, 1960.

-
- [29] S. Sciutto, “AIRES: A system for air shower simulations. User’s guide and reference manual,” 1999.
- [30] D. Heck *et al.*, “CORSIKA: A Monte Carlo code to simulate extensive air showers,” 1998.
- [31] S. Ostapchenko, “Monte Carlo treatment of hadronic interactions in enhanced Pomeron scheme: QGSJET-II model,” *Phys. Rev. D*, vol. 83, p. 014018, 2011.
- [32] T. Pierog *et al.*, “EPOS LHC: Test of collective hadronization with data measured at the CERN Large Hadron Collider,” *Phys. Rev.*, vol. C92, no. 3, p. 034906, 2015.
- [33] F. Riehn *et al.*, “The hadronic interaction model SIBYLL 2.3c and Feynman scaling,” *PoS*, vol. ICRC2017, p. 301, 2018.
- [34] T. Pierog, “Air Shower Simulation with a New Generation of post-LHC Hadronic Interaction Models in CORSIKA,” *PoS*, vol. ICRC2017, p. 1100, 2018.
- [35] J. V. Jelley, “Cherenkov radiation and its applications,” *British Journal of Applied Physics*, vol. 6, no. 7, p. 227, 1955.
- [36] F. G. Schröder, “Radio detection of cosmic-ray air showers and high-energy neutrinos,” *Progress in Particle and Nuclear Physics*, vol. 93, p. 1, 2017.
- [37] K. Daniel and I. Lerche, “Radiation from cosmic ray air showers,” *Proc. R. Soc. Lond. A*, vol. 289, 1966.
- [38] A. A. Abdo *et al.*, “Measurement of the Cosmic Ray $e^+ + e^-$ Spectrum from 20 GeV to 1 TeV with the Fermi Large Area Telescope,” *Phys. Rev. Lett.*, vol. 102, p. 181101, 2009.
- [39] O. Adriani *et al.*, “PAMELA Measurements of Cosmic-Ray Proton and Helium Spectra,” *Science*, vol. 332, no. 6025, p. 69, 2011.
- [40] R. Battiston, “The antimatter spectrometer (AMS-02): A particle physics detector in space,” *Nucl. Instrum. Methods A*, vol. 588, no. 1, p. 227, 2008.
- [41] E. Seo *et al.*, “Cosmic-ray energetics and mass (CREAM) balloon experiment,” *Advances in Space Research*, vol. 30, no. 5, p. 1263, 2002.
- [42] L. Baldini, “Space-Based Cosmic-Ray and Gamma-Ray Detectors: a Review,” 2014.
- [43] K. Bernlöhr, “Measuring cosmic-ray and gamma-ray air showers.” <https://www.mpi-hd.mpg.de/hfm/CosmicRay/ShowerDetection.html>. [Online; accessed 30-September-2019].
- [44] A. Haungs, “Cosmic Rays from the Knee to the Ankle,” *Physics Procedia*, vol. 61, p. 425, 2015.

- [45] A. J. Smith, “HAWC: Design, Operation, Reconstruction and Analysis,” *PoS*, vol. ICRC2015, p. 966, 2016.
- [46] R. Abbasi *et al.*, “IceTop: The surface component of IceCube,” *Nucl. Instrum. Methods A*, vol. 700, p. 188, 2013.
- [47] W. Apel *et al.*, “The KASCADE-Grande experiment,” *Nucl. Instrum. Methods A*, vol. 620, no. 2, p. 202, 2010.
- [48] R. Monkhoev *et al.*, “The Tunka-Grande experiment,” *Journal of Instrumentation*, vol. 12, no. 06, p. C06019, 2017.
- [49] N. Chiba *et al.*, “Akeno Giant Air Shower Array (AGASA) covering 100 km² area,” *Nucl. Instrum. Methods A*, vol. 311, no. 1, p. 338, 1992.
- [50] T. Abu-Zayyad *et al.*, “The surface detector array of the Telescope Array experiment,” *Nucl. Instrum. Methods A*, vol. 689, p. 87, 2012.
- [51] G. Aielli *et al.*, “Highlights from the ARGO-YBJ experiment,” *Nucl. Instrum. Methods A*, vol. 661, p. S50, 2012. X. Workshop on Resistive Plate Chambers and Related Detectors (RPC 2010).
- [52] R. Cornils *et al.*, “The optical system of the H.E.S.S. imaging atmospheric Cherenkov telescopes. Part II: mirror alignment and point spread function,” *Astroparticle Physics*, vol. 20, no. 2, p. 129, 2003.
- [53] D. Tesaro, “The upgraded MAGIC Cherenkov telescopes,” *Nucl. Instrum. Methods A*, vol. 766, p. 65, 2014.
- [54] J. Holder, “Latest results from VERITAS: Gamma 2016,” *AIP Conference Proceedings*, vol. 1792, no. 1, p. 020013, 2017.
- [55] C. Bigongiari, “The Cherenkov Telescope Array,” *Nuclear and Particle Physics Proceedings*, vol. 279-281, p. 174, 2016.
- [56] G. Thomson, “New Results from the HiRes Experiment,” *Nuclear Physics B - Proceedings Supplements*, vol. 136, p. 28, 2004.
- [57] M. Cassidy *et al.*, “CASA-BLANCA: A Large Non-imaging Cherenkov Detector at CASA-MIA,” 1997.
- [58] S. Berezhnev *et al.*, “The Tunka-133 EAS Cherenkov light array: Status of 2011,” *Nucl. Instrum. Methods A*, vol. 692, p. 98, 2012.
- [59] N. Budnev *et al.*, “The TAIGA experiment: From cosmic-ray to gamma-ray astronomy in the Tunka valley,” *Nucl. Instrum. Methods A*, vol. 845, p. 330, 2017.
- [60] H. R. Allan and J. K. Jones, “Radio Pulses from Extensive Air Showers,” *Nature*, vol. 212, no. 5058, p. 129, 1966.

-
- [61] M. Gottowik, “Measurements of Inclined Air Showers with the Auger Engineering Radio Array at the Pierre Auger Observatory,” *PoS*, vol. ICRC2019, p. 274, 2019.
- [62] P. Bezyazeev *et al.*, “Measurement of cosmic-ray air showers with the Tunka Radio Extension (Tunka-Rex),” *Nucl. Instrum. Methods A*, vol. 802, p. 89, 2015.
- [63] T. Gaisser, “Viewpoint: Cosmic-Ray Showers Reveal Muon Mystery,” *Physics* 9, no. 125, 2016.
- [64] A. Aab *et al.*, “The Pierre Auger Observatory Upgrade - Preliminary Design Report,” 2016.
- [65] A. Botti, “The AMIGA underground muon detector of the Pierre Auger Observatory - performance and event reconstruction,” *PoS*, vol. ICRC2019, p. 202, 2019.
- [66] I. Allekotte *et al.*, “The surface detector system of the Pierre Auger Observatory,” *Nucl. Instrum. Methods A*, vol. 586, no. 3, p. 409, 2008.
- [67] J. Abraham *et al.*, “The fluorescence detector of the Pierre Auger Observatory,” *Nucl. Instrum. Methods A*, vol. 620, no. 2, p. 227, 2010.
- [68] C. Meurer and N. Scharf, “HEAT – a low energy enhancement of the Pierre Auger Observatory,” *Astrophysics and Space Sciences Transactions*, vol. 7, no. 2, p. 183, 2011.
- [69] S. BenZvi *et al.*, “The Lidar system of the Pierre Auger Observatory,” *Nucl. Instrum. Methods A*, vol. 574, no. 1, p. 171, 2007.
- [70] B. Fick *et al.*, “The Central Laser Facility at the Pierre Auger Observatory,” *Journal of Instrumentation*, vol. 1, no. 11, p. P11003, 2006.
- [71] A. Aab *et al.*, “Observation of inclined EeV air showers with the radio detector of the Pierre Auger Observatory,” *Journal of Cosmology and Astroparticle Physics*, vol. 2018, no. 10, p. 026, 2018.
- [72] J. Abraham *et al.*, “Trigger and aperture of the surface detector array of the Pierre Auger Observatory,” *Nucl. Instrum. Methods A*, vol. 613, no. 1, p. 29, 2010.
- [73] S. Argirò *et al.*, “The offline software framework of the Pierre Auger Observatory,” vol. 580, no. 3, p. 1485, 2007.
- [74] Pierre Auger Collaboration, “Reconstruction of Events Recorded by the Surface Detector of the Pierre Auger Observatory,” *to be published*, 2020.
- [75] C. Bonifazi, “The angular resolution of the Pierre Auger Observatory,” *Nuclear Physics B - Proceedings Supplements*, vol. 190, p. 20, 2009.
- [76] J. Hersil *et al.*, “Observations of Extensive Air Showers near the Maximum of Their Longitudinal Development,” *Phys. Rev. Lett.*, vol. 6, p. 22, 1961.

- [77] V. Verzi, “Measurement of the energy spectrum of ultra-high energy cosmic rays using the Pierre Auger Observatory,” *PoS*, vol. ICRC2019, p. 450, ICRC2019.
- [78] V. Verzi, “The Energy Scale of the Pierre Auger Observatory,” in *Proceedings, 33rd International Cosmic Ray Conference (ICRC2013): Rio de Janeiro, Brazil, July 2-9, 2013*, p. 0928.
- [79] T. P. A. collaboration, “Measurement of the cosmic ray spectrum above 4×10^{18} eV using inclined events detected with the Pierre Auger Observatory,” *Journal of Cosmology and Astroparticle Physics*, vol. 2015, no. 08, p. 049, 2015.
- [80] A. Aab *et al.*, “Muons in air showers at the Pierre Auger Observatory: Mean number in highly inclined events,” *Physical Review D*, vol. 91, no. 3, 2015.
- [81] A. Aab *et al.*, “Reconstruction of Inclined Air Showers Detected with the Pierre Auger Observatory,” *JCAP*, vol. 1408, p. 019, 2014.
- [82] J. Rosado *et al.*, “On the absolute value of the air-fluorescence yield,” *Astroparticle Physics*, vol. 55, p. 51, 2014.
- [83] J. Abraham *et al.*, “Measurement of the Energy Spectrum of Cosmic Rays above 10^{18} eV Using the Pierre Auger Observatory,” *Phys. Lett.*, vol. B685, p. 239, 2010.
- [84] A. Aab *et al.*, “Measurement of the Cosmic Ray Spectrum above 4×10^{18} eV Using Inclined Events Detected with the Pierre Auger Observatory,” *JCAP*, vol. 1508, p. 049, 2015.
- [85] A. Haungs *et al.*, “Investigating the 2nd knee: The KASCADE-Grande experiment,” *Journal of Physics: Conference Series*, vol. 47, p. 238, oct 2006.
- [86] A. Yushkov, “Mass composition of cosmic rays with energies above $10^{17.2}$ eV from the hybrid data of the Pierre Auger Observatory,” *PoS*, vol. ICRC2019, p. 482, ICRC2019.
- [87] A. Aab *et al.*, “An Indication of anisotropy in arrival directions of ultra-high-energy cosmic rays through comparison to the flux pattern of extragalactic gamma-ray sources,” *Astrophys. J.*, vol. 853, no. 2, p. L29, 2018.
- [88] L. Cazon *et al.*, “A model for the transport of muons in extensive air showers,” *Astroparticle Physics*, vol. 36, no. 1, p. 211, 2012.
- [89] S. Andringa *et al.*, “The muonic longitudinal shower profiles at production,” *Astroparticle Physics*, vol. 35, no. 12, p. 821, 2012.
- [90] R. R. Prado *et al.*, “Interpretation of measurements of the number of muons in extensive air shower experiments,” *Astroparticle Physics*, vol. 83, p. 40, 2016.

-
- [91] A. Aab *et al.*, “Muons in air showers at the Pierre Auger Observatory: Mean number in highly inclined events,” *Phys. Rev. D*, vol. 91, p. 032003, 2015.
- [92] R. U. Abbasi *et al.*, “Study of muons from ultrahigh energy cosmic ray air showers measured with the Telescope Array experiment,” *Phys. Rev. D*, vol. 98, p. 022002, 2018.
- [93] F. Riehn, “Measurement of the fluctuations in the number of muons in inclined air showers with the Pierre Auger Observatory,” *PoS*, vol. ICRC2019, p. 404, ICRC2019.
- [94] L. Cazon *et al.*, “Probing the high energy spectrum of neutral pions in ultra-high energy proton-Air interactions,” *PoS*, vol. ICRC2019, p. 226, ICRC2019.
- [95] R. Santonico and R. Cardarelli, “Development of resistive plate counters,” *Nucl. Instrum. Methods Phys. Res.*, vol. 187, no. 2, pp. 377 – 380, 1981.
- [96] L. Lopes *et al.*, “Study of standalone RPC detectors for cosmic ray experiments in outdoor environment,” *Journal of Instrumentation*, vol. 8, no. 03, p. T03004, 2013.
- [97] L. Lopes *et al.*, “Resistive Plate Chambers for the Pierre Auger array upgrade,” *Journal of Instrumentation*, vol. 9, p. C10023, 2014.
- [98] L. Lopes *et al.*, “Outdoor field experience with autonomous RPC based stations,” *Journal of Instrumentation*, vol. 11, no. 09, p. C09011, 2016.
- [99] R. Conceição *et al.*, “Autonomous RPCs for a Cosmic Ray ground array,” *PoS*, vol. ICRC2017, p. 379, 2018.
- [100] R. Conceição *et al.*, “MARTA simulation in the Offline,” *GAP2020-019*, 2020.
- [101] P. Abreu *et al.*, “MARTA’s (Muon Array with RPC for Tagging Air showers) DAQ system,” *PoS*, vol. TWEPP2019, p. 98, 2019.
- [102] P. Assis *et al.*, “The MARTA (Muon Array With RPCs for Tagging Air Showers) Front-End Acquisition System,” *IEEE Transactions on Nuclear Science*, vol. 65, no. 12, p. 2920, 2018.
- [103] OMEGA, “Datasheet MAROC3.” https://www.ge.infn.it/~musico/DownloadFiles/Maroc/datasheet_MAROC3_V7.pdf. [Online; accessed 25-November-2019].
- [104] Weeroc, “Datasheet MAROC3A.” <https://www.weeroc.com/my-weeroc/download-center/maroc-3a/29-maroc-3a-datasheet/file>. [Online; accessed 17-January-2020].
- [105] Intel, “Cyclone V Hard Processor System Technical Reference Manual.” 2018.

- [106] P. Assis *et al.*, “Design and characterization of the PREC (Prototype Readout Electronics for Counting particles),” *Journal of Instrumentation*, vol. 11, no. 08, p. T08004, 2016.
- [107] S. Agostinelli *et al.*, “Geant4—a simulation toolkit,” *Nucl. Instrum. Methods A*, vol. 506, no. 3, pp. 250 – 303, 2003.
- [108] J. Allison *et al.*, “Geant4 developments and applications,” *IEEE Transactions on Nuclear Science*, vol. 53, no. 1, p. 270, 2006.
- [109] J. Allison *et al.*, “Recent developments in Geant4,” *Nucl. Instrum. Methods A*, vol. 835, p. 186, 2016.
- [110] A. Supanitsky *et al.*, “Underground muon counters as a tool for composition analyses,” *Astroparticle Physics*, vol. 29, no. 6, p. 461, 2008.
- [111] L. Cazon *et al.*, “Depth development of extensive air showers from muon time distributions,” *Astroparticle Physics*, vol. 23, no. 4, p. 393, 2005.
- [112] A. Aab *et al.*, “Muons in air showers at the Pierre Auger Observatory: Measurement of atmospheric production depth,” *Phys. Rev. D*, vol. 90, p. 012012, 2014.
- [113] J. Espadanal *et al.*, “Sensitivity of EAS measurements to the energy spectrum of muons,” *Astroparticle Physics*, vol. 86, p. 32, 2017.
- [114] R. Conceição, “MARTA Engineering Array physics,” Presented at the 9th MARTA Progress Meeting, Lisbon, Portugal, October 2016.
- [115] A. Aab *et al.*, “Studies on the response of an Auger water-Cherenkov detector to atmospheric muons using a RPC hodoscope,” *To be published*, vol. TBP, p. TBP, 2020.
- [116] A. Roberts, “Development of the Spark Chamber: A Review,” *Review of Scientific Instruments*, vol. 32, no. 5, p. 482, 1961.
- [117] V. Parkhomchuck, Y. Pestov, and N. Petrovykh, “A spark counter with large area,” *Nuclear Instruments and Methods*, vol. 93, no. 2, p. 269, 1971.
- [118] R. Cardarelli *et al.*, “Progress in resistive plate counters,” *Nucl. Instrum. Methods A*, vol. 263, no. 1, 1988.
- [119] R. Cardarelli *et al.*, “Performance of a resistive plate chamber operating with pure CF₃Br,” *Nucl. Instrum. Methods A*, vol. 333, no. 2, pp. 399 – 403, 1993.
- [120] E. C. Zeballos *et al.*, “A new type of resistive plate chamber: The multigap RPC,” *Nucl. Instrum. Methods A*, vol. 374, no. 1, p. 132, 1996.
- [121] E. C. Zeballos *et al.*, “A comparison of the wide gap and narrow gap resistive plate chamber,” *Nucl. Instrum. Methods A*, vol. 373, no. 1, p. 35, 1996.

-
- [122] P. Fonte *et al.*, “A new high-resolution TOF technology,” *Nucl. Instrum. Methods A*, vol. 443, no. 1, p. 201, 2000.
- [123] P. Fonte and other, “High-resolution RPCs for large TOF systems,” *Nucl. Instrum. Methods A*, vol. 449, no. 1, p. 295, 2000.
- [124] C. Lippmann, *Detector Physics of Resistive Plate Chambers*. PhD thesis, Frankfurt U., 2003.
- [125] E. C. Zeballos *et al.*, “Pure avalanche mode operation of a 2 mm gap resistive plate chamber,” *Nucl. Instrum. Methods A*, vol. 396, no. 1, pp. 93 – 102, 1997.
- [126] C. Lippmann *et al.*, “Space charge effects in Resistive Plate Chambers,” *Nucl. Instrum. Methods A*, vol. 517, no. 1, p. 54, 2004.
- [127] M. Abbrescia *et al.*, “The simulation of resistive plate chambers in avalanche mode: charge spectra and efficiency,” *Nucl. Instrum. Methods A*, vol. 431, no. 3, p. 413, 1999.
- [128] M. Abbrescia *et al.*, “Progresses in the simulation of resistive plate chambers in avalanche mode,” *Nuclear Physics B - Proceedings Supplements*, vol. 78, no. 1, p. 459, 1999. Advanced Technology and Particle Physics.
- [129] G. Aielli *et al.*, “Saturated logistic avalanche model,” *Nucl. Instrum. Methods A*, vol. 508, no. 1, p. 6, 2003. Proceedings of the Sixth International Workshop on Resistive Plate Chambers and Related Detectors.
- [130] P. Fonte and V. Peskov, “High-resolution TOF with RPCs,” *Nucl. Instrum. Methods A*, vol. 477, no. 1, p. 17, 2002. 5th Int. Conf. on Position-Sensitive Detectors.
- [131] P. Fonte, “Analytical calculation of the charge spectrum generated by ionizing particles in Resistive Plate Chambers at low gas gain,” *Journal of Instrumentation*, vol. 8, p. P04017, apr 2013.
- [132] W. Riegler and C. Lippmann, “The physics of Resistive Plate Chambers,” *Nucl. Instrum. Methods A*, vol. 518, no. 1, p. 86, 2004. Frontier Detectors for Frontier Physics: Proceedin.
- [133] P. Fonte, “Review of RPC simulation and modelling,” *PoS*, vol. RPC2012, p. 033, 2012.
- [134] H. Raether, *Electron avalanches and breakdown in gases*. Butterworths, 1964.
- [135] I. Kitayama *et al.*, “Optical observation of discharge in resistive plate chamber,” *Nucl. Instrum. Methods A*, vol. 424, no. 2, p. 474, 1999.
- [136] A. Semak *et al.*, “Properties of discharge in the narrow gap glass RPC,” *Nucl. Instrum. Methods A*, vol. 456, no. 1, p. 50, 2000. Proceedings of the 5th Int. Workshop on Resistive Plate Chambers and Related Detectors.

- [137] R. Cardarelli *et al.*, “Avalanche and streamer mode operation of resistive plate chambers,” *Nucl. Instrum. Methods A*, vol. 382, no. 3, p. 470, 1996.
- [138] R. Arnaldi *et al.*, “Study of Resistive Plate Chambers for the ALICE dimuon spectrometer,” *Nuclear Physics B - Proceedings Supplements*, vol. 78, no. 1, p. 84, 1999. Advanced Technology and Particle Physics.
- [139] C. Bacci *et al.*, “High altitude test of RPCs for the Argo YBJ experiment,” *Nucl. Instrum. Methods A*, vol. 443, no. 2, p. 342, 2000.
- [140] A. Aloisio *et al.*, “Long-term performance of the L3 RPC system,” *Nucl. Instrum. Methods A*, vol. 456, no. 1, p. 113, 2000. Proceedings of the 5th Int. Workshop on Resistive Plate Chambers and Related Detectors.
- [141] F. Bossù, “The trigger system of the muon spectrometer of the ALICE experiment at the LHC,” *Nuclear Physics B - Proceedings Supplements*, vol. 215, no. 1, p. 204, 2011. Proceedings of the 12th Topical Seminar on Innovative Particle and Radiation Detectors (IPRD10).
- [142] A. Ferretti, “The upgrade of the RPC-based ALICE Muon Trigger,” *Journal of Instrumentation*, vol. 14, p. C06011–C06011, Jun 2019.
- [143] J. G. Wang, “RPC performance at KLM/BELLE,” *Nucl. Instrum. Methods A*, vol. 508, no. 1, p. 133, 2003. Proceedings of the Sixth International Workshop on Resistive Plate Chambers and Related Detectors.
- [144] Y. Xie *et al.*, “First results of the RPC commissioning at BESIII,” *Nucl. Instrum. Methods A*, vol. 599, no. 1, p. 20, 2009.
- [145] A. Bertolin *et al.*, “The RPC system of the OPERA experiment,” *Nucl. Instrum. Methods A*, vol. 602, no. 3, p. 631, 2009. Proceedings of the 9th International Workshop on Resistive Plate Chambers and Related Detectors.
- [146] F. Ferroni, “The second generation BaBar RPCs: Final evaluation of performances,” *Nucl. Instrum. Methods A*, vol. 602, no. 3, p. 649, 2009. Proceedings of the 9th International Workshop on Resistive Plate Chambers and Related Detectors.
- [147] G. Agnetta *et al.*, “Use of RPC in EAS physics with the COVER_PLASTEX experiment,” *Nucl. Instrum. Methods A*, vol. 381, no. 1, p. 64, 1996.
- [148] D. S. Giuseppe *et al.*, “Latest results from the ARGO-YBJ experiment,” *Journal of Physics: Conference Series*, vol. 632, p. 012089, 2015.
- [149] G. Bari *et al.*, “Analysis of the performance of the MONOLITH prototype,” *Nucl. Instrum. Methods A*, vol. 508, no. 1, p. 170, 2003. Proceedings of the Sixth International Workshop on Resistive Plate Chambers and Related Detectors.

-
- [150] A. Bhatt *et al.*, “Improvement of time measurement with the INO-ICAL resistive plate chambers,” *Journal of Instrumentation*, vol. 11, p. C11001, nov 2016.
- [151] W. Riegler, “Trigger detectors for the LHCb muon system VCI 2001,” *Nucl. Instrum. Methods A*, vol. 478, no. 1, p. 180, 2002. Proceedings of the ninth Int.Conf. on Instrumentation.
- [152] G. Aielli *et al.*, “Test and performances of the RPC trigger chambers of the ATLAS experiment at LHC,” *Nucl. Instrum. Methods A*, vol. 533, no. 1, p. 193, 2004. Proceedings of the Seventh International Workshop on Resistive Plate Chambers and Related Detectors.
- [153] M. Konecki, “The RPC based trigger for the CMS experiment at the LHC,” *Journal of Instrumentation*, vol. 9, p. C07002, jul 2014.
- [154] X. He, “Results from the PHENIX RPC R&D and long-term performance monitoring,” *Nucl. Instrum. Methods A*, vol. 661, p. S86, 2012. X. Workshop on Resistive Plate Chambers and Related Detectors (RPC 2010).
- [155] “ATLAS muon spectrometer: Technical design report,” 1997.
- [156] M. Williams, “The multigap RPC: the time-of-flight detector for the ALICE experiment,” *Nucl. Instrum. Methods A*, vol. 478, no. 1, p. 183, 2002. Proceedings of the ninth Int.Conf. on Instrumentation.
- [157] V. Ammosov *et al.*, “The HARP resistive plate chambers: Characteristics and physics performance,” *Nucl. Instrum. Methods A*, vol. 602, no. 3, p. 639, 2009. Proceedings of the 9th International Workshop on Resistive Plate Chambers and Related Detectors.
- [158] F. Geurts *et al.*, “Performance of the prototype MRPC detector for STAR,” *Nucl. Instrum. Methods A*, vol. 533, no. 1, p. 60, 2004. Proceedings of the Seventh International Workshop on Resistive Plate Chambers and Related Detectors.
- [159] D. Belver *et al.*, “The HADES RPC inner TOF wall,” *Nucl. Instrum. Methods A*, vol. 602, no. 3, p. 687, 2009. Proceedings of the 9th International Workshop on Resistive Plate Chambers and Related Detectors.
- [160] A. Schüttauf *et al.*, “Multi-strip MRPCs for FOPI,” *Nucl. Instrum. Methods A*, vol. 602, no. 3, p. 679, 2009. Proceedings of the 9th International Workshop on Resistive Plate Chambers and Related Detectors.
- [161] N. Tomida *et al.*, “The TOF-RPC for the BGO-EGG experiment at LEPS2,” *Journal of Instrumentation*, vol. 9, no. 10, p. C10008, 2014.
- [162] Z. Wu *et al.*, “First results of the new endcap TOF commissioning at BESIII,” *Journal of Instrumentation*, vol. 11, no. 07, p. C07005, 2016.

- [163] V. Kekelidze *et al.*, “Status of the NICA project at JINR,” *Nuclear and Particle Physics Proceedings*, vol. 273-275, p. 170, 2016. 37th International Conference on High Energy Physics (ICHEP).
- [164] I. Deppner and N. Herrmann, “The CBM Time-of-Flight system,” *Journal of Instrumentation*, vol. 14, no. 09, p. C09020, 2019.
- [165] D. D. Gruttola, “Particle IDentification with the ALICE Time-Of-Flight detector at the LHC,” *Journal of Instrumentation*, vol. 9, no. 10, pp. C10019–C10019, 2014.
- [166] A. Blanco *et al.*, “TRAGALDABAS: a new RPC based detector for the regular study of cosmic rays,” *Journal of Instrumentation*, vol. 9, no. 09, p. C09027, 2014.
- [167] E. L. Menedeu, “RPC application in muography and specific developments,” *Journal of Instrumentation*, vol. 11, no. 06, p. C06009, 2016.
- [168] P. Baesso *et al.*, “Toward a RPC-based muon tomography system for cargo containers,” *Journal of Instrumentation*, vol. 9, no. 10, p. C10041, 2014.
- [169] X. Chen *et al.*, “The performance study of MRPCs used for muon tomography,” *Journal of Instrumentation*, vol. 14, no. 06, p. C06012, 2019.
- [170] A. Blanco *et al.*, “RPC-PET: a new very high resolution PET technology,” in *IEEE Symposium Conference Record Nuclear Science 2004.*, vol. 4, p. 2356, 2004.
- [171] P. Martins *et al.*, “Towards very high resolution RPC-PET for small animals,” *Journal of Instrumentation*, vol. 9, no. 10, pp. C10012–C10012, 2014.
- [172] D. Watts *et al.*, “The use of multi-gap resistive plate chambers for in-beam PET in proton and carbon ion therapy,” *Journal of Radiation Research*, vol. 54, p. 136, 2013.
- [173] M. Nizam *et al.*, “Feasibility study for Time Of Flight PET imaging based on six gap MRPC,” *Journal of Instrumentation*, vol. 14, no. 09, p. C09010, 2019.
- [174] G. Aielli *et al.*, “RPC front-end electronics for the ATLAS LVL1 trigger detector,” *Nucl. Instrum. Methods A*, vol. 409, no. 1, p. 291, 1998.
- [175] M. Abbrescia *et al.*, “New developments on front-end electronics for the CMS Resistive Plate Chambers,” *Nucl. Instrum. Methods A*, vol. 456, no. 1, p. 143, 2000. Proceedings of the 5th Int. Workshop on Resistive Plate Chambers and Related Detectors.
- [176] F. Anghinolfi *et al.*, “NINO: an ultrafast low-power front-end amplifier discriminator for the time-of-flight detector in the ALICE experiment,” *IEEE Transactions on Nuclear Science*, vol. 51, no. 5, p. 1974, 2004.
- [177] M. Petriş *et al.*, “In-beam test of the RPC architecture foreseen to be used for the CBM-TOF inner wall,” *Journal of Physics: Conference Series*, vol. 1023, p. 012007, 2018.

-
- [178] M. Ciobanu *et al.*, “PADI, an Ultrafast Preamplifier - Discriminator ASIC for Time-of-Flight Measurements,” *IEEE Transactions on Nuclear Science*, vol. 61, no. 2, p. 1015, 2014.
- [179] M. Ciobanu *et al.*, “PADI, a fast Preamplifier - Discriminator for Time-of-Flight measurements,” in *2008 IEEE Nuclear Science Symposium Conference Record*, p. 2018, 2008.
- [180] F. Dulucq *et al.*, “HARDROC: Readout chip for CALICE/EUDET Digital Hadronic Calorimeter,” in *IEEE Nuclear Science Symposium Medical Imaging Conference*, p. 1678, 2010.
- [181] A. Steen, “Results of the CALICE SDHCAL technological prototype,” *Journal of Physics: Conference Series*, vol. 587, p. 012035, 2015.
- [182] OMEGA, “Products presentation.” <https://portail.polytechnique.edu/omega/en/products/products-presentation>. [Online; accessed 22-November-2019].
- [183] D. Cussans *et al.*, “A readout system for a cosmic ray telescope using Resistive Plate Chambers,” *Journal of Instrumentation*, vol. 8, no. 03, pp. C03003–C03003, 2013.
- [184] M. Bouchel *et al.*, “SKIROC : A front-end chip to read out the imaging silicon-tungsten calorimeter for ILC,” in *2007 IEEE Nuclear Science Symposium Conference Record*, vol. 3, p. 1847, 2007.
- [185] J. Fleury *et al.*, “Petiroc, a new front-end ASIC for time of flight application,” in *2013 IEEE Nuclear Science Symposium and Medical Imaging Conference (2013 NSS/MIC)*, p. 1, 2013.
- [186] Weeroc, “Hardroc 3B.” <https://www.weeroc.com/products/other-read-out/hardroc-3b>. [Online; accessed 23-November-2019].
- [187] S. Manen *et al.*, “FEERIC, a very-front-end ASIC for the ALICE muon trigger resistive plate chambers,” in *2013 IEEE Nuclear Science Symposium and Medical Imaging Conference (2013 NSS/MIC)*, p. 1, 2013.
- [188] P. Dupieux *et al.*, “Upgrade of the ALICE muon trigger electronics,” *Journal of Instrumentation*, vol. 9, no. 09, p. C09013, 2014.
- [189] D. Belver *et al.*, “Performance of the Low-Jitter High-Gain/Bandwidth Front-End Electronics of the HADES tRPC Wall,” *IEEE Transactions on Nuclear Science*, vol. 57, no. 5, p. 2848, 2010.
- [190] NXP, “BGM1013 MMIC wideband amplifier.” <https://www.nxp.com/docs/en/data-sheet/BGM1013.pdf>. [Online; accessed 23-November-2019].

- [191] Maxim Integrated Products, “Dual ECL and Dual/Quad PECL, 500ps, Ultra-High-Speed Comparators.” <https://datasheets.maximintegrated.com/en/ds/MAX9600-MAX9602.pdf>. [Online; accessed 23-November-2019].
- [192] Texas Instruments, “OPA690 Wideband, Voltage-Feedback Operational Amplifier With Disable.” <http://www.ti.com/lit/ds/sbos223g/sbos223g.pdf>. [Online; accessed 23-November-2019].
- [193] M. Bogomilov *et al.*, “The HARP RPC time-of-flight system,” *Nucl. Instrum. Methods A*, vol. 508, no. 1, p. 152, 2003. Proceedings of the Sixth International Workshop on Resistive Plate Chambers and Related Detectors.
- [194] A. Schüttauf *et al.*, “Performance of the Multistrip-MRPCs for FOPI,” *Nuclear Physics B - Proceedings Supplements*, vol. 158, p. 52, 2006. Proceedings of the 8th International Workshop on Resistive Plate Chambers and Related Detectors.
- [195] D. Belver *et al.*, “Performances of the Front-End Electronics for the HADES RPC TOF wall on a 12C beam,” *Nucl. Instrum. Methods A*, vol. 602, no. 3, p. 788, 2009. Proceedings of the 9th International Workshop on Resistive Plate Chambers and Related Detectors.
- [196] N. Cavallo *et al.*, “Electronics design of the front-end for the RPC muon detector at BaBar,” *Nuclear Physics B - Proceedings Supplements*, vol. 61, no. 3, p. 545, 1998. Proceedings of the Fifth International Conference on Advanced Technology and Particle Physics.
- [197] Texas Instruments, “SNx5LVDx3xx High-Speed Differential Line Receivers.” <http://www.ti.com/lit/ds/symlink/sn751vds386.pdf>. [Online; accessed 23-November-2019].
- [198] E. Balsamo *et al.*, “The OPERA RPCs front end electronics; a novel application of LVDS line receiver as low cost discriminator,” *Journal of Instrumentation*, vol. 7, no. 11, p. P11007, 2012.
- [199] J. Repond, “Construction of a Digital Hadron Calorimeter,” in *International Linear Collider Workshop (LCWS10 and ILC10) Beijing, China, March 26-30, 2010*.
- [200] Rhode & Schwarz RTO 1014, “RTO Digital Oscilloscope.” https://www.rohde-schwarz.com/webhelp/rto_html_usermanual_en_1/RTO_HTML_UserManual_en.htm. [Online; accessed 25-November-2019].
- [201] D. González-Díaz *et al.*, “The effect of temperature on the rate capability of glass timing RPCs,” *Nucl. Instrum. Methods A*, vol. 555, no. 1, p. 72, 2005.
- [202] P. Assis *et al.*, “R&D for future SiPM cameras for Fluorescence and Cherenkov Telescopes,” in *Proceedings, 32nd International Cosmic Ray Conference (ICRC 2011): Beijing, China, August 11-18, 2011*, vol. 3.

-
- [203] FTDI, “FT2232H Dual High Speed USB to Multipurpose UART/FIFO IC.” https://www.ftdichip.com/Support/Documents/DataSheets/ICs/DS_FT2232H.pdf. [Online; accessed 21-January-2020].
- [204] Mini-Circuits, “MAR-8ASM+ datasheet.” <https://www.minicircuits.com/pdfs/MAR-8ASM+.pdf>. [Online; accessed 6-January-2020].
- [205] Analog Devices, “Rail-to-Rail, Very Fast, 2.5 V to 5.5 V, Single-Supply LVDS Comparators: ADCMP604/ADCMP605.” https://www.analog.com/media/en/technical-documentation/data-sheets/ADCMP604_605.pdf. [Online; accessed 6-January-2020].
- [206] Texas Instruments, “8-/10-/12-Bit, Octal-Channel, Ultra-Low Glitch, Voltage Output, Two-Wire Interface Digital-to-Analog Converters.” <http://www.ti.com/lit/ds/symlink/dac7578.pdf>. [Online; accessed 8-January-2020].
- [207] Intel, “8-/10-/12-Bit, Octal-Channel, Ultra-Low Glitch, Voltage Output, Two-Wire Interface Digital-to-Analog Converters.” https://www.intel.com/content/dam/www/programmable/us/en/pdfs/literature/hb/cyc3/cyclone3_handbook.pdf. [Online; accessed 27-January-2020].
- [208] M. Firlej *et al.*, “Development of front-end electronics for LumiCal detector in CMOS 130 nm technology,” *Journal of Instrumentation*, vol. 10, no. 01, p. C01018, 2015.
- [209] S. Di Lorenzo *et al.*, “PARISROC, a photomultiplier array integrated read out chip,” in *Nuclear Science Symposium Conference Record (NSS/MIC), 2009 IEEE*, pp. 1074–1081, 2009.
- [210] Tektronix, “AFG3000 Series Manual.” <https://www.tek.com/signal-generator/afg3000-function-generator-manual/afg3000-series-1>. [Online; accessed 8-January-2020].
- [211] P. Assis, “Measurement of the water-Cherenkov detector response to inclined muons using an RPC hodoscope,” *PoS*, vol. ICRC2015, p. 620, 2016.
- [212] A. Aab *et al.*, “Studies on the response of a water-Cherenkov detector of the Pierre Auger Observatory to atmospheric muons using an RPC hodoscope,” *Journal of Instrumentation*, vol. Approved for publication, 2020.
- [213] P. Assis *et al.*, “A large area TOF-tracker device based on multi-gap Resistive Plate Chambers,” *Journal of Instrumentation*, vol. 11, no. 10, p. C10002, 2016.
- [214] B. Rosário, “Development of a Cosmic Ray Telescope,” Master’s thesis, Instituto Superior Técnico, Universidade de Lisboa, Portugal, 2016.
- [215] Hamamatsu, “MPPC and MPPC module for precision measurement.” https://www.hamamatsu.com/resources/pdf/ssd/mppc_kapd0004e.pdf. [Online; accessed 14-January-2020].

BIBLIOGRAPHY

- [216] Weeroc, “MAROC3A software and test board user guide.” <https://www.weeroc.com/my-weeroc/download-center/maroc-3a/54-maroc-3a-evaluation-board-user-guide/file>. [Online; accessed 14-January-2020].
- [217] R. Luz, “Development of a data acquisition system based on the family of ASICs ROC,” Master’s thesis, Instituto Superior Técnico, Universidade de Lisboa, Portugal, 2014.
- [218] Weeroc, “MAROC 3A one sheet description.” <https://www.weeroc.com/my-weeroc/download-center/maroc-3a/4-maroc-3a-one-sheet-description/file>. [Online; accessed 17-January-2020].
- [219] LIP, “E-CRLAB.” <https://www.lip.pt/?section=infrastructures&page=infrastructures-ecrlab&projectid=81>. [Online; accessed 20-January-2020].
- [220] Intel, “Cyclone Device Handbook, Volume 1.” https://www.intel.com/content/dam/www/programmable/us/en/pdfs/literature/hb/cyc/cyc_c5v1.pdf. [Online; accessed 21-January-2020].
- [221] TE connectivity, “MICTOR SB Vertical Connector for Surface Mount Technology (SMT) Printed Circuit (PC) Board Applications.” https://www.te.com/commerce/DocumentDelivery/DDEController?Action=showdoc&DocId=Specification+Or+Standard%7F114-13116%7FC%7Fpdf%7FEnglish%7FENG_SS_114-13116_C.pdf%7F1658013-5. [Online; accessed 21-January-2020].
- [222] Intel, “Cyclone IV Device Handbook.” <https://www.intel.com/content/dam/www/programmable/us/en/pdfs/literature/hb/cyclone-iv/cyclone4-handbook.pdf>. [Online; accessed 21-January-2020].
- [223] Intel, “Intel Quartus Prime Standard Edition Handbook Volume 1 Design and Synthesis.” <https://www.intel.com/content/dam/www/programmable/us/en/pdfs/literature/hb/qts/archives/qts-qps-5v1-17-0.pdf>. [Online; accessed 22-January-2020].
- [224] Texas Instruments, “TPS382x Voltage Monitor With Watchdog Timer.” <http://www.ti.com/lit/ds/symlink/tps3828.pdf>. [Online; accessed 22-January-2020].
- [225] Analog Devices, “LTC2242-12 - 12-Bit, 250Msps ADC.” <https://www.analog.com/media/en/technical-documentation/data-sheets/224212fc.pdf>. [Online; accessed 21-January-2020].
- [226] Miguel Ferreira, “MARTA DAQ V.” https://www.lip.pt/~miguel/Marta_DAQ/index.html. [Online; accessed 20-January-2020].

-
- [227] Intel, “INTEL CYCLONE 10 LP FPGA.” <https://www.intel.com/content/www/us/en/products/programmable/fpga/cyclone-10/lp.html>. [Online; accessed 27-January-2020].
- [228] R. Brun and F. Rademakers, “ROOT — An object oriented data analysis framework,” *Nucl. Instrum. Methods A*, vol. 389, no. 1, 1997. New Computing Techniques in Physics Research V.
- [229] D. Breton, “A normalized USB interface based on the FT245B chip from FTDI.” http://lalusb.free.fr/Firmware/Documentation/en/USB_23_en.pdf. [Online; accessed 23-January-2020].
- [230] Intel, “IP and Megafunctions.” <https://www.intel.com/content/www/us/en/programmable/support/literature/lit-ip.html>. [Online; accessed 7-February-2020].
- [231] P. Assis *et al.*, “Charge distribution measurement of MARTA’s RPCs,” *to be published*, 2020.
- [232] J. Machado *et al.*, “Performance of timing Resistive Plate Chambers with protons from 200 to 800 MeV,” *Journal of Instrumentation*, vol. 10, no. 01, p. C01043, 2015.
- [233] A. Blanco *et al.*, “Performance of timing resistive plate chambers with relativistic neutrons from 300 to 1500 MeV,” *Journal of Instrumentation*, vol. 10, no. 02, p. C02034, 2015.
- [234] T. Ullrich and Z. Xu, “Treatment of errors in efficiency calculations,” 2007.
- [235] S. Park *et al.*, “Charge distribution dependency on gap thickness of CMS endcap RPC,” *Journal of Instrumentation*, vol. 11, no. 11, p. C11034, 2016.
- [236] R. Luz, “RPC hodoscope for SSD quality control,” *GAP2019-017*, 2019.
- [237] R. Luz and B. Tomé, “RPC hodoscope simulation,” *GAP2020-XXX*, 2020.
- [238] Pico Technology, “PicoScope 3000 Series Pc Oscilloscopes and MSOs.” <https://www.picotech.com/download/datasheets/PicoScope3000SeriesDataSheet.pdf>. [Online; accessed 7-March-2020].
- [239] D. Schmidt, “Scintillator Surface Detector simulations for AugerPrime,” *EPJ Web Conf.*, vol. 210, p. 06010, 2019.
- [240] D. Schmidt, *Sensitivity of AugerPrime to the masses of ultra-high-energy cosmic rays*. PhD thesis, KIT, 2018.
- [241] S. Procureur, “Muon imaging: Principles, technologies and applications,” *Nucl. Instrum. Methods A*, vol. 878, p. 169, 2018. Radiation Imaging Techniques and Applications.

BIBLIOGRAPHY

- [242] L. W. Alvarez *et al.*, “Search for Hidden Chambers in the Pyramids,” *Science*, vol. 167, no. 3919, p. 832, 1970.
- [243] P. Checchia, “Review of possible applications of cosmic muon tomography,” *Journal of Instrumentation*, vol. 11, no. 12, p. C12072, 2016.
- [244] Ciência Viva, “Centro de Ciência Viva do Lousal, Mina de Ciência.” <https://www.lousal.cienciaviva.pt/>. [Online; accessed 16-March-2020].